Molecular Mechanism and Inhibition of Human ATIC

Heather Louise Cox

Submitted in accordance with the requirements for the degree of Doctor of Philosophy

University of Leeds

School of Chemistry

September 2013

Intellectual Property Statement

This candidate confirms that the work submitted is her own and that appropriate credit has been given where reference has been made to the work of others.

This copy has been supplied on the understanding that it is copyrighted material and that no quotation from this thesis may be published without proper acknowledgement.

©2013 The University of Leeds and Heather Louise Cox

Acknowledgements

First and foremost, I would like to acknowledge my supervisor, Dr Mike Webb, for his continued support, understanding and patience over the past 5 years. I would also like to thank Dr Bruce Turnbull for always having time for me.

I am appreciative of the help provided by Dr Iain Mansfield with ITC maintenance and welcome advice, and to Dr Arwen Pearson for crystallography tuition.

I am extremely grateful for all the academic and emotional support freely given from all members of the Webb and Turnbull groups past and present (and from a few outsiders). Without this I would have struggled to keep motivated and sane.

I would like to express my gratitude to all the many people who have helped me along the way: to the people who have given their time and effort to pass on expertise of specific techniques and equipment, to those who have engaged me in interesting discussions and broadened my knowledge, and finally to anyone who has indulged me long enough to hear about my research. In particular I would like to thank the support staff at the University of Leeds, without whom much of this work would have been impossible.

This research could not have taken place without the financial support of the ESPRC and Yorkshire Cancer Research and as such I am very grateful for the opportunity to pursue all I have undertaken.

Finally I would like to thank my friends and family, whose understanding has helped ease some of the stresses and frustrations, who provided welcome distractions, and reminders of the world outside.

Abstract

ATIC is a dimeric bifunctional protein, with two distinct catalytic domains located on each monomer. These catalyse the penultimate and final steps of the *de novo* purine biosynthetic pathway. It has been extensively studied as a target for chemotherapeutics and anti-viral inhibitors, but the enzyme has not been fully characterized.

An ordered binding model for AICAR transformylase has been deduced using a new two-dimensional high-throughput assay; from this the true K_M for substrate and cofactor have been measured. The binding affinities for various ligands and small molecules were determined by ITC. Isolation of the IMPCH domain was achieved to analyse binding to a single active site and elucidate the binding parameters observed for both ATIC domains.

The potassium dependence has been defined for the first time as $K_a = 796 \pm 48\mu M$. The role of the potassium ion has been investigated through the characterization of site directed mutants of the potassium binding site.

The thermal stability of ATIC was investigated with DSC and DSF, which suggest that the unfolding landscape of ATIC proceeds initially through the separation of the dimer, and then the IMPCH domain or monomer unfolds at a higher temperature. AICAR, $PteGlu_4$ and KCl all enhance protein stability.

The dimerisation of ATIC was investigated by ITC dilution, dimerisation inhibitors, and fluorescent techniques. Unfortunately, none of these techniques were capable of detecting the monomer-dimer equilibrium. However, the dimerisation of ATIC appears to be an entropically-driven event.

Table of Contents

Intellectual Property Statement ii

Acknowledgements iii

Abstract iv

Abbreviations 8

1 Introduction 10

1.1 The de novo purine biosynthetic pathway 10

1.2 Aminoimidazole-4-carboxamide ribonucleotide Transformylase/ Inosine monophosphate Cyclohydrolase (ATIC) 17

1.3 Regulation of de novo purine biosynthesis 36

1.4 Objectives 41

2 Materials and methods 43

2.2 Materials 44

2.3 Solutions 45

2.4 DNA Primers 48

2.5 Plasmid maps 50

2.6 Genotypes 52

2.7 Molecular biology 52

2.8 Sequencing and in silico tools 58

2.9 Protein expression 58

2.10 Protein purification protocols 59

2.11 Gel electrophoresis- denaturing SDS-PAGE 60

2.12 UV-vis spectrometry 62

2.13 Isothermal Titration Calorimetry (ITC) studies 66

2.14 Differential Scanning Calorimetry 70

2.15 Differential Scanning Fluorimetry 70

2.16 Analytical UltraCentrifugation (AUC) 72
2.17 Mass Spectrometry 72
2.18 Protein Crystallisation 73
2.19 Chemistry experimental 73
3 Characterisation of ATIC 76
3.1 Introduction 76
3.2 Protein purification 77
3.3 Kinetic analysis 81
3.4 Small molecule binding 89
3.5 Thermal stability of ATIC 97
3.6 Discussion and Conclusion 101
4 Isolation of the two domains of ATIC 106
4.1 Truncation mutants of ATIC 106
4.2 Discussion and Conclusion 119
5 Assaying dimerisation of ATIC 121
5.1 Biophysical characterisation 121
5.2 Use of small molecule probes 124
5.3 Fluorescently labelled ATIC 134
5.4 Conclusion 144
6 Potassium dependence of human ATIC 145
6.1 Metal dependence of ATIC 145
6.2 Cloning, overexpression and purification of site-directed mutants of human ATIC 148
6.3 Characterisation of potassium binding site mutants 154
6.4 AICAR KM of site-directed mutants 171
6.5 Discussion 172

7 Summary and conclusions 176

7.1 Summary 176

7.2 Future work 179

7.3 Conclusions 182

8 Bibliography 183

9 Appendix 191

9.1 ITC traces 191

9.2 Sequence Alignments 196

Abbreviations

10-f H_4F	10-formyl tetrahydrofolate
10-f-H_2F	10-formyl-dihydrofolate
ADP	Adenosine diphosphate
AICAr	5-amino-4-imidazolecarboxamide riboside
AICAR	Aminoimidazole-4-carboxamide ribonucleotide
AIR	Aminoimidazole ribonucleotide
ALCL	Anaplastic large cell lymphomas
ALK	Anaplastic lymphoma kinase
AMP	Adenosine monophosphate
AMPK	AMP kinase
ATIC	Aminoimidazole-4-carboxamide ribonucleotide transformylase inosine monophosphate cyclohydrolase
ATP	Adenosine triphosphate
AUC	Analytical ultracentrifugation
B. subtilis	*Bacillus subtilis*
CAIR	Carboxyaminoimidazole ribonucleotide
DDATHF	5,10-Dideazatetrahydrofolate
DNA	Deoxyribonucleic acid
DSC	Differential scanning calorimetry
DSF	Differential scanning fluorimetry
E. coli	*Escherichia coli*
FAICAR	Formyl AICAR
FGAM	*N*-formylglycinamidine ribonucleotide
FGAR	*N*-Formylglycinamide ribonucleotide
GAR	Glycinamide ribonucleotide synthetase
GDP	Guanosine diphosphate
GMP	Guanosine monophosphate
GTP	Guanosine triphosphate
H_4F	Tetrahydrofolate
HGPT	Hydroxanthine guanine phosphoribosyl transferase
IMP	Inosine monophosphate
IMPCH	Inosine monophosphate cyclohydrolase

ITC	Isothermal titration calorimetry
kbp	Kilo base pairs
kDa	Kilo daltons
M. jannaschii	*Methanocaldococcus jannaschii*
MTX	Methotrexate
PCR	Polymerase chain reaction
PRA	5-phosphoribosylamine
PRPP	Phosphoribosyl pyrophosphate
$PteGlu_4$	Pteridine tetraglutamate
RNA	Ribonucleic acid
SAICAR	*N*-Succinocarboxamide-5-aminoimidazole ribonucleotide
SDS PAGE	Sodium dodecyl sulphate polyacrylamide gel electrophoresis
TDAF	5,8,10-trideazafolate
XMP	Xanthosine monophosphate

1 Introduction

1.1 The de novo purine biosynthetic pathway

Purine nucleotides are required for the synthesis of DNA and RNA in all organisms[1]. They are formed by two independent routes, either *de novo* or *via* a salvage pathway. The *de novo* biosynthetic pathway (Figure 1-1) provides purines by converting phosphoribosyl pyrophosphate (PRPP) to inosine monophosphate (IMP) (Figure 1-2) *via* a ten step enzymatic route,whereas the salvage pathway generates IMP, GMP and AMP directly through the reaction of PRPP with the free bases hypoxanthine, xanthine and adenine which are obtained through the diet. Use of this salvage pathway economises on the energy balance and nitrogen consumption of the organism. The other building blocks of DNA and RNA, pyrimidines, are also created by either the *de novo* pyrimidine biosynthetic pathway or the pyrimidine salvage pathway[2].

The *de novo* biosynthesis of purines generates the 'first purine' IMP from PRPP through ten distinct enzymatic activities which are summarised in Figure 1-1[3]. The synthesis of 5-phosphoribosylamine (PRA) is catalysed by PRPP amidotransferase (step 1) which transfers ammonia, obtained from the hydrolysis of glutamine, to phosphoribosylpyrophosphate. The hydrolysis and the transfer reactions occur in separate domains which are linked by a channel for ammonia[4]. Glycinamide ribonucleotide synthetase (GAR synthetase, step 2) attaches glycine to the PRA amino group to form glycinamide ribonucleotide (GAR). *N*-Formylglycinamide ribonucleotide (FGAR) is then formed by GAR transformylase (step 3) which uses 10-formyl tetrahydrofolate to formylate GAR. *N*-Formylglycinamidine ribonucleotide synthetase (FGAR synthetase, step 4) catalyzes the amidation of FGAR to form *N*-formylglycinamidine ribonucleotide (FGAM). Aminoimidazole ribonucleotide

synthase (AIR synthetase, step 5) performs a ring-closing reaction on FGAM to produce aminoimidazole ribonucleotide (AIR). AIR carboxylase (step 6) then catalyzes the carboxylation of AIR by CO_2 to give carboxyaminoimidazole ribonucleotide (CAIR). *N*-Succinocarboxamide-5-aminoimidazole ribonucleotide synthetase (SAICAR synthetase, step 7) catalyzes the ligation of the CAIR carboxylate group to the amino group of an aspartate to produce *N*-succinocarboxamide-5-aminoimidazole ribonucleotide (SAICAR) Aminoimidazole-4-carboxamide ribonucleotide (AICAR) is formed by the β-elimination of fumarate from SAICAR by Adenylosuccinatelyase (step 8). In the penultimate step, AICAR is converted to formyl AICAR (FAICAR) by Aminoimidazole-4-carboxamide ribonucleotidetransformylase (AICAR transformylase, step 9) which catalyses the transfer of a formyl group from 10-formyl tetrahydrofolate. Inosine monophosphate cyclohydrolase (IMP cyclohydrolase, step 10) organises the ring-closure reaction of FAICAR with the elimination of water to produce the final product of the pathway, IMP.

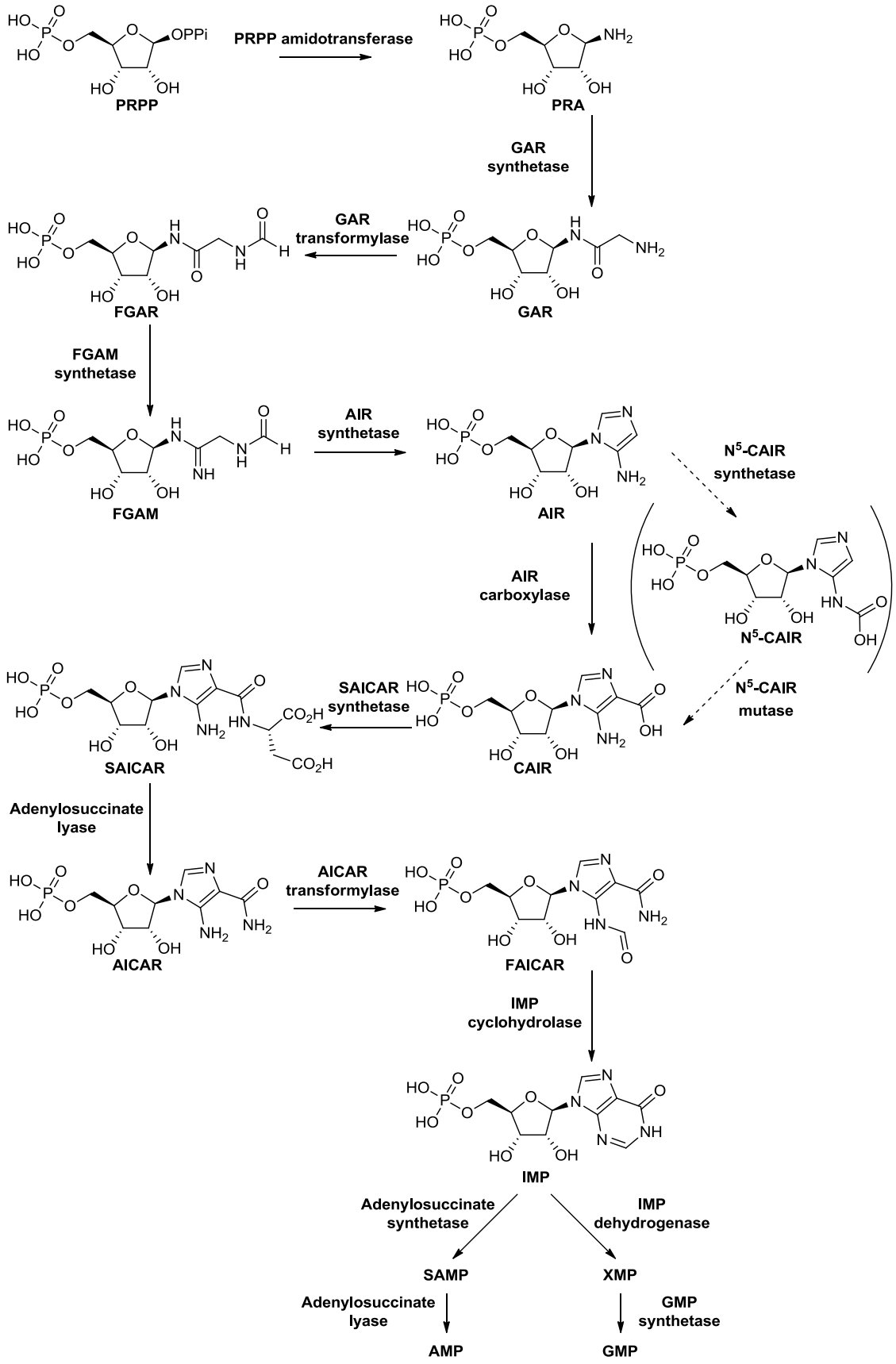

Figure 1-1:The *de novo* purine biosynthetic pathway. The conversion of PRPP to IMP proceeds *via* 10 enzymatic steps. Intermediate in brackets is unique to bacteria. IMP is then converted to AMP by adenylosuccinate synthetase and adenylosuccinate lyase, or GMP by IMP dehydrogenase and GMP synthetase.

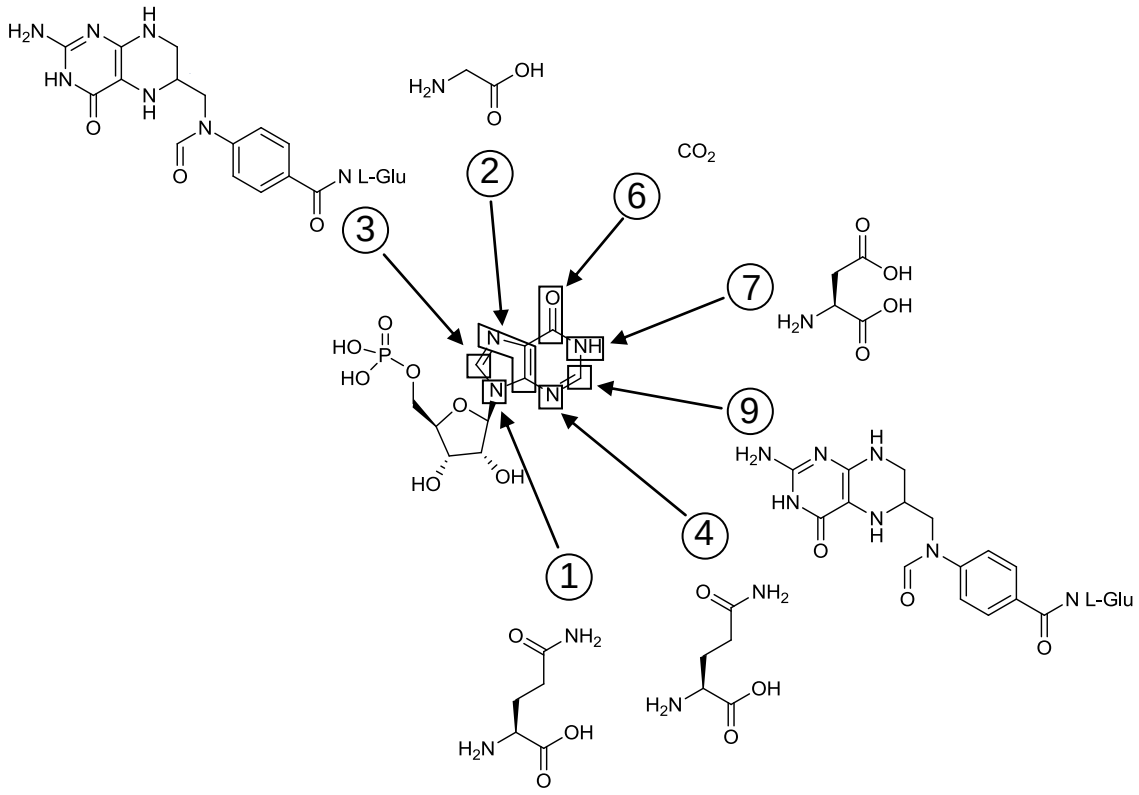

Figure 1-2: R5′-P, ribose 5′-phosphate. The numbers indicate the step number in which the highlighted atoms are synthesised in the *de novo* purine biosynthetic pathway. Steps 1 and 4 incorporate nitrogen from glutamine, step 2 incorporates atoms from glycine, steps 3 and 9 incorporate carbon from a folate co-factor, step 6 incorporates carbon dioxide and step 7 incorporates nitrogen from an aspartic acid. Steps 5 and 10 are cyclisation reactions so no new atoms are incorporated in these steps[5].

1.1.1.1 Discovery of the pathway

The first studies of the *de novo* purine biosynthetic pathway investigated the incorporation of ^{15}N into the ring structure of purines in tissues from rats and pigeons through the administration of labelled urea and ammonium citrate[2]. This showed that purines could be synthesized by the body, rather than relying on purines absorbed through the diet. A basic characterisation of the biosynthetic pathway was published by Buchanan *et al.* in 1959, who conducted experiments on enzymes extracted from pigeon and chicken livers[6], the results showed that purine synthesis *de novo* consists of 9

intermediates that are converted by 10 distinct enzymes. Since then, the *de novo* pathway has been extensively studied in mammalian[7], avian[6, 8], yeast and bacterial systems[9].

The pathway in *Escherichia coli* requires an extra enzyme involved in step 6. Firstly, N^5-carboxyaminoimidazole ribonucleotide synthetase (N^5-CAIR synthetase) catalyses the formation of N^5-CAIR from AIR, ATP and carbon dioxide, then N^5-CAIR mutase forms CAIR[10] (Figure 1-1). A significant body of work was conducted by Flaks *et al.* into discerning the enzymes and pathway intermediates from avian liver[11], detailing the purification procedures and assay conditions for each of the enzymes in the pathway. Several of the *de novo* purine pathway enzymes exist as multifunctional proteins where activities are combined onto a single polypeptide. A trifunctional protein containing GAR synthetase, GAR transformylase and AIR synthetase activities has been isolated from both human and avian sources; and confirmed by functional complementation in bacteria and yeast[12]. AIR carboxylase and SAICAR synthetase (steps 6 and 7) are located on the same bifunctional protein[12d], and the final two steps of the pathway are catalysed by a single protein exhibiting AICAR transformylase and IMP cyclohydrolase activities[13]. The gene designations for vertebrates, yeast and bacteria are summarised in Table 1.1.

		Gene designation		
Step of pathway	Enzyme	Vertebrates	Yeast	Bacteria
1	PRPP amidotransferase EC 2.4.2.17	PPAT	Ade4	PurF
2	GAR synthetase EC 6.3.4.13	GART	Ade5	PurD
3	GAR transformylase EC 2.1.2.2	GART	Ade8	PurN
4	FGAM synthetase EC 6.3.5.3	PFAS	Ade6	PurL
5	AIR synthetase EC 6.3.3.1	GART	Ade7	PurM
6	AIR carboxylase EC 4.1.1.21	PAICS	Ade2	-
6a	N^5-CAIR synthetase EC 6.3.4.18	-	-	PurK
6b	N^5-CAIR mutase EC 5.4.99.18	-	-	PurE
7	SAICAR synthetase EC 6.3.2.6	PAICS	Ade1	PurC
8	Adenylosuccinate lyase EC 4.3.2.2	ADSL	Ade13	PurB
9	AICAR transformylase EC 2.1.2.3	ATIC	Ade16/17	PurH
10	IMP cyclohydrolase EC 3.5.4.10	ATIC	Ade16/17	PurH

Table 1.1: Summary of the enzymes of the *de novo* purine biosynthetic pathway with the gene designations found in mammals, yeast and bacteria.

De novo purine synthesis is active in a wide range of tissues including the liver[11, 14], kidney[15] and skeletal muscle[16], human peripheral blood lymphocytes[17], bone marrow[18] and brain[14]. Activity of *de novo* synthesis is known to change with stages of the cell life cycle, there is high activity in the early development of certain tissues[19] including brain, liver, kidney and spleen, and also during wound healing[20]. Conversely there is a dramatic loss of activity (approximately 95%) in G1 phase-arrested mammalian cells[21] and no activity in intestinal mucosa that rely completely on the salvage pathway for purine synthesis[22].

Plants also use the pathway for purine biosynthesis, for example tropical legumes utilise the *de novo* purine pathway to synthesise ureides, which are major nitrogen-fixation end products found in root nodules[23]. The enzymatic activities of the pathway are all located on individual proteins, except for AICAR transformylase and IMP cyclohydrolase which are located on a bifunctional protein. The pathway has been studied in soybean, mothbean and cowpea nodules and has been found to have similar substrate and cofactor requirements to other systems.

More recently, a search of the Integrated Microbial Genome system has started to elucidate purine biosynthesis in archaea[24]. Archaea encode several unique enzymes for purine biosynthesis, several species are able to form purines despite certain enzyme activities found in other organisms being completely absent. In non-folate containing archaea, AICAR transformylase activity is replaced with an archaeal signature PurP gene product which uses formate as a cofactor[25]. In *M. jannaschii* the PurO gene product contains IMP cyclohydrolase activity, but has a structure and sequence that is completely unrelated to that seen in other organisms[26]. The crystal structure of archaeal IMP cyclohydrolase has been solved in complex with IMP (to 2.0 Å

resolution) and AICAR (to 2.6 Å resolution). The PurO gene product has glutamate and arginine as the catalytic residues, compared to the tyrosine and aspartate residues found in all other organisms. The mechanism of cyclisation employed by PurO is analogous to that of GFP chromophore maturation[27]. There is much variation in the archaeal pathway with some species producing a bifunctional enzyme that catalyses steps 9 and 10, as is found in other organisms, as well as other combinations of PurP, PurO and PurH[24]. Several species are purine auxotrophs and rely on exogenous purines for growth. These include the parasitic protozoa[28]such as *Plamsmodia*[29] and *Toxoplasma*[30].

1.2 Aminoimidazole-4-carboxamide ribonucleotide Transformylase/ Inosine monophosphate Cyclohydrolase (ATIC)

Aminoimidazole-4-carboxamide ribonucleotide Transformylase Inosine monophosphate Cyclohydrolase (ATIC) is a bifunctional enzyme of the *de novo* purine biosynthesis pathway. ATIC catalyzes the final two steps of this pathway, with each reaction occurring in a specific catalytic domain. One domain contains the aminoimidazole-4-carboxamide ribonucleotide transformylase (AICAR transformylase) active site. This domain binds the substrate AICAR and cofactor 10-formyl tetrahydrofolate (10-f H_4F), and facilitates the transfer of a formyl group from 10-f H_4F to the exocyclic amino group of AICAR to give the products formyl AICAR (FAICAR) and tetrahydrofolate (H_4F). The second step is then catalysed by the inosine monophosphate cyclohydrolase (IMPCH) domain which causes a ring-closure reaction in FAICAR to form inosine monophosphate (IMP) with the loss of a molecule of water. The reaction scheme for these 2 steps is shown in Figure 1-3.

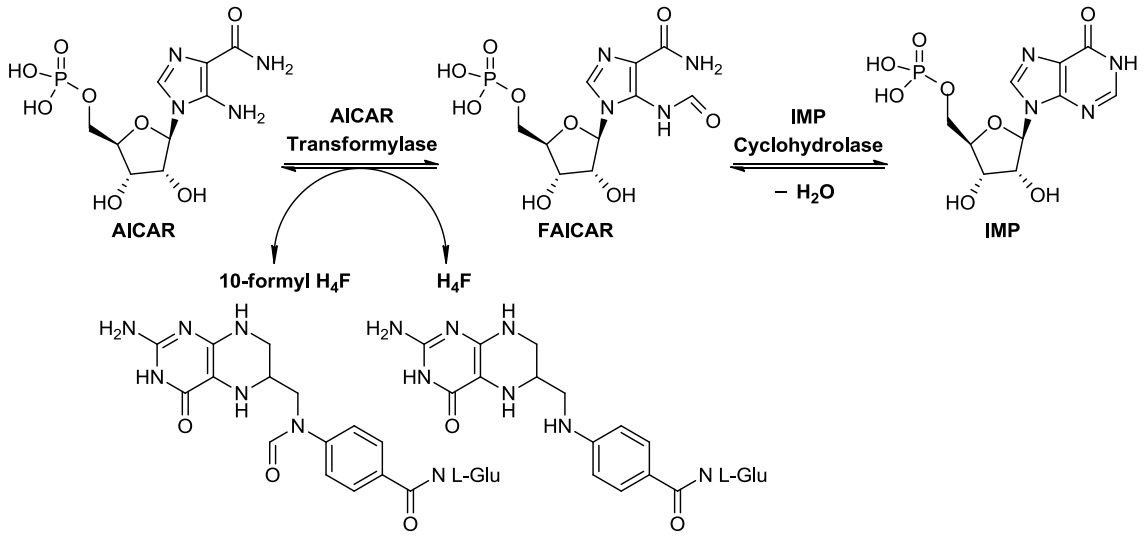

Figure 1-3: A summary of the reactions catalysed by ATIC. AICAR transformylase transfers a formyl group from the 10-f-H_4F cofactor to the AICAR substrate before IMP cyclohydrolase catalyses a ring closing reaction with the loss of H_2O.

1.2.1.1 Identification and purification

Two isoforms of human ATIC were originally reported, hATIC-a[31] and hATIC-b[32], from the sequencing of a cDNA library. They are almost identical with the exception of the *N*-terminal sequence; hATIC-b contains one extra amino acid at its *N*-terminus (MAPGQL) whereas hATIC-a has the sequence (MSSLS). Also, position 165 (in hATIC-b) has glycine substituted for aspartate. A BLAST search of the human genome performed by Vergis noted that the glycine found in hATIC-a must be the product of a point mutation as it is not encoded within the human genome[33]. The *N*-terminal regions of hATIC-a and hATIC-b are both encoded, but it was concluded the second isoform (hATIC-b) is the more common form of human ATIC as it is the most predominant[32]. Closer inspection of the genome sequence suggests that the hATIC-a is an artefact generated as a result of incorrect splicing and will not be expressed *in vivo* (Dr M. E. Webb, personal communication).

Early purification procedures for AICAR transformylase noted the co-purification of IMP cyclohydrolase activity[11]. Truncation mutation studies conducted by Rayl *et al.* demonstrated that the final 2 steps of the *de novo* purine synthesis were contained in different catalytic domains. Two amino-terminal mutants containing only the first 223 and 230 amino acids residues of hATIC-b were found to only exhibit IMPCH activity. A carboxyl-terminal mutant consisting of 406 amino acids was subjected to kinetic analysis and was found to show only AICAR transformylase catalytic activity. This provided evidence that bifunctional ATIC contains 2 separate functional domains[31].

1.2.1.2 The folate cofactor

The formyl donor for the formyl transferase reactions catalysed by GAR transformylase and AICAR transformylase is N^{10}-formyltetrahydrofolic acid (10-f-H_4F)[8]. In cells, the folate cofactor likely exists as folylpoly-γ-glutamates (10-f-H_4PteGlu$_n$). 10-f-H_4PteGlu$_n$ with n=1, 3, 4, 5, 6 and 7 have been analysed as cofactors for AICAR transformylase at physiological [K^+] of 150 mM; with V_{max}/K_m of 1, 52, 250, 93, 120 and 59 for n=1, 3, 4, 5, 6 and 7 respectively[34] demonstrating a preference for the tripolyglutamated form of 10-f-H_4F.

The structure and active site of AICAR transformylase is not consistent with other 10-f-H_4F requiring enzymes[35]. Evidence has been presented that the *in vivo* substrate utilised by AICAR transformylase is not 10-f-H_4F, but instead 10-formyl-dihydrofolate (10-f-H_2F)[36]. This oxidised form was shown to have approximately a 5-fold decrease in K_M values when compared to the K_M measured for 10-f-H_4F. The aforementioned kinetic advantage of 10-f-H_2F was seen when AICAR transformylase from Jurkat-cell

and rat bone marrow was analysed, but the same effect was not significantly demonstrated with AICAR transformylase from chicken liver[36]. In contrast, GAR transformylase is not able to utilise 10-f-H_2F[36-37]. The bioactivity of unnatural (6*R*)-5-formyl tetrahydrofolate and (6*S*)-5,10-methenyltetrahydrofolate can therefore be explained by conversion to 10-f-H_2F, which proceeds with the loss of the carbon-6 asymmetric centre[38]. The formation of the multienzyme complex consisting of GAR transformylase, serine hydroxylmethyltransferase and the trifunctional folate metabolising protein (see section 1.3.1.2) is suggested to channel 10-f-H_4F produced by the trifunctional folate metabolising protein to the GAR transformylase active site[3]. As no such complex is seen with ATIC, the 10-f-H_4F has to diffuse a greater distance to encounter the AICAR transformylase active site, and so has a greater risk of oxidation to 10-f-H_2F. As micromolar concentrations of iron (Fe^{3+}) in solution have been shown to oxidise 10-f-H_4F *in vitro*[39], Cytochrome *c* was suggested to non-enzymatically convert 10-f-H_4F to 10-f-H_2F and was subsequently shown to oxidise both the natural (6*S*)-10-f-H_4F and unnatural (6*R*)-10-f-H_4F isomers[38b]. Cytochrome *c* containing complex IV of rat mitochondria has also been shown to oxidise both isomers of 10-f-H_4F[40]. The observation of exchange from carbon-2 to carbon-8 in the IMP product is seen *in vitro* but cannot be replicated *in vivo*[41]. The carbon exchange can only be achieved if AICAR transformylase utilises 10-f-H_4F as a cofactor (Figure 1-4), therefore, as the exchange is not observed *in vivo*, this lends further support to the suggestion that 10-f-H_2F, not 10-f-H_4F, may be the true cofactor used by AICAR transformylase[42].

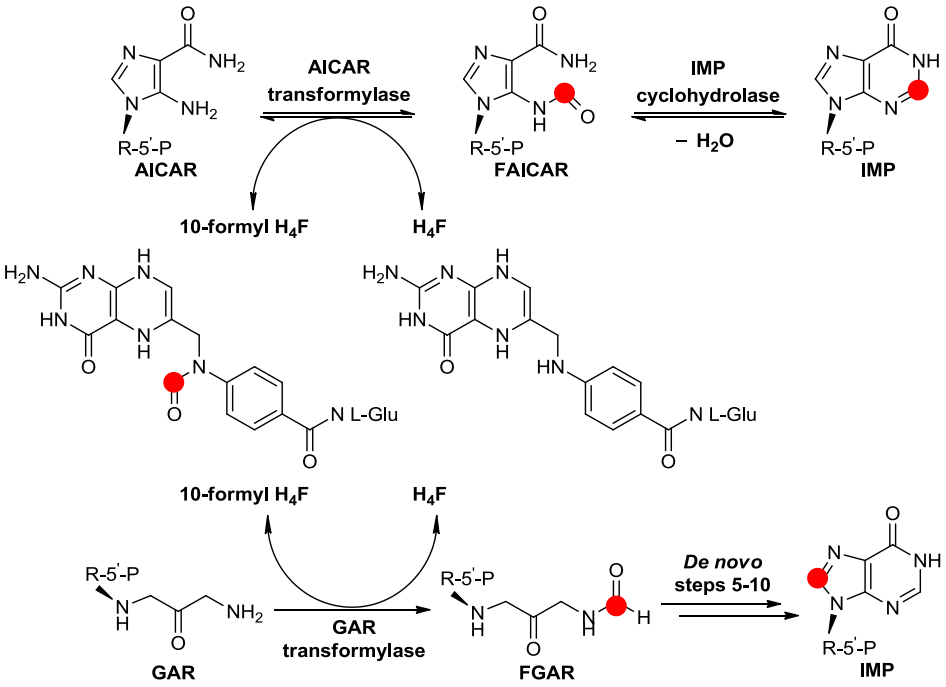

Figure 1-4: The proposed scheme by which carbon-2 can switch to the carbon-8 position in IMP as observed *in vitro*. The IMP cyclohydrolase and AICAR transformylase reactions are reversible which locates carbon-2 onto the tetrahydrofolate to form 10-formyl tetrahydrofolate. This is then the cofactor for the GAR transformylase reaction and positions the former carbon-2 into what will become carbon-8 after conversion to IMP by the remaining *de novo* pathway.

The most commonly used method for analysing AICAR transformylase catalytic turnover is the rapid assay described by Black *et al.*[43]. The assay measures the production of H_4F from the turnover of the 10-f-H_4F cofactor (Figure 1-3), calculated from the increase in absorbance seen at 298 nm, caused by the difference in the absorption spectra of H_4F and10-f-H_4F. The difference in the extinction coefficients is used to determine the rate. The alternative cofactor proposed by Baggott and co-workers, 10-f-H_2F, claims a kinetic advantage over 10-f-H_4F for certain types of AICAR transformylase (Jurkat-cell and rat bone marrow). For analysing the enzyme kinetics of this reaction, the turnover of 10-f-H_2F is followed by monitoring the absorbance change at 312 nm[36]. A more sensitive, but more complicated radioassay has been devised by Szabados *et al.* involving analysis of radiolabeled substrate by

TLC[44]. By using this method the ratio of specific activities of AICAR transformylase:IMPCH were measured to be 1:44.

1.2.1.3 Structure

Human ATIC consists of a single polypeptide chain of 592 amino acids with a molecular mass of 64 kDa. Avian ATIC is 81% homologous to the human enzyme amino acid sequence. Avian ATIC is 593 amino acids long, and so has human ATIC amino acid positions +1, and this needs to be taken into account when comparing structures[31]. On evaluating the human and avian ATIC structures they were found to be highly conserved[45].

The active sites of ATIC were identified when the crystal structure of the avian enzyme was first determined by the Wilson group[46]. ATIC crystallised as a homodimer with an extensive dimer interface of ~5000 $Å^2$. The IMPCH catalytic site is contained in the N-terminal domain in residues 4-199, and the C-terminal domain of residues 200-593 contains the AICAR transformylase activity. These two domains are linked by a unique small substructure that consists of two β-hairpin motifs that form an interlocked 8-stranded β-sheet. In the dimer the catalytic domains are approximately 50 Å apart (Figure 1-5).

The IMPCH domain has α-β-α type structure. The central β-sheet resembles a Rossman fold topology, surrounded on one side by 3 α-helices and 7 on the opposite. One monomer was found to have a bound purine nucleotide that was identified as xanthine monophosphate (XMP). This is bound by an extensive hydrogen bonding network with high affinity (K_i = 0.12 μM)[47], it is acquired in the bacterial cell used to overexpress the protein and remains through the purification process. The IMPCH active site undergoes several conformational changes when a ligand binds. The most significant

change is conducted by residues 103-108 which act to flip Tyr104 and attain its substrate from the bulk solvent[45].

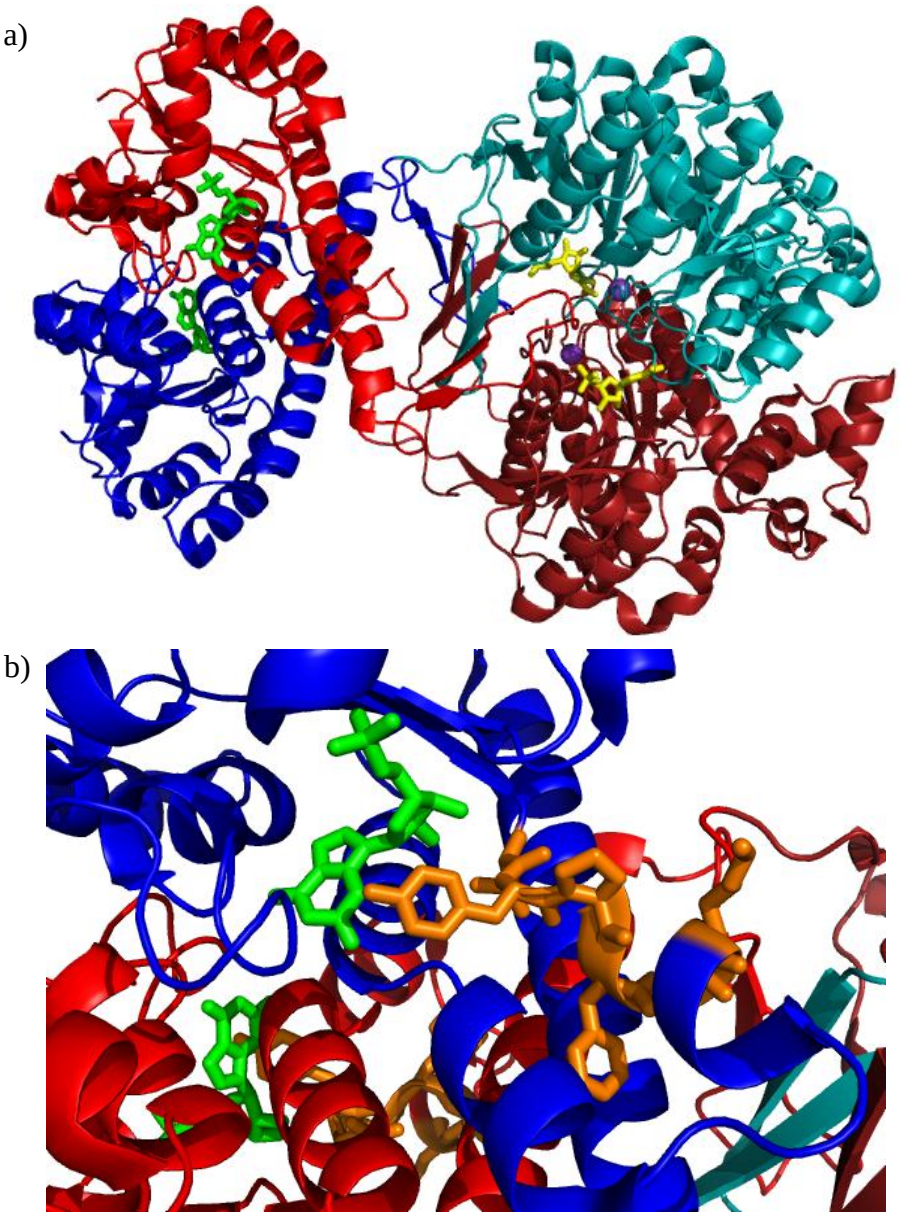

Figure 1-5: Crystal structure of homodimeric avian ATIC at 1.93 Å[47]. Monomer chains are shown in blue and red. a) The IMPCH domain is located in the left portion of the structure and is depicted with XMP (green) bound in the active site. The AICAR transformylase domain (right hand portion) has AICAR (yellow) bound in the active site and shows the position of the 2 bound potassium ions (purple spheres). b) Close up of the IMPCH active site with XMP (green) bound. Residues 103 to 108 are highlighted in orange, Tyr104 points towards the XMP ligand.

The AICAR transformylase domain is more complex and consists of 3 sub-domains 'domain 2' (200-374) and 'domain 3' (469-532) which is inserted into 'domain 4' (375-

593). Domains 2 and 4 are similar and both contain a core 5-stranded β-sheet surrounded by α-helices. Domain 3 is only 64 residues long and is unique in its topology which consists of 4 α–helices and 2 short β–sheets.

The binding mode of AICAR was resolved crystallographically by Wolan *et al*.[47] who observed that AICAR is bound in a 3'-*endo* sugar pucker conformation with the enzyme orientating the carboxamide amino group up away from the imidazole ring. A Multisubstrate Adduct Inhibitor (MAI) β-DADF (6i, Figure 1-9) was used to identify the folate binding site as the enzyme crystallises in the absence of bound folate[48]. β-DADF (**6i** Figure 1-9) represents a covalently-linked AICAR and folate co-factor (K_M = 102 μM)[49] and allowed for characterisation of the folate binding site. The AICAR and folate binding sites were found to be located in a cavity at the dimer interface. AICAR was found to interact more with residues from one monomer of the dimer while the folate co-factor interacted mainly with residues on the opposite monomer, most notably Lys266.

ATIC has previously been shown to participate in a monomer/dimer equilibrium (K_d = 240 ± 50 nM)[33]. AICAR transformylase requires dimerisation for activity to occur, as predicted by the mode of AICAR binding, but IMPCH is still active when the enzyme is monomeric (albeit 6 times less active). The addition of the 10-f-H_4F cofactor with the AICAR substrate stabilises the enzyme in its dimeric form[33].

1.2.1.4 Catalytic mechanism

The first step catalyzed by ATIC is the transfer of a formyl group to an AICAR substrate from a folate cofactor. This reaction is unfavourable (K_{eq} = 0.024 ± 0.001) but the reaction is driven forwards due to the second step which involves an entropically favourable ring-closing reaction on the unfavourably formed FAICAR. FAICAR is a

product inhibitor (K_i = 0.4 ± 0.1 μM) of AICAR transformylase[50]. The rate limiting step is the release of the tetrahydrofolate formed from the turnover of the 10-f-H_4F in the reaction[51]. Coupling the two catalytic domains on a single polypeptide may aid the reaction to go to completion, as the first step is unfavourable and driven forwards by the favourable subsequent reaction. Unexpectedly, there is no substrate channelling within the enzyme between the two active sites, and thus the proximity of the two sites and local concentration gradient between them is thought to be the reason for their coupling[51-52]. AICAR transformylase activity requires ATIC to be in its dimeric form to be catalytically active, since the residues which make up the active site are supplied by both monomers. The 4-carboxamide of the AICAR is positioned by the binding pocket to increase the nucleophilicity of the C5 amide, ready for nucleophillic attack on the formyl group of 10-f-H_4F. Turnover of alternative substrates suggests that the 4-carboxamide participates in proton transfer. The catalytic activity of AICAR transformylase was found to have virtually no pH dependence in the range 6-10.5. The lack of pH dependence was thought to suggest that the ammonium component of a lysine or arginine residue is acting as a general acid catalyst with pK_a greater than 10.5[53]. His267 and Lys266 interact to aid the positioning of the general acid catalyst to the N3 of the AICAR imidazole. His267 is thought to be involved in proton abstraction and Lys266 stabilises the oxyanion transition state and facilitates proton transfer to the N10 of the tetrahydrofolate leaving group, either directly or through His267 or water molecules[47-48, 50]. The crystal structure of avian ATIC determined with β-DADF confirms that a buried Lys267 residue (equivalent to Lys266 in human ATIC) is protonated during formyl transfer[48]. This causes the stabilization of the oxyanion transition state and the following protonation of the tetrahydrofolate leaving group[48] (Figure 1-6).

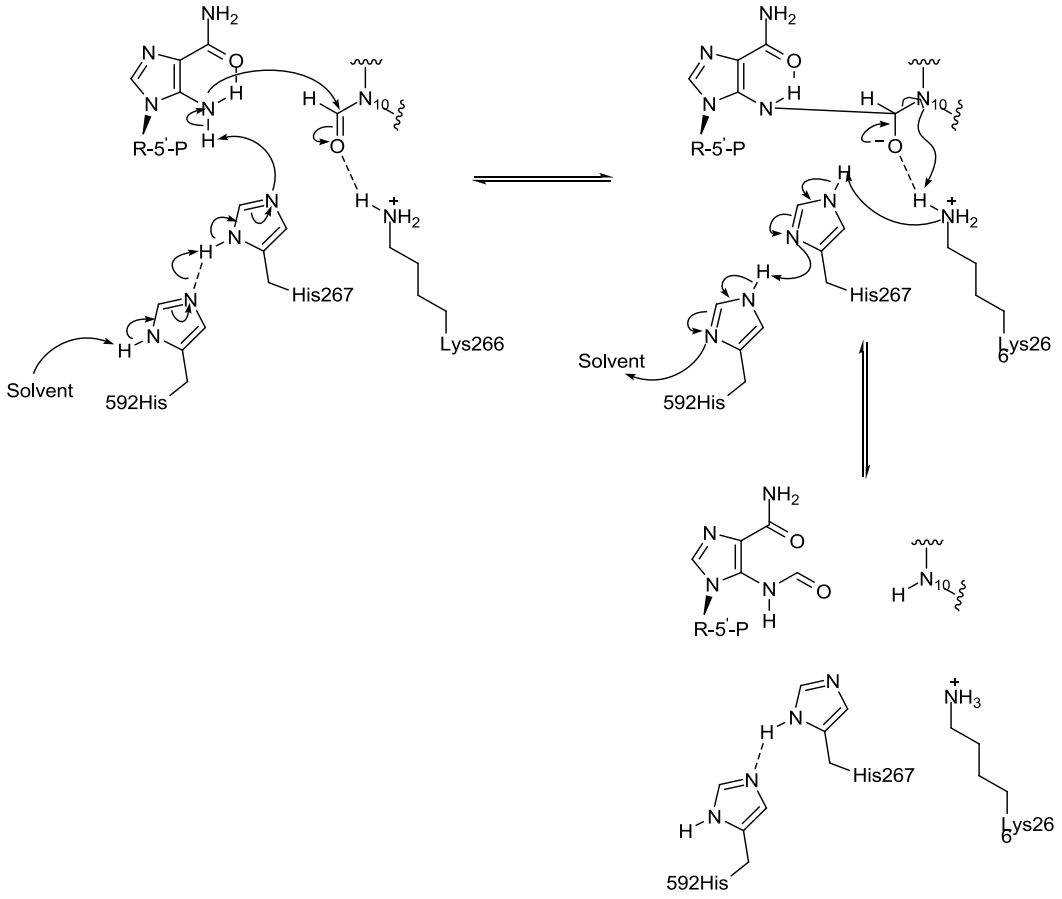

Figure 1-6: The catalytic mechanism of AICAR transformylase. Proton shuffling from the bulk solvent proceeds *via* His592 and His 267.

The catalytic mechanism for IMPCH has been deduced by analysis of ATIC with various inhibitors[54], and mutation studies[45, 55]. Loop residues 103-108 and 65-67 undergo varying degrees of conformational change when substrates or transition state analogues bind giving open, half-closed or closed conformations. Upon substrate binding changes twist Tyr104 into the active site, sheilding the substrate from the bulk solvent and preventing its diffusion out again. The enzyme is then in its closed conformation with residues positioned optimally for intermolecular nucleophilic attack, with Tyr104 and Asp124 residues close to the substrate in an environment that perturbs their pK_a values ready for catalysis[45, 55]. Tyr104 is stabilised by a hydrogen bonding interaction with Lys66. The negatively charged C2 sp^3 centre created in the transition

state is stabilised by an oxyanion hole formed by the backbone amides of Ile125 and Gly126. The side chains of Tyr104 and Asp124 from one monomer and Lys137 from the other, along with bridging water molecules, are important in facilitating catalysis. The interactions from opposite monomer residues are consistent with the increased efficiency but not dependence of the IMPCH catalytic activity upon dimerisation[45].

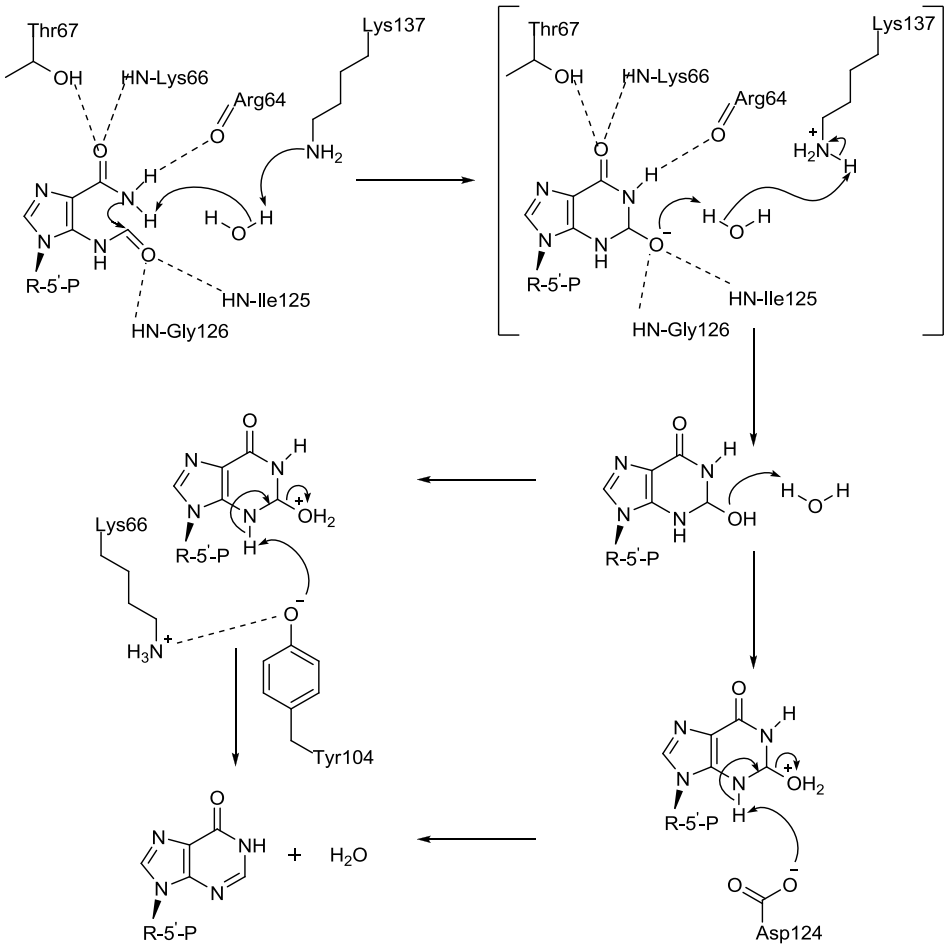

Figure 1-7: Catalytic mechanism of IMP cyclohydrolase. Loss of water is proposed to be catalysed by either Asp124 or Lys66 and Tyr104.

ATIC has a higher activity in potassium containing buffers[31] and two bound potassium ions were identified in the crystal structure[47]. The potassium ion interacts with the backbone carbonyls of Val425, Thr428 and Leu589, the hydroxyls of Ser430 and Ser432 and the carboxyl side chain of Asp539 in domain 4 (Figure 1-8). The precise

role of these metal ions is not known, but metal cofactors in other enzymes are known to have structural or catalytic roles, for example as redox reagents[56]. Potassium is essential for maximal activity[57]. Kinetic characterisation of ATIC AICAR tfase with polyglutamated tetrahydrofolates at 25 mM K^+ and physiological 150 mM K^+ was conducted by Baggott and Krumdieck[34]. An inhibitory effect on the rate was seen with monoglutamated 10-f-H_4F at physiological potassium concentrations. The K_M for AICAR increased two fold when measured at 150 mM K^+. The phases of colonisation of *B. subtilis* are dependent on potassium levels, as potassium is required for the synthesis of purines and pyrimidines so the colonies cannot grow without sufficient potassium[58].

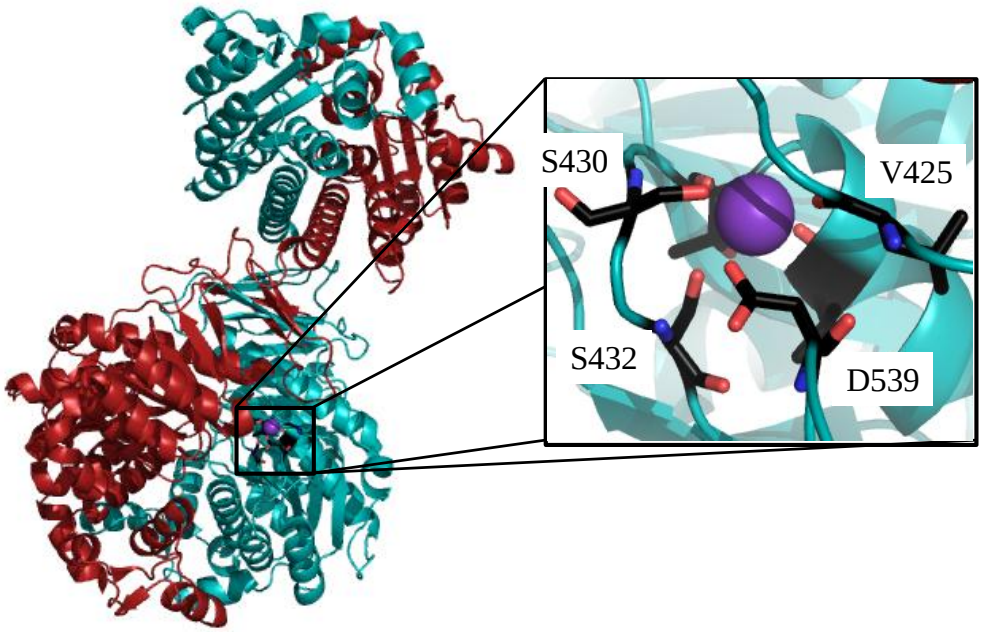

Figure 1-8: Crystal structure of human ATIC highlighting one of the bound potassium ions and the residues surrounding it. S430, S432 and D539 all make side chain interactions, with V425, T428 and L589 interacting through their backbone carbonyl groups.

1.2.1.5 Diseases

There are several diseases associated with aberrations in the *de novo* purine biosynthetic pathway, including autism, muscular dystrophy and lymphoma. Mutations of enzymes within the pathway are associated with various alterations in cell metabolism, and therefore the enzymes of the pathway are potential targets for chemotherapeutics and inhibitors of viral replication.

Hyperuricema is the condition associated with the overproduction of purines. A mutant cell line displaying hyperuricema was shown to have normal levels of PRPP, and instead overproduced purines through an altered sensitivity to the feedback regulation of nucleotides inhibiting amidophosphoriboyltransferase[59]. When cells are not under energy-limiting conditions a high rate of *de novo* synthesis leads to purine excretion[60]. A four fold increase in the *de novo* purine pathway has, however, been linked to patients suffering classic infantile autism, which effects around 20% of the autistic population[61].

In contrast, Duchenne muscular dystrophy (DMD) is associated with structural and metabolic irregularities at the cellular level, including changes to the plasma membrane in erythrocytes[62] and a lack of adenine and guanine nucleotides[63]. The alterations to the cell that interfere with the *de novo* synthesis of IMP in DMD are unknown[63b].

Alteration of a single residue of ATIC has been shown to lead to severe neurological defects, dysmorphic features and blindness in the case of a 4-year old girl[64]. The mutation K426R completely destroys AICAR transformylase activity which causes the build up of AICAR mono-, di-, and tri-phosphates in erythrocytes and the excretion of 5-amino-4-imidazolecarboxamide riboside (AICAr). AICAr affects a number of

biological processes involved with cell metabolism, such as inhibiting carbohydrate[65] and lipid[66] metabolism, and promoting glucose uptake[67]. AICAr is toxic and induces apoptosis in neuroblastoma cells[68]. The monophosphorylated compound, AICAR, accumulates in the erythrocytes of patients suffering from Lesch-Nyhan syndrome[69]. Lesch-Nyhan syndrome is an inherited disorder that affects the synthesis and degradation of purines through the absence or severe lack of hydroxyxanthine guanine phosphoribosyl transferase (HGPT). This causes the build up of atypically high levels of uric acid, neurological defects, and behavioural issues[70]. Unusually high concentrations of PRPP are found in Lesch-Nyhan patients[71]. The behavioural and neurological dysfunctions have been related to abnormalities in the dopamine neuron function in the basal ganglia[72], but the relationship to the overproduction of purines is still unknown.

ATIC is also implicated in Anaplastic Large Cell Lymphomas (ALCLs), which can be separated into two subcatagories, Anaplastic Lymphoma Kinase (ALK)-positive and ALK-negative[73]. Once activated ALK-fusion proteins lead to cellular transformation through a complex signalling network. The N-terminus of ATIC fuses to the intracytoplasmic region of ALK to form a novel oncogenic dimeric protein[73-74]. The ATIC-ALK chimera is found in the cytoplasm[75] and is the product of the chromosomal inversion inv(2)(p23;q35)[76]. Detection of ALK-fusion protein allows for further analysis of disease progression and outcome; ALK-positive ALCLs have a better prognosis than ALK-negative ALCLs[77].

AMP kinase (AMPK) regulates the energy sources within cells. AMPK is activated when the AMP:ATP ratio increases, and responds by phosphorylating a variety of substrates which leads to inhibition of ATP consuming processes (such as glucogenesis,

protein and lipid synthesis) and activation of ATP generating processes. Cancer cells use glucose at a higher rate compared to that of healthy cells as accelerated cell growth is energetically demanding. Being able to regulate a basic metabolic process that is altered only in the cancer cells means AMPK is a potential target for chemotherapeutics and cancer prevention[78]. AICAR can activate AMPK by mimicking AMP[79]. Inhibiting AICAR transformylase (e.g. by disrupting dimerisation) would lead to inhibition of the *de novo* purine biosynthetic pathway and also the activation of AMPK (from the build up of AICAR), both of which would have a chemotherapeutic effect. AMPK agonists are also known to inhibit viral replication[80].

1.2.1.6 Inhibition

Inhibitors of ATIC are not only of interest as potential chemotherapeutic agents, they have also been shown to be useful in the treatment of inflammatory diseases. A wide variety of such inhibitors have been synthesized as inhibitors of IMP cyclohydrolase and AICAR transformylase activities and to directly interrupt enzyme dimerisation[81].

1.2.1.7 Folate-based inhibitors of transformylase activity

The major class of ATIC inhibitors are based on the folate-binding pocket, for example, 5,10-Dideazatetrahydrofolate (DDATHF, **1i**) has inhibitory action in the *de novo* purine synthesis pathway. DDATHF is a potent inhibitor of GAR transformylase and inhibits AICAR transformylase at high concentrations (>10 μM)[82]. Acyclic forms of DDATHF bearing a non-transferable formyl (**2i**)[83] or trifluoroacetyl (**3i**)[84] group bind to the enzymes as *gem*-diols, which mimic the formyl transfer transition state. Sulfonyl-containing antifolates have also been analysed. BW1540 (**4i**) (K_i = 8 nM) and BW2315 (**5i**) (K_i = 6 nM) are sulfamido-bridged 5,8-dideazafolate analogues that are inhibitors of AICAR transformylase. These potent inhibitors have been designed to occupy the oxyanion hole of AICAR transformylase[85]. β-DADF (**6i**) (K_d = 20 μM,

IC_{50} = 125 nM) is a Multisubstrate Adduct Inhibitor (MAI) that was used to probe the folate binding site[48]. β-DADF was designed to incorporate AICAR- and folate-like moieties linked by a trans double-bond through 2 methenyls[50].

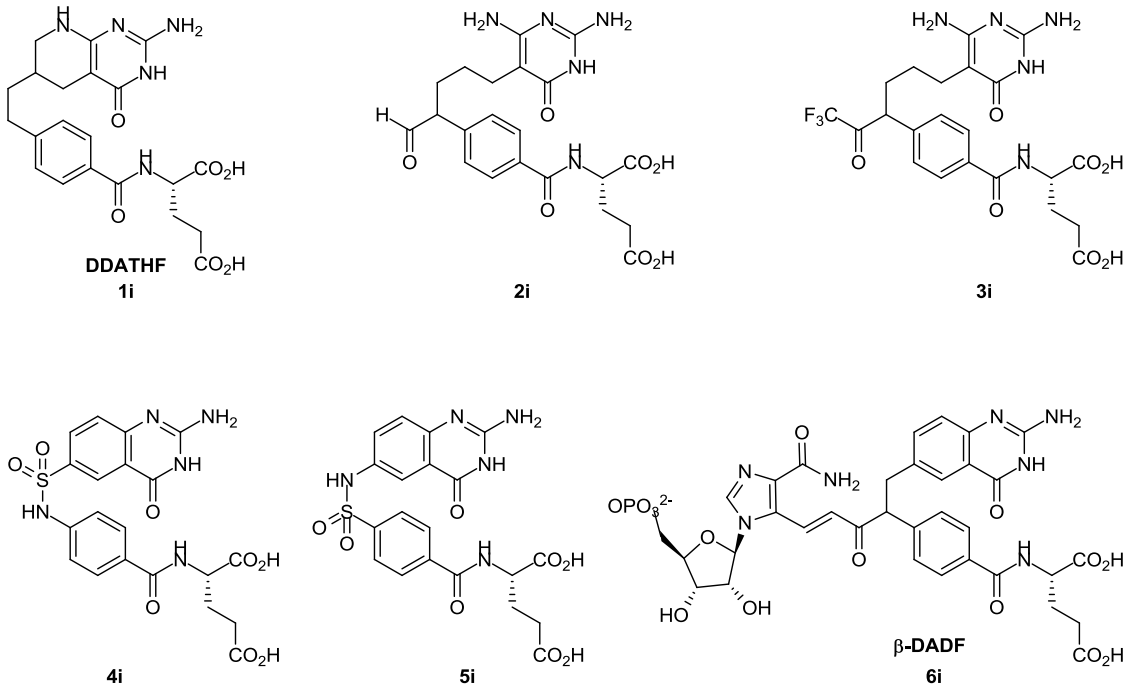

Figure 1-9: A selection of ATIC inhibitors.

Other inhibitors of the *de novo* formyl transferase enzymes have been synthesised with various different design principles in mind. A number of functionalised analogues of 5,8,10-trideazafolate (TDAF) were designed which incorporated different electrophilic centres, functionalised with acyl groups that would be incapable of transferring a carbonyl group to the substrate[86]. Compound **7i** was designed as a competitive inhibitor by mimicking the tetrahedral transition state formed during formyl transfer[86]. Multisubstrate analogue **8i** attaches a phosphate group via a flexible linker to the TDAF moiety in an attempt to target both cofactor and substrate binding sites[87]. The benzoyl and glutamate functions are important to the inhibitory activity of TDAF as compounds (**9i** and **10i**) not containing these features are far less potent[88]. Conformationally restricted analogue **11i** utilises a nitrogen atom incorporated into a 6-membered ring to

mimic the electrophilicity of the formyl transfer group of the folate cofactor[89]. AG2034 (**12i**) potently inhibited specifically GAR transformylase with K_i = 28 nM, which went on to phase 1 trials[90] and through further study was shown to increase AMPK phosphorylation[91].

Inhibitors based on the folate cofactors are usually subject to polyglutamation within the cell, increasing their retention times. Compound **13i** is an example of an inhibitor designed to be non-polyglutamateable by replacing the γ-carboxylic acid with a tetrazole[92]. This would aid in excretion of the drug, ensuring it is not retained in the cell for a prolonged period of time.

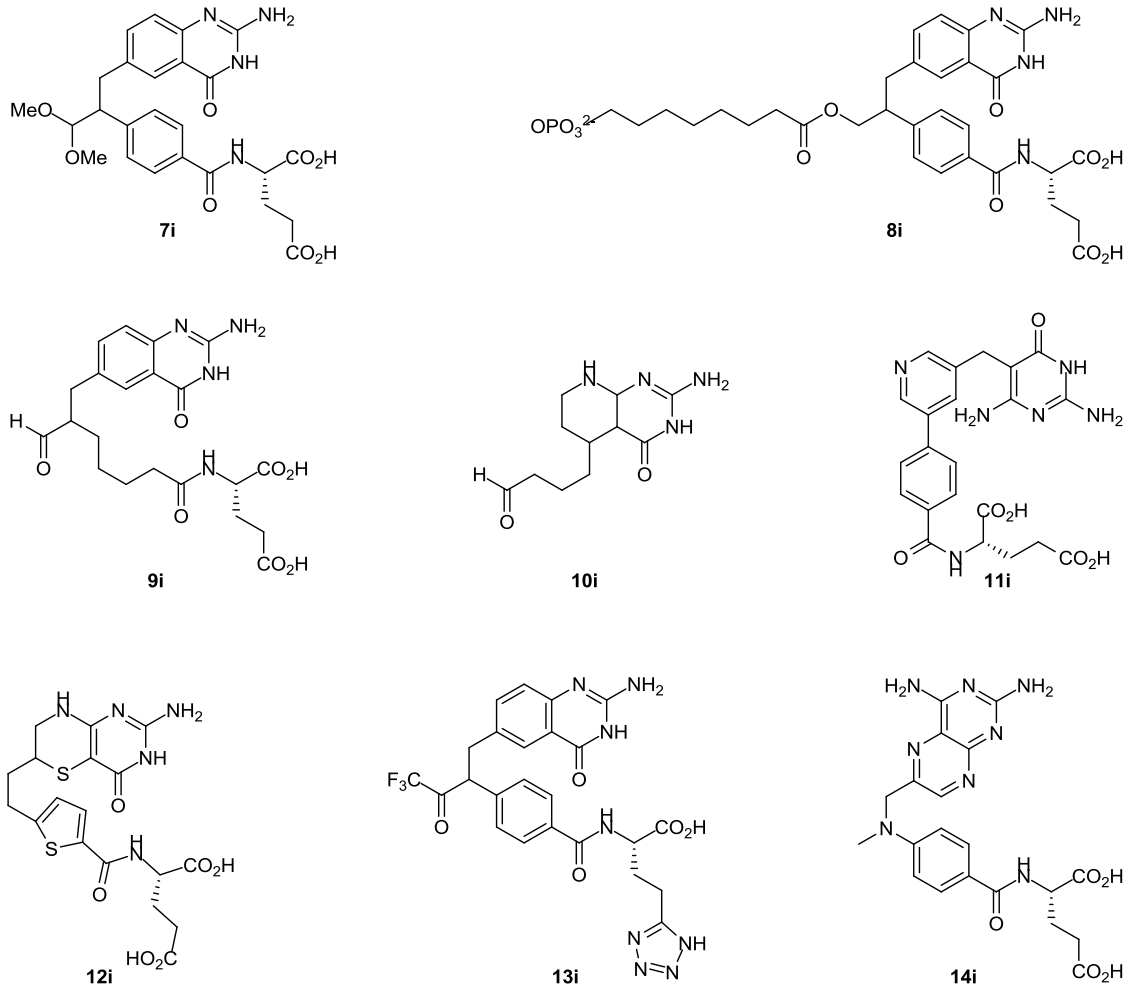

Figure 1-10: A selection of ATIC inhibitors.

Methotrexate (MTX, **14i**) is a clinically prescribed folate antagonist[93], used to treat rheumatoid arthritis, psoriasis[38a], leukemia[94] and breast cancer[95]. MTX inhibits dihydrofolate reductase and folate dependent enzymes, including AICAR transformylase[93]. AICAr, the nucleoside precursor of AICAR, builds up and promotes the release of adenosine[96] which brings about an anti-inflammatory response by inducing apoptosis of activated T-lymphocytes[97]. AICAr is also proposed to inhibit neutrophil adherence to connective tissue[98]. A single nucleotide polymorphism in the ATIC gene, C347→G which encodes for the single point mutation Thr116Ser, is being monitored to provide a pharmacogenetic biomarker to predict patient response to MTX treatment[99] in rheumatoid arthritis[94, 100] and psoriasis[101]. Higher AICAr excretion is also associated with better MTX efficacy[42]. Administering folic acid in conjunction with MTX treatment has been found to attenuate side effects[99a]. MTX enters the cell through the reduced folate carrier protein and is converted by folypolyglutamate synthase to MTX polyglutamates, the higher forms of which are retained in the cell longer[93]. 7-OH MTX is a major metabolite of MTX, catabolised by aldehyde oxidase. Comparing the monoglutamated and tetraglutamated forms revealed a 10-fold increase in potency[102] showing the importance of cellular processing on administered drugs.

1.2.1.8 Inhibitors of IMP cyclohydrolase activity

Only a small number of IMP cyclohydrolase inhibitors have been described. The IMPCH inhibitors 1,5-dihydroimidazol[4,5-*c*][1,2,6]thiadiazin-4(3*H*)-one 2,2-dioxide (**15i**) (K_i = 0.13 μM) and the corresponding nucleoside (K_i = 0.23 μM) and nucleotide (K_i = 0.15 μM) were designed to imitate the tetrahedral transition state formed in the cyclisation reaction[54]. The nucleoside and nucleotide were found to mimic XMP binding. The nucleotide inhibitor also binds to the AICAR transformylase domain which raises the possibility of designing inhibitors to block both ATIC catalytic sites.

1.2.1.9 Inhibitors of ATIC dimerisation

As the catalytic activity of AICAR transformylase is dependent on the oligomerisation state of the enzyme being that of a homodimer, it has been suggested that small molecules that could block dimerisation would provide a new mode of selectively inhibiting AICAR transformylase. 2 examples of such inhibitors are cyclic peptides[81b] and a generation of molecules known as cappsins[81a]. The most potent cyclic peptide (**16i**) had K_i =17 ± 4.2 μM and the most potent cappsin, cappsin 1 (**17i**), had K_i =3.1 ± 0.3 μM.

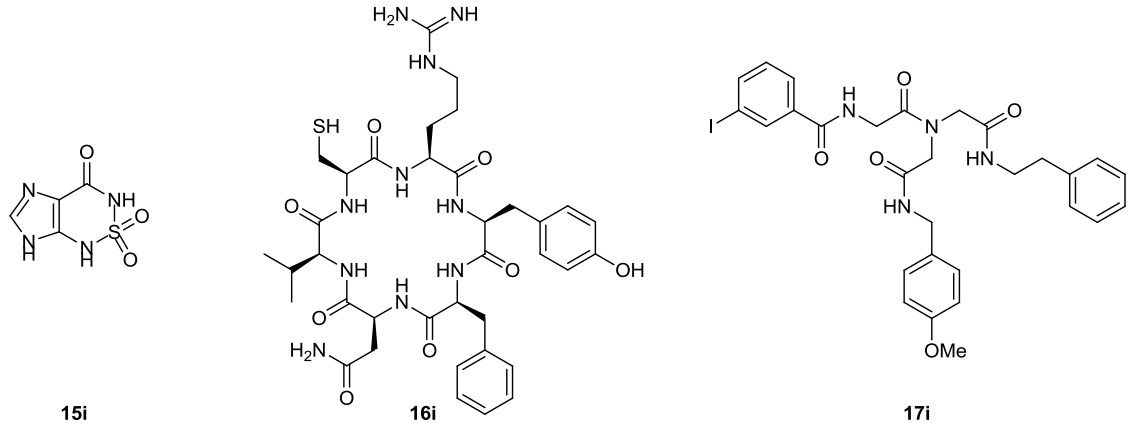

Figure 1-11: Inhibitors of the IMPCH domain of ATIC (15i) and of ATIC dimerisation (16i and 17i).

1.3 Regulation of de novo purine biosynthesis

1.3.1.1 Feedback regulation

When the salvage pathway is also functioning, *de novo* purine biosynthesis is suppressed by 70%[103]. There are multiple points for feedback regulation found within the *de novo* pathway as summarised in Figure 1-12. Phosphoribosylpyrophosphate synthetase (PRPP synthetase), catalyses the formation of the first substrate of the *de novo* and salvage pathway, PRPP, from ribose 5-phosphate (R 5-P) and ATP[3]. The physiological PRPP concentration is rate-limiting for purine synthesis[104]. Cyclic AMP decreases the availability of PRPP and thus slows the rate of *de novo* and salvagepurine synthesis[105]. PRPP synthetase is negatively regulated by IMP, AMP, GMP, ADP and GDP[106], the products of the purine pathways regulate the activity of their formation. PRPP synthetase consists of single polypeptide subunits of 33 kDa. These are capable of self-association to give aggregated forms containing 2, 4, 8, 16 and 32 subunits, of which only the 16 and 32 subunit forms were found to be significantly active *in vitro*[107].

PRPP amidotransferase catalyses the first step of *de novo* purine biosynthesis and is also allosterically inhibited by AMP, GMP and IMP ribonucleotide end products[4, 108]. PRPP amidotransferase exists in two forms, a smaller 133 kDa and larger 270 kDa protein. The presence of the PRPP substrate stabilises the active 133 kDa enzyme whilst the regulatory inhibiting purine nucleotides convert the smaller protein into the 270 kDa inactive form[109]. Synergistic inhibition is seen with mixtures of purine nucleotides, for example with AMP + GMP or AMP + IMP the inhibition effect measured is far greater than the additive effect expected[110].

The fifth step of the pathway, catalysed by AIR synthetase, is inhibited by AMP and AIR synthetase is the second slowest step of *de novo* purine synthesis[108b]. There are two other sites of feedback inhibition which occur following the formation of IMP. Adenylosuccinate synthetase is inhibited by AMP, and GMP inhibits IMP dehydrogenase. An excess of a triphosphate nucleotide influences the production of its monophosphate counterpart, i.e. GTP stimulates AMP production and ATP stimulates GMP production[108a].

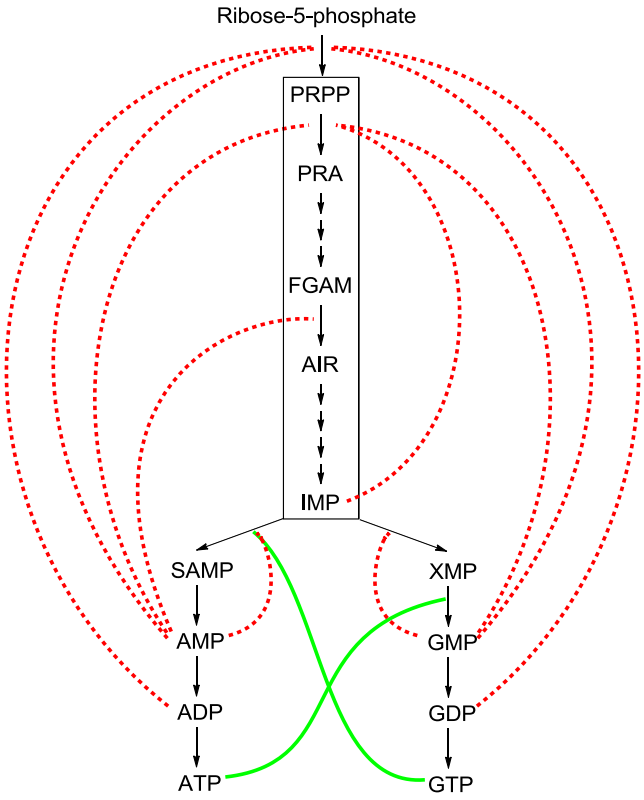

Figure 1-12: Feedback regulation of the *de novo* purine biosynthetic pathway. Steps also included are the synthesis of PRPP from 5-ribose phosphate catalysed by PRPP synthetase, and the conversion of IMP to ATP and GTP. Red dashed lines indicate negative feedback and solid green lines positive feedback.

1.3.1.2 Regulation via formation of macromolecular complexes

As previously mentioned, several of the *de novo* purine pathway enzymes exist as multifunctional proteins where activities are combined onto a single polypeptide. The trifunctional 'GART' protein containing GAR synthetase, GAR transformylase and AIR synthetase (steps 2, 3 and 5) activities, bifunctional 'PAICS' with AIR carboxylase and SAICAR synthetase (steps 6 and 7) activities, and bifunctional 'ATIC' exhibiting AICAR transformylase and IMP cyclohydrolase activities catalysing the final two steps of the pathway. ATIC bifunctionality is conserved through bacteria, yeast, vertebrates and some species of archaea.

Both folate requiring enzymes GAR transformylase and AICAR transformylase have been described as purifiying as a multienzyme complex[3]. The formyltransferases extracted from chicken liver each copurify with serine hydroxylmethyltransferase and the trifunctional folate metabolising protein containing 10-f-H_4F synthetase, 5,10-methenyl H_4F cyclohydrolase and methylene H_4F dehydrogenase activities[111]. This provides an interesting possibility for substrate channelling of the unstable 10-f-H_4F, by the close proximity of the trifunctional protein to convert folate species into the required 10-f-H_4F cofactor. Only the complex containing GAR transformylase has been shown to cross-link to the trifunctional protein in solution[112]

All six enzymes of the *de novo* purine biosynthetic pathway have been postulated to cluster together and form a multi-enzyme complex termed the 'purinosome' in purine-depleted conditions (Figure 1-13) by Benkovic *et al.*[113]. This is intuitive as the *de novo* pathway is essential under purine-depleted conditions, when the salvage pathway will have minimal substrates available and purine synthesis must proceed *via* the *de novo* pathway. Formation of the purinosome is proposed to be regulated by the

activation of endogenous $G\alpha_i$-coupled receptors[114]. The purinosome is punctate bodies distributed throughout the cytoplasm by a microtubule network[115].

Advantages of such multifunctional proteins and multienzyme complexes could include channelling of the product of one enzyme to the substrate site of the next and preservation of the stoichiometry of the pathway.

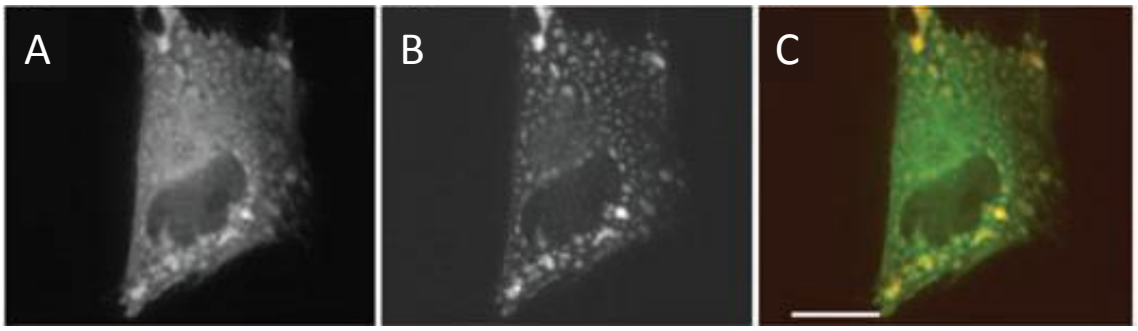

Figure 1-13: Cellular localisation of GART and FGAMS in HeLa cells grown in purine depleted media[113]. A) GART-GFP fusion protein. B) FGAMS-ORF protein fusion. C) GART-GFP (green) and FGAMS-ORF (red) overlaid. Scale bar = 10 μM.

However, in a recent publication by Marcotte *et al.*, further investigation into the purinosome phenomenon suggests that the formation of these punctate bodies is actually the result of protein aggregation[116]. Hydrogen peroxide induces the localisation of *de novo* pathway proteins irrespective of the concentration of purines in the growth medium. This coincides with the co-localisation of endogenous ubiquitin, HSP70 (Figure 1-14) and HSP90, which are normally associated with aggregates present within the cell[116]. Ubiquitin assigns large aggregates for degradation, whilst HSP70 and HSP90 are chaperone proteins. Analysis of the cells using time-lapse microscopy showed that cells containing the punctate bodies died at greater rates than those without, suggesting there is an association between the punctate bodies and cellular stress; survival rates were largely unaffected by purine availability[116]. Punctate body construction seems to be either a cause or consequence of stress to the cell. These experiments suggest the aforementioned purinosome is likely to be formed

from aggregated protein, caused by fusion of the proteins to GFP, excess protein expression or compromised protein homeostasis, rather than a functional multienzyme complex.

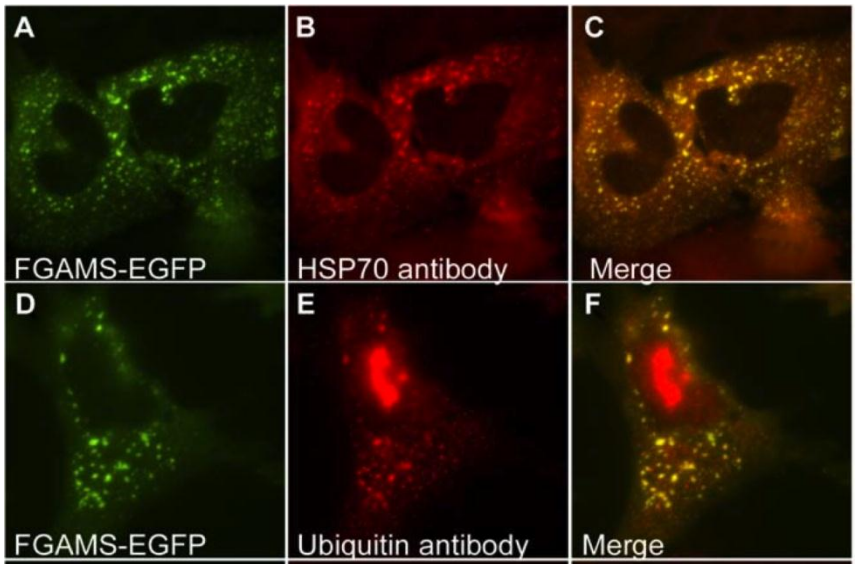

Figure 1-14: Co-localisation of FGAMS-EGFP with endogenous HSP70 and ubiquitin measured by immunofluorescence[116].

1.3.1.3 Regulation by post-translational modification

Post-translational modifications of ATIC that have been identified in humans include the phosphorylation of tyrosine 104[117], which is found in the active site of the IMPCH domain, and acetylation of lysine 199[118]. K199 is a surface residue and acetylation could potentially mediate the interaction with other proteins, such as those of the purinosome multienzyme complex. In *E. coli*, acetylation at lysine residue 287 occurs. K287 is the catalytic lysine residue found in the AICAR transformylase active site and would inhibit the enzyme; this could be a means of regulation of *de novo* activity in bacteria.

1.3.1.4 Other potential forms of regulation in E. coli

The gene product of PurR regulates the transcription of the enzymes involved purine biosynthesis and the enzymes that convert IMP to AMP or GMP in *E. coli*[119]. A large-scale identification of protein-protein interactions in *E. coli* discovered a putative protein-protein interaction between ATIC and YecF, an uncharacterised protein of unknown function[120]. This may have a regulatory role by catalysing post-translatory modifications to mediate activity, or even the formation of such multienzyme complexes as seen in human cells.

1.4 Objectives

This thesis aims to further the characterisation of ATIC. There have been no reports on the thermal stability of ATIC within the literature. The thermal stability of human and avian ATIC will be investigated through the use of various biophysical techniques, including differential scanning calorimetry and differential scanning fluorimetry.

The kinetic and physical binding properties of ATIC will be investigated. The binding constants of various small molecules relevant to the *de novo* pathway will be determined for the first time, by isothermal titration calorimetry. ATIC catalyses two successive reactions, from an AICAR substrate and a folate cofactor. The kinetics of these ligands will be investigated using the standard spectroscopic assay described by Black[43]. This assay will be developed into a two dimensional, high throughput assay to allow for the simultaneous determination of substrate and cofactor K_Ms, and allude to a binding model for the AICAR tfase reaction.

The crystal structure shows ATIC is a homodimeric protein, with two distinct catalytic domains. The full length ATIC peptide will be cloned into two separate constructs, each containing a separate catalytic domain. These truncation mutants will be used to assign kinetic and binding parameters to each of the separate domains. The

dimerisation of ATIC will be investigated through several biophysical techniques including isothermal titration calorimetry and analytical ultracentrifugation. Small molecule inhibitors will be synthesised, and deployed to probe ATIC dimerisation. Single molecule fluorescence studies with *N*-terminally fluorescently labelled ATIC will be used as a further probe of enzyme dimerisation in the presence of the substrates and dimerisation inhibitors. This may reveal the true dimerisation constant of the Michaelis complex which has not previously been determined.

Within the *C*-terminal AICAR tfase domain, potassium is always present in the crystal structures bound to the ATIC polypeptide. This thesis presents an investigation into the potassium dependence of ATIC. The K_d of potassium for ATIC has not been reported in the literature. The use of an 18-crown-6 ether complexing agent able to chelate endogenous potassium to determine the ATIC K_d for potassium will be investigated. The potassium binding site will be probed using site-directed mutagenesis, characterising the mutants in an effort to elucidate the role of the potassium ion in ATIC.

2 Materials and methods

2.1.1.1 Instrumentation

Samples and reagents were stored at optimum temperature using a Labcold fridge-freezer (4 °C/–20 °C) or New Brunswick Scientific ultra low temperature freezer U570 premium (–80 °C). A sterile environment was provided by a Microbiological safety cabinet SAFE 2010 Class II (Thermo Electron Corporation). Solutions and waste were sterilised using either a Prestige Medical bench top autoclave, or a LTE Touchclave-R autoclave Fisher-brand Hydrus 300. Bacterial cultures were grown using a Labnet 311DS shaker incubator, Stuart SI500 orbital shaker, or in a KuhnerSHAKERX shaker incubator. Transformations were performed using a Grant SUB14 water bath (heat shock method). Culture plates were grown in a Binder incubator. Cell disruption was performed by using the Bandelin SONOPULS HD2070 or Constant cell disruption system (T2/40/AA/AA, Constant Systems Ltd). Centrifugation was performed using the Beckman Coulter™Avanti™ J-30I Centrifuge (with Beckman JLA- 9.1000, Beckman JA-10 and Beckman JA- 25.50 rotors) and bench-top centrifuges Heraeus® Pico™, Heraeus® Fresco™ and Heraeus® Multifuge® from the Thermo Electron corporation. Size exclusion purification was achieved using a 20/60 Superdex 200 column or a 10/300 Superdex 200 gel filtration column, run using the Pharmacia AKTÄ Purifier FPLC system housed in a Foster Professional Refrigeration cabinet. Analysis of protein samples by SDS-PAGE was performed using the BioRad tetragel system; a LabnetAccuBlock™ was used to thermally denature samples. The molecular weight of samples was determined by electrospray ionisation mass spectrometry using a BrukerDaltonics® HCT Ultra™ mass spectrometer. A Varian Cary 50 Bio UV-visible spectrophotometer and Varian Cary PCB150 water peltier was used with the Cary WinUV software to conduct all UV-Vis studies. For Isothermal Titration Calorimetry

studies a MicroCal VP-ITC or a MicroCal ITC_{200} were used and VPViewer and Origin software employed to analyse the data. Analytical UltraCentrifugation studies were performed on a Beckman Coulter™ ProteomeLab™ XL-I. FRET experiments were conducted using the JobinYvonHosiba SPEX FluroMax-3®. Differential Scanning Fluorimetry was performed using a Bio-Rad CFX96 touch real-time PCR detection system. Sequencing was carried out by GATC Biotech and analysed with BioEdit sequence alignment editor ClustalW[121].

2.2 Materials

Analytical grade reagents were obtained from Sigma Aldrich, Fisher Scientific, Alfa Aesar and VWR International. Water was purified using an ELGA PURLAB® Classic. DNA samples were purified using the Qiagen QIAquick gel extraction kit and Miniprep kit. Molecular biology reagents (including enzymes, plasmids and buffers) were obtained from Promega, Novagen, New England Biolabs, Roche Diagnostics and Invitrogen. Oligonucleotide primers were synthesised by Sigma-Aldrich or IDT. Laboratory plasticware and consumables were supplied by Starlab, Fisher Scientific and Greiner. Kanamycin 100× stock at 50 mg/ml was made from kanamycin sulfate (BioChemica). DNA ladder marker Hyperladder I was obtained from New England Biolabs (12 bands, 100 bp-1.5 kbp), the Molecular Weight Marker used in SDS-PAGE gel electrophoresis was obtained from Fermentas and recombinant DNase 1 from Roche Diagnostics. The resin used in the Ni-NTA column was Qiagen agarose. 5,10-methylene tetrahydrofolate and (6S)-5-formyl tetrahydrofolate were obtained from Schircks laboratories. Plasmids encoding wild type human ATIC (Pur9) and avian ATIC with an *N*-terminal His-Tag were obtained from Dr M. E. Webb. Plasmids encoding some site-directed mutants used were prepared by Dr M. M. Spiering (Penn State University).

2.3 Solutions

All solutions were made up to 1 litre with ≥18.2 MΩ purified water and stored at ambient temperature unless stated otherwise.

2.3.1.1 Polymerase Chain Reactions

Pwo polymerase: purified in house by Dr L Kime.

Pwo buffer + $MgSO_4$: 100 mM Tris-HCl (pH 8.85), 250 mM KCl, 50 mM $(NH_4)_2SO_4$, 20 mM $MgCl_2$.

2.3.1.2 Bacterial Media

Auto-Inducing Media (AIM)[122]: Tryptone (10 g/l), Yeast Extract (5 g/l), 50 × Salts (20 ml/l), Magnesium Chloride (407 mg/l), 1000× Metals (200 µl/l), 50% (v/v) Glycerol (10 ml/l). The AIM media was autoclaved at 121 °C for 20 minutes as required before the remaining components of 50% (w/v) glucose (1 ml/l) and 50% (w/v) lactose (4 ml/l) were added. Kanamycin (50 µg/ml) was added as required.

50× Salts Stock (500 ml)[122]*:* Na_2HPO_4 (88.7 g), KH_2PO_4 (85 g), NH_4Cl (67 g), Na_2SO_4 (17.8 g).

1000× Metals Stock (100 ml)[124]*:*$FeCl_3.6H_2O$ (1.35 g), $CaCl_2.6H_2O$ (438 mg), $MnCl_2.4H_2O$ (198 mg), $ZnSO_4.7H_2O$ (288 mg), $CoCl_2.6H_2O$ (47.6 mg) $CuCl_2.2H_2O$ (34.1 mg), $Na_2MoO_4.2H_2O$ (48.8 mg) Na_2SO_3 (34.6 mg), H_3BO_3 (12.4 mg), $NiSO_4.6H_2O$ (52.6 mg), HCl (60µM).

LB Media: Tryptone (10 g), NaCl (10 g), Yeast Extract (5 g).

Agar (LBK) Plates: Agar (15 g) was added to 1 l LB media before being autoclaved at 121 °C for 20 minutes. When the solution had cooled to 40-60 °C, kanamycin (50 µg/ml) was added, the plates poured in a sterile environment and left to cool. Agar plates were stored at 4 °C.

2.3.1.3 Protein purification buffers

DNase 1 recombinant, grade 1: (*for use and long term storage at –20 °C)* 1 tablet (10,000 units) was dissolved in 2ml of a buffer consisting of: 20 mM Tris.HCl pH 7.5, 1 mM $MgCl_2$, Glycerol (50% v/v). Stored at –20 °C.

10× PBS (phosphate-buffered saline): 500 mM Potassium phosphate pH 7.0 (0.213 M KH_2PO_4, 0.286 M K_2HPO_4 at 20 °C), 3 M NaCl.

Lysis buffer: 1× PBS, 10 mM Imidazole.

Wash buffer: 1×PBS, 50 mM Imidazole.

Elution buffer: 1× PBS, 250 mM Imidazole.

ATIC buffer: 50 mM Tris-HCl pH 7.4, 25 mM KCl.

ATIC low potassium buffer: 50 mM Tris-HCl pH 7.4, 5 mM KCl.

ATIC zero potassium buffer: 50 mM Tris-HCl pH 7.4.

*TEV cleavage buffer:*50 mM Tris-HCl pH 8.0, 0.5 mM EDTA, 1 mM DTT, 100 mM KCl.

*Sortase labelling buffer:*50 mM HEPES pH 7.5, 150 mM NaCl, 5 mM $CaCl_2$, 50 mM KCl.

AUC 'HB' buffer: 20 mM Tris.HCl pH 7.5, 150 mM NaCl, 50 mM KCl.

2.3.1.4 Buffers for SDS-PAGE

SDS-PAGE loading buffer: 160 mM Tris.HCl pH 6.8, 4% SDS (*w/v*), 20% glycerol (*v/v*),

2 M β-mercaptoethanol, 0.02% (w/v) Bromophenolblue.

5× SDS-PAGE running buffer: 125 mM Tris base, 960 mM glycine, 0.5% SDS (*w/v*).

Coomassie stain: 0.1 % coomassie G250 (*w/v*), 40% methanol (*v/v*), 10% acetic acid (*v/v*).

Coomassie destain: 40% methanol (*v/v*), 10% Acetic acid (*v/v*).

2.3.1.5 Buffers for Agarose gel electrophoresis

50× TAE buffer: 2 M Tris base, 1 M acetic acid, 50 mM EDTA.

6× DNA loading buffer: 6% Orange G (*w/v*), 80% glycerol (*v/v*).

2.3.1.6 Buffers for rubidium chloride chemically competent cells

Tfb1: 30 mM potassium acetate pH 5.8, 100 mM $RbCl_2$, 50 mM $MnCl_2$, 10 mM $CaCl_2$, 15% glycerol (*v/v*).

Tfb2: 10 mM MOPS pH 6.6, 10 mM RbCl, 75 mM $CaCl_2$, 15% (v/v) glycerol.

2.3.1.7 Buffers for protein analysis

5 M Guanidinium Hydrochloride: for denaturing protein samples to estimate concentration using a calculated extinction coefficient

Bradford reagent: 20% concentrated Bradford reagent (*v/v*) in water.

2.3.1.8 Substrate solutions

AICAR: made up in various concentrations by dilution from a stock of 1-10 mM, in the required buffer.

6(R,S)-10-formyl tetrahydrofolate: 6(R,S)-10-formyl tetrahydrofolate was prepared by acid hydrolysis of 5,10-methylene tetrahydrofolate (Schircks). 5,10-methenyltetrahydrofolate (5 mg) was dissolved in 10 mM HCl (1 ml) to which 1.5 M Tris.HCl at pH 8.8 (25 μl) and 0.25 M β-mercaptoethanol (40 μl) were added before shaking in the dark for at least 1 hour. The solution (final concentration ~10 mM, absorbance measured at 253 nm at pH 13) was stored in the dark at −80 °C. The stock was diluted into an appropriate buffer and left to equilibrate to the required pH for 1 hour at room temperature before use.

6(S)-10-formyl tetrahydrofolate: 5-formyl tetrahydrofolate (5 mg) was dissolved in 0.1 M H_2SO_4 (1 ml) at 40 °C before 5,10-methenyl tetrahydrofolate was allowed to

precipitate at 4 °C. The precipitate was collected by centrifugation (17,000 rcf, 10 min), dissolved in 10 mM HCl (1 ml) to which 1.5 M Tris.HCl at pH 8.8 (25 µl) and 0.25 M β-mercaptoethanol (40 µl) were added before shaking in the dark for at least 1 hour. The solution (final concentration ~10 mM, absorbance measured at 253 nm at pH 13) was stored in the dark at −80 °C. The stock was diluted into an appropriate buffer and left to equilibrate to the required pH for 1 hour at room temperature before use.

2.4 DNA Primers

Table 2-1: Primers used in PCR to generate human ATIC site directed mutants F590A (P01) and F590I (P02). Each mutation has a forward primer (f) and a corresponding reverse primer (r). All sequences are written 5′ to 3′, with the codon site of the mutation underlined.

Primer code	***Primer name***	***Sequence 5′→3′***
P01f	F590Af	CGA ACC TTC GGC TCG CCC ACC
P01r	F590Ar	GGA TCC TCA GTG GTGGGC GAG
P02f	F590If	CGA ACC TCC GGC TCA TCC ACC
P02r	F590Ir	GGA TCC TCA GTG GTGGAT GAG

Table 2-2: Primers used in PCR to generate truncation mutants of human ATIC, through the introduction of restriction sites to the ends of the sequence of interest. All sequences are written 5′ to 3′, with the restriction site of the mutation underlined.

Primer code	***Primer name***	***Restriction site***	***Sequence 5′→3′***
P03	TFforNco1	Nco1	GAT TCA CCA TGG GCG TAT CTC
P04	TFforNhe1	Nhe1	GAT TCA GCT AGC GTA TCT CAG
P05	TFrevBamH1	BamH1	GAT TCA GGA TCC TCA GTG GTG
P06	IMPCHforNco1	Nco1	GAT TCA CCA TGG CTC CCG GCA
P07	IMPCHforNde1	Nde1	GAT TCA CAT ATG GCT CCC GGC
P08	IMPCHrevBamH1	BamH1	GAT TCA GGA TCC TCA TTT GCT

Table 2-3: Primers used to synthesise the pET28aTEV plasmid

Primer code	***Primer name***	***Sequence 5'→3'***
P09f	Spe1intopET28af	TCA CAG CAG CGG ACT AGT GCC GCG CGG CAG CCA T
P09r	Spe1intopET28ar	ATG GCT GCC GCG CGG CAC TAG TCC GCT GCT GTG A
P10f	TEVinsertf	CTA GTT GAG AAC CTG TAC TTC CAA GGT CA
P10r	TEVinsertr	TAT GAC CTT GGA AGT ACA GGT TCT CAA

2.5 Plasmid maps

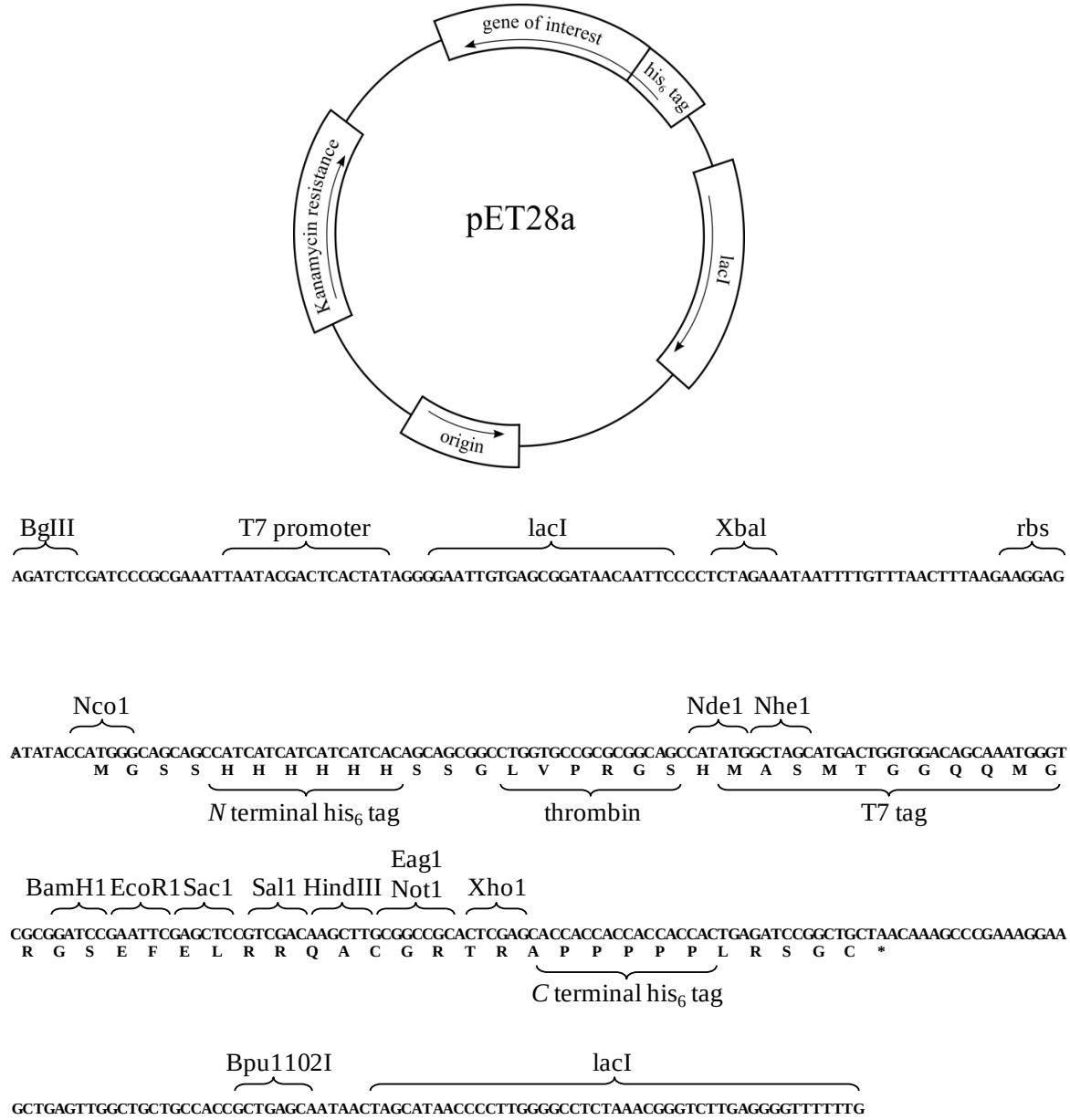

Figure 2-1: Top: the pET28a plasmid map containing the gene of interest. Bottom: the pET28a multiple cloning site.

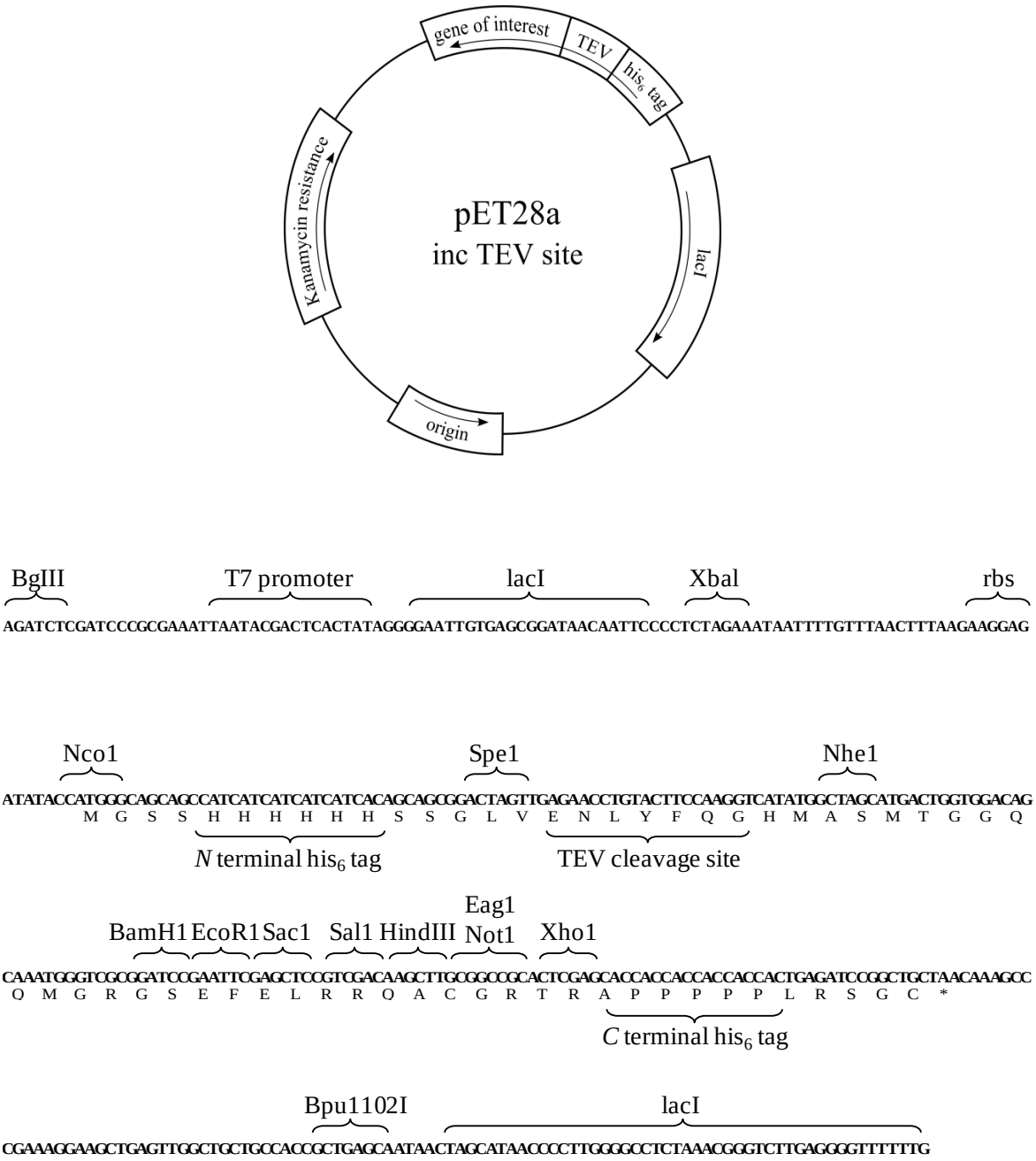

Figure 2-2: The plasmid map and a multiple cloning site for pET28aTEV. This vector is an adaption of pET28a in which the thrombin cleavage site has been exchanged for a TEV cleavage site. The TEV recognition site is ENLTFQG with cleavage occurring between the glutamine and glycine residues. Following cleavage with TEV, the plasmid is designed to leave a glycine-histidine dipeptide, followed by the gene of interest.

2.6 Genotypes

Table 2-4: Cell strains and corresponding genotypes used in cloning (DH5α, XL10 gold) and protein expression (BL21 (DE3), BL21* (DE3), C41 (DE3)).

Cell Strain	***Genotype***
DH5α	F– Φ80*lac*ZΔM15 Δ(*lac*ZYA-*arg*F) U169 *rec*A1 *end*A1 *hsd*R17 (rK–, mK+) *pho*A*sup*E44 λ– *thi*-1 *gyr*A96 *rel*A1
XL10 gold	Tetr Δ(*mcrA*)183Δ(*mcrCB-hsdSMR-mrr*)173 *end*A1 *sup*E44 *thi*-1 *rec*A1 *gyr*A96 *rel*A1 *lac* Hte [F′ *pro*AB *lac*IqZΔM15Tn*10* (Tetr) Amy Cam^r]
BL21 (DE3)	F– *omp*T*hsd*SB(rB–, mB–) *gal dcm*(DE3)
BL21* (DE3)	F– *omp*T*hsd*SB(rB–, mB–) *gal dcm rne*131 (DE3)
C41 (DE3)	F– *omp*T*hsd*SB(rB–, mB–) *gal dcm*(DE3)

2.7 Molecular biology

2.7.1.1 Polymerase Chain Reactions (PCRs)

PCR mixtures were made using the recipe from Table 2-5.

Table 2-5: Recipe for PCR.

Component	***Volume/ µl***
H_2O	43.2
10× Polymerase Buffer + $MgSO_4$	5
DNA template	0.2
25 mM dNTPs	0.4
Forward primer	0.5
Reverse primer	0.5
PWO enzyme	0.2

2.7.1.2 Site-directed mutagenesis

Site-directed mutants were made following the program settings previously used by Shim et al.[53] with the exception of the annealing temperature that was altered from 65 °C to 55 °C. The program is shown in Table 2-6.

Table 2-6: PCR program used for site-directed mutagenesis of human ATIC. Denaturing, annealing and extension steps were cycled 16 times.

Cycle stage	*Temperature/ °C*	*Time*
Initial denaturing	95	30 s
Hot start	Disabled	-
Denaturing	95	30 s
Annealing	55	1 min
Extension	68	14 mins
Final extension	Disabled	-
Final hold	4	∞

2.7.1.3 Truncation mutants

PCR was performed using the general program in Table 2-7. Variations in primer annealing temperatures were used for individual reactions and are stated in the results section.

Table 2-7: The PCR program used for the truncation mutants of human ATIC. Denaturing, annealing and extension steps were cycled 35 times.

Cycle stage	*Temperature (°C)*	*Time*
Initial denaturing	95	30 s
Hot start	Disabled	-
Denaturing	95	30 s
Annealing	Specified in results section	1 min
Extension	68	2 min
Final extension	Disabled	-
Final hold	4	∞

2.7.1.4 Agarose gel electrophoresis

Agarose gels between 0.6% and 1.5% (*w*/v) were used to analyse and purify DNA samples. The following protocol makes 40 ml of 1.2% *(w/v)* agarose gel solution.

Agarose (480 mg) was dissolved in 1 × TAE buffer (50 ml) by heating at 800 W in a microwave for 30 second intervals. When dissolved, the solution was made up to 40 ml with 1 × TAE buffer, to which ethidium bromide (1.33 μl) was added, mixed and poured into gel casting apparatus, adding a comb to create loading wells. Once set (approximately 20 mins), the comb was removed and the gel transferred to the BioRad running apparatus. The gel was covered with 1 × TAE buffer and the samples (usually 5 μl sample mixed with 1 μl 6 × DNA loading buffer) and DNA marker added. The apparatus was run at 100 V until the samples had moved to the area indicated by yellow tape (approximately 4 cm, taking 20 min). All waste, gloves and used gels were disposed of in the ethidium bromide waste.

2.7.1.5 Purification of molecular biology grade DNA

DNA was purified using QIAGEN QIAprep Spin Miniprep and QIAquick Gel Extraction kits following the protocol supplied by the manufacturer.

2.7.1.6 QIAprep Spin Miniprep

A pellet of bacterial cells from 5 ml overnight *E. coli* culture in LB medium was re-suspended in P1 buffer (250 μl) and transferred to a 1.5 ml microcentrifuge tube. To lyse the cells, P2 buffer (250 μl) was added and mixed 4-6 times by inversion causing the solution to go blue. N3 buffer (350 μl) was added and immediately mixed 4-6 times by inversion. The white precipitate formed was isolated by centrifugation (17,000 rcf, 10 min) and the supernatant was applied to a QIAprep spin column before further centrifugation (17,000 rcf, 1 min). The flow through was discarded and the column washed first with PB buffer (500 μl) followed by PE buffer (750 μl) with centrifugation (17,000 rcf, 1 min) after each wash. The column was centrifuged (17,000 rcf, 1 min) to remove any residual buffer before being transferred to a clean microcentrifuge tube. Sterile H_2O or elution buffer EB (50 μl) was applied to the centre of the column, incubated at room temperature for 1 min before the column was centrifuged (17,000 rcf, 1 min) to elute the purified DNA which was stored at −20 °C.

2.7.1.7 QIAquick Gel Extraction

DNA samples were separated by agarose gel electrophoresis at 100 V and visualised by irradiation with UV light. Irradiation was kept to a minimum to preserve the DNA. Gel segments containing the DNA of interest were isolated using a razor blade and weighed in 1.5 ml microcentrifuge tubes. The gel segments were dissolved by adding QG buffer (three equivalents to the weight of the gel segment) which was heated at 50 °C with intermittent mixing by vortex. One equivalent of isopropanol was added to the dissolved solution, which was then applied to a QIAprep spin column and centrifuged

(17,000 rcf, 1 min). The flow through was discarded and QG buffer (500 µl) was applied to the column to remove any remaining agarose and centrifuged (17,000 rcf, 1 min). The flow through was discarded and the column washed with PE buffer (750 µl) and left at room temperature for 5 mins before centrifugation (17,000 rcf, 1 min). The flow through was discarded and the column centrifuged (17,000 rcf, 1 min) to remove any residual buffer. The column was transferred to a clean 1.5 ml microcentrifuge tube and sterile H_2O or elution buffer EB (30 µl) added to the centre of the column. After incubating at room temperature for 1 min the column was centrifuged (17,000 rcf, 1 min) to elute the purified DNA sample which was stored at −20 °C.

2.7.1.8 Restriction digests

All buffers and enzymes used for restriction digests were supplied by New England Biolabs (NEB). Single digests were prepared following the recipe in Table 2-9 and double digests were prepared following the recipe in Table 2-8. Reaction mixtures were incubated at 37 °C for at least 90 min. Agarose gel electrophoresis was used to ensure the reactions had gone to completion. The restriction enzymes were deactivated by incubation at 80 °C for 20 min.

Table 2-8: Recipe for single restriction digests. The digest buffer used is that recommended by NEB.

Component	***Volume/ µl***
10× digest buffer (+BSA)	2
DNA sample	2
H_2O	15
Restriction enzyme	1

Table 2-9: Recipe for double restriction digests. The digest buffer used is that recommended by NEB as being compatible with both restriction enzymes

Component	*Volume/ µl*
10× digest buffer (+BSA)	2
DNA sample	10
H_2O	4
Restriction enzyme 1	2
Restriction enzyme 2	2

2.7.1.9 Ligation reactions

The ligation reaction was left to incubate overnight at 4 °C and set up according to the recipe in Table 2-10. Ligation reactions used 1 µl pET28a vector (1-17.5 ng) with insert in a 3:1 insert to vector ratio. 2 µl of the ligase mixture was transformed into 10 µl XL10-Gold competent cells using the heat shock method.

Table 2-10: Ligation reaction recipe

Component	*Volume/ µl*
5× ligation buffer	2
pET28a vector	1
Insert	x
T4 ligase	1
H_2O	10-x

2.8 Sequencing and in silico tools

All DNA was submitted for sequencing to GATC Biotech. Sequence alignments were confirmed using the ClustalW[121] alignment program in BioEdit software. Molecular masses and theoretical extinction coefficients for the expressed protein were calculated using ExPASy ProtParam[123]. For human ATIC ε=54820 M^{-1} cm^{-1}, and for avian ATIC ε=50350 M^{-1} cm^{-1}.

2.9 Protein expression

2.9.1.1 Rubidium chloride competent cells

All chemically competent cell preparation was conducted under sterile conditions. Starter cultures of LB (5 ml) were inoculated with the competent cell strain required and incubated at 37 °C with shaking overnight. The starter culture (1 ml) was added to LB (500 ml) and incubated with shaking at 37 °C until an OD A_{600} reading of 0.5 was reached. The media was cooled on ice for 15 min before the cells were harvested by centrifugation (JLA- 9.1000, 4500 rpm, 10 min, 4 °C). The pellet was re-suspended in Tbf1 (30 ml) and incubated on ice for 15 min before the cells were re-harvested by centrifugation (JLA- 9.1000, 4000 rpm, 5 min, 4 °C). The pellet was re-suspended in Tbf2 (6 ml) and the chemically competent cells were flash frozen in liquid nitrogen before storage at −80 °C in 100 µl aliquots. C41 (DE3), BL21 (DE3), BL21* (DE3), and DH5α competent cells were prepared.

2.9.1.2 Transformations

All transformations were carried out under sterile conditions at 4 °C unless otherwise stated. Plasmids (1 µl) were added to chemically competent *E. coli* BL21(DE3), BL21*(DE3), C41(DE3) or DH5α (50 µl), incubated on ice for 10 minutes and then heated at 42 °C for 45-60 seconds before returning to ice for a further 10 minutes. LB

(900 µl) was added and the cells incubated at 37 °C with shaking for 60-90 minutes. A small sample (100 µl) was plated on agar (LBK) plates and incubated overnight at 37 °C. The plates were sealed and stored at 4 °C.

2.9.1.3 Protein overexpression

Starter cultures of LB (5 ml) inoculated with kanamycin (50 µg/ml) and one colony from the plates, under sterile conditions, were incubated at 37 °C with shaking overnight. The starter cultures were added to auto-inducing media (1 l) with kanamycin (final concentration 50 µg/ml) and incubated at 30 °C with shaking overnight. The cells were harvested by centrifugation (JLA- 9.1000, 6000 rpm, 30 min, 4 °C) and stored at −80 °C.

2.10 Protein purification protocols

2.10.1.1 Cell disruption

The frozen cell pellet was re-suspended in lysis buffer on ice. Recombinant DNase 1 (5,000 units/l) was added to the lysis buffer. The cell suspensions were lysed using the Constant cell disruption system (20 psi, 5 ml injections). Alternatively, the cell suspensions were lysed by sonication (40% power, 6 min). The cell debris was sedimented by centrifugation using 50 ml Oak Ridge style centrifuge tubes (JA- 25.50, 16,000 rpm, 40 min) and the supernatant decanted and stored on ice before purification.

2.10.1.2 Ni-NTA column

The Ni-NTA resin (~5 ml) was equilibrated with lysis buffer; the protein lysates loaded and non-binding fractions collected. Lysis buffer (40 ml) followed by wash buffer (40 ml) were applied to the column and wash fractions collected. Elution buffer was applied to the column and fractions containing protein (5 ml) were collected. Elution fractions were analysed by Bradford assay and SDS-PAGE. The column was

regenerated with 0.1% SDS (25 ml), 0.1 M NaOH (25 ml), 10 mM EDTA (25 ml), H_2O (100 ml), ~500 mM $NiSO_4$ (10 ml), H_2O (50 ml) and lysis buffer (50 ml). For storage the column was left in 20% EtOH (50 ml) at 4 °C.

2.10.1.3 Gel filtration

The fractions containing the ATIC protein obtained from the Nickel-affinity column were concentrated to a volume of 1 ml via centrifugal concentration (Vivaspin and Amicon) and applied to a 26/60 Superdex 200 gel filtration column using a Pharmacia AKTÄ FPLC system. The purified ATIC was eluted using 50 mM Tris.HCl pH 7.4, 25 mM KCl buffer (or 50 mM Tris.HCl pH 7.4, 5 mM KCl buffer) at a rate of 1.0 ml/min, larger protein fragments being eluted first. Fractions were identified using UV absorbance (280 nm) and SDS-PAGE. Smaller volumes of protein (100 µl) were purified using a 10/300 Superdex 200 gel filtration column eluted at a rate of 0.5 ml/min.

2.11 Gel electrophoresis- denaturing SDS-PAGE

2.11.1.1 Casting the gel

SDS-polyacrylamide gel electrophoresis was performed using the BioRad tetragel apparatus (1 mm plates).

Table 2-11: Components and quantities for denaturing SDS-PAGE resolving and stacking gels (casts 2 gels using 1.0 mm casting plates).

Component	*10% resolving gel* *Volume/ ml*	*5% stacking gel* *Volume/ ml*
H_2O	4	2.45
30% (v/v) acrylamide/bisacrylamide mix	3.3	0.67
1.5 M Tris (pH 8.8)	2.5	-
1 M Tris (pH 6.8)	-	0.75
10% (w/v) sodium dodecyl sulfate	0.1	0.04
15% (w/v) ammonium persulfate	0.1	0.04
Tetramethylethylenediamine	0.005	0.005

10% SDS-PAGE gels were prepared as in Table 2-11 with the addition of APS and TEMED just before pouring the gel. Gels were poured to approximately ¾ the height of the plate and water saturated butanol (5 µl) added to the surface. The gel was left to set (10-20 minutes) before the butanol was removed (washed with water and blotted with filter paper). A 5% stacking gel was prepared as in Table 2-11, again with the addition of TEMED immediately prior to pouring the gel. The gels were poured on top of the separating gel, the comb inserted and left until set.

2.11.1.2 Preparing, running and processing the gels

Protein samples (15µl) were added to an equal volume of SDS loading buffer and heated at 95 °C for 10 minutes (Digital Dry Bath-Labnet). Samples (10 µl) were loaded into different lanes of the SDS-PAGE gel using a syringe, along with a Molecular Weight Marker (10 µl).

An appropriate volume of SDS-PAGE running buffer was poured into the apparatus (as indicated on the apparatus). The gel was run at a limiting power of 200 V, until the blue stained samples were seen to reach the bottom of the gel (30-50 minutes).

The gel was separated from the glass plates and the top stacking gel removed. Coomassie Blue stain was added to the gel and heated (20 secs, 800 W) before being left to rock at room temperature (1 hour+). The stain was then removed and Coomassie destain added and left again at room temperature (usually overnight) until the bands on the gel could be clearly seen. The gel was imaged using *trans*-white illumination in the Molecular Imager® Gel Doc^{TM} XR.

2.12 UV-vis spectrometry

The following experiments were carried out using a Varian Cary 50 Bio UV-visible spectrophotometer and a quartz cuvette (1 ml or 600 µl).

2.12.1.1 Determining enzyme concentrations

The absorbance at 280 nm of 1 ml of protein sample, or a known volume of sample made up to 1 ml or 600 µl with potassium buffer, was measured using the 'scan' program between 300-260 nm. The baseline was set using a cuvette containing buffer without any protein. The concentration of enzyme was determined *via* Beers Law.

$$A = \varepsilon c l \qquad (2\text{-}1)$$

Where A= absorbance, ε= molar extinction coefficient ($M^{-1}cm^{-1}$), c= concentration (M) and l= path length (cm)

In this case; A= measured value per ml, l= 1 cm and ε= 54820 $M^{-1}cm^{-1}$ for human ATIC, and ε = 50350 $M^{-1}cm^{-1}$, as determined from the protein sequence.

2.12.1.2 Determining DNA concentrations

DNA concentration was determined by measuring UV absorption at 260 nm, 280 nm and 320 nm. Measurements were obtained using a 50 µl quartz cuvette, a blank sample of 50 µl H_2O was used to zero the readings.

$$Concentration\ (\mu g\ /\ (ml) = (A_{260} - A_{320}) \times \text{dilution factor} \times (\text{ss or ds}) \quad (2\text{-}2)$$

Where ss denotes single stranded DNA (equal to 35), and ds denotes double stranded DNA (equal to 50).

2.12.1.3 Standard ATIC assay

The absorbance of the tetrahydrofolate at 298 nm was used to measure the turnover of the reaction. Different solutions were prepared, each to a volume of 1 ml or 600 µl depending on the size of cuvette used. For a basic assay potassium buffer was used (25 mM KCl) along with enzyme, AICAR and 10-formyl tetrahydrofolate. The conversion of 10-formyl tetrahydrofolate to tetrahydrofolate is measured by an increase in absorption at 298 nm. Therefore the rate of AICAR transformylase activity can be measured as a change in absorbance at 298 nm. Scans were conducted using the scanning kinetics program operating at 298 nm for 5 minutes. The rate was measured using the 'ruler least squares' function in the Cary WinUV software to measure the gradient of the change in absorbance.

The initial scan which measured the solution of buffer, AICAR and enzyme was first determined to be flat (no turnover) before 10-formyl tetrahydrofolate was added to initiate catalysis, and returned immediately to the beam after a few inversions of the cell to mix.

2.12.1.4 EnVision Plate Reader assay

A two-dimensional assay was developed to simultaneously determine the substrate and cofactor K_Ms. A 96-well plate format was designed to contain 48 different assay conditions, with increasing cofactor across the columns (left to right) and increasing substrate with descending row (A to H). Table 2-12 summarises the volumes and components dispensed into each well.

Table 2-12: Volumes of each solution dispensed into a 96 well plate by a Hamilton Microlab Star robot. Each row contains six different assay conditions, in duplicate. The volume of folate cofactor added increases across the columns, left to right. The total volume of the well decreases with descending row; row A is 195 µl, B is 190 µl, C is 180 µl, D is 170 µl, E is 160 µl, F is 150 µl, H is 140 µl and I is 120 µl. AICAR substrate was added to give a total well volume of 200 µl.

		1	***2***	***3***	***4***	***5***	***6***	***7***	***8***	***9***	***10***	***11***	***12***
	Buffer	175	175	165	165	155	155	145	145	125	125	105	105
A	**Enzyme**	10	10	10	10	10	10	10	10	10	10	10	10
	Folate	10	10	20	20	30	30	40	40	60	60	80	80
	Buffer	170	170	160	160	150	150	140	140	120	120	100	100
B	**Enzyme**	10	10	10	10	10	10	10	10	10	10	10	10
	Folate	10	10	20	20	30	30	40	40	60	60	80	80
	Buffer	160	160	150	150	140	140	130	130	110	110	90	90
C	**Enzyme**	10	10	10	10	10	10	10	10	10	10	10	10
	Folate	10	10	20	20	30	30	40	40	60	60	80	80
	Buffer	150	150	140	140	130	130	120	120	100	100	80	80
D	**Enzyme**	10	10	10	10	10	10	10	10	10	10	10	10
	Folate	10	10	20	20	30	30	40	40	60	60	80	80
	Buffer	140	140	130	130	120	120	110	110	90	90	70	70
E	**Enzyme**	10	10	10	10	10	10	10	10	10	10	10	10
	Folate	10	10	20	20	30	30	40	40	60	60	80	80
	Buffer	130	130	120	120	110	110	100	100	80	80	60	60
F	**Enzyme**	10	10	10	10	10	10	10	10	10	10	10	10
	Folate	10	10	20	20	30	30	40	40	60	60	80	80
	Buffer	120	120	110	110	100	100	90	90	70	70	50	50
G	**Enzyme**	10	10	10	10	10	10	10	10	10	10	10	10
	Folate	10	10	20	20	30	30	40	40	60	60	80	80
	Buffer	100	100	90	90	80	80	70	70	50	50	30	30
H	**Enzyme**	10	10	10	10	10	10	10	10	10	10	10	10
	Folate	10	10	20	20	30	30	40	40	60	60	80	80

These studies were based on the standard assay protocol but used a black, clear-bottomed Greiner bio-one micro assay 96 well plate (transparent to 260 nm) and measured absorbance at 296 nm using an EnVision Multilabel Plate Reader. An exclusion filter, 'Photometric 300', was used to allow only light of wavelength 300 ± 20 nm to reach the detector. A single row of the 96-well plate was processed at a time. AICAR substrate was dispensed across the columns (left to right) at a speed of 200 µl/s. The volume of AICAR dispensed was different for each row, to ensure a final well

volume of 200 μl. The plate was then subjected to a five second shake operation, in an orbital motion. The absorbance at 296 nm was then measured in each well, moving from left to right across the columns. This method of measuring absorbance from left to right was then repeated for a minimum of 12 minutes. Data was exported using EnVision Workstation version 1.09 and analysed using Microsoft Excel.

2.12.1.5 Measuring Potassium dependence

The assay was conducted as in 2.12.1.3, but this time two buffers were used to vary the concentration of potassium in final assay mixture, the potassium buffer (25 mM KCl) and the zero potassium buffer (0 mM KCl). The AICAR and 10-formyl tetrahydrofolate substrates were made up using the zero potassium buffer whilst the enzyme was stored in the potassium buffer. Human ATIC was purified in 5 mM KCl containing buffer, hence the lowest concentration of KCl in the assay was limited by the dilution of the enzyme stock solution into the assay mixture.

A similar approach was taken to investigate the effect of various metal cations on human ATIC. This experiment was conducted on a single purification batch of human ATIC in 5 mM KCl. This enzyme stock was diluted into the assay mixture to give a background concentration of 83 nM KCl. Metal chloride solutions (KCl, NaCl, LiCl, RbCl, CsCl, $MgCl_2$ and $CaCl_2$) were added to the assay mixture to achieve a final concentration of 1 mM. Samples containing human ATIC, AICAR substrate and metal chloride were either incubated at 25 °C for 3 minutes, or incubated for 20 minutes on ice before 5 minutes at 25 °C. The reaction was initiated by addition of 10-formyl tetrahydrofolate, and the increase in absorbance at 298 nm was measured.

2.12.1.6 TEV cleavage reaction

Protein bearing a TEV cleavage site was incubated with TEV (0.2 molar equivalents) at room temperature in TEV buffer until the reaction was complete (2 h), as measured by electrospray ionisation mass spectrometry.

2.12.1.7 Sortase labelling reaction

Protein bearing an *N*-terminal glycine was incubated with fluorescently labelled peptide (3.5 molar equivalents) and Sortase A (0.2 molar equivalents) in sortase buffer at room temperature until the reaction was shown to be complete by electrospray ionisation mass spectrometry (approximately 7 h).

2.13 Isothermal Titration Calorimetry (ITC) studies

A VP-ITC MicroCalorimeter (MicroCal) and VPViewer and Origin software were used.

2.13.1.1 ITC theory

Isothermal Titration Calorimetry (ITC) can be used to measure protein affinities for known ligands and other small molecules of interest. The affinity is related to the change in thermal energy that is generated upon ligand binding, as either a release of energy (exothermic) or intake of energy (endothermic). The ITC experimental set-up is shown in Figure 2-3; it consists of a reference cell that contains water or buffer, a sample cell containing the receptor species of interest and a syringe which is used to inject the ligand in to the sample cell in a controlled manner. The syringe also stirs the sample cell contents at a constant rate to ensure thorough mixing during the experiment. These cells are held within an adiabatic shield, and have a heater for each cell to allow the temperature of each cell to be controlled. The temperature of both cells is maintained by a power supply to the heaters; if a heat change occurs in the sample cell, such as that caused by ligand binding, then the power supply is adjusted to ensure the

temperature returns to that of the reference cell. The ligand is injected to the sample cell in stages; a normal experiment would involve around 20 injections, during which the variations in power supply are recorded. The magnitude of the change in temperature, measured by the change in resulting power supply, corresponds to dilution of the ligand into the sample cell and the enthalpy of binding of the ligand to sample. The concentrations used in ITC are designed to achieve binding saturation before the completion of the experiment. The initial injections are accompanied by a large heat change which requires a large variation in power supply to maintain the temperature between sample and reference cells, whereas the final injections cause a smaller heat change as the receptor sites are now saturated with ligand which is measured as a smaller variation in the power supply. Analysing the changes in power supply over the course of the ligand injections gives information on the rate constant, enthalpy and stoichiometry of binding.

When considering a 1:1 ligand:receptor binding model ($M + X \leftrightarrow MX$), the data obtained from the titration experiment is fitted using the Wiseman isotherm[124] (Equation 2-3).

$$\frac{dQ}{d[X]_t} = \Delta H V_0 \left[\frac{1}{2} + \frac{1\text{-}X_R\text{-}r}{2\sqrt{(1+X_R+r)^2\text{-}4X_R}} \right] \quad (2\text{-}3)$$

Where:

Q = heat of the system

$[X]_t$ = ligand concentration

ΔH = change in enthalpy

V_0 = volume of the sample cell

$X_R = \frac{[X]_t}{[M]_t}$

$[M]_t$ = receptor concentration

$r = \frac{1}{c} = \frac{1}{K_a[M]_t} = \frac{K_d}{[M]_t}$

K_a = association constant

K_d = dissociation constant

c = Wiseman constant

The Wiseman constant c is the ratio of the receptor concentration to the dissociation constant, K_d. For receptors that have several identical non-interacting binding sites, $c = nK_a[M]_t$, where n is the number of binding sites per receptor molecule. With low c systems, greater equivalents of ligand are needed to reach receptor saturation[125].

The Gibbs free energy and entropy of binding can be determined by the following equations:

$$\Delta G = -RT \ln K_a \tag{2-4}$$

$$\Delta S = \frac{\Delta H - \Delta G}{T} \tag{2-5}$$

Where R = ideal gas constant and T = temperature.

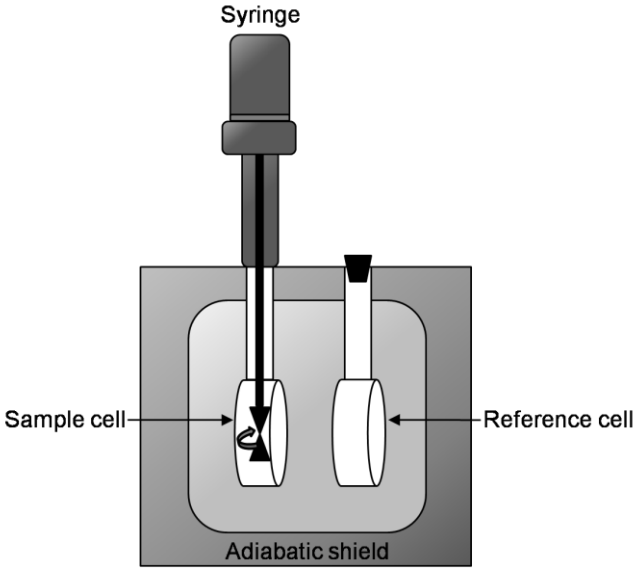

Figure 2-3: Schematic of the Isothermal Titration Calorimetry (ITC) equipment. The reference cell is filled with water or buffer. The receptor is loaded into the sample cell. To this the ligand is injected by the syringe, which also continuously stirs the sample cell.

2.13.1.2 ITC200 experimental

Matched buffers were used for ligand and cell solutions, which were equilibrated to 25 °C. The buffer containing a known concentration of the protein of interest was injected into the sample cell (volume ~200µl) using a gas-tight syringe, ensuring no air bubbles were left in the cell. The buffer containing a known concentration of ligand was drawn into the injection syringe using the loading syringe. The injection syringe was then placed into the sample cell and suitable parameters entered into the VPViewer program along with the concentrations present in each component. Typically ITC experiments were conducted at 25 °C and at a stirring speed of 1000 rpm. Titrations involved an initial 2 µl injection followed by 18 × 10 µl injections with a 180 s delay between each injection. The 'fast equilibrium' and 'auto' boxes were checked so the injections started as soon as the instrument had equilibrated to a steady baseline. The results were analysed using the fitting routines provided in microcal origin 7.0.

2.14 Differential Scanning Calorimetry

Differential scanning calorimetry was used to provide a qualitative analysis of human ATIC stability using a MicroCal VP-DSC. The temperature was cycled between 10 °C and 100 °C, at a rate of 90 °C/hour. The DSC cycling was started the evening before, using degassed water to ensure that the thermal history of the cells and between scans remains constant. The Thermovac used to degas samples and the buffer reference was set to 10 °C for two cycles of 8 minutes. Cells were thoroughly rinsed with water (×3), buffer (×2) and degassed buffer (×1) before filling with the degassed sample. Cell filling was conducted between 15 °C and 25 °C. The sample cell contained human ATIC at 56 μM, or human ATIC (56 μM) with 1 mM AICAR. Results were analysed using origin 7.0.

2.15 Differential Scanning Fluorimetry

Differential Scanning Fluorimetry (DSF) is a method that can be used to monitor the stability of proteins in solution[126]. This method does not require a system that can reversibly fold and unfold. Stability is related to the Gibbs free energy of unfolding, $\Delta G_{U,}$ which is temperature-dependent. Where the protein is in equilibrium between native and unfolded states $\Delta G_U=0$. This is equivalent to the melting temperature of the protein, T_m. The technique utilises certain dyes that are highly fluorescent in hydrophobic environments, such as the sites at the core of a protein that are revealed upon protein unfolding, but that have their fluorescence quenched in aqueous solution. Thus protein unfolding can be monitored as the increase of fluorescence intensity with temperature. When fluorescence intensity is plotted as a function of temperature, this gives a sigmoidal curve similar to that shown in Figure 2-4. Deviation from the curve at high temperatures (dotted green line) occurs due to aggregation of the protein sample. This aggregation releases some of the dye back into aqueous solution and so quenches

fluorescence. The inflection point of the curve corresponds to the T_m and can be calculated using the Boltzman equation, or by determining the maximum of the first derivative. DSF is often used to monitor the effects of ligands and other small molecules on T_m.

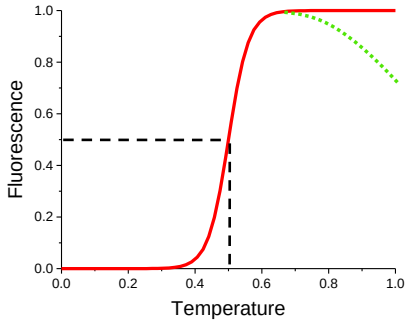

Figure 2-4: Theoretical sigmoidal curve obtained from Differential Scanning Fluorimetry (DSF). Fluorescence intensity increases as a function of temperature upon binding of dye to hydrophobic regions of unfolding protein. Melting temperature (T_m) is determined from where the equilibrium between folded and unfolded states is equal (dashed black line), which is when the Gibbs free energy of unfolding (ΔG_U) is zero. In reality, Fluorescence intensity decays away as shown by the green dotted line as protein aggregates.

SYPRO orange was chosen as the fluorescent dye due to its favourable properties when applied to this technique; it has a high excitation wavelength at 492 nm, so it is unlikely any small molecules to be examined will cause interference, high signal to noise ratio, and high fluorescence gain upon binding to hydrophobic regions (as demonstrated by a ~500% gain when measuring the denaturation of lysozyme) [126]. The fluorescence emission was measured at 570 nm.

DSF experiments were carried out in opaque 96 well plates with a sealed, clear lid to prevent evaporation of the samples and to enable visualisation of the SYPRO orange dye. The measurements were taken using a real-time PCR machine to ensure a constant increase in temperature, starting at 25 °C and increasing by 1 °C/sec to a final

temperature of 100 °C. The data were differentiated and normalised, to give a tallest peak that corresponds to the T_m.

2.16 Analytical UltraCentrifugation (AUC)

A sample volume of 405 µl and a reference volume of 410 µl were centrifuged in 1.2 cm pathlength 2-sector aluminium centrepiece cells (sample in right hand sector, reference buffer in left hand sector) built with sapphire windows in a 4-place An-50 Ti analytical rotor running in an Optima XL-I analytical ultracentrifuge (48,000 rpm, 20 °C). Different volumes were used to allow differentiation between the reference and sample cells. Changes in solute concentration were detected by interference optics at 280 nm. A total of 150 scans per cell were collected. Data were analysed using Sedfit and Sedphat software[127]. Fitting parameters for the protein and buffer ('HB' buffer) were calculated using Sednterp from the primary sequence of the protein to give: $\tilde{\nu} = 0.7375$ ml/g, $\eta = 0.010211$ and $\rho = 1.00736$ g/ml.

2.17 Mass Spectrometry

Protein samples were analysed by electrospray ionisation mass spectrometry using a Bruker Daltonics® HCT Ultra™ mass spectrometer. Samples were diluted 1:1 with 99% acetonitrile, 1% formic acid to achieve a final concentration of between 10 and 50 µM, and run using the 'protein best sense method'. Data were analysed using the Compass Open Access software and exported in pdf format.

2.18 Protein Crystallisation

Protein crystallisation trials were conducted using a 2 µl + 2 µl hanging drop method in 24 well plates. The precipitating 'mother liquor' was dispensed into the well, each well contained different precipitating conditions. 2 µl drops of human ATIC at various concentrations were pipetted onto a glass cover slip, ensuring enough space between drops to prevent bleeding between drops. 2 µl of the mother liquor was then pipetted on top of the ATIC-containing drops, and mixed by being drawn back into the pipette tip four times. The cover slip was then inverted over the appropriate well which contained the mother liquor mixed into the ATIC-containing drops on the cover slip surface. Vacuum grease was used to form a seal between the well and cover slip.

The plates were left to incubate undisturbed at a constant temperature (a range of temperatures were investigated during the optimisation trials). The drops were examined for crystal growth after 1 week, 2 weeks and 1 month.

2.19 Chemistry experimental

Peptide elongations were performed manually using standard Fmoc solid phase peptide synthesis as described by Chan and White[128] using vaculate tubes (Alltech) and a vacuum manifold attached to a water aspirator.

Low-loading Rink Amide resin (500 mg, 0.22 mmole/g) was swollen in DMF for at least 30 min. The resin was separated by filtration. Amino acids used (in order of coupling) were: Fmoc- Asp-OAll; Fmoc- Phe-OH; Fmoc-Tyr(tBu)-OH; Fmoc-Arg(Pbf)-OH; Fmoc-Cys(Trt)-OH; Fmoc-Val-OH. The Fmoc-protected amino acid (5 mmol) and HCTU (5 mmol) were dissolved in DMF (~10 ml). DIPEA (10 mmol) was added and the solution was transferred to the dry resin (0.11 mmol). The mixture was gently agitated for 1 h. The resin was isolated by filtration and washed with DMF (3 ×

10 ml for 2 min). The resin was treated with a solution of 20% piperidine in DMF (5 x 10 ml x 2 min) to remove Fmoc protecting groups and then washed with DMF (5 × 10 ml for 2 min).

Allyl group removal was carried out under a nitrogen atmosphere. Tetrakis(triphenylphosphine)palladium(0) (29.43 mg, 25 mol%) and morpholine (200 µl, 2.2 mmole) in DMF (8 ml) were added to the resin and agitated with the nitrogen stream until deprotection was complete (22 h). The resin was then filtered from the deprotection solution and washed with DMF (5 × 10 ml for 2 min). A small sample of the resin was removed for use in the synthesis of the linear peptide. HCTU (5 mmol) and DIPEA (10 mmol) were dissolved in DMF (~10 ml) and the solution added to the remaining resin and gently agitated at room temperature until cyclisation was complete (2 h). The resin was washed with DMF (5 × 10 ml for 2 min), DCM (3 × 10 ml for 2 min) and MeOH (3 × 10 ml for 2 min) before being dried overnight under vacuum.

The dried resin was treated with a cleavage cocktail of TFA/TIS/H_2O/EDT (94:2.5:2.5:1) (15 ml) and the mixture was gently agitated for 1 h 45. The resin beads were removed by filtration and rinsed with TFA. The combined filtrates were added drop-wise to ice-cold Et_2O (2 × 50 ml). The orange precipitate was isolated by centrifugation (4000 rpm, 5 min) and washed with ice-cold Et_2O (5 × 50 ml). The crude peptide was dried under a stream of N_2 to remove the remaining Et_2O and lyophilized from MeCN. The crude peptide (10.1 mg, 12%) was purified by preparative reverse phase HPLC (gradient elution t=0, MeOH:MeCN 95:5; t=35, 5:95 elution at 12.58 min), lyophilised and purity confirmed by LCMS (calculated: 782.9, found: 783.6 $[M]^+$) and analytical HPLC (Figure 2-5).

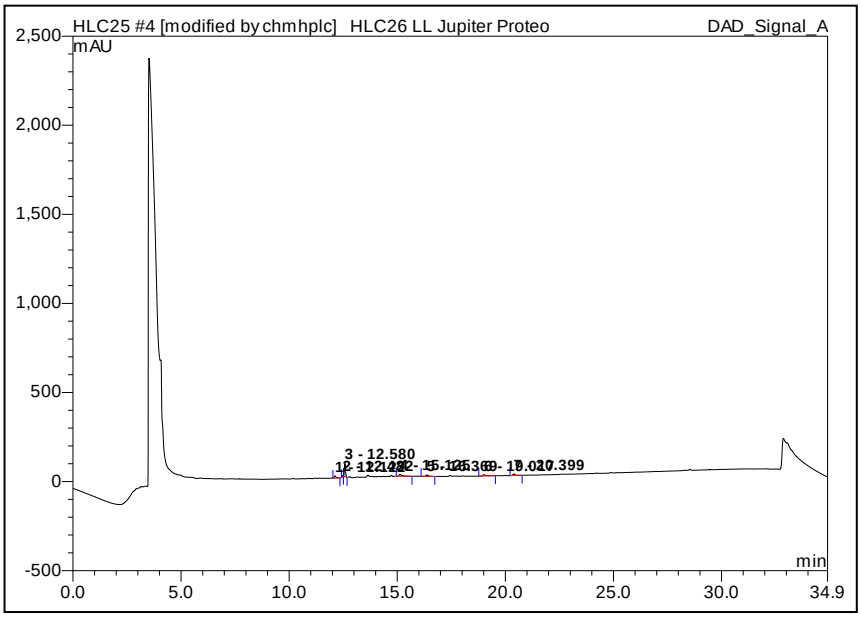

Figure 2-5: Analytical HPLC trace of the cyclic peptide to determine purification conditions. Elution at 12.58 min

3 Characterisation of ATIC

3.1 Introduction

Since the discovery of ATIC activity in 1959[6], the enzyme has been extensively studied, ultimately leading to the determination of the crystal structure[46], which showed ATIC crystallises as a dimer which has a very large interface between monomers. The crystal structure also showed ATIC has two distinct active sites, the second of which, AICAR transformylase, is formed by residues from both of the monomers. Hence, AICAR transformylase activity is entirely dependent upon enzyme dimerisation. To date, there have been no reports on the thermal stability of ATIC found in the literature.

The kinetics of various ligands and inhibitors of ATIC have been examined, and a selection of results from the literature is presented in

Table 3-1. No experiments to determine the binding order or binding constants of the substrates and small molecules associated with ATIC have been reported in the literature.

Table 3-1: Summary of some of the kinetic properties of various small molecules found in the literature.

Ligand	***Human ATIC***		***Avian ATIC***
	K_M/µM	**K_i/µM**	**K_M/µM**
AICAR	1.9± 0.4[50], 16.8± 1.5[31]		1.9± 0.4[53]
10-f-H_4F	39.0 ± 6.0[50],, 60.2± 5.0[31]		7.6± 0.6[53]
AMP		27± 3[50],	
XMP		1.2± 0.4[50],	

Further characterisation of ATIC was undertaken, to fill the gaps in understanding found in the literature.

3.2 Protein purification

Full length human and avian ATIC bearing *N*-terminal his tags were overexpressed in *E. coli* BL21(DE3), *E. coli* BL21*(DE3) and *E. coli* C41(DE3) strains growth in auto-induction media for 24 h at 30 °C. Cells containing the overexpressed ATIC were harvested by centrifugation and stored at -80 °C. The cells were resuspended in buffer, and lysed by sonication or cell disruption, and the lysates cleared by centrifugation before further purification.

Ni-NTA affinity chromatography under gravity flow was used to purify the protein of interest from the crude lysates after cell disruption, as described in Chapter 2. Crude protein lysates were applied to the column to bind the $his_{(6)}$-tagged proteins before the column was washed step-wise with increasing concentrations of imidazole (50 and 150 mM). The protein was then eluted with 250 mM imidazole. Fractions were analysed for protein content by using a Bradford dye binding assay, and then for protein purity by SDS-PAGE. Figure 3-1a shows a typical 10% SDS-PAGE analysis of the fractions collected during the purification of human ATIC using Ni-NTA affinity chromatography. The elution fractions (lane 7, and onwards) show a high concentration of a protein at approximately 66 kDa, consistent with the monomer molecular weight of human ATIC (including the $his_{(6)}$-tag) of 66.8 kDa. Some trace impurities are present in the elution fractions after the affinity purification. To remove these remaining impurities, the fractions containing ATIC were combined and concentrated using centrifugal concentrators, prior to further purification by size exclusion chromatography.

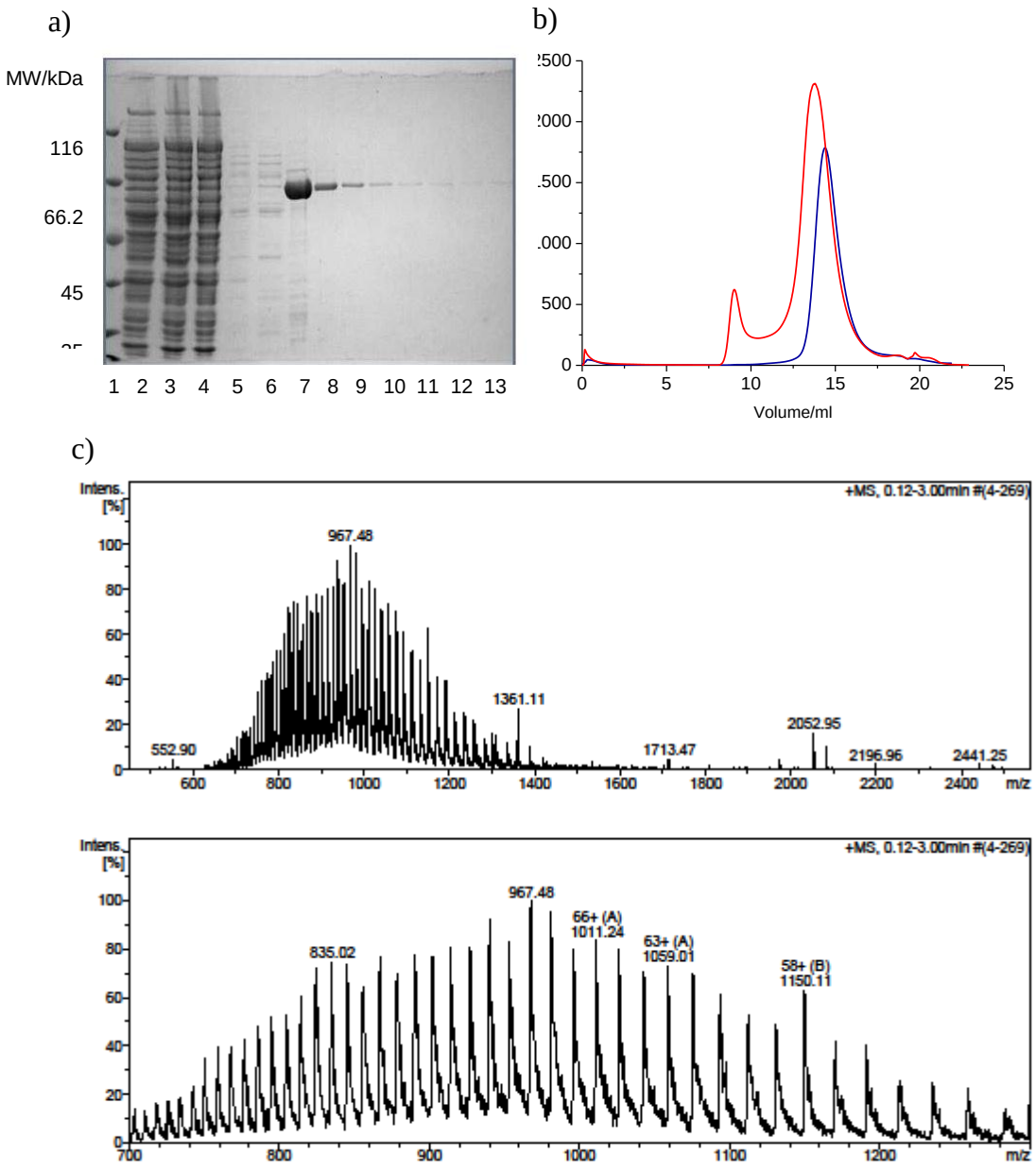

Figure 3-1: a) SDS-PAGE of the purification of human ATIC from *E. coli* using a gravity flow NTA column. Lane 1: molecular weight marker, lane 2: flow through 1, lane 3: flow through 2, lane 4: flow through 3, lane 5: wash 1 (10 mM imidazole), lane 6: wash 2 (150 mM imidazole), lanes 7-14: elution fractions 1 to 8 (5 ml)

b) Absorption at 280 nm of size exclusion purification. Human ATIC is shown in red and has an elution volume of 13.79 ml. Avian ATIC is shown in blue with an elution volume of 14.4 ml.

c) Mass spectrum of human ATIC reported a mass of 66669.5 kDa, the bottom panel is a expanded view of the 700 to 1300 m/z region.

The size exclusion chromatography was performed using a Pharmacia AKTA FPLC system, using either a 26/60 Superdex 200 column or 10/300 Superdex 200 column depending on the scale of protein preparation. Elution typically yielded a single monodisperse peak. Figure 3-1 shows a typical trace for purification of human (red) and avian (blue) ATIC using a 10/300 Superdex 200 column (used for smaller scale protein preparations), where pure protein was collected in 1 ml fractions from 13 to 15 ml elution volume. Protein purity was reassessed and confirmed by SDS-PAGE analysis, and the protein identity was confirmed by electrospray ionisation mass spectrometry.

The approximate size, and therefore the oligomeric state of the samples purified by size exclusion can be determined from the retention time. The analytical Superdex 200 10/300 gel filtration column was therefore calibrated using molecular weight standards (Sigma Aldrich), as shown in Figure 3-2b, to give an appropriate range of data to create a calibration curve (Figure 3-2a). Thyroglobulin (red line), shows a small amount of aggregated protein which elutes at the same volume as Blue dextran; this corresponds to the void volume of the column.

To construct the calibration graph, the elution volumes for each of the marker proteins were normalised to the void volume, and plotted against the corresponding molecular weight (kDa). This yields a logarithmic relationship that was fitted to an empirical equation of the form $\ln(\mathrm{Mw}) = \ln c - m\left(\frac{V_e}{V_0}\right)$ (Figure 3-2b). The Molecular weight (Mw) was then calculated from the elution volume (V_e) of the species of interest.

The size estimated by the size exclusion column (Table 3-2), shows human ATIC elutes at a volume that corresponds to a molecular weight of 110 kDa, which is larger than a monomer (66.8 kDa) but smaller than a dimer (133.6 kDa). Estimation of molecular weight by size exclusion chromatography also depends on the shape of the protein of

interest. Human ATIC is thought to elute at a slightly larger volume than would be expected for a dimer, due to its streamlined shape. Avian ATIC appears to elute at a volume that corresponds to a molecular weight larger than a monomer (66.6 kDa), but smaller than a dimer (133.2 kDa) at 80 kDa. This could suggest that the dimeric form of avian ATIC is also streamlined, but is more compact than human ATIC, or that it is eluting as a monomer.

Rayl[31] reports ATIC eluting as a 65.63 kDa species, but this was measured on a Superdex 75 column (eluted with 20 mM Tris-Cl pH 7.5, 150 mM NaCl, 50 mM KCl and 20% (v/v) glycerol) and was only calibrated using albumin (67 kDa), ovalbumin (43 kDa), chymotrypsin (25 kDa) and ribonuclease A (13.7 kDa), which will have resulted in a different calibration curve, and may have not calibrated for higher molecular weight species as effectively as the molecular weight standards chosen in this study.

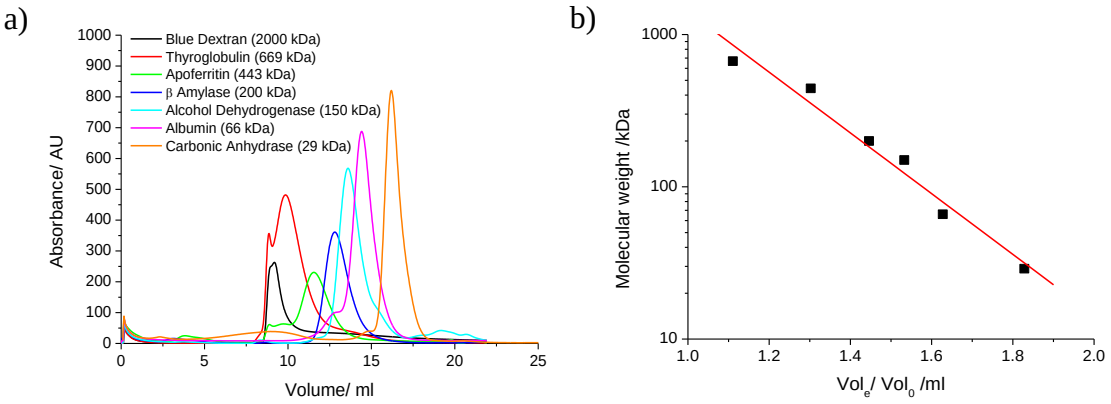

Figure 3-2: Calibration of the GE Healthcare Superdex 200 10/300 gel filtration column with molecular weight standards. The elution traces of seven standards of known molecular weight, monitored at 280 nm, are reported in (a): blue dextran (2000 kDa), thyroglobulin (669 kDa), apoferritin (443 kDa), β amylase (200 kDa), alcohol dehydrogenase (150 kDa), albumin (66 kDa), and carbonic anhydrase (29 kDa). The elution volume of each standard is plotted against molecular weight to give a calibration curve (b) with equation $\ln y = \ln 13983 - 4.59x$. Approximate molecular weights were calculated for human and avian ATIC by imputing the normalised elution volume (V_e/V_0) into this equation.

Table 3-2: Estimation of molecular weight from size exclusion chromatography elution volume for human and avian ATIC

Enzyme	V_e*/ml*	*MW/kDa*
Human ATIC	13.79	110
Avian ATIC	14.38	80

The mass of human ATIC was determined by LCMS to be 66669.5 kDa, which is consistent with the human ATIC monomer after loss of the *N*-terminal methionine and the addition of a potassium ion (see Chapter 6). The expected mass, as calculated from the sequence, of human ATIC including the $his_{(6)}$-tag is 66779.2 kDa.

3.3 Kinetic analysis

ATIC catalyses both the formyl transfer reaction, which converts AICAR to FAICAR, and the subsequent cyclisation reaction to form IMP. The formyl transfer reaction proceeds by the conversion of the folate cofactor 10-f-H_4F to H_4F. Two assays for monitoring AICAR transformylase turnover are reported in the literature; a sensitive assay that uses radiolabeled substrates for which the products are then analysed by TLC[43] and a spectroscopic assay reported by Black[43]. This assay measures the rate of production of H_4F from the turnover of 10-f-H_4F which is equivalent to the rate of formation of FAICAR. The reaction is monitored by an increase in absorption at 298 nm. Both folate compounds absorb at 298 nm but the increase arises from the difference in the extinction coefficients. Figure 3-3 shows the absorption profile of the catalytic turnover of ATIC, an increase in absorption at 298 nm is seen as the reaction progresses.

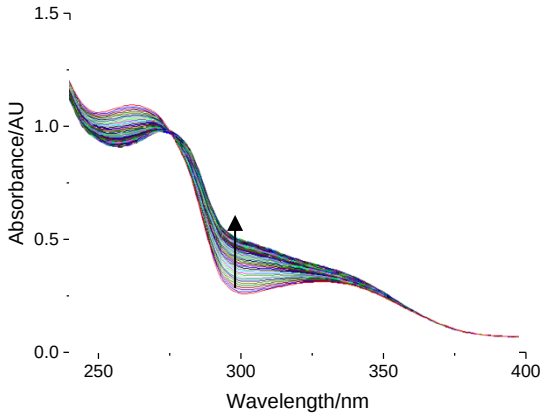

Figure 3-3: Spectra following the catalytic turnover of AICAR transformylase converting 10-f-H_4F to H_4F. The arrow indicates the increase in absorption at 298 nm.

The AICAR Tfase activity in the forwards direction is measured as the aggregate with the IMPCH activity, which drives the reaction forward to completion.

3.3.1.1 Standard spectroscopic assay

A typical trace from a single assay of the turnover of ATIC is shown in Figure 3-4. The absorption at 298 nm is recorded for a quartz cell containing the initial assay mixture of buffer, enzyme and AICAR; this corresponds to the flat line measured for the first 30 seconds of Figure 3-4. As there is no increase in absorption, this confirms there is no turnover taking place. Then the cell is removed from the spectrophotometer and the cofactor 10-f-H_4F is added to initiate the reaction. The cell is inverted a few times to mix, and returned to the spectrophotometer to measure the increase in absorption. The increase in absorption at 298 nm is caused by the conversion of 10-f-H_4F to H_4F, and is therefore a measure of the turnover of the enzyme.

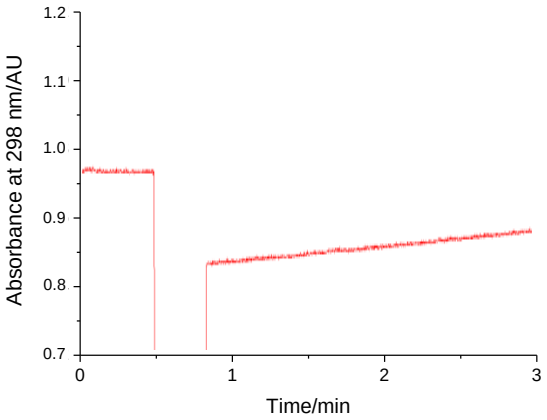

Figure 3-4: A typical trace from the Varian Cary 50 Bio UV-visible spectrophotometer monitoring the catalytic reaction of ATIC. The turnover over of 10-f-H_4F to H_4F is measured at 298 nm.

3.3.1.2 Considerations with 10-f-H4F

10-f-H_4F was synthesised either from 5,10-methenyl H_4F, or in a two-step process from 5-f-H_4F *via* 5,10-methenyl H_4F (Figure 3-5). The three folate compounds are interconverted through pH driven reactions[129]. 10-f-H_4F is synthesised by exploiting the equilibria of the reactions. In the first reaction, 5,10-methenyl H_4F is the dominant species under acidic conditions and is isolated under thermodynamic control. The pH is then adjusted to alkaline (pH 8.8) to afford the 10-f-H_4F cofactor. The reactions are performed in the presence of the reducing agent β-mercaptoethanol to prevent oxidation to the dihydrofolate cofactor. 10-f-H_4F slowly reverts back to 5-f-H_4F at room temperature, and faster at higher temperatures[130]. With this in mind, 10-f-H_4F was stored at –80 °C and each batch of compound was only used for a couple of days before discarding and replacing with a new batch.

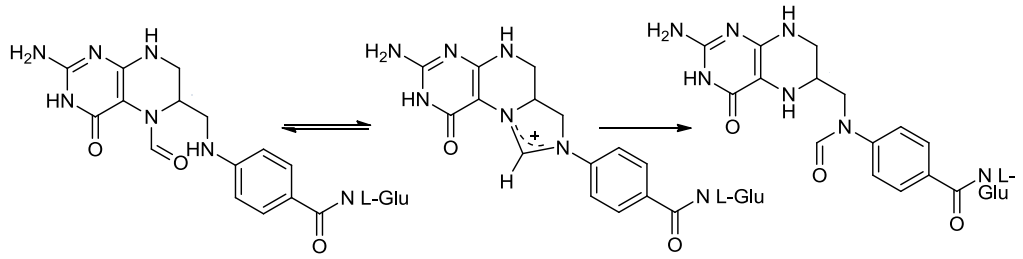

Figure 3-5: The synthesis of 10-f-H_4F from 5-f-H_4F *via* the *in situ* formation of 5,10-methenyl H_4F.

The 10-f-H_4F solution must be equilibrated for at least 1 hour before use in UV-visible studies. 10-f-H_4F has a pH-dependent absorption profile, so if the 10-f-H_4F is not equilibrated to the assay conditions (pH 7.4) then this will interfere with the rate measurements. Figure 3-6 shows the initial scan (red line) of 10-f-H_4F, diluted 1 in 10 from the synthesis solution which has a pH of 8.8 into an assay buffer of pH 7.4. Scans were then performed every 5 minutes for a total of 70 minutes. The ATIC assay is measured at 298 nm, so if the folate cofactor was not at pH 7.4 before addition to the assay mixture an increase in absorption would be measured that corresponds to the pH equilibration, not the turnover of ATIC. As can be seen from Figure 3-6, equilibration from pH 8.8 to pH 7.4 at 298 nm takes a minimum of 30 minutes; therefore a 1 hour equilibration time was used to ensure complete conversion.

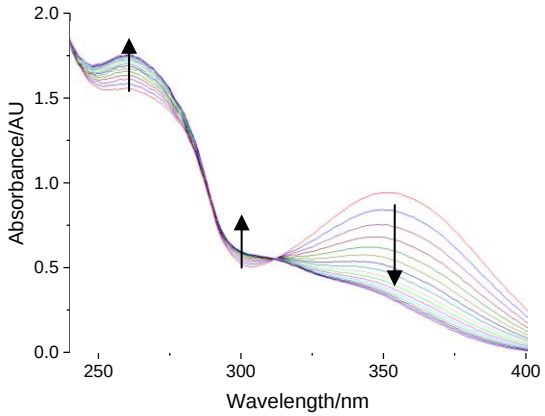

Figure 3-6: A scan of the changing absorption profile of 10-f-H_4F with pH, where red is the initial scan of 100 µl of 10-f-H_4F synthesis solution (pH 8.8) diluted into 900 µl assay buffer (pH 7.4) at 37 °C. Subsequent scans are taken every 5 min. At 298 nm the absorption of the 10-f-H_4F solution increases as it equilibrates to pH 7.4 (standard ATIC assay conditions).

3.3.1.3 Determination of AICAR and 10-f-H4F KM

Using the standard spectroscopic assay, the K_M for AICAR was determined to be 3.75 ± 0.65 µM at a fixed 10-f-H_4F concentration of 66 µM at 37 °C. This value is within the range of values found in the literature of 1.9 µM[50] **(**measured at 25 °C) and 16.8 µM[31]. The K_M for the 10-f-H_4F cofactor was determined to be 9.05 ± 0.45 µM (Figure 3-8).

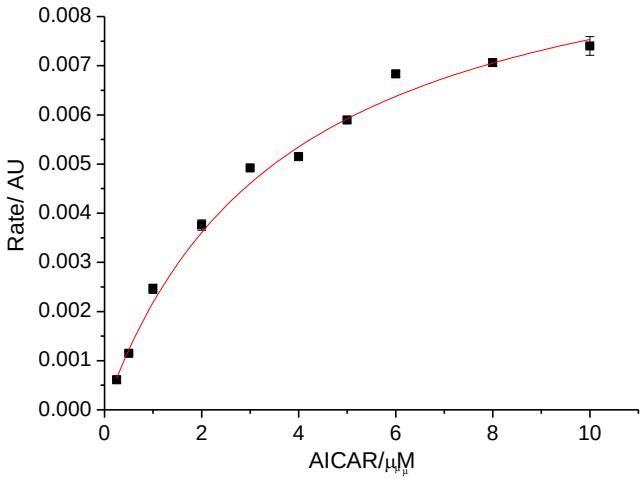

Figure 3-7: The effect of AICAR concentration on reaction rate of human ATIC at a fixed concentration of (6S)-10-f-H_4F (66 µM)

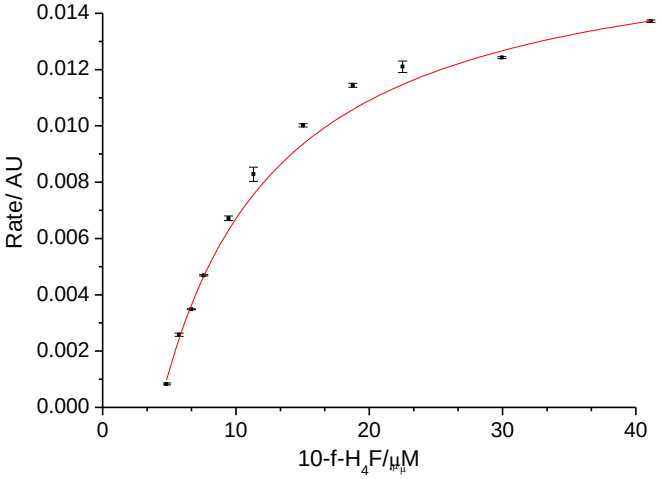

Figure 3-8: The effect of (6S)-10-f-H_4Fconcentration on reaction rate of human ATIC at a fixed concentration of AICAR (20 μM)

3.3.1.4 Determination of a binding model

To determine the binding model and order of binding of AICAR and 10-f-H_4F, a method for measuring the kinetics in two dimensions was developed. This high-throughput method utilised the EnVision plate reader system, to determine the substrate K_M and cofactor K_M simultaneously, in a two-dimensional, 96 well plate format. The ATIC assay protocol is shown in the methods section (Chapter 2), and involves dispensing the AICAR substrate to each well, a shake operation followed by repeated UV-visible absorption measurements. The wavelength was chosen to be comparable with the standard ATIC assay (298 nm), and was achieved using a compatible filter of 296 ± 3 nm. The protocol was designed to conduct measurements on a single row of the plate at a time and to dispense a different amount of substrate for each row, to reduce error from a time delay in measurements that would arise from running 96 assays at one time.

Data collected from the high-throughput assay using wild type ATIC were analysed using Origin 7.0 and fitted using Equation 3-10. Figure 3-9 represents how the rate changes with varying AICAR and 10-f-H_4F concentrations.

a)

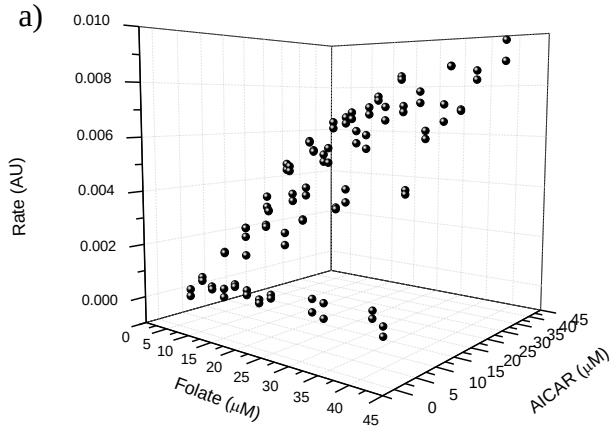

Model	Orderedbinding (User)	
Equation	A*x*y/(K1*K2+K2*x+x*y)	
Reduced Chi-Sqr	6.65989E-7	
Adj. R-Square	0.91757	
Value	Standard Error	
	A	0.01679 ± 0.00177
	K1	14.07065 ± 4.46033
	K2	41.56069 ± 11.8939

b)

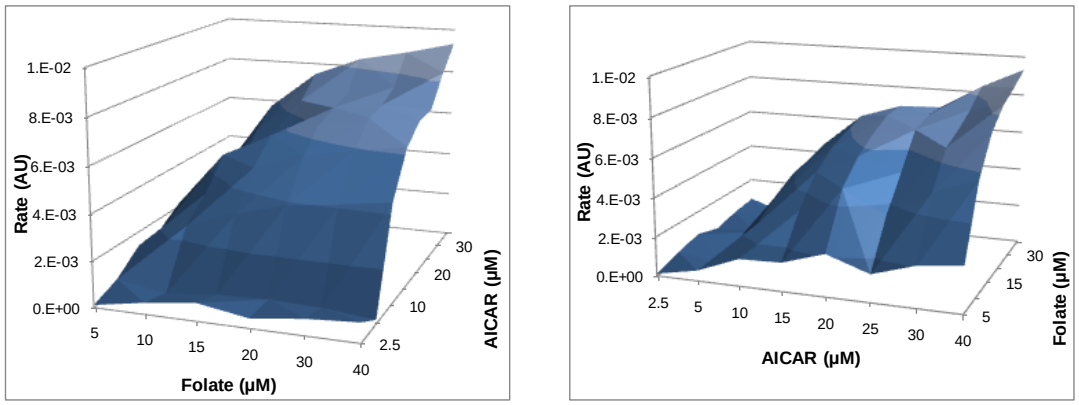

Figure 3-9: a) 3D plot of how the catalytic rate of reaction varies with varying AICAR and 10-f-H_4F concentrations for human ATIC, measured using the EnVision plate reader system. b) 3D surface plot (shown for clarity).

The data were fitted to a rapid equilibrium sequential ordered binding model, derived assuming the binding model shown in Equation 3-1, where E is the enzyme, A and B are the substrate and cofactor, EA is the enzyme-substrate or enzyme-cofactor complex, EAB is the enzyme-substrate-cofactor complex and P is the resultant product. The

rapid equilibrium binding model assumes that the rate determining step is the chemical reaction, not the binding or release of the substrates or products.

$$E + A \overset{K_1}{\leftrightarrow} EA + B \overset{K_2}{\leftrightarrow} EAB \overset{k_{cat}}{\longrightarrow} P \tag{3-1}$$

$$K_1 = \frac{[E][A]}{[EA]} \tag{3-2}$$

$$K_2 = \frac{[EA][B]}{[EAB]} \tag{3-3}$$

$$[EA] = \frac{K_2[EAB]}{[B]} \tag{3-4}$$

$$[E] = \frac{K_1[EA]}{[A]} = \frac{K_1K_2[EAB]}{[A][B]} \tag{3-5}$$

$$E_0 = [E] + [EA] + [EAB] \tag{3-6}$$

$$E_0 = \frac{K_1K_2[EAB]}{[A][B]} + \frac{K_2[EAB]}{[B]} + [EAB] \tag{3-7}$$

$$E_0 = \left(\frac{K_1K_2}{[A][B]} + \frac{K_2}{[B]} + 1\right)[EAB] \tag{3-8}$$

$$v = k_{cat}[EAB] = \frac{k_{cat}E_0}{\frac{K_1K_2}{[A][B]} + \frac{K_2}{[B]} + 1} = \frac{k_{cat}E_0[A][B]}{K_1K_2 + K_2[A] + [A][B]} \tag{3-9}$$

$$v = \frac{V_M[A][B]}{K_1K_2 + K_2[A] + [A][B]} \tag{3-10}$$

When the data obtained for the automated assay were fitted to Equation 3-10, the binding order for the ATIC reaction was determined to be A = AICAR and B = 10-f-H_4F. The cofactor cannot bind before the substrate. The rate constants were calculated as K_1 = 14.1 ± 4.5 μM which is the constant at which the enzyme binds AICAR to form an enzyme-substrate complex, and K_2 = 41.6 ± 11.9 μM which is the constant the enzyme–AICAR complex binds the 10-f-H_4F cofactor:

$$E + AICAR \overset{K_1}{\leftrightarrow} [E - AICAR] + 10\text{f}H_4\text{F} \overset{K_2}{\leftrightarrow} [E - AICAR - 10\text{f}H_4\text{F}] \overset{k_{cat}}{\longrightarrow} P$$

These data therefore suggests that ATIC proceeds by an ordered binding mechanism, in which AICAR binds to the enzyme before the 10-f-H_4F cofactor can bind. After the enzyme-substrate-cofactor complex has formed ATIC catalyses the formation of FAICAR and H_4F. The associated rate constants measured for AICAR and 10-f-H_4F through this two dimensional analysis are lower than the apparent K_Ms measured using the standard spectroscopic assay.

3.4 Small molecule binding

Isothermal Titration Calorimetry (ITC) can be used to measure protein affinities for known ligands and other small molecules of interest. The affinity is calculated in terms of the change in thermal energy that is generated upon ligand binding, as either a release of energy (exothermic) or intake of energy (endothermic). No binding affinities for any ligands of ATIC have been reported in the literature.

The binding affinities of the substrate and cofactor for human and avian ATIC were measured by ITC, along with a selection of other small molecules. AICAR is the natural substrate for ATIC, and IMP is the product of the two-step reaction catalysed by ATIC. AMP is structurally analogous to both AICAR and IMP and is one of the downstream products of enzymatic reactions that use IMP as a substrate. AMP is almost identical to IMP, having a primary amine in place of a carboxyl group. XMP is structurally similar to IMP, but contains another amide group within its secondary ring structure. In protein crystals of ATIC, electron density that matches XMP has been identified within the IMPCH binding site[46]. 10-f-H_4F is the cofactor for ATIC and provides the formyl group that is attached to AICAR in the first catalytic step. The *in vivo* cofactor is in the polyglutamated form, but this glutamate tail is too readily hydrolysed so 10-f-H_4F has been used for this kinetic analysis. $PteGlu_4$ is identical to

the *in vivo* cofactor but crucially does not contain the formyl group required for catalysis. This small molecule was chosen to investigate the role the polyglutamated tail plays in cofactor binding. The results of the binding experiments conducted with these molecules with human and avian ATIC are shown in Table 3-3 and discussed below.

Table 3-3: Binding affinities of ligands and small molecules with human and avian ATIC determined by ITC. Measurements were taken using a MicroCal ITC_{200} at a constant temperature of 25°C. Ligand:enzyme concentrations were adjusted as required to achieve saturation. Data were fitted using MicroCal Origin® software to calculate number of binding sites, dissociation constant and enthalpy of binding.

Ligand	***Human ATIC***					***Avian ATIC***				
	Ligand conc/ mM	**Enzyme conc/ µM**	**Number of sites**	**K_d/ µM**	**ΔH/ kcal mol^{-1}**	**Ligand conc/ mM**	**Enzyme conc/ µM**	**Number of sites**	**K_d/ µM**	**ΔH/ kcal mol^{-1}**
AICAR	1.2	60	0.78 ± 0.04	6.14 ± 1.37	-7.68 ± 0.38	1	35	1.23 ± 0.07	13.83 ± 2.15	-4.83 ± 0.35
IMP	1.5	60	0.35 ± 0.06	53.19 ± 4.50	-8.39 ± 0.16					
XMP	1	60	1.67 ± 0.02	4.64 ± 0.37	-3.47 ± 0.06	2	26	2.02 ± 0.16	40.83 ± 4.10	-2.29 ± 0.21
AMP	0.75	60	0.44 ± 0.03	8.40 ± 2.01	-3.54 ± 0.33	1	70	0.73 ± 0.03	10.96 ± 1.78	-3.14 ± 0.18
10-f-H_4F	1.96	60	1.12 ± 0.16	120.92 ± 11.48	-7.53 ± 1.23	4.9	56	1.26 ± 0.36	267.95 ± 23.23	-4.70 ± 0.32
$PteGlu_4$	1	60	0.96 ± 0.00	0.22 ± 0.03	-9.43 ± 0.06	0.5	56	0.96 ± 0.00	0.44 ± 0.02	-9.68 ± 0.03

Each monomer of ATIC contains two possible binding domains, IMPCH and AICAR tfase. These are highlighted in Figure 3-10.

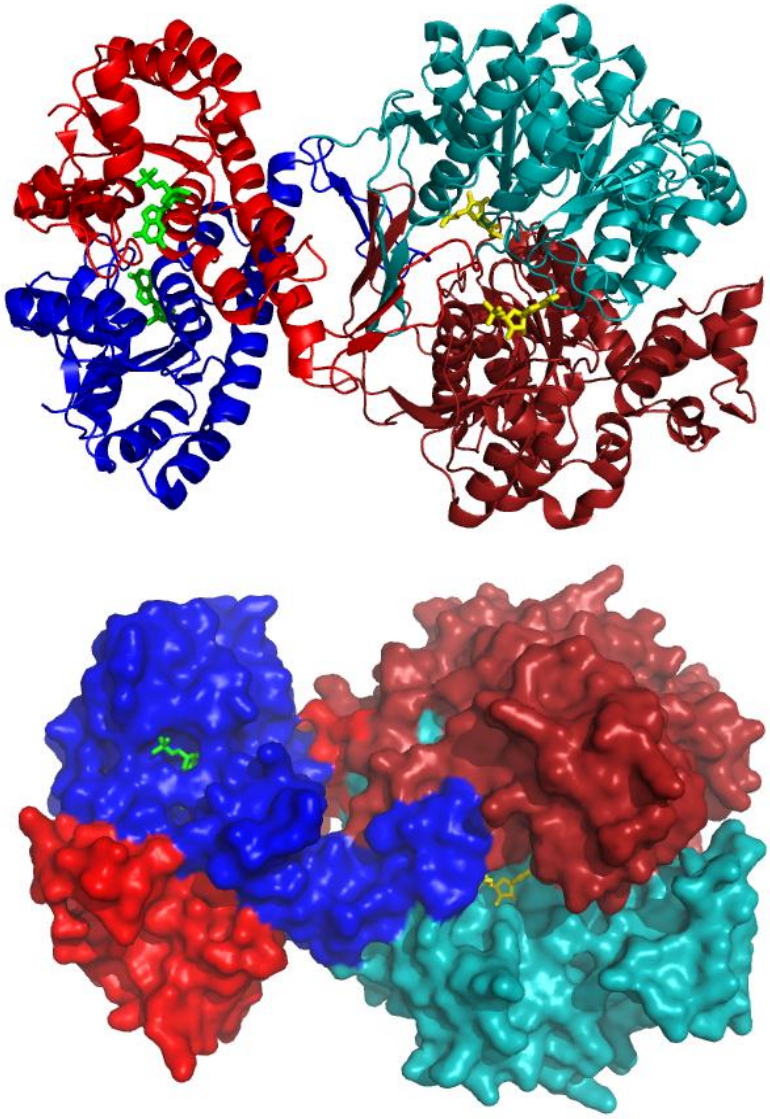

Figure 3-10: Crystal structure of human ATIC highlighting the IMPCH (left hand side, bright colours) and AICAR tfase (right hand side) binding domains. XMP is shown in yellow bound in the IMPCH active site, and AICAR is shown in green bound to the AICAR tfase active site.

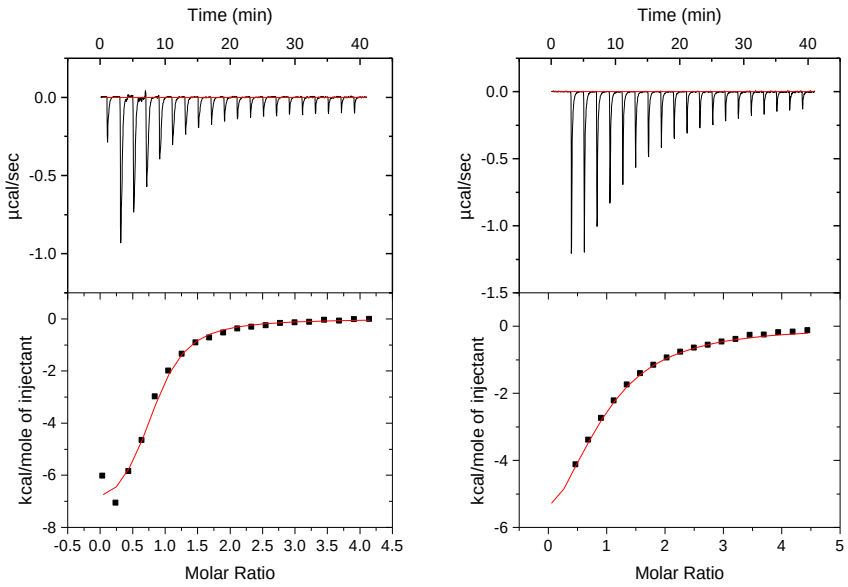

Figure 3-11: ITC of AICAR binding to human ATIC (left) and avian ATIC (right) measured at 25 °C.

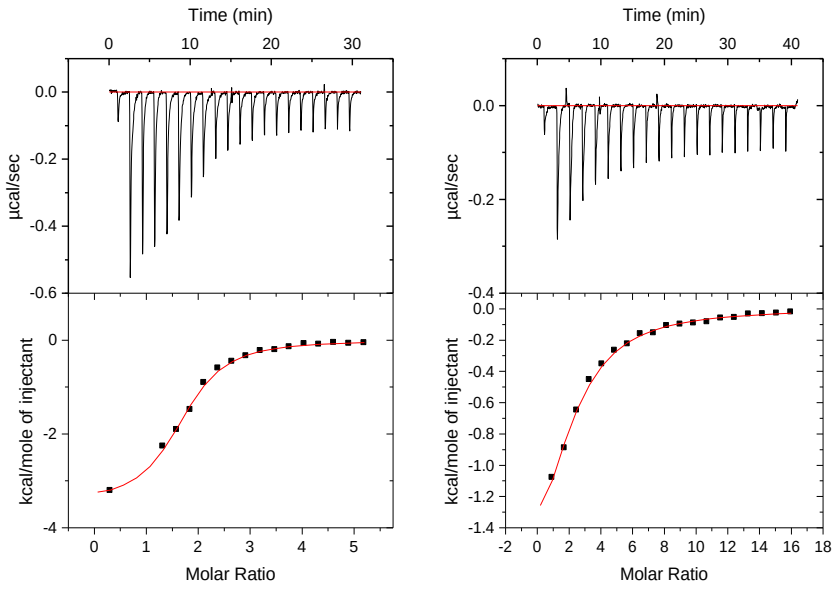

Figure 3-12: ITC of XMP binding to human (left) and avian ATIC (right) measured at 25 °C.

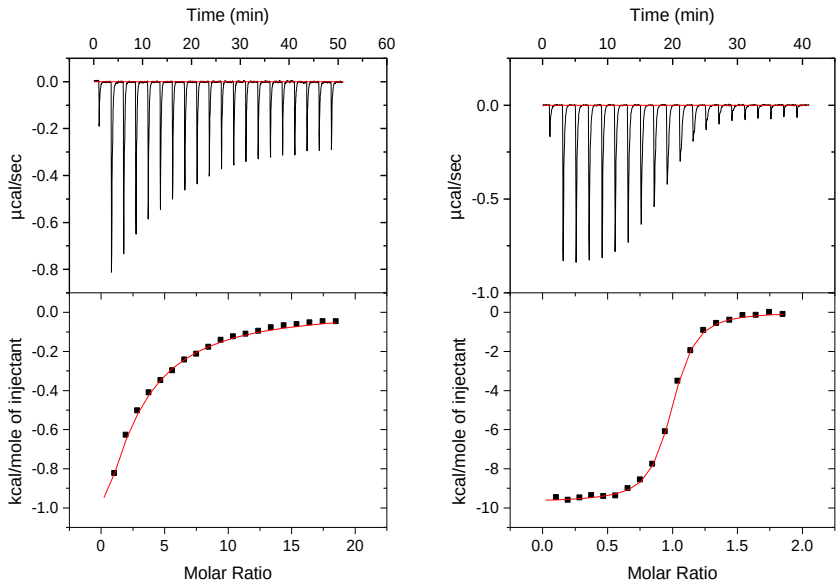

Figure 3-13:ITC showing binding of 10-f-H_4F (left) and $PteGlu_4$ (right) to avian ATIC measured at 25 °C.

3.4.1.1 Isothermal titration calorimetry of human ATIC

AICAR binds tightly to human ATIC with a K_d of 6.14 ± 1.37 µM to approximately one site per monomer (0.78 ± 0.04). This implies that AICAR does not bind into the IMPCH site, and only binds to the AICAR transformylase site. IMP binds weakly to human ATIC (53.19 ± 4.50 µM) and with less than half a binding site per monomer (0.35 ± 0.06). It is expected that IMP should bind more weakly than the natural substrate AICAR as it is the product of the ATIC catalytic reaction. It is desirable for the product to be released upon its formation. XMP binds to between one and a half and two sites per monomer (1.67 ± 0.02), which suggests XMP can bind to both the AICAR transformylase and the IMPCH sites. XMP would present chemical groups in the same orientation as the formyl AICAR product of the first catalytic step, and so would be expected to be able to bind to both sites; in AICAR transformylase as a product mimic and in IMPCH as a substrate mimic. The binding constant (4.64 ± 0.37 µM) is tighter than for AICAR, which may explain why XMP has been identified in

certain crystal structures over the natural substrate. As XMP binds more tightly than the natural substrate AICAR, it might act as another route for negative feedback within the *de novo* purine biosynthetic pathway (Figure 1-12). AMP binds to half a binding site per monomer (0.44 ± 0.03). AMP binds with a similar affinity as AICAR, with a slightly weaker K_d of 8.40 ± 2.01 μM, but within the error of the AICAR K_d. As AICAR and AMP have similar affinities it may imply that the NH_2 group of the AICAR amide is more important to binding than the carboxyl. This is consistent with the proposed mechanism (Figure 1-6) that has the carboxyl holding the primary amine in position ready to attack the formyl group of the folate cofactor. 10-f-H_4F binds to one site per monomer (1.12 ± 0.16) but very weakly with a K_d of 120.92 ± 11.48 μM. As $PteGlu_4$ binds with a much tighter K_d of 0.22 ± 0.03 μM it would appear the polyglutamated tail of the natural substrate is a major driving force in binding to human ATIC.

3.4.1.2 Isothermal titration calorimetry of avian ATIC

ITC experiments were conducted on avian ATIC with the same range of ligands analysed for binding to human ATIC. Binding experiments were carried out at a constant temperature (25 °C) with ligand and receptor in degassed 25 mM KCl, 25 mM Tris pH 7.4 buffer, following the same procedure used for the human ATIC ITC experiments. Avian ATIC (26-70 μM) was contained in the sample cell, and the ligand was injected to the cell in 2 μl portions (with a first injection of 0.5 μl). The ligand concentrations were varied for each ligand to ensure saturation was achieved. Data were fitted using MicroCal Origin® software to calculate number of binding sites, dissociation constant and enthalpy of binding (Table 3-3).

The natural substrate, AICAR, bound to avian ATIC with a K_d of 13.83 ± 2.15 μM, to approximately one site per monomer (1.23 ± 0.07) which suggests AICAR binds solely

in the AICAR transformylase pocket. XMP binds fairly weakly to avian ATIC with a K_d of 40.83 ± 4.10 µM ,and appears to bind in both the AICAR transformylase and IMPCH sites as it binds to 2.02 ± 0.16 sites per monomer. AMP binds to one site (0.73 ± 0.03) with a similar affinity (10.96 ± 1.78 µM) to the natural substrate AICAR. IMP did not appear to bind to avian ATIC; this might be due to XMP or similar already filling the sites from co purification. If IMP binds very weakly to the apo enzyme, the presence of higher affinity molecules bound to avian ATIC would mean IMP could not bind. 10-f-H_4F binds once per monomer (1.26 ± 0.36) very weakly, with an affinity of 267.95 ± 23.23 µM. As for human ATIC the $PteGlu_4$ binds extremely tightly with a K_d of 0.44 ± 0.02 µM which implies the lack of a polyglutamated tail will cause the 10-f-H_4F cofactor to bind less tightly than its *in vivo* equivalent.

Both human and avian ATIC have AICAR and AMP affinities that are very similar, which suggests that they could be binding in the same manner. Comparing the chemical structures, both ligands have two amine groups which, if binding was through these groups, would explain the similarity in affinity. That this can be inferred from data across the two organisms gives greater weight to this hypothesis.

XMP seems to bind in both active sites for human and avian ATIC, but human ATIC has a much higher affinity than the avian ATIC. As would be expected for 10-f-H_4F, both organisms show one binding site per monomer. Although both have very weak affinity for 10-f-H_4F, avian ATIC is two fold weaker than human ATIC. This weak, high micro molar affinity is unexpected for a small molecule cofactor, but 10-f-H_4F is lacking a polyglutamated tail that is found on the *in vivo* cofactor. By comparison with the $PteGlu_4$ results, which have extremely high affinities for human and avian ATIC, it can be inferred that the glutamate chain that is found on the *in vivo* substrate would cause a greater increase in the binding affinity to ATIC. The weak binding seen with 10-f-H_4F also supports the ordered binding mechanism; the K_d measured for 10-f-H_4F is

far larger than the measured K_M of 42 μM. This supports the hypothesis that AICAR binds to the enzyme first, and then 10-f-H_4F binds. If AICAR was present in the active site, 10-f-H_4F would be expected to bind with a higher affinity, but the lack of AICAR explains why such a low affinity is seen for 10-f-H_4F. Unfortunately, this cannot be measured by ITC, as titrating 10-f-H_4F into an AICAR-enzyme mixture would just result in a massive enthalpy change associated with catalytic turnover.

3.5 Thermal stability of ATIC

The thermal stability of ATIC has not been reported in the literature. Ligand binding can enhance the stability of a protein. The thermal stability of human and avian ATIC in the presence of various ligand was investigated to provide an alternative technique for investigating ligand binding.

3.5.1.1 Differential Scanning Calorimetry (DSC)

Differential Scanning Calorimetry (DSC) can be used to monitor the stability of proteins by measuring the enthalpy changes that occur during protein unfolding. DSC was used to determine the T_m of human ATIC, with and without AICAR phosphate bound. Unfolding occurred between 50 °C and 62 °C. The T_m of the apoprotein was 55 °C, which increases to 58 °C upon addition of AICAR (1 mM). After the protein had been subjected to a cycle with a final temperature of 100 °C, no re-folding was seen to occur. Figure 3-14b is a graphical representation of the raw data obtained. The light and dark blue lines show the scan of human ATIC. The protein scan was repeated to show the reproducibility of the experiment. The red line shows the increase in T_m when AICAR is added to the protein.

As no refolding occurred during these temperature ranges, a suitable baseline could not be fitted to the data set, and so the area under the melting curve could not be estimated.

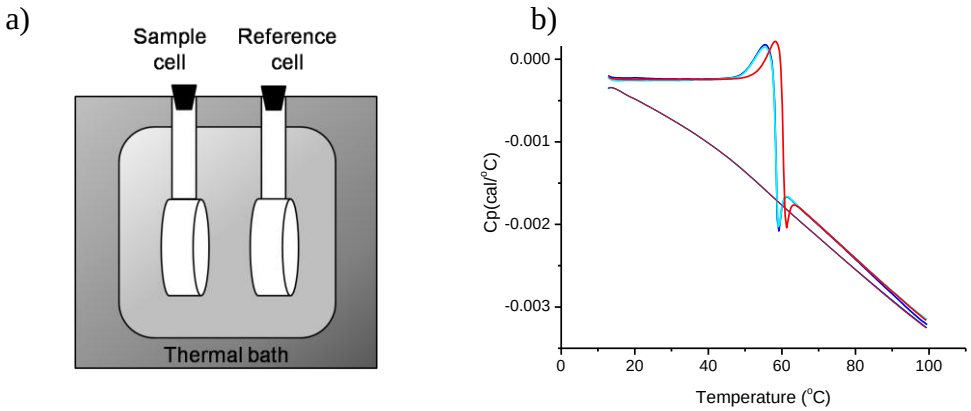

Figure 3-14: a) The experimental set up for DSC. b) The sample and reference cells are cycled up and down in temperature. The difference in heat required to the sample and reference cells are measured as a function of temperature to calculate the T_m of the sample. The blue lines show the DSC trace obtained for human ATIC (T_m=55 °C), and the red line shows the increase in stabilisation upon addition of 1 mM AICAR (T_m= 58 °C).

This experiment provides qualitative data that addition of the AICAR substrate stabilises the human ATIC enzyme. The stabilisation effect of AICAR (1 mM) is shown as a 3 °C increase of the T_m to 58 °C. This experiment with the addition of AICAR should be repeated to determine the error associated with this value.

3.5.1.2 Differential Scanning Fluorimetry (DSF)

An alternative high-throughput assay of thermal stability is DSF, which monitors the unfolding of a protein by a change in fluorescence upon exposure of regions of hydrophobicity. Human and avian ATIC unfolding were measured in the presence of varying concentrations of AICAR, 10-f-H_4F, $PteGlu_4$ and a fixed concentration of KCl.

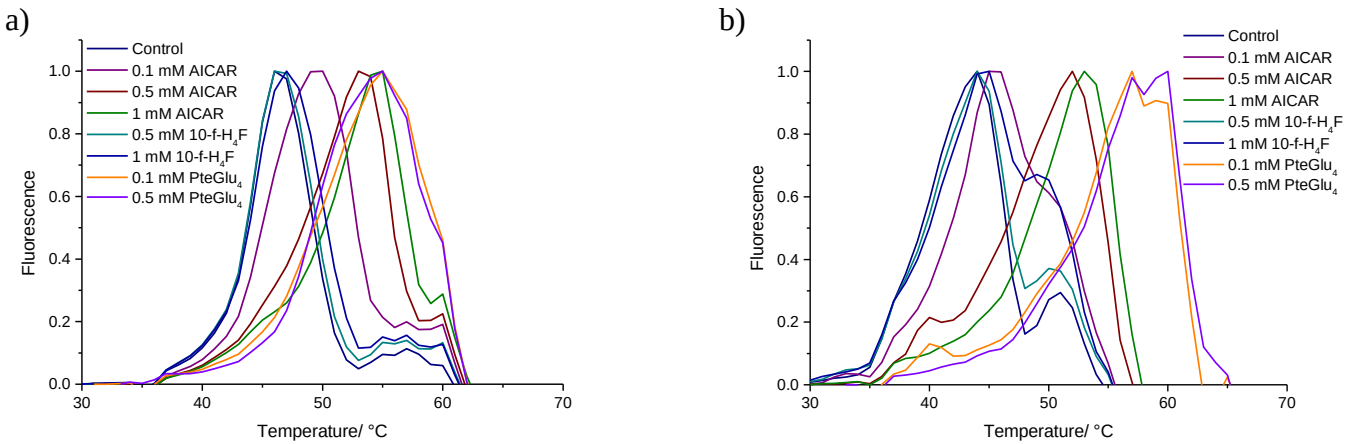

Figure 3-15:Normalised DSF traces for a) human ATIC, and b) avian ATIC at certain concentrations of various small molecules

Table 3-4: T_m (°C) of human and avian ATIC, as apoproteins (control) and in the presence of various small molecules at specified concentrations, as measured by DSF. AICAR is the substrate for ATIC and 10-f-H_4F is representative of the cofactor used *in vivo*. $PteGlu_4$ was included in the experiment to monitor the effects of the polygluatmate tail of the *in vivo* cofactor on the thermal stability of the enzymes.

	Enzyme	***Control***	***0.1 mM AICAR***	***0.5 mM AICAR***	***1 mM AICAR***	***0.5 mM 10-f-H_4F***	***1 mM 10-f-H_4F***	***0.1 mM $PteGlu_4$***	***0.5 mM $PteGlu_4$***
T_m/°C	Human	46	50	53	55	46	47	55	55
	Avian	44	45	52	53	44	45	57	60
ΔT_m /°C	Human	0	4	7	9	0	1	9	9
	Avian	0	1	8	9	0	1	13	16

The T_m gives a reasonable interpretation of the data, but the shape of the curves can give qualitative information too. For example, if a curve is comparably broader to another then that sample is unfolding over a wider temperature range, or the unfolding process could pass through more than one transition. The peak shape for ATIC suggests that there are two transitions to unfolding or two domains unfolding, each occurring at a different temperature. The first peak is the largest which implies this transition uncovers a large hydrophobic area. This occurs at 46 °C in human ATIC and 43 °C in avian ATIC (both measured at 25 mM KCl, as apoprotein). The first peak could be attributed to a dimer to monomer transition, which would result in the exposure of a very large hydrophobic face. A second peak, much less intense and broader than the first, occurs at 57 °C in human ATIC and 51 °C in avian ATIC. The height of the second peak for human ATIC at 1 mM AICAR gives a second transition T_m of 60 °C, which is in agreement with the T_m calculated by DSC of 58 °C. The increase in stabilisation to the second unfolding transition observed in DSF upon addition of 1 mM AICAR is 3 °C. The discrepancy between DSC and DSF calculated values could be attributed to the different rate of temperature increase with each technique. The large first unfolding event does not appear to have been measured by DSC, which suggests this potential unfolding of dimer to monomer could be an entropically driven event, as it is not a transition associated with a thermal change. The first transition is measured by a large increase in fluorescence as a hydrophobic surface is exposed, but is not accompanied by a change in enthalpy. The second transition is characterised by a much weaker fluorescence signal, and coincides with the transition measured by the DSC. Therefore, the second transition is an enthalpic unfolding which results in the exposure of a far smaller area of hydrophobic residues than observed for the first transition. It would be useful to determine the 'T_m' associated with the second transition and analyse the effect of the various substrates. However, these are difficult to obtain from the data

set as this second transition signal is fairly weak and noisy (especially in human ATIC), and becomes buried beneath the first peak as this transition is stabilised.

The stability for both human and avian ATIC increases with increasing concentration of AICAR, implying that the enzyme is more stable upon binding the natural substrate (Figure 3-16). On average, the 10-f-H_4F cofactor only causes a small stabilisation at the higher concentrations analysed in this study, requiring 1 mM 10-f-H_4F to produce 1 °C stabilisation. The *in vivo* substrate is a polyglutamated form of 10-f-H_4F, so $PteGlu_4$ was included to mimic any stabilisation effects of the glutamate tail. An increase in stabilisation is seen on addition of small amounts of $PteGlu_4$ (0.1 mM).

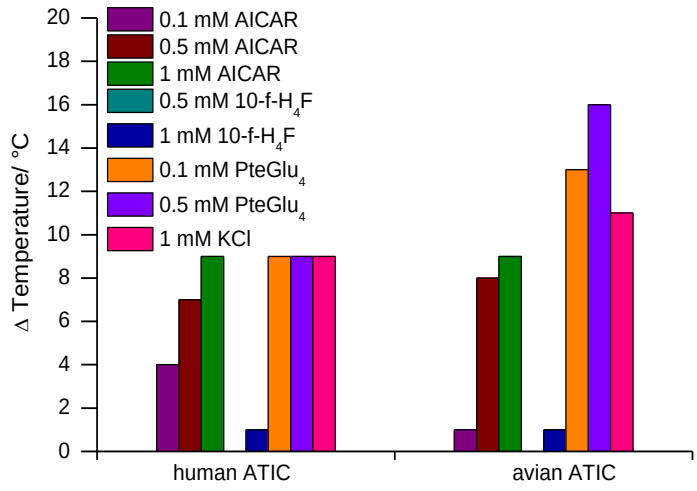

Figure 3-16: Summary of the stabilisation effects of various small ligands

3.6 Discussion and Conclusion

The true K_M for AICAR and 10-f-H_4F have been determined for human ATIC using a two dimensional assay as 14.1 ± 4.5 µM and 41.6 ± 11.9 µM respectively. These are within the range of previously determined literature values for AICAR of 1.9 ± 0.4 µM[50] (measured at 25 °C) and 16.8 ± 1.5 µM[31] (temperature of experiment not stated), and 10-f-H_4F values of 39.0 ± 6.0µM[50] (measured at 25 °C) and 60.2 ± 5.0

μM[31] (temperature of experiment not stated). This indicates the automated assay method is a suitable means for simultaneous determination of substrate and cofactor kinetic parameters. Analysis of the data obtained from the automated assay suggested the sequential binding of substrate and cofactor, where AICAR must bind to the enzyme first, followed by 10-f-H_4F, before catalysis can take place.

Section 3.4 provides the first determination of the thermodynamic binding properties of AICAR, IMP, AMP, XMP, 10-f-H_4F and $PteGlu_4$ to ATIC, measured at 25 °C. AICAR binds fairly tightly to both human and avian ATIC, with a K_d of 6.14 ± 1.37 μM and 13.83 ± 2.15 μM respectively. AICAR binds once per monomer unit, which is presumed to be the AICAR transformylase site (see Chapter 4 for further analysis of site determination). As expected, the product of the ATIC reaction, IMP, binds more weakly than the substrate, with a K_d of 53.19 ± 4.50 μM to human ATIC. IMP binds to only 0.35 ± 0.06 sites per monomer, suggesting that binding to the IMPCH active site may be blocked, potentially from a more tightly binding molecule carried through from overexpression in *E. coli*. Human ATIC binds AMP in a similar number of sites (0.44 ± 0.03) as IMP, which suggests AMP is also binding to the IMPCH site, and is subsequently blocked by the same small molecule inhibiting IMP binding. AMP binds to human ATIC more tightly than IMP, which is unusual as AMP presents opposite hydrogen bonding partners to formyl AICAR and IMP. This suggests AMP must be binding in a different orientation to the substrate and product in the IMPCH active site. AMP binds with a similar affinity to AICAR in human and avian ATIC (8.40 ± 2.01 μM and 10.96 ± 1.78 μM respectively). XMP binds tightly (K_d = 4.64 ± 0.37 μM) to 1.67 ± 0.02 sites per monomer of human ATIC. This implies XMP can bind to both the AICAR transformylase and IMPCH active sites, which can be explained by the similarity in positioning of chemical groups to formyl AICAR. Hence, XMP can act as a product mimic in the AICAR transformylase site, and a substrate mimic in the IMPCH

site. As XMP binds more tightly than the natural substrate AICAR, it might act as another route for negative feedback within the *de novo* purine biosynthetic pathway (Figure 3-17).

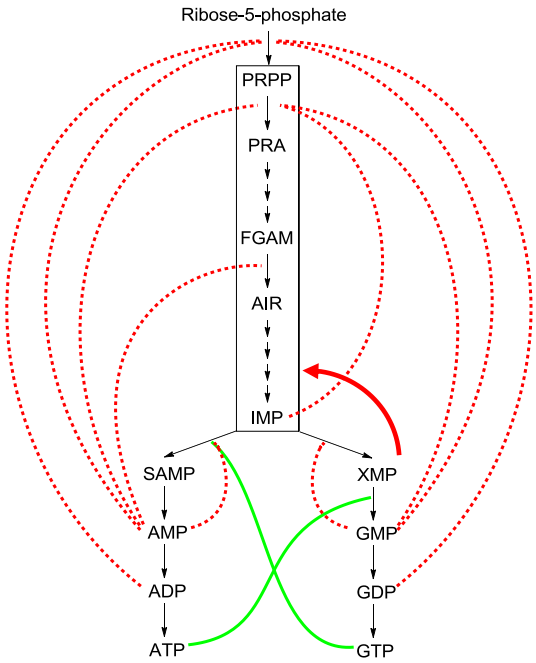

Figure 3-17:Feedback regulation of the *de novo* purine biosynthetic pathway. Steps also included are the synthesis of PRPP from 5-ribose phosphate catalysed by PRPP synthetase, and the conversion of IMP to ATP and GTP. Red dashed lines indicate negative feedback and solid green lines positive feedback. Potential negative feedback loop of XMP inhibition of AICAR transformylase is shown as a solid red arrow indicating the direction of feedback.

Binding of 10-f-H_4F to both human and avian ATIC was weak, in the high micro molar range (120.92 ± 11.48 µM and 267.95 ± 23.23 µM respectively) to approximately one site per monomer. The dissociation constants for 10-f-H_4F may be being observed at a weaker value than would be seen if AICAR was bound, since the substrate is known to bind prior to cofactor binding. This supports the ordered binding mechanism where AICAR must bind to ATIC before 10-f-H_4F. Also, the *in vivo* substrate has a polyglutamate tail, extending from the single glutamate of 10-f-H_4F. Binding studies on $PteGlu_4$ confirm that the glutamate extension has a huge effect on increasing the binding

strength of the cofactor for ATIC. $PteGlu_4$ K_d = 0.22 ± 0.03 μM for human ATIC and 0.44 ± 0.02 μM for avian ATIC. The addition of three glutamates increases the binding constant by around 500-600 fold; although this does not include the binding contribution of the formyl group, it serves to give a good indication of the effect adding glutamates to the cofactor would have on binding affinity. The thermal stability data obtained from DSF experiments supports the conclusion that the polyglutamate tail is an important aspect of the cofactor. $PteGlu_4$ (0.5 mM) increases the melting temperature of human ATIC by 9 °C and avian ATIC by 16 °C, whereas 10-f-H_4F at the same concentration has no effect on the T_m for ATIC from either organism. $PteGlu_4$ would not be expected to interfere with AICAR substrate binding as the glutamate tail binding pocket sits on the surface of the enzyme and does not obstruct the AICAR binding pocket.

ATIC runs as a monomer by SDS-PAGE, which is due to the denaturing conditions of the analysis. Size exclusion chromatography appears to show a mass of just under that for the dimer, but this is thought to be due to the shape of the ATIC dimer. The large dimeric interface that forms from the two monomers allows the ATIC dimer to take up a volume that is less than double the volume of the ATIC monomer. As the ATIC dimer has a streamlined shape occupying less than the expected volume area for two monomers, the molecular weight is under predicted by the size exclusion calibration. Human and avian ATIC both appear to purify as dimers if the streamlined shape of the enzymes, observed in the crystal structures, is taken into consideration. DSC performed on human ATIC reported a single melting transition, with a T_m of 55 °C, unfolding over a range of 50 to 60 °C. DSC measures any unfolding processes that occur with a change in temperature, so an orthogonal technique, DSF, was also used which measures unfolding by the exposure of hydrophobic areas. Analysis of the data obtained from DSF showed two unfolding transitions; the exposure of a large hydrophobic area at

46 °C, and a smaller, broader transition at 57 °C. These data suggest an entropic unfolding of the dimeric interface (which has a 5000 $Å^2$ area) occurs at 46 °C, followed by an enthalpically driven unfolding of the remaining monomer, or the unfolding of the two separate domains.

DSC and DSF show that the enthapically driven unfolding of ATIC is stabilised by addition of the native substrate AICAR, both show a 3 °C stabilisation of human ATIC on addition of 1 mM. This shows good reproducibility across orthogonal techniques. The differences in T_m measured (58 °C by DSC, 60 °C by DSF) are likely caused by the different temperature ramps used by each technique; DSC increases the temperature more slowly than DSF.

A greater stabilisation affect is seen for AICAR compared to 10-f-H_4F. This is consistent with the binding affinities measured by ITC that show AICAR binds more tightly to ATIC than 10-f-H_4F, and therefore also supports the ordered binding model, where AICAR binds to ATIC before 10-f-H_4F. AICAR binding may enhance the stability and structure of the enzyme in such a way that it enhances the 10-f-H_4F binding; 10-f-H_4F binding is more favourable when AICAR is already bound to ATIC. Data obtained from kinetics, DSC, DSF and ITC therefore all support the ordered binding reaction:

$$E + AICAR \overset{K_1=14\ \mu M}{\longleftrightarrow} [E-AICAR] + 10\text{fH}_4\text{F} \overset{K_2=42\mu M}{\longleftrightarrow} [E-AICAR-10\text{fH}_4\text{F}] \rightarrow Product$$

4 Isolation of the two domains of ATIC

ATIC contains two distinct catalytic domains, IMPCH, which is located towards the *N* terminus of the protein, and AICAR transformylase, which is situated towards the *C* terminus. The characterisation of ATIC contained in Chapter 3 investigated the thermal stability and the kinetic and physical binding properties of the full length ATIC. To be able to separate out and assign certain properties to each domain would aid in the interpretation of some of the results obtained in Chapter 3. For example, the ITC experiments conducted on ATIC suggest that AMP may bind to ATIC in the IMPCH site, and ITC analysis shows XMP appears to bind in both the AICAR transforymlase and IMPCH active sites. Truncation mutants were designed to provide a single polypeptide encoding IMPCH activity and another incorporating AICAR transformylase activity.

4.1 Truncation mutants of ATIC

The crystal structure of human ATIC was analysed to design an *N*-terminal truncation mutant of ATIC containing the IMPCH domain, and a *C*-terminal truncation containing the AICAR transformylase domain. The ATIC protein sequence was chosen to be 'cut' at residue G200 (Figure 4-1), thus providing an IMPCH containing mutant consisting of residues 1-199, and an AICAR transformylase mutant containing residues 201-592. The transformylase domain-containing mutant was designed to include the β-sheet motif that connects the domains, as this may help the mutant dimerise by providing a greater area of interactions A dimeric *C*-terminal mutant is desirable as the transformylase domain is only active when the enzyme is in its dimeric form.

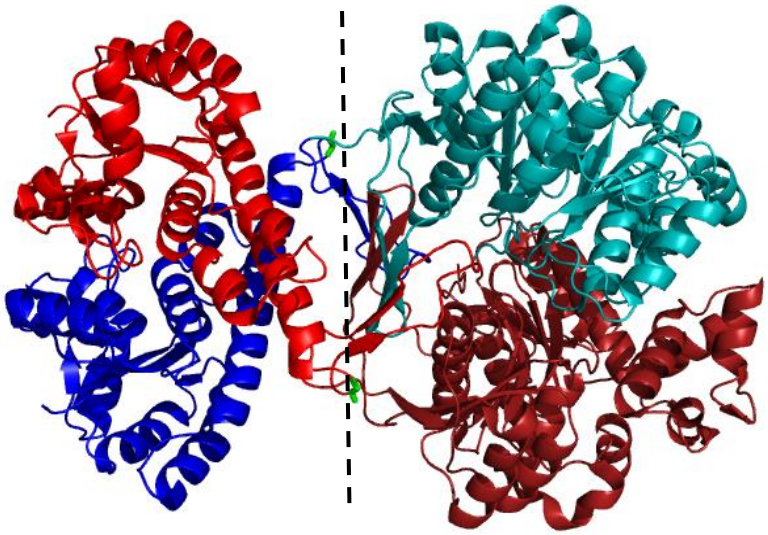

Figure 4-1: The structure of ATIC. The highlighted green residue is G200 and indicates where the protein is 'cut' to create two truncation mutants, each containing a separate catalytic domain.

4.1.1.1 Cloning

The pET28a vector encoding human ATIC was used as the template for amplification PCR. The regions of interest (where bases 1, 2 and 3 code for the first methionine residue of the ATIC sequence) bases 1 to 597 were amplified to encode the IMPCH site, and bases 598-1776 were amplified encoding ATIC residues 201 to 592. To clone the IMPCH truncation mutant expressed with an *N*-terminal his_6tag, an Nco1 restriction site was added to the forward primer P06 and a BamH1 restriction site was added to the reverse primer P08. To clone an IMPCH mutant without a his_6 tag an Nde1 restriction site was added to the forward primer P07 the same reverse primer was used (P08). An annealing temperature of 50 °C was used and amplification was checked against a molecular marker ladder (Figure 4-2, lanes 4 and 5).

To clone the AICAR transformylase truncation mutant into the pET28a vector an Nco1 restriction site was added to the forward primer P03 and a BamH1 restriction site was added to the reverse primer P05. This encodes for the recombinant protein to be

expressed with an *N*-terminal his_6 tag. To create an AICAR transformylase mutant without a his_6 tag the same reverse primer was used (P05) but an Nhe1 restriction site was added to the forward primer P04. Initial annealing temperatures of 50 °C were used but these resulted in mixed products (Figure 4-2, lanes 2 and 3). The PCR reaction was repeated at 60 °C and the products of this PCR were clean. Amplification was checked against a molecular marker ladder (Figure 4-2, lanes 7-8).

PCR products that contain the Nco1 restriction site were cloned into pET28a upstream of the his_6 tag coding region, resulting in mutants that do not bear *N*-terminal his_6 tags. Nde1 and Nhe1 sites were chosen to ensure the sequences encoding IMPCH and AICAR transformylase, respectively, were in the correct frame for expression.

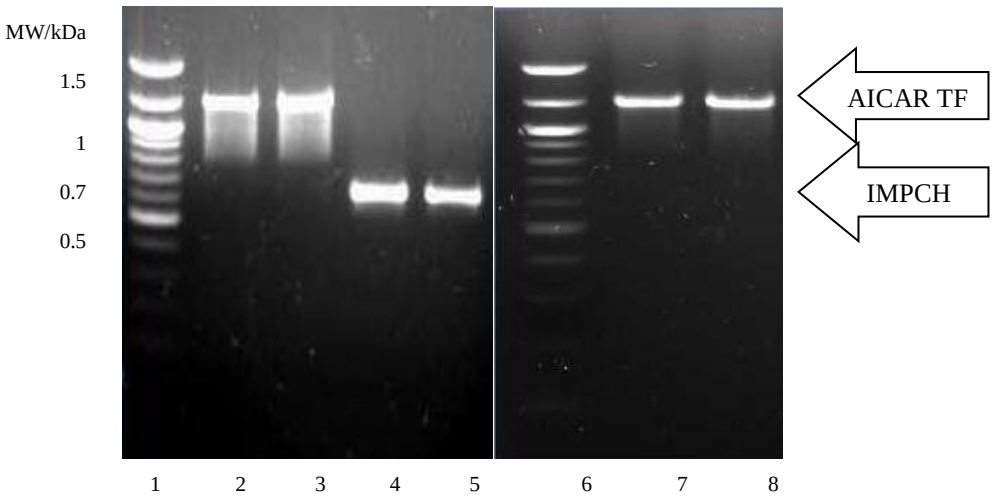

Figure 4-2: 1.2% agarose gel of AIIC truncation mutants. Lane 1 and 6: DNA marker, lane 2: PCR product of primers P03 and P05 at an annealing temperature of 50 °C to produce an AICAR transformylase mutant with an *N*-terminal his_6 tag, lane 3: PCR product of primers P04 and P05 at an annealing temperature of 50 °C to produce an AICAR transformylase mutant without a his_6 tag, lane 4: PCR product of primers P06 and P08 at an annealing temperature of 50 °C to produce an AICAR transformylase mutant with an *N*-terminal his_6 tag, lane 5: PCR product of primers P07 and P08 at an annealing temperature of 50 °C to produce an AICAR transformylase mutant without an *N*-terminal his_6 tag, lane 7: PCR product of primers P03 and P05 at an annealing temperature of 60 °C to produce an AICAR transformylase mutant with an *N*-terminal his_6 tag, lane 8: PCR product of primers P04 and P05 at an annealing temperature of 60 °C to produce an AICAR transformylase mutant without a his_6 tag.

The PCR products were purified (QIAprep Spin Miniprep, Qiagen) and digested using the appropriate restriction enzymes. The DNA was then fractionated on a 1.2% agarose gel and the DNA bands extracted using the QIAquick gel extraction kit (Qiagen). The truncate genes were ligated into the appropriate digested pET28a expression vectors and transformed into chemically competent XL10-Gold cells. The expression vectors containing the required genes were then extracted using a QIAprep Spin Miniprep (Qiagen) and the plasmid sent for sequencing. Sequencing data confirmed the successful ligation of the truncation mutants into pET28a.

4.1.1.2 Protein expression

All 4 truncation mutants were first expression tested in *E. coli* C41 (DE3) cells using auto-inducing media and grown at 30 °C. For each expression test, two cultures were grown, the second induced 12 hours after the first to allow for regular sampling. Samples of the growth media were taken every hour for 24 hours and frozen at −20 °C. These samples were then analysed by SDS-PAGE to monitor protein expression which is summarised in Figure 4-3.

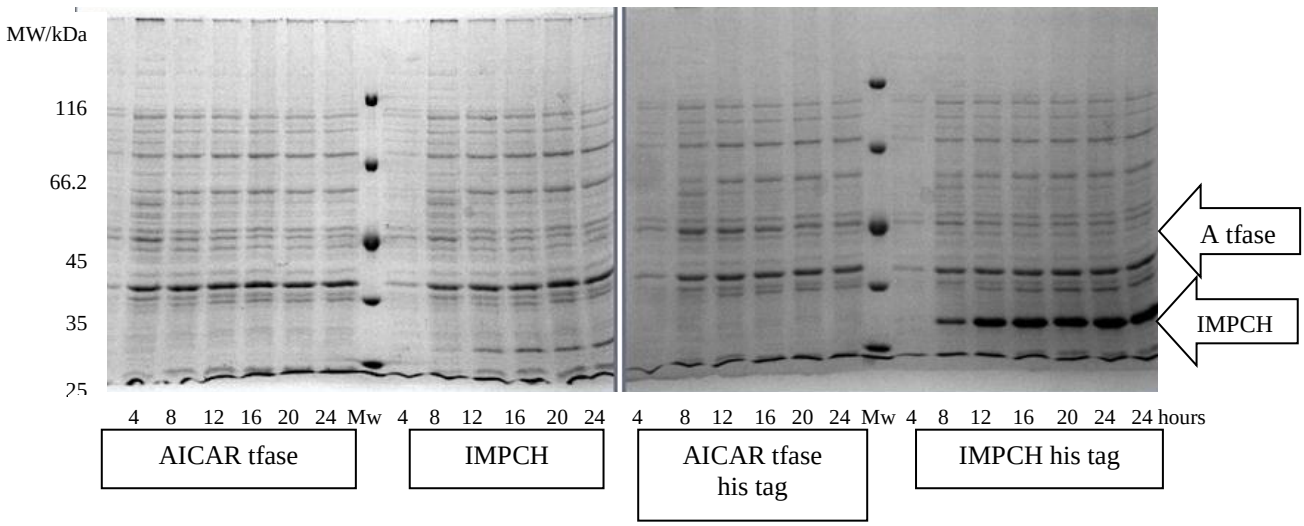

Figure 4-3:SDS-PAGE analysis of the protein expression of un-tagged AICAR transformylase domain and IMPCH domain (left) and his-tagged transformylase domain and IMPCH domain (right) from C41 (DE3) cells. Time points of the samples are shown below the relevant lane.

Expression was seen for both tagged and un-tagged IMPCH domain mutants, but there was no overexpression for the AICAR transformylase truncation mutant (expected at 45.4 kDa). The IMPCH domain of the full length ATIC has a well-defined potential *C*-terminal structure, ending in an α-helix which implies the IMPCH domain will be stable and lead to good overexpression. The his_6 tagged form of IMPCH seems to have greater overexpression than the un-tagged form, possibly due to the his_6 tag inferring extra stability.

The lack of overexpression seen for the transformylase mutants may be due to the inclusion of the β-sheet motif. The transformylase truncation mutant expression starts with this β-sheet sequence which may not be able to fold correctly without the presence of the IMPCH domain to stabilise it. This expressed but unfolded protein could then be targeted for degradation by the cell. To attempt to overcome this potential problem, another set of truncation mutants were designed to include the β-sheet with the IMPCH domain containing mutant and not with the transformylase domain. Figure 4-4 highlights the G360 residue chosen as the new cleavage point. There was insufficient time to complete the cloning for this system.

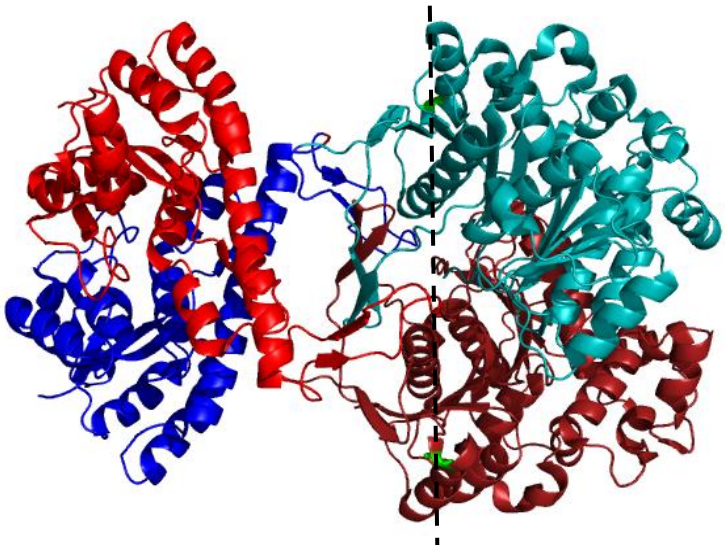

Figure 4-4: The structure of ATIC. The green highlighted residue G360 was the point of cleavage used to produce different truncation mutants, each containing a separate catalytic domain

The his_6tagged IMPCH mutant was overexpressed in C41 (DE3) cells, on a larger scale (2 × 1 l) in auto-inducing media at 37 °C. The cells were harvested after 24 h and stored at –80 °C. The IMPCH protein was purified by metal affinity and size-exclusion chromatography through a Superdex 200 column (Figure 4-5).

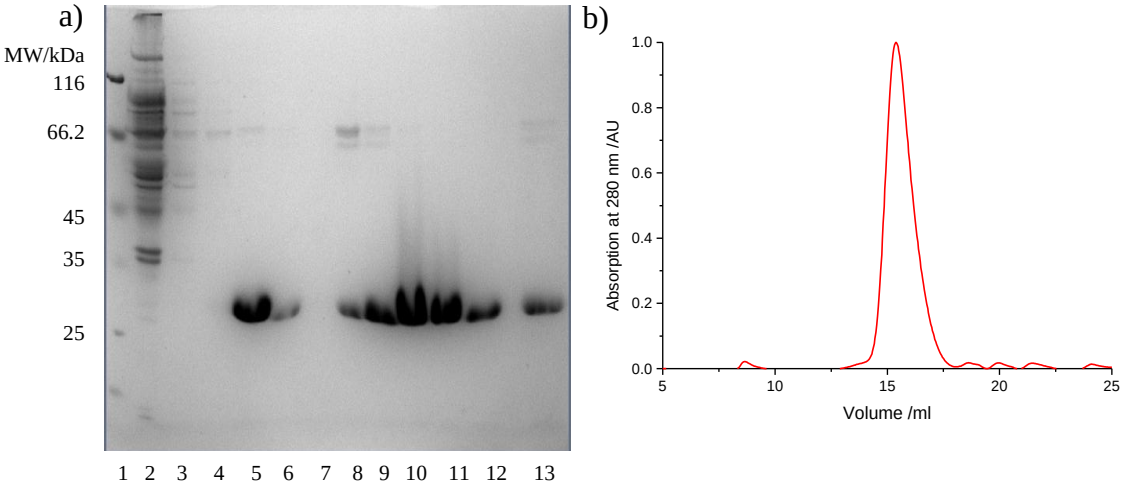

Figure 4-5: a) SDS-PAGE analysis of the purification of the IMPCH truncation mutant from *E. coli* using a Ni-NTA gravity flow column. Lane 1: molecular weight marker, lane 2: flow through 1, lane 3: wash 1 (10 mM imidazole), lane 4: wash 2 (150 mM imidazole), lane 5: elution 1 (250 mM imidazole), lane 6: elution 2, lane 7: blank, lanes 8 to 13: samples from the eluent of the Superdex 200 gel filtration column.

b) Absorption at 280 nm of size exclusion purification. The IMPCH truncation mutant is shown in red and has an elution volume of 15.4 ml.

The IMPCH domain eluted from the gel filtration column with a peak height at 15.4 ml, which corresponds to a molecular weight of 48 kDa, calculated using the calibration curve constructed in Chapter 3. The expected mass of the his_6-tagged IMPCH construct is 23.70 kDa, calculated from the sequence. This suggests that the IMPCH truncation mutant purifies as a dimer under non-denaturing conditions, which would have an expected mass of 47.40 kDa. IMPCH does not need to be in dimeric form to be catalytically active, but it still exists in the dimeric form under the conditions used for gel filtration.

4.1.1.3 ITC of IMPCH

The binding parameters of small molecules to the IMPCH mutant were sought to help elucidate the ITC results obtained for the full length human ATIC. $PteGlu_4$ was analysed, but was not expected to bind to the *N*-terminal portion of ATIC as it is thought to bind to the same site as the 10-f-H_4F cofactor. This experiment was

conducted to ensure no binding occurs to a different site within the first 200 residues of ATIC. Figure 4-6 is an example isotherm showing AICAR titrating into IMPCH. The results of small molecule binding to the IMPCH truncation mutant are shown in Table 4-1.

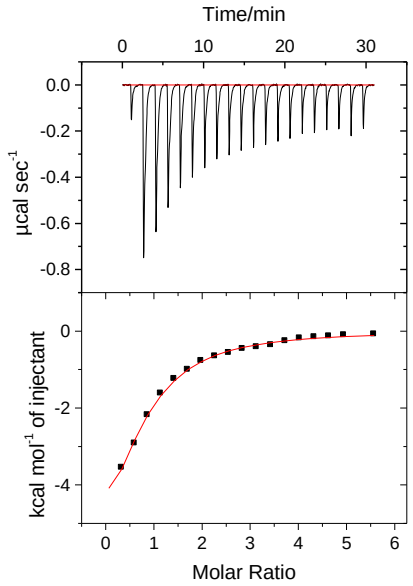

Figure 4-6: ITC titration of AICAR (1.5 mM) into IMPCH truncation mutant (56 µM) at 25 °C.

Table 4-1: Binding affinities of ligands and small molecules to IMPCH truncation mutant of human ATIC determined by ITC. Measurements were taken using a MicroCal ITC_{200} at a constant temperature of 25 °C. Enzyme concentration was fixed at 56 µM and ligand concentrations were adjusted as required to achieve saturation. Data were fitted using MicroCal Origin® software to calculate number of binding sites, dissociation constant and enthalpy of binding.

	IMPCH ATIC			
Ligand	**Ligand concentration/ mM**	**Number of sites**	**K_d/ µM**	**ΔH/ kcal mol^{-1}**
AICAR	1.5	0.721 ± 0.054	35.8± 3.0	-7.92 ± 0.70
IMP	1.0	0.639 ± 0.042	26.8 ± 2.4	-7.74 ± 0.62
XMP	1.0	1.1607 ± 0.033	12.1 ± 1.5	-4.12 ± 0.16
AMP	1.2	nd	nd	nd
$PteGlu_4$	1.0	nd	nd	nd

XMP binds to the IMPCH truncation mutant with the highest affinity of the small molecules investigated, but the measured K_d of 12.1 ± 1.5 μM is almost three times weaker than the binding seen for XMP to human ATIC (K_d of 4.64 ± 0.37 μM). This implies that XMP binds primarily and most tightly to the AICAR transformylase domain.

Whilst IMP binds weakly to the IMPCH mutant with a K_d of 26.8 ± 2.4 μM, it binds twice as tightly as IMP to the protein containing both domains. The IMPCH mutant cannot catalyse the AICAR Tfase activity, which could result in a lower concentration of endogenous IMP. This could potentially lead to the observation of 'tighter' binding between IMP and the IMPCH mutant.

AICAR binds to the IMPCH domain with a weak K_d of 35.8 ± 3.0 μM to 0.721 ± 0.054 sites. This is much weaker binding than was seen for the full length ATIC chain, implying the previously measured AICAR K_d for human ATIC of 6.14 ± 1.37 μM may be dominated by a tight binding interaction to the AICAR transformylase domain. AICAR can weakly bind to the IMPCH site, but this is most likely due to the structural similarity to the natural substrate, FAICAR. It would be expected for the naturally occurring human ATIC that AICAR binds preferentially to the AICAR transformylase domain. Alternatively, as the number of binding sites and enthalpy of binding are similar to those measured for full length ATIC, AICAR may only be being measured binding to the IMPCH active site. The affinity may be weaker to the truncation mutant due to a loss of stability through a reduction in dimerisation; the IMPCH turnover does not require dimerisation, but the monomer shows a 6-fold reduction in activity[33]. If AICAR has only been measured binding to the IMPCH site, this implies the AICAR transformylase site is already occupied with a higher affinity ligand, potentially XMP, which blocks AICAR binding. If AICAR cannot bind to the AICAR transformylase site

then the stability inferred by AICAR binding measured by DSC and DSF may have been achieved by stabilising the IMPCH binding domain.

AMP and $PteGlu_4$ do not bind to the first 200 residues of human ATIC. The binding site for $PteGlu_4$ must be located within residues 200-592. This was as expected as the 10-f-H_4F is situated within the AICAR transfomylase active site. This suggests that $PteGlu_4$ may be binding in the 10-f-H_4F binding pocket. AMP does not bind within the IMPCH active site as previously thought (Section 3.6), so the previously measured K_d of 8.4 ± 2.0 μM must have been the affinity of AMP for the AICAR transformylase domain.

4.1.1.4 DSF of IMPCH

The unfolding profile for the apoprotein IMPCH truncation mutant is shown as a black curve in Figure 4-7. There is a single positive peak followed by a negative dip in fluorescence. The single peak confirms IMPCH has a single melting transition, and the point of the peak height gives a T_m of 56 °C. The trough corresponds to the aggregation of the protein after it has unfolded. The T_m of 56 °C is consistent with the second, smaller unfolding transition seen with human ATIC at 57 °C, but the IMPCH mutant does not have the initial large peak that corresponds to the unfolding dimer. This supports the hypothesis that the large peak at 46 °C is caused by the exposure of the large area of hydrophobicity between the AICAR transformylase domains. Size exclusion chromatography predicts that the IMPCH mutant is present in dimeric form, but only one unfolding transition is seen, unlike the two transitions seen for the full length ATIC thought to correspond to dimer unfolding, then monomer unfolding. However, the dimeric interface between the IMPCH monomers is relatively scant, so either the dimer separation occurs at the same temperature as the protein unfolding, the dimer has fallen apart over the time between size exclusion purification and the DSF

experiment (approximately 5 hours), or the dissociation does not correspond to an increase in fluorescence.

Table 4-2:T_m (°C) of IMPCH truncation mutant in the presence of various small molecules at specified concentrations, as measured by DSF. Samples were heated from 25°C to 100°C at an increase of 1°C/s. T_m was calculated from the peak of the differential of fluorescence intensity. IMPCH apoprotein had a T_m of 56 °C.

Ligand	***Concentration/ mM***			
	0.25	**0.5**	**1**	**1.5**
AICAR	57	58	59	60
AMP	56	56	56	57
IMP	58	58	60	61

Table 4-3: ΔT_m (°C) of IMPCH truncation mutant in the presence of various small molecules at specified concentrations compared to the IMPCH apoprotein. Values were calculated from Table 4-2.

Ligand	***Concentration/ mM***			
	0.25	**0.5**	**1**	**1.5**
AICAR	1	2	3	4
AMP	0	0	0	1
IMP	2	2	4	5

The IMPCH truncation mutant was also incubated with increasing concentrations of AICAR, AMP and IMP to investigate the stabilising effects of these small molecules by DSF. The addition of AICAR gave a small increase in T_m, and showed a concentration dependence with an overall increase in T_m of 4 °C at 1.5 mM AICAR. AMP had no significant effect on the stability of IMPCH, implying that AMP may not have bound to the truncation mutant. IMP conferred the most stability of the ligands analysed, increasing the melting temperature by 5 °C at a concentration of 1.5 mM. In comparison to the small molecule stabilisations observed with the full length ATIC, the increases in the melting temperature of the IMPCH mutant are small; 1 mM of AICAR causes a ΔT_m of 9 °C for the full length protein compared to a ΔT_m of 3 °C for the single IMPCH domain.

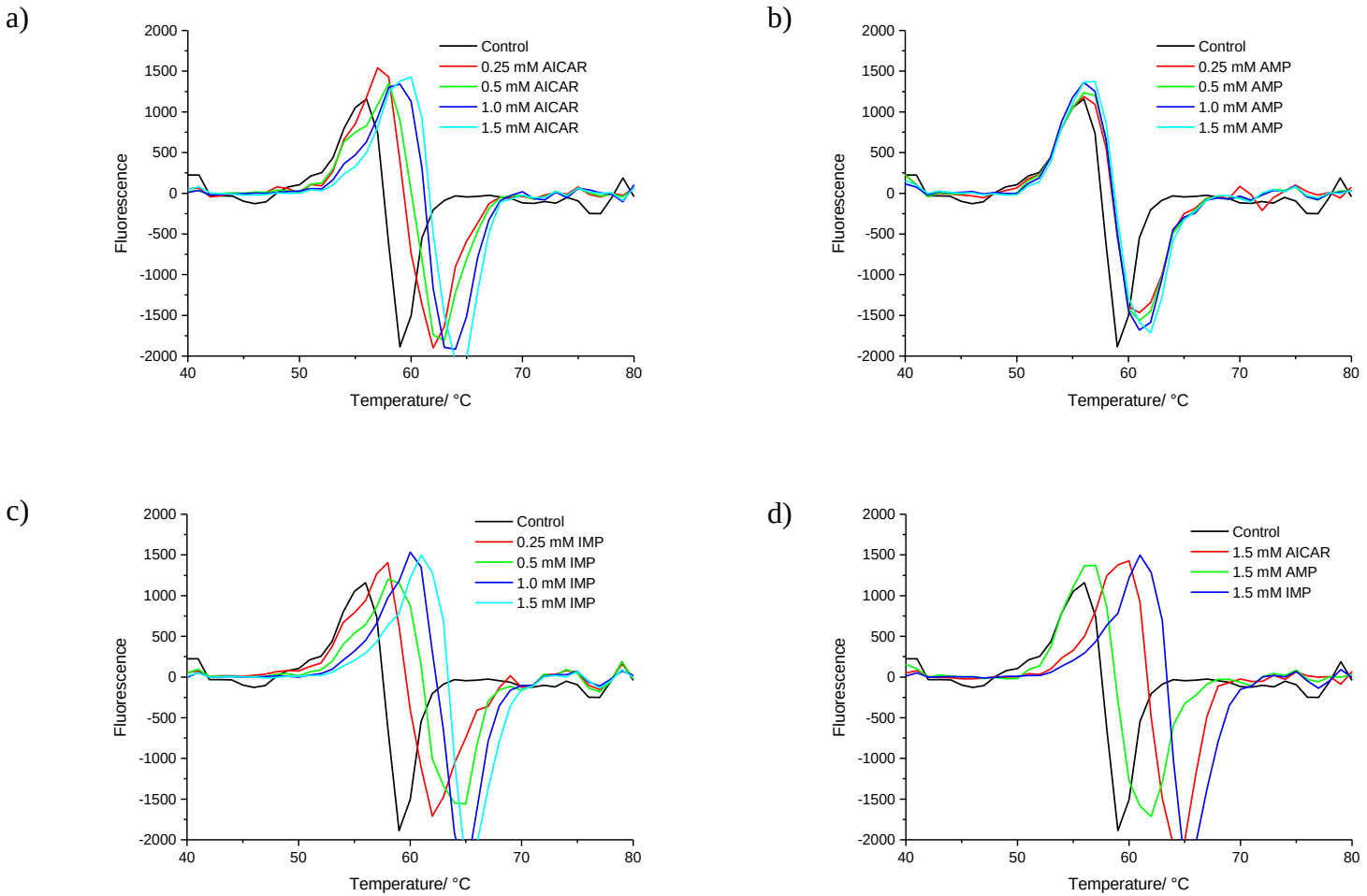

Figure 4-7:Differentiated DSF traces for IMPCH with increasing concentrations of a) AICAR, b) AMP, c)IMP, d) compiled traces at 1.5 mM of each small molecule

4.2 Discussion and Conclusion

A truncation mutant consisting of residues 1-200 of human ATIC incorporating the IMPCH domain, but not the AICAR transformylase domain was cloned and overexpressed in *E. coli* C41 (DE3) cells. The remaining residues 200-592 were cloned to provide a second truncation mutant containing only the AICAR transformylase domain, but this construct did not overexpress. The lack of overexpression was possible due to the *N*-terminal section of the polypeptide chain which encoded the β-sheet region of the ATIC structure, which may have caused mis-folding without the IMPCH domain to act as an anchor, and have been targeted for degradation within the *E. coli* cells.

IMPCH purified as a dimer by size exclusion chromatography, but DSF shows the domain unfolds by a single transition at 56 °C. This is either due to the dimer and monomers all unfolding at the same temperature, or that the IMPCH dimer is a fairly weak interaction that falls apart in the time before the DSF experiment can be conducted, hence only the single monomer unfolding transition is seen. This could be easily tested by re-purifing IMPCH samples by gel filtration, at set times points after the initial purification, and was merely not completed due to time constraints. If a second elution peak appears at approximately 16.8 ml, this would be representative of the monomer IMPCH and support the hypothesis of IMPCH dimer degradation with time. As the melting temperature of the IMPCH mutant corresponds with the second peak seen in the unfolding profile of human ATIC, this provides further evidence that the first unfolding peak of human ATIC (46 °C) is a measure of the falling apart of the AICAR transformylase domains to expose a large hydrophobic interface, and that the second peak at 57 °C is contributed by the unfolding of the remaining protein (including the IMPCH domain).

The greater the binding constant of a particular small molecule, the greater the increase is measured in the T_m of IMPCH when incubated with the molecule of interest. AMP

does not bind to the IMPCH domain and AMP causes no appreciable increase in T_m. AICAR and IMP both bind to IMPCH, AICAR slightly more weakly than IMP. This is translated to an increase in stability monitored by DSF when IMPCH is incubated with each of the ligands, IMP causes a slightly greater stabilisation effect than AICAR.

The binding of small molecules to the IMPCH domain was measured by ITC to help elucidate the binding data obtained for the full length ATIC in Chapter 3. The binding parameters measured for AICAR titrated into IMPCH are consistent with those obtained for the full length ATIC, suggesting the previously measured affinity and stabilisation effects were caused by AICAR binding to the IMPCH domain, not to the AICAR transformylase domain as would be expected. This could be due to a higher affinity ligand such as XMP blocking the transformylase active site. In contradiction to this, however, is the binding of AMP, which is measured binding to the AICAR transformylase site only. To explain the results of the binding experiments to full length ATIC and the IMPCH truncation, a new construct must be created that has the full length ATIC structure, but has the IMPCH active site knocked out. Binding experiments would then be performed on the knock-out mutant, the results of which would be compared to the data obtained for the IMPCH truncation mutant and the full length ATIC to deduce the binding locations.

5 Assaying dimerisation of ATIC

In Chapter 3, the structure of ATIC was analysed by various biophysical techniques. The thermal stability as determined by DSC displayed a single unfolding transition which corresponded to a melting temperature of 55 °C. However, when the protein was analysed by DSF, an extra unfolding event was seen at 46 °C which was not observable using DSC. As DSC only monitors enthalpic events, this first unfolding transition must be entropically driven. This entropic transition corresponded to a very large increase in fluorescence, corresponding to exposure of a large amount of hydrophobic surface area, we hypothesised that this large unfolding event is the dissociation of the ATIC dimer, which would expose the large, hydrophobic dimeric interface.

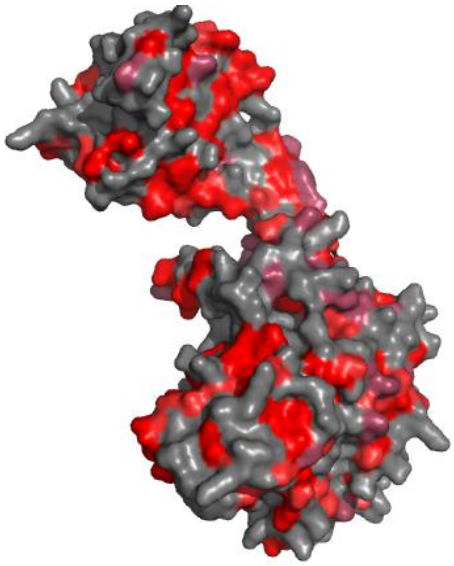

Figure 5-1: Surface representation of a monomer of human ATIC, shaded according to hydrophobicity. Bright red indicates Ala, Leu, Val, Ile, Phe, Met and Cys residues, pale red indicates Gly, Ser, Thr and Trp residues, and grey indicates hydrophilic residues.

5.1 Biophysical characterisation

Analytical UltraCentrifugation (AUC) can analyse a mixture of different species to determine the size and shape of the species present. Here, AUC was employed to confirm the oligomeric assemblies present in a sample of human ATIC. This approach, using sedimentation equilibrium has previously been used to identify a monomer-dimer

equilibrium in human ATIC[131]. We explored sedimentation velocity, in which the sedimentation of the sample with time is analysed to calculate information on the size of the species present. The coloured inset in Figure 5-2 shows the raw data for the sedimentation of a sample of human ATIC. The curves represent the absorbance at 280 nm in the cell, at different time points during the sedimentation process. The initial sedimentation profile is shown in dark blue and progresses to red over the time course of the experiment. These curves were processed in Sedfit to identify the size of species in solution.

The first small peak corresponds to a species of 32 kDa, the second and dominating species has a mass of 132 kDa, and the third hump equates to a species of 225 kDa. The dimer of human ATIC has a molecular weight of 133.6 kDa, as calculated from the sequence. AUC sedimentation velocity confirms human ATIC is primarily present in dimeric form, and therefore suggests that at this concentration very little monomer is present.

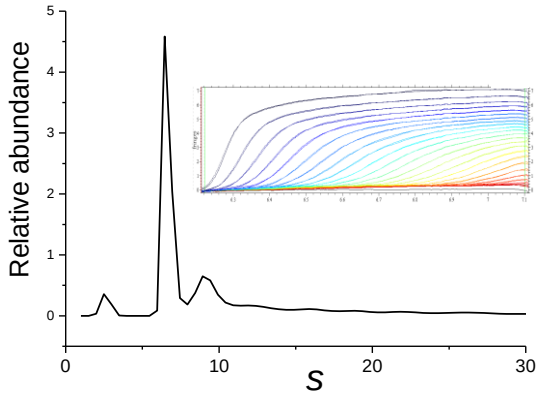

Figure 5-2: Sedfit analysis of AUC sedimentation velocity experiment conducted with human ATIC (20 μM) at 48,000 g and 20 °C. The inset shows the absorption at 280 nm over time, as the traces change from blue to red.

The strength of homodimeric interactions can be measured by ITC dilution experiments. In this experiment the protein is highly concentrated in the syringe, and is injected into a cell containing only buffer. As the concentrated protein is injected into the cell it is diluted, and dissociates as defined by the dissociation constant K_d, which determines the ratio of the monomeric and dimeric species. With progressive injections the protein concentration in the cell increases and the dissociation process becomes less favoured. The dissociation constant can be derived from the resulting isotherm

ITC dilution experiments were performed with human ATIC, over a range of concentrations from 300 μM to 1 mM, and conducted between 20 °C and 25 °C. Figure 5-3 shows a typical trace for the human ATIC dilution experiment. A slight weak endothermic dilution can be seen, but none of the data collected could be fitted to determine K_d of the monomer-dimer equilibrium. A typical dilution isotherm would be expected to show significantly stronger curvature. This result suggests that the dimerisation of ATIC is an entropically driven reaction, as ITC only measures binding and dissociations by changes in enthalpy.

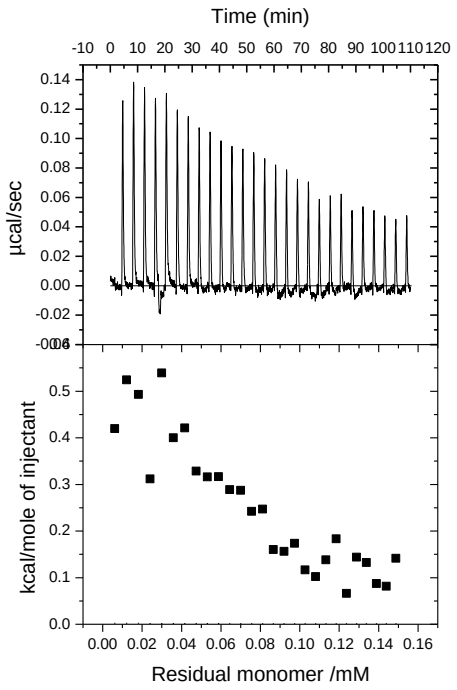

Figure 5-3: ITC dilution experiment for human ATIC conducted at 25 °C

This also perhaps explains why the large unfolding signal detected by DSF at 46 °C is not observed by DSC, since DSF measures unfolding by the exposure of hydrophobic sites whilst DSC monitors unfolding through changes in enthalpy.

5.2 Use of small molecule probes

Several small molecule inhibitors of ATIC dimerisation have been reported in the literature. It was hoped that direct observation of binding by these inhibitors to ATIC would allow them to be used as probes of dimerisation. Two classes of such inhibitors have been reported, the cappsins[105] and the cyclic peptides[104]. We focussed on the latter class of compounds.

5.2.1.1 Synthesis of the cyclic peptide c[CRYFNV]

A novel method was developed to synthesise the cyclic hexamer peptide c[CRYFNV], utilising SPPS protocol using a Fmoc protecting strategy on a low loading rink amide resin (0.22 mmole/g). The precursor linear peptide was synthesised, Fmoc deprotected and then cyclised on-bead before global deprotection and cleavage to yield the cyclic peptide. This new strategy for the synthesis of the cyclic peptide couples the peptide through the side chain, which becomes an asparagine residue upon cleavage from the resin (Figure 5-4).

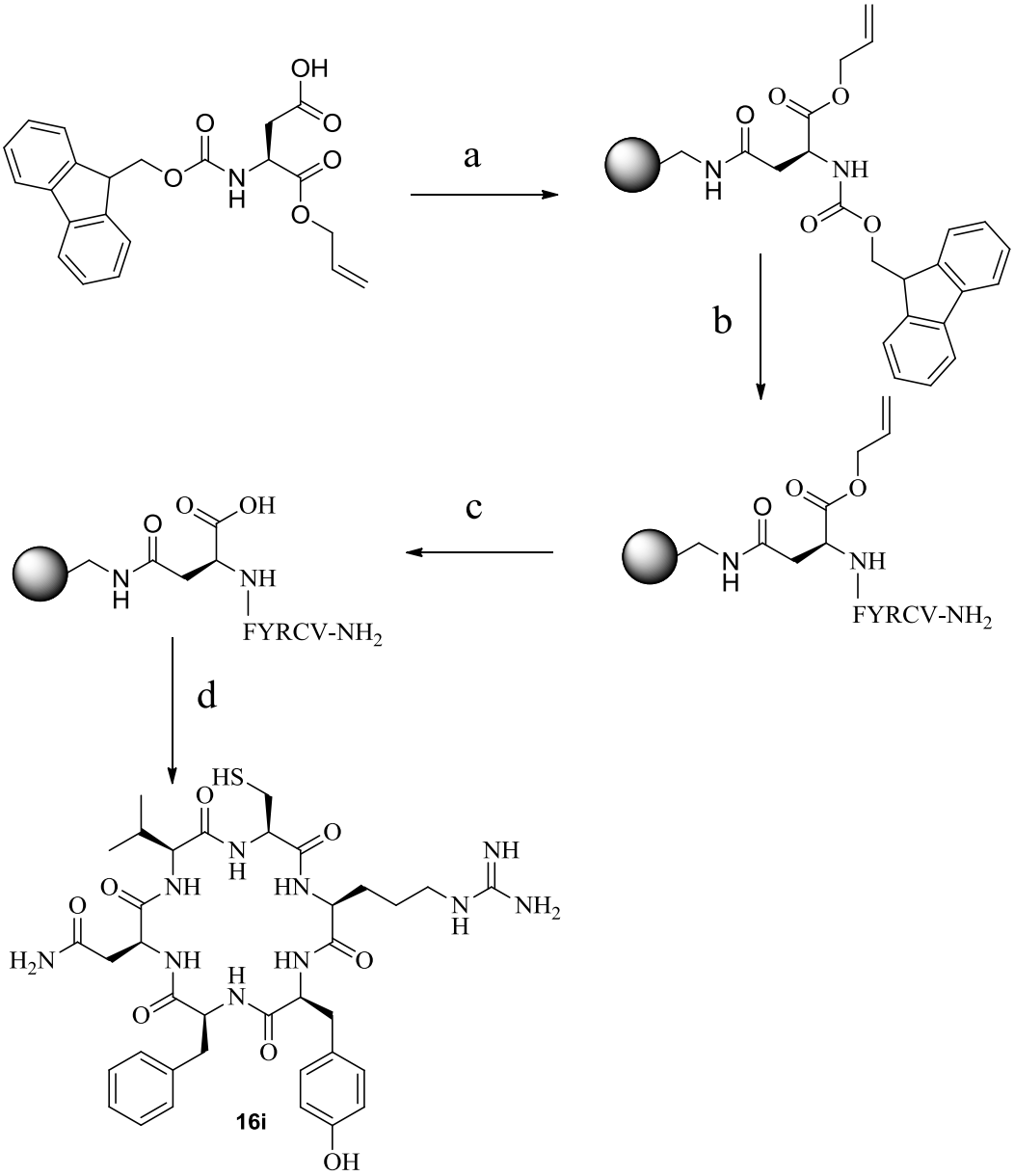

Figure 5-4: Synthetic route taken to the cyclic peptide c[CRYFNV] (**16i**), a) coupling of Fmoc-Asp(OAll) to a low loading rink amide resin, b) standard SPPS protocol used to couple the amino acids F, Y, N, C and V, c) removal of the allyl protecting group; tetrakis(triphenylphosphine)palladium(0) (25 mol%), morpholine, DMF, d) cyclisation and cleavage from the resin.

The first amino acid to be attached to the rink amide resin was Asp(OAll)-OH, which upon cleavage forms the asparagine amino acid of the cyclic peptide (Figure 5-5). Subsequent amino acids were added to the *N*-terminus of the Asp(OAll) residue. The allyl protecting group was removed using a tetrakis(triphenylphosphine)palladium(0) catalyst (25 mol%) with morpholine as a base. Cyclisation was then achieved with standard peptide coupling agents HCTU and DIPEA. Purification using a LH-20 size exclusion column eluted with MeOH was attempted but no material was recovered. With no fluorophore present, and no signal from the tyrosine residue at the dilution required to solubilise the compound, the fractions containing the purified compound could not be identified from the LH-20 purification. Instead, the compound was purified by high performance liquid chromatography.

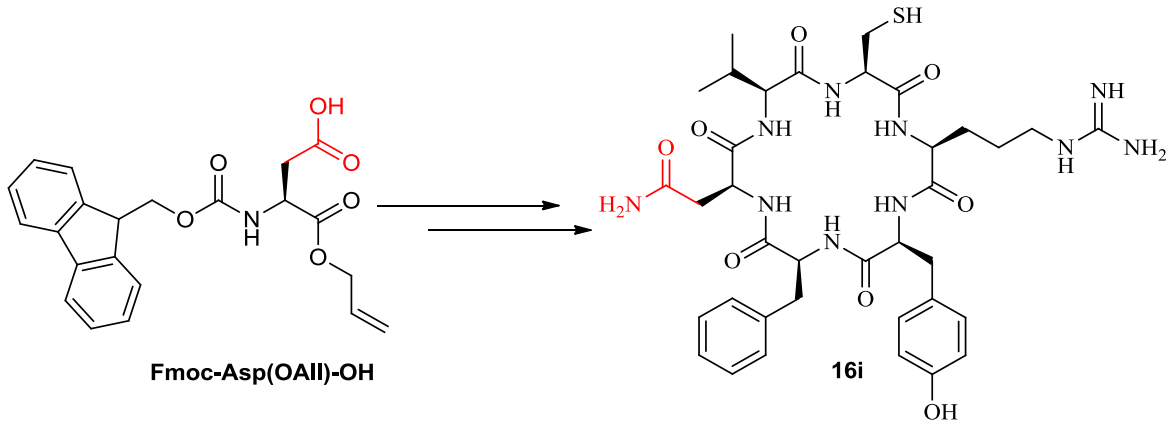

Figure 5-5: Synthesis of the cyclic peptide **16i**. The side chain of Fmoc-Asp(OAll)-OH (red) is attached to the rink amide resin. Upon cleavage the aspartate side chain is converted into asparagine.

5.2.1.2 Analysis of the cyclic peptide inhibitor

The purified cyclic peptide inhibitor was analysed by a kinetic inhibition assay. The assay was conducted at twice the K_M for both AICAR and10-f-H_4F substrates, at a range of concentrations of the cyclic inhibitor. The rates measured were plotted against a log scale of the concentration of inhibitor and fit using a logistic function. The IC_{50} was determined to be 3.6 ± 0.8 μM (Figure 5-6). The K_i reported previously by Tavassoli *et al.* for this cyclic peptide inhibitor was 17.1 μM with respect to 10-f-H_4F. It is believed that the actual IC_{50} of this inhibitor could be lower, but due to its insolubility measuring the true value was problematic.

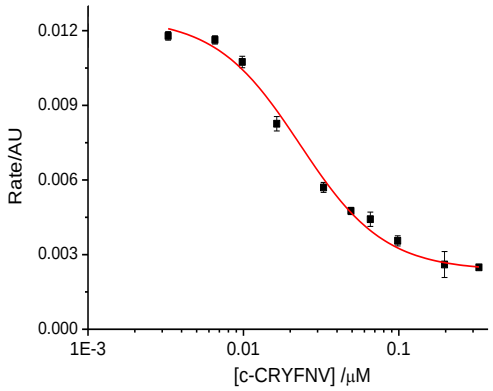

Figure 5-6: A log plot showing the inhibitory action of the cyclic peptide inhibitor. IC_{50} was determined to be 3.6 ± 0.8 μM.

Preliminary analysis of the binding of the cyclic peptide inhibitor to human ATIC was obtained by ITC (Figure 5-7). The binding constant K_d of the cyclic peptide is 3.61 ± 0.76 μM with a binding stoichiometry of 0.320 ± 0.016. This is consistent with the K_i measured by Tavassoli *et al.* of 17 μM. This was repeated to try and obtain a larger signal but all attempts to measure binding failed, either due to precipitation of protein or peptide. The cyclic peptide is only soluble in DMSO-containing buffers so there is a

fine balance between the concentration of peptide that can be used and the effect of DMSO on the stability and solubility of the protein.

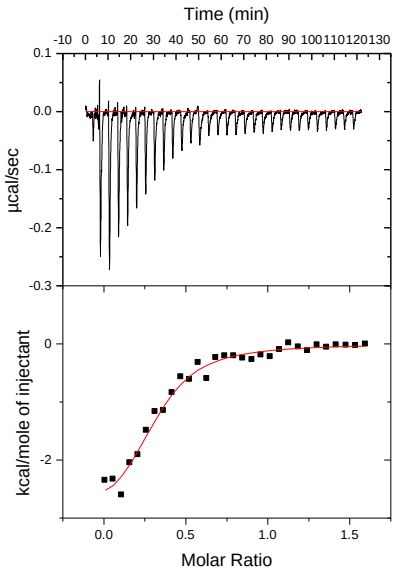

Figure 5-7: ITC analysis of the cyclic peptide and human ATIC interaction. K_d was measured at 3.61 ± 0.76 µM.

5.2.1.3 c[CRYFNV] inhibition of hepatitis C viral replication

AMP-activated Kinase (AMPK) regulates energy sources within the cell and AMPK agonists have been known to inhibit viral replication[80]. AICAR is a known agonist of AMPK[79], so the cyclic peptide dimerisation inhibitor was investigated with respect to its potential to inhibit viral replication, as inhibition of ATIC dimerisation will inhibit the AICAR transformylase reaction leading to an increase of AICAR in the cell.

The crude cyclic peptide dimerisation inhibitor underwent preliminary testing (Ana Carolina, Harris group, University of Leeds) to observe any effects on viral replication. 100 µM of c[CRYFNV] was found to inhibit HCV reproduction in Huh-7 cells after 48 h (Figure 5-8). The Huh-7 cells are transformed with luciferase-encoding HCV sub-

genomic replicons. A reduction in HCV replication is measured as a reduction in luminescence in the c[CRYFNV] treated cells compared to the control cells.

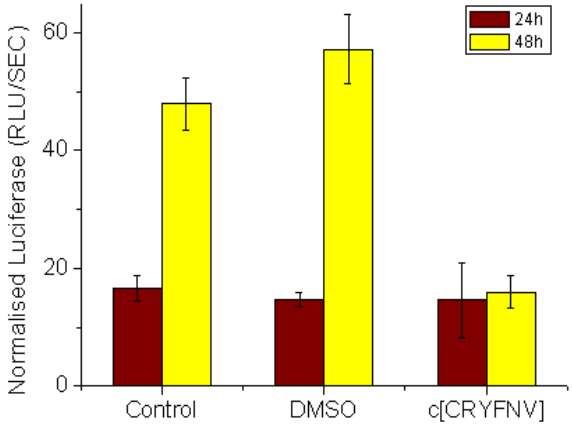

Figure 5-8: Effect of c[CRYFNV] on HCV replication. The normalized luciferase is used as a measure of HCV replication

The cyclic peptide was also tested for cell toxicity by the 3-(4,5-dimethylthiazol-2-yl)-2,5-diphenyltetrazolium bromide (MTT) assay, and found not to have any non-specific effects. Unfortunately, when the HPLC purified cyclic peptide was resubmitted for testing (Doug Ross, Harris Group, University of Leeds) no inhibition of viral replication was observed. After purification, the compound was even less soluble than it had been in the slightly impure state. Either some impurity was a potent agonist of AMPK, or the lowered solubility meant the compound was no longer taken up into the cells.

5.2.1.4 Crystallisation trials

Attempts to crystallize human ATIC with and without the cyclic peptide inhibitor have been undertaken. Trials were carried out using 2 µl + 2 µl hanging drop method in 24 well plates. We initially attempted to identify crystallization conditions using the commercially available Hampton Crystal Screen and Hampton Crystal Screen 2. These screens are based on the original sparse matrix screen and contain 96 crystallization buffers covering a wide range of pH, salts, polymers and organics commonly reported

to promote crystal growth[132]. Human ATIC was diluted to concentrations of 7.5 mg ml^{-1}, 10 mg ml^{-1}, 12.5 mg ml^{-1} and a drop containing the cyclic peptide inhibitor and protein at 10 mg ml^{-1} in the standard ATIC purification buffer. From this crystallization trial the most promising conditions seemed to be 30% (*w/v*) PEG 1500 or 10% (*w/v*) PEG 8000 with 8% (*v/v*) ethylene glycol in 0.1 M HEPES pH 7.5, but these results did not produce crystals of sufficient quality to obtain X-ray diffraction data.

The crystal structure for human ATIC was solved in 2001 by Wilson *et al.*[46]. The literature conditions reported for crystallizing human ATIC include 15-17% PEG 3000 in 0.1 M Tris pH 7.5-8.0 using protein concentrated to 10 mg ml^{-1}. Human ATIC is reported to be difficult to crystallize when compared to avian ATIC, with the avian homologue crystallizing overnight, but the human form requiring seeding to obtain crystals. Based on these literature conditions a crystal screen to analyse the effects of PEG molecular weight and concentration was designed. The trial included PEGs of different molecular weight (and of different ages) varying from left to right across the 24-well tray and varying concentration of PEG increasing down the tray. Two trays were created with identical compositions of PEG, one at a fixed concentration of 0.05 M NaCl and the other at 0.2M NaCl. Each well contained four drops for crystal growth analysis; 7.5 mg ml^{-1}, 10 mg ml^{-1}, 12.5 mg ml^{-1} and protein and inhibitor at 10 mg ml^{-1}. After 12 days incubation at 18 °C the drops were analysed for crystal formation with photos of each well taken to record the results.

The quality of the crystals in the multiple drops were graded using a colour scheme. Drops which contained no crystals or precipitated protein were annotated red, drops which contained tiny crystals which were of very poor quality were given orange (Figure 5-9), yellow was assigned to drops which contained larger fern-like crystals (a product of the nucleation stage being too fast, Figure 5-10), and green was assigned to drops containing larger flat plates and needles (Figure 5-11). This colour coded scoring

system is summarized for each plate (low and medium salt conditions) in

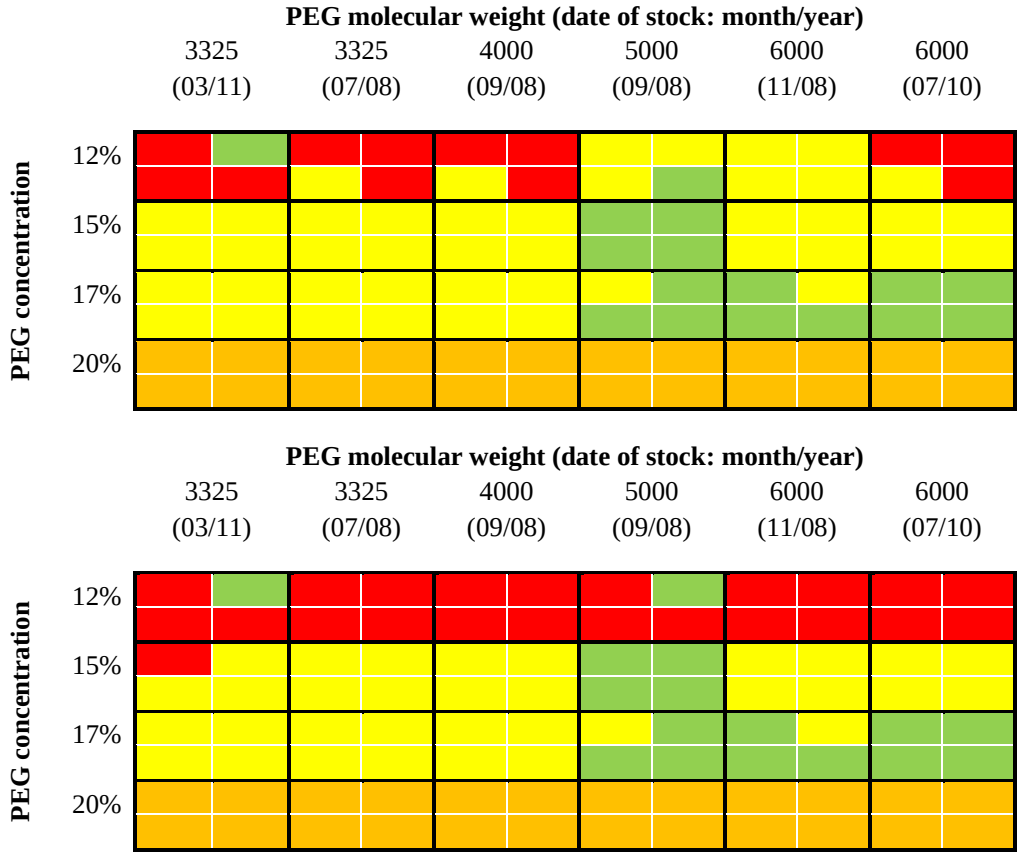

Figure 5-12.

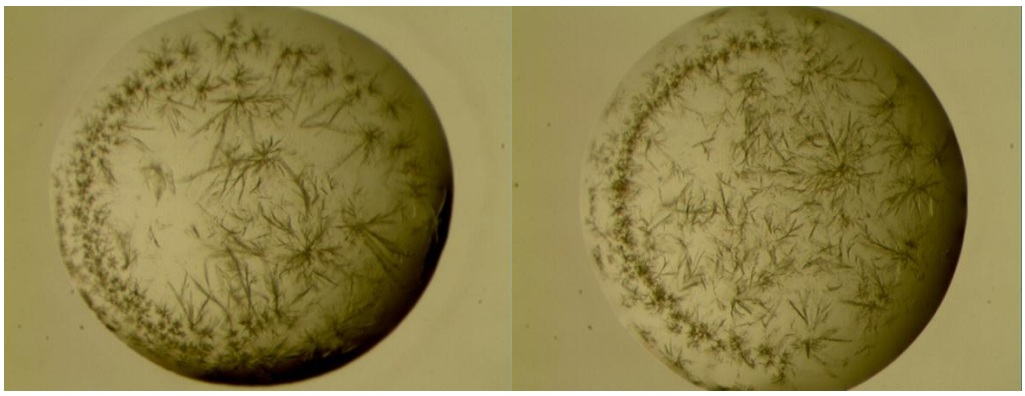

Figure 5-9: Examples of drops that were assigned ‘orange’.

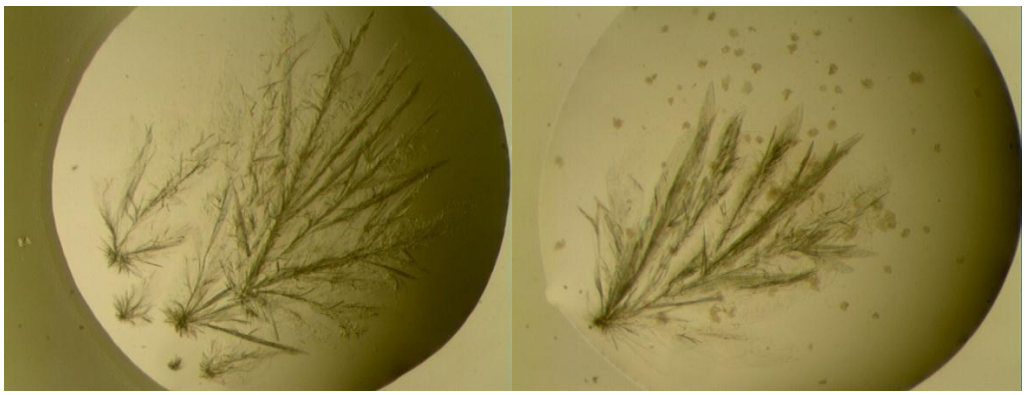

Figure 5-10: examples of drops assigned ‘yellow’.

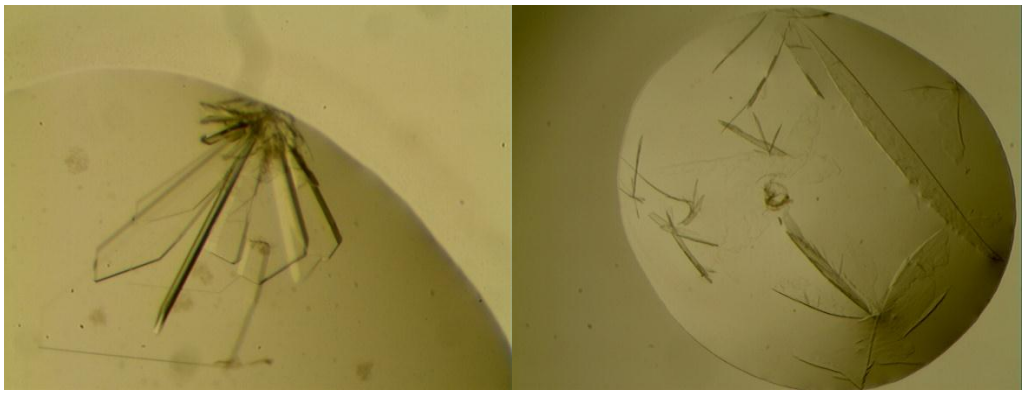

Figure 5-11: examples of drops assigned ‘green’.

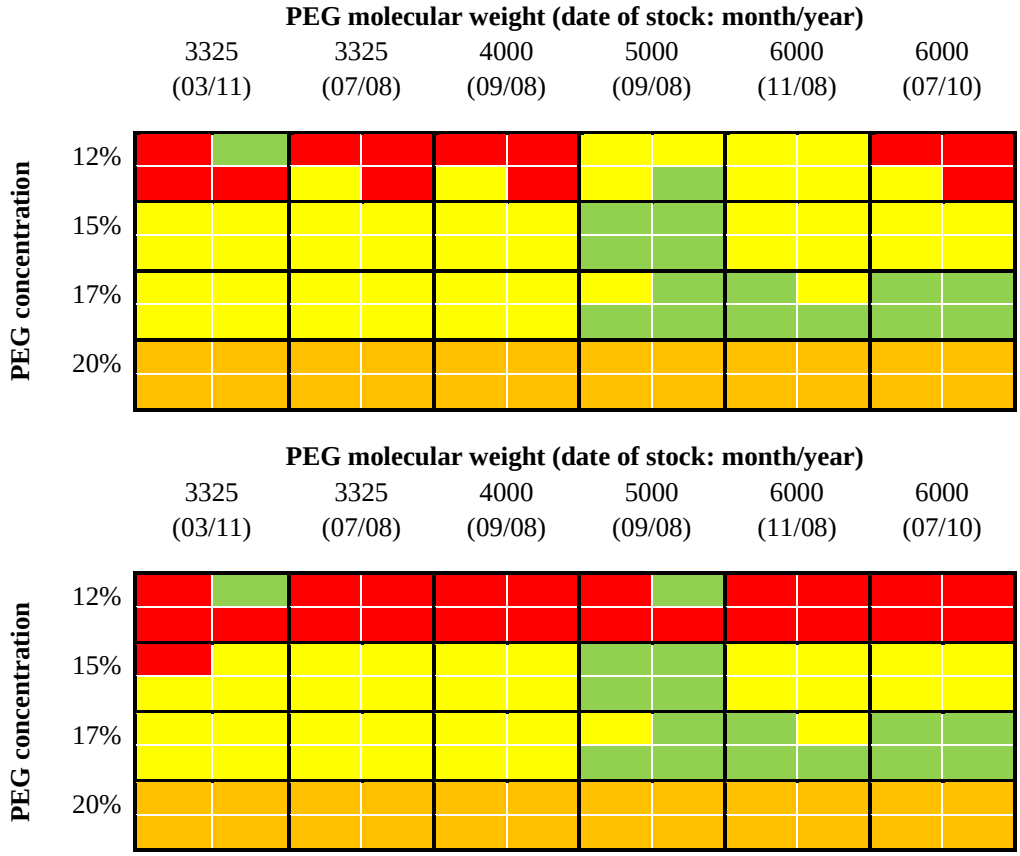

Figure 5-12: These tables represent the trays created for the PEG screen trial. Each well is represented by a dark border and each drop is represented by a single white outlined square. Each drop is graded by colour according to the quality of crystals produced. Red shows drops in which no crystals grew or the protein precipitated, whereas green shows the drops which produced the best quality crystals from this screen. The conditions are PEG concentration (far left) and PEG molecular weight (and date of stock) (top). The top table contains a constant concentration of 0.05 M NaCl and the lower 0.2 M NaCl.

After comparing the two PEG screen trays it appeared that different concentrations of NaCl do not make a noticeable contribution to the quality of the crystals. To measure any affects different cations and anions may have on crystal growth and try and approve the appearance of the crystals obtained from the PEG screen, new plates at PEG 3325 (03/11) and PEG 6000 (07/10) were created. NaCl, KCl, $MgCl_2$, Na_2SO_4, K_2SO_4 and $MgSO_4$ were used. Protein concentrations of 5 mg ml^{-1}, 7.5 mg ml^{-1}, 10 mg ml^{-1}, 12.5 mg ml^{-1}, 7.5 mg ml^{-1} plus inhibitor and 10 mg ml^{-1} plus inhibitor were used. None of the crystals obtained from this salt-type screen showed significant improvement and none were deemed suitable to be used for X-ray diffraction data collection.

A sample of human ATIC with the inhibitor was taken to the Hauptman-Woodward Institute in Buffalo where 1536 conditions were screened for crystallization using the High-Throughput liquid handling robot with the microbatch-under-oil method. This technique was carried out in a single plate with each well containing 200 nl of protein (at 10 mg ml^{-1}) and 200 nl of the crystallization solution. Digital photographs were taken of the wells at regular intervals (After 1 day then weekly for a month). After crystal formation they were analysed under a fluorescence microscope at 280 nm (tryptophan fluorescence) to differentiate salt from protein crystals. Two conditions provided promising crystals (Figure 5-13); 0.1 M calcium acetate, 0.1 M HEPES pH 7.5, 20% (w/v) PEG 8000 produced small cube shaped crystals; 0.1 M Rubidium chloride, 0.1 M bis-tris propane pH 7, 20% PEG 4000 produced flat plates with neat edges. The crystals were taken by collaborators at the Hauptman-Woodward Institute to be shot at the synchrotron but unfortunately there was not enough time to collect diffraction data. These conditions should be explored and expanded to grow crystals of the human ATIC and inhibitor complex which will be shot at the Diamond synchrotron source, UK.

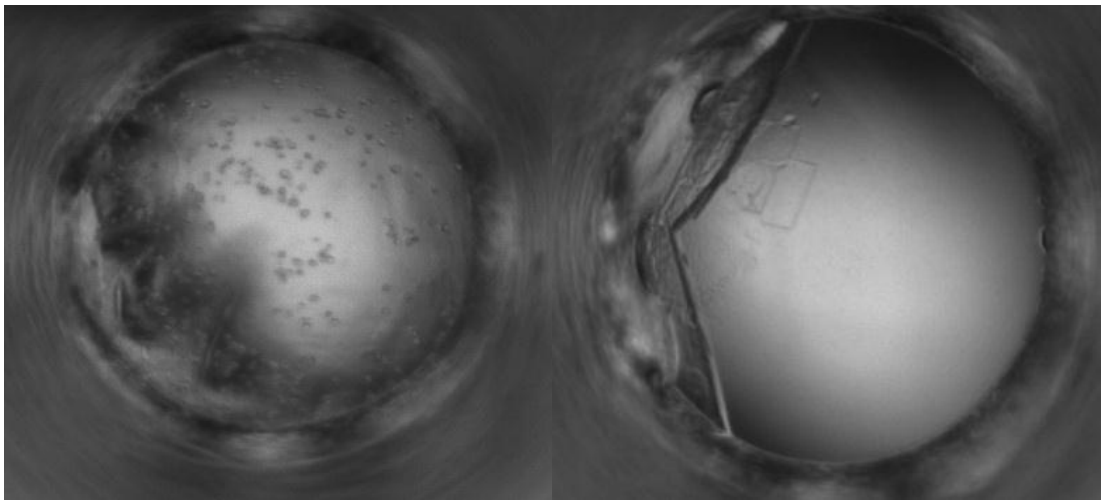

Figure 5-13: Photos of promising wells from the high-throughput screen taken after 7 days. The left well contains 0.1 M calcium acetate, 0.1 M HEPES pH 7.5, 20% (w/v) PEG 8000 and the right well contains 0.1 M Rubidium chloride, 0.1 M bis-tris propane pH 7, 20% PEG 4000.

5.3 Fluorescently labelled ATIC

The dimerisation interaction is entropically driven, and so the dimerisation constant cannot be measured by ITC dilution experiments. Therefore, another approach to investigate the dimerisation of ATIC was considered. The monomer-dimer equilibrium could be measured as a function of distance, when the monomers are close together they would be in the dimeric form, and when they are further apart this would signify the monomeric form. Förster Resonance Energy Transfer (FRET) is a distance dependent non-radiative transfer of energy from a donor molecule to an acceptor molecule. The FRET process is initiated as the donor molecule is promoted to an excited state by irradiation at a certain wavelength. The excited donor molecule then loses some of the excitation through internal conversion before transferring the remaining energy to the acceptor molecule non-radiatively, without the emission of a photon. The acceptor is then promoted to an excited state which decays by internal conversion, and then finally by acceptor emission of a photon. For two molecules to function as a FRET pair they

must have different excitation wavelengths and good spectral overlap between the donor emission and acceptor absorption spectra. The distance at which the energy transfer is conducted with 50% efficiency is known as the Förster radius; this is different for individual donor-acceptor pairs. The distance between the Gly4 residues of each monomer chain is around 40 Å, as measured from the crystal structure[85], so a FRET pair with a large Förster radius is required. Fluorescein and rhodamine were chosen as the donor acceptor pair, as they have a Förster radius of 55 Å[133], which will allow for the inevitable flexibility of the linker chain from the dye molecule to the *N* terminus. This should mean that when the enzyme is in dimeric form, the dye molecules will be positioned to allow FRET to occur, but as the dimer falls apart to two monomers the FRET should dramatically decrease as FRET has a distance dependence of $\frac{1}{r^6}$.

The approach taken was to use Sortase A to label the *N* terminus of both human and avian ATIC with fluorescein and rhodamine dyes. Sortase is a transpeptidase that cleaves the threonine glycine bond of substrate proteins bearing an LPXTG motif, to produce a thioacyl intermediate which is subsequently reacted with an *N* terminal glycine to form the new peptide bond[134]. The reaction is reversible as the aminoacetyl by-product can react to produce the reactant, so a large excess of nucleophile is required to push the reaction to completion. Sortase can be used to label a protein bearing an *N*-terminal oligoglycine with a short peptide containing the LPXTG recognition sequence. In 2012, Williamson *et al.* reported a new method which improved the efficiency of the sortase reaction using depsipeptide substrates to label proteins in quantitative yields[134]. Depsipeptide substrates contain an ester bond in place of the amide bond between the theronine and glycine of the recognition motif. This produces anhydroxyacetyl by-product which cannot perform the reverse reaction, so an excess of the nucleophile is no longer required.

The first step was to design a construct that would yield an *N*-terminal glycine on ATIC. The current pET28a construct used to express ATIC contains a thrombin cleavage site between the *N*-terminal his_6 tag and the start of the ATIC sequence. As removal of thrombin after cleavage can be inefficient, TEV cleavage was preferred. The site can be added in such a way that a single glycine residue would remain after cleavage with the TEV protease. This approach has the added benefit that the his_6 tag can be used to purify the protein by metal affinity before cleavage and, if a his_6 tagged TEV enzyme is used, then the TEV and cleaved ATIC fragment can be pulled from the reaction mixture upon completion. ATIC bearing a single *N*-terminal glycine residue can then undergo the sortase labelling reaction with the fluorescent depsipeptide (Figure 5-14). This approach is summarised in Figure 5-15. The fluorescently labelled peptides along with stocks of TEV and sortase enzymes were kindly provided by D. Williamson.

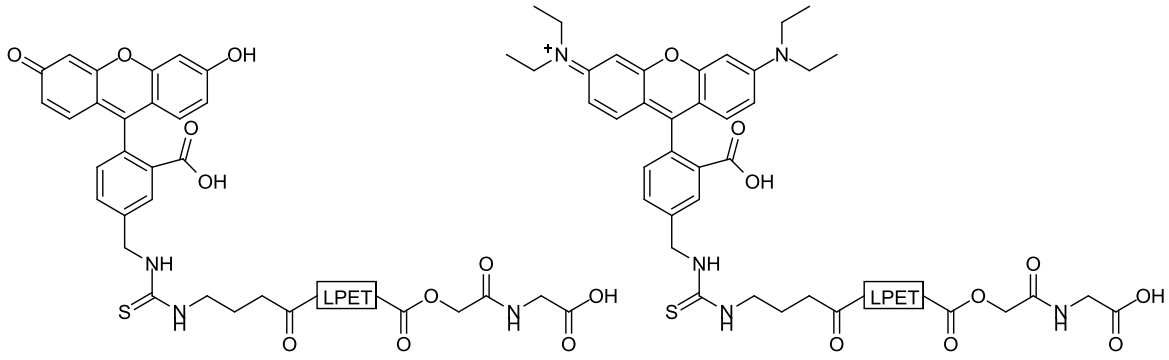

Figure 5-14: The structures of the fluorescent peptides used to label ATIC with sortase. The fluorescein derivative is shown on the right, and the rhodamine containing peptide on the left.

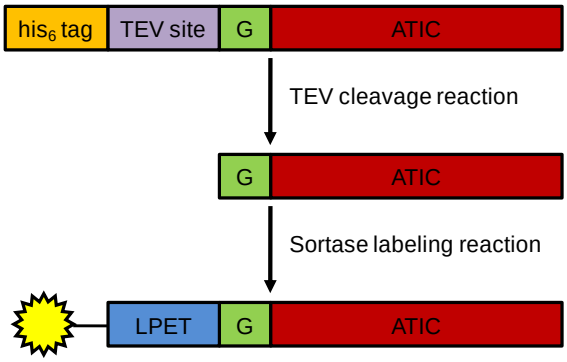

Figure 5-15: Scheme showing the methodology behind the approach to labelling ATIC. TEV cleavage exposes a single *N* terminal glycine which acts as the substrate for the subsequent sortase reaction, resulting in fluorescently labelled ATIC.

The first step in exchanging the thrombin cleavage site for a TEV recognition site was to mutate an Spe1 restriction site into pET28a as shown in Figure 5-16. Spe1 was chosen as it is not already found in the pET28a sequence and involved the mutation of only 2 bases. The incorporation of Spe1 was achieved by PCR using primers P09f and P09r and pET28a as a template. The product of the reaction was digested to remove the methylated template DNA before being transformed into XL-10 gold cells. The resulting colonies were cultured and the DNA was extracted and sent for sequencing. The sequencing results confirmed the incorporation of the Spe1 mutation.

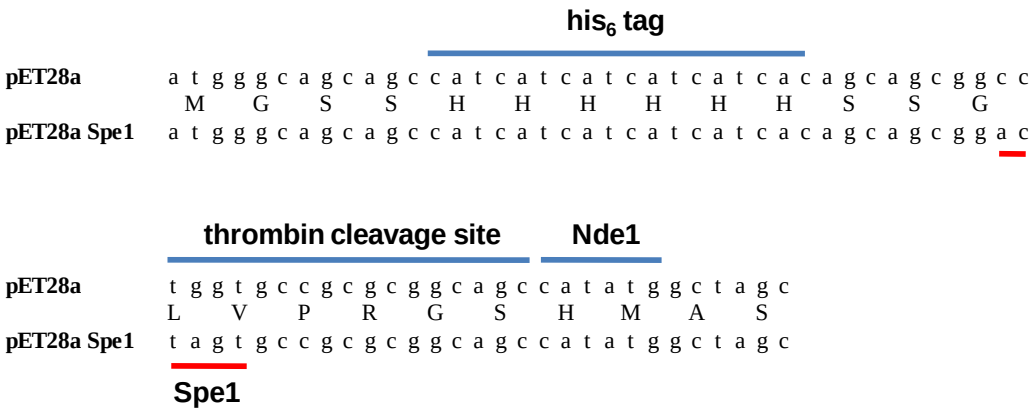

Figure 5-16: Mutation of pET28a to include an Spe1 performed by PCR using primers P09f and P09r.

Now Spe1 was incorporated into pET28a, the thrombin cleavage site was digested out through incubation with Spe1 and Nde1. The resulting pET28a vector was purified by agarose gel extraction, and then ligated with primers P10f and P10r through complementary sticky ends. These primers encode for the TEV recognition sequence. Successful ligation reactions were confirmed by sequencing (Figure 5-17, Figure 5-18).

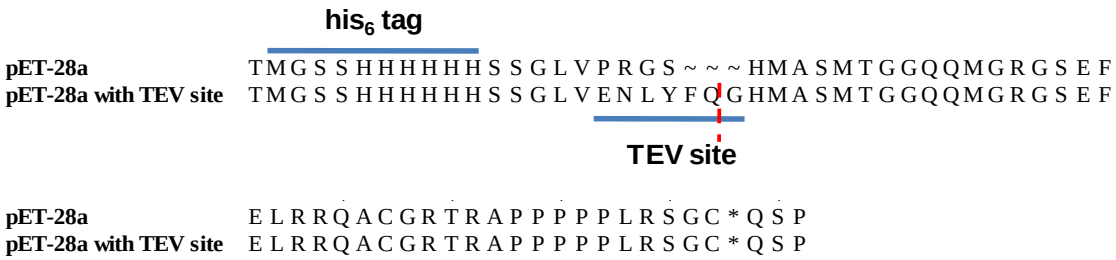

Figure 5-17: Incorporation of the TEV recognition site after the his_6 tag which will result in an *N* terminal glycine.

Figure 5-18: Incorporation of the TEV recognition site after the his_6 tag which will result in an *N* terminal glycine, followed by a hisitidine then the human ATIC sequence (highlighted in green).

This cloning process was conducted on pET28a encoding human ATIC, pET28a encoding avian ATIC, and the empty pET28a vector which may be used to clone any other proteins of interest.

5.3.1.1 Labelling of ATIC using sortase

Human and avian ATIC bearing N-terminal his6 tags, linked to the protein through a TEV recognition site, were overexpressed in *E. coli* C41 (DE3) cells grown in auto-inducing media at 30 °C. Cells containing the overexpressed protein were harvested by centrifugation and stored at −80 °C. Cell pellets were resuspended in buffer and lysed by sonication. Cell debris was cleared by centrifugation, and the protein of interest was purified from the crude cell lysate by metal affinity chromatography (Figure 5-18. lanes 1 to 6). Further purification was achieved through size exclusion chromatography, which was also used to buffer exchange into the TEV reaction buffer. Protein concentrations were measured by absorption at 280 nm, with the molar extinction coefficients calculated from the sequence (including the his tag with TEV cleavage site).

The his tag was then removed *via* a TEV cleavage reaction to leave an *N*-terminal glycine. This reaction was monitored using electrospray ionisation mass spectrometry. Small scale test cleavage reactions showed the reaction was complete in 2 hours, using 20% TEV in the reaction mixture (Table 5-1). The measured mass is the calculated mass plus the addition of a potassium ion, as the *N*-terminus has been cleaved to leave a glycine residue so there was no loss in mass for potential cleaved methoinine, as observed for the his tagged human and avian ATIC. Small scale metal affinity chromatography was used to pull out the his tagged TEV protease and the cleaved ATIC his tags. The flowthrough was concentrated and purified by size exclusion chromatography to exchange the enzyme into the sortase reaction buffer (Figure 5-18, lanes 7 to 15).

The sortase labelling reaction was performed on the purified, cleaved protein using 3.5 molar equivalents of peptide and 0.2 molar equivalents of his tagged sortase incubated at room temperature. An initial labelling reaction conducted at the recommended literature temperature of 37 °C[134] resulted in the formation of a precipitate in the reaction vessel, however when the reaction was repeated at a room temperature, no precipitation was observed. The labelling reaction was monitored by electrospray ionisation mass spectrometry and was typically completed after 7 hours. Upon completion, his tagged sortase was removed using small scale metal affinity chromatography, and the flowthrough mixture of labelled ATIC and excess fluorescent

peptide were separated by size exclusion chromatography (Figure 5-20). The labelled protein eluted at around 14 ml, whilst the excess peptide eluted after 20 ml.

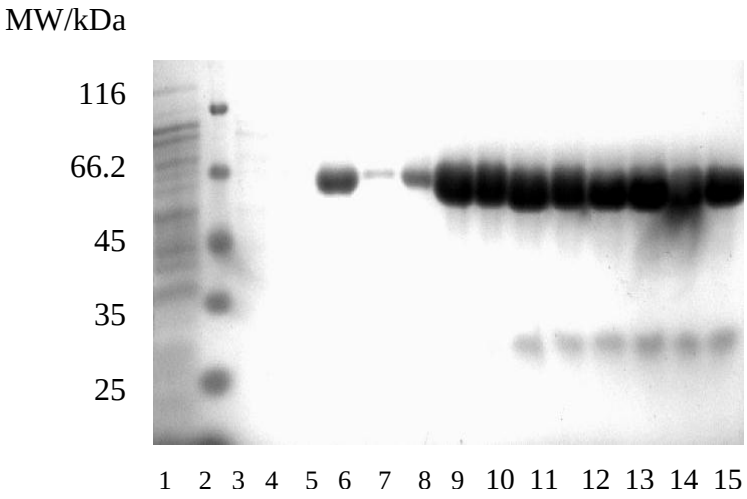

Figure 5-19: SDS-PAGE analysis of the metal affinity purification of human ATIC containing the TEV cleavage site and the subsequent TEV cleavage of human ATIC after gel filtration. Lane 1: flowthrough, lane 2: molecular weight marker, lane 3: wash 1, lane 4: wash 2, lane 5: elution 1, lane 6: elution 2, lane 7-15: fractions collected from the gel filtration purification.

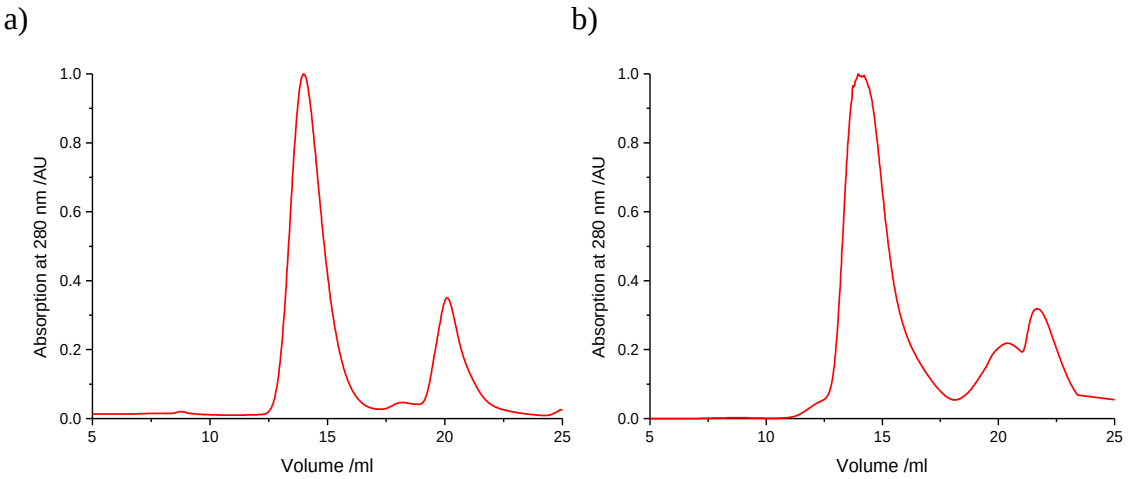

Figure 5-20: Purification of the sortase labelling reaction by size exclusion. a) absorption peak at 14 ml corresponds to fluorescein labelled human ATIC, with excess fluorescein peptide eluting at 20 ml, b) absorption peak at 14 ml corresponds to rhodamine labelled avian ATIC, with excess rhodamine peptide eluting from 20 ml onwards.

Table 5-1: Calculated and observed masses (Da) for the different protein species used in the process of fluorescently labelling ATIC.

Protein	*Human ATIC*	*Avian ATIC*
Calculated TEV cleaved	64810	64609
Measured TEV cleaved (2 h)	64849	64650
Calculated fluorescein labelled	65859	65658
Measured fluorescein labelled	65843	65666
Calculated rhodamine labelled	65969	65768
Measured rhodamine labelled	65947	65781

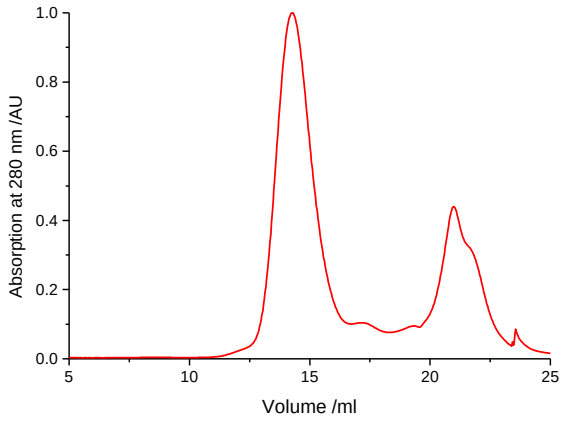

Figure 5-21: Size exclusion purification of avian ATIC after labelling with sortase and both fluorescein and rhodamine peptides in 1:1 ratio.

To enable the determination of labelled protein concentrations, extinction coefficients were calculated for each of the fluorescently labelled peptides. These were then added to the molar extinction coefficients calculated for each protein from the sequence (Table 5-2).

Table 5-2: Molar extinction coefficients calculated for each of the fluorescent labels ($M^{-1} cm^{-1}$).

Compound	*Fluorescein*	*Rhodamine*
Free peptide	18000	16800
Labelled human ATIC	72820	71620
Labelled avian ATIC	68350	67150

5.3.1.2 FRET

Different mixtures of the labelled proteins were investigated using fluorimetry to observe FRET between the dye pairs. Optimisation studies showed the best wavelength to monitor rhodamine emission was 580nm. Each experiment was repeated at excitation wavelengths of 460 nm, 480 nm, and 494 nm, although 480 nm was the optimal excitation wavelength, the others were monitored to record a lower (460 nm) and higher (494 nm) excitation of fluorescein. The differently labelled proteins were mixed and incubated at room temperature for at least 30 mins, to allow the monomers to redistribute through monomer-dimer equilibrium. Different ratios of the FRET pairs were investigated, fluorescein:rhodamine, 1:1, 1:2, 1:3, 1:4 and 1:5. The fluorescence observed at 580 nm was recorded for the excitation of fluorescein (5 μM) without the presence of rhodamine to measure the background emission of fluorescein. Background scans of rhodamine emission when subjected to the excitation wavelength without the presence of fluorescein showed a slight emission at 580 nm, for example at 5 μM rhodamine-labelled protein excitation at 480 nm caused an emission at 580 nm of 6650 fluorescence units.

No detectable FRET signal was ever observed between the fluorescein and rhodamine dyes even when incubated at 4 °C (temperature chosen for stability reasons) for 2 days. The fluorescence emission measured at 580 nm was equal to the sum of the background

emissions for each dye. To investigate if no FRET was seen due to a lack of dynamic behaviour between the monomeric and dimeric forms, the sortase labelling reaction was repeated with a 1:1 mixture of fluorescein and rhodamine peptides to generate dimeric protein containing both labels, but still no FRET was observed.

This system was designed to have the shortest practical linker between the dye and the protein, but inevitably this is still very flexible. The dyes cannot be fixed into a known position. The hydrophobic dyes may potentially have flexed around to bind to a hydrophobic pocket on the surface of the protein, or the peptide linker may have formed favourable interactions with some part of the protein that prevents the dyes from interacting within a preferential distance.

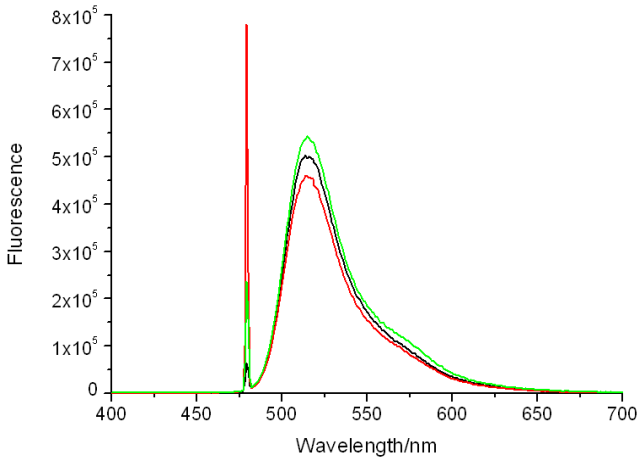

Figure 5-22: Fluorescence emission profile from rhodamine dye after fluorescein excitation and subsequent FRET.

5.3.1.3 Fluorescence correlation spectroscopy

As the attempts to monitor ATIC dimerisation through a FRET interaction between dyes located at the *N*-terminus of each monomer were unsuccessful, different concentrations of labelled protein were investigated using fluorescence correlation spectroscopy. This technique can determine the size of particles by monitoring the diffusion times through an aqueous solution. The diffusion of individual molecules is tracked using a fluorescent label. Each of the labelled proteins was measured at a fixed concentration

(60 nM), unlabelled protein was then added incrementally to increase the overall enzyme concentration up to 10 μM. If the dimerisation constant was with the range of these concentrations, fluorescence correlation spectroscopy should be able to measure the diffusion of the monomer at the low concentrations, increasing in size to form the dimer with increasing the enzyme concentration. However, no diffusion constant or changes in diffusion time were measured, suggesting that ATIC dimerisation cannot be monitored by this technique either. Potentially the size difference between monomer and dimer is too small to be analysed by this technique.

5.4 Conclusion

The lack of enthalpic signal measured during the ITC dilution experiments supports the previous hypothesis that the dimerisation is entropically driven, supporting the results shown with DSC and DSF experiments. To further characterise the monomer/dimer equilibrium, a new vector construct was created based on pET28a that incorporates a TEV recognition site after the *N*-terminal his tag, designed to leave an *N*-terminal glycine residue as a substrate for a sortase catalysed labelling reaction.

Two techniques have been investigated to be able to measure ATIC dimerisation using fluorescently labelled monomers. Fluorescence measurements to observe FRET between dimers containing one fluorescein-labelled monomer and one rhodamine-labelled monomer showed no FRET emission from the rhodamine acceptor molecule. This is thought to be due to the position of the dye molecules relative to each other, the flexible linker between the dye and the monomer may allow the dye to flex around and interact with the surface of the protein in some way that destroys any possibility of FRET between the donor and acceptor molecules. No change in particle size could be detected by fluorescence correlation spectroscopy over a 60 nM to 10 μM concentration range.

6 Potassium dependence of human ATIC

6.1 Metal dependence of ATIC

In 1957, Flaks *et al.* reported that AICAR transformylase has an absolute requirement for potassium ions, with an optimal activity being shown over a concentration range of 3 to 30mM[56]. The K_a for potassium has not been published, but all experiments have been conducted in potassium containing buffers. Crystal structures of ATIC from different organisms all show the presence of two bound potassium ions, one per monomer[47].

Kryptofix 222 has a high affinity for potassium cations. The determination of the potassium K_a for human and avian ATIC was attempted using ITC. Kryptofix 222 was titrated into the sample cell which contained ATIC, and ATIC was also titrated into kryptofix 222. These experiments resulted in highly precipitated protein, suggesting that once the potassium is removed from ATIC the protein is no longer stable in solution.

To be certain that this dependence upon a metal ion for activity was unique to potassium, a metal dependence screen was undertaken. The standard spectroscopic assay (monitoring the absorbance at 298 nm) was used to quantify catalytic turnover. The enzyme was added last to the buffer, AICAR and metal solution contained in the cuvette, and was incubated at 25 °C for 3 min before the change in absorbance at 298 nm was monitored. A 'standard' activity was measured at a concentration of 83 nM KCl, as the ITC experiment titrating kryptofix 222 into human ATIC suggested that removal of endogenous potassium would result in protein precipitation. To this 'background' amount of potassium, various monovalent and divalent metal chlorides were added, to achieve a final concentration of 1 mM. The results of this experiment, Figure 6-1, show a unique dependence upon potassium ions for maximal activity but,

substantial activity is still seen in the presence of the other metal cations. This was thought to be due to the 83 nM K^+ present in each sample. The activities recorded for all other metal ions except potassium have similar activities to the control sample. Addition of 1 mM K^+ only seems to have a small effect on increasing the catalytic activity. This was thought to result from the short incubation time the enzyme was left to incubate with the metal ion solution, as the enzyme was added to the assay mixture just prior to measurement.

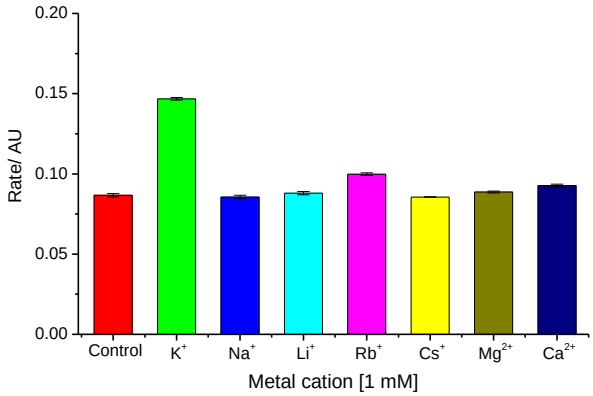

Figure 6-1: The effects of various metal cations on human ATIC activity. The control sample contains human ATIC, AICAR, 10-f-H_4F and 83 nM KCl. All other samples contain an additional metal chloride at a final concentration of 1 mM. Sample were prepared without 10-f-H_4F and incubated at 25°C for 3 min prior to initiation of the catalytic reaction by the addition of 10-f-H_4F.

Therefore, the enzyme was incubated with the buffer, AICAR and metal solution on ice for 20 min and then incubated in the cuvette at 25 °C for 5 min before the change in absorbance at 298 nm was measured. Figure 6-2 confirms that the metal dependence exhibited by human ATIC is unique for potassium; the presence of other monovalent cations or magnesium or calcium divalent cations does not increase activity.

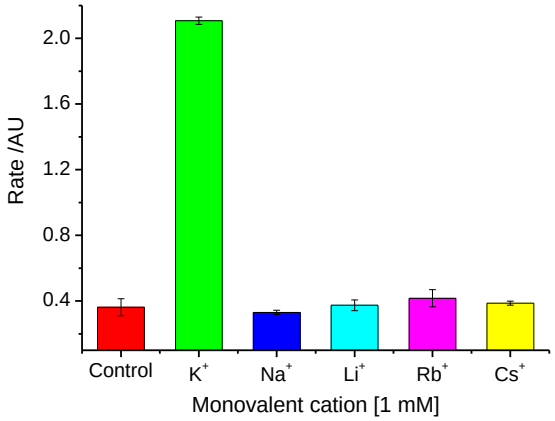

Figure 6-2: The effects of the addition of different monovalent metal chlorides upon rate of catalysis of human ATIC. The control sample contains human ATIC, AICAR, 10-f-H_4F and 83 nM KCl. All other samples contain an additional metal chloride at a final concentration of 1 mM. Samples were prepared without 10-f-H_4Fand incubated on ice for 20 min, and then at 25°C for 5 min before 10-f-H_4F was added to initiate the reaction.

The potassium dependence of the wild type ATIC was measured by changing the concentration of KCl present in the assay cell. The K_d for potassium was found to be 796 ± 48 μM (Figure 6-3) when AICAR is at a final concentration of 66.7 μM and 10-f-H_4F is present at 230 μM. This is consistent with the potassium concentration required for maximal activity, as described by Flaks, *et al.* of 3 to 30 mM[57], and confirms that working at a standard buffer concentration of 25 mM will ensure maximal ATIC activity.

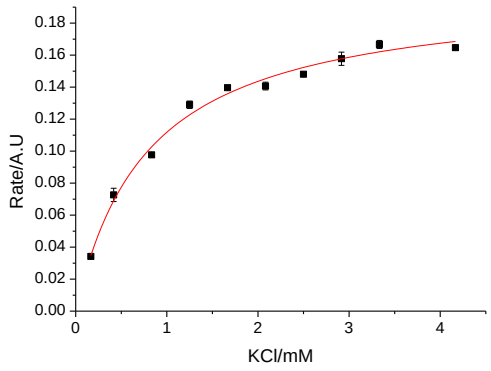

Figure 6-3: The potassium dependence of human ATIC at 25°C

6.2 Cloning, overexpression and purification of site-directed mutants of human ATIC

The crystal structure of human ATIC has been used to identify the residues that form the potassium binding site, Figure 1-8. The potassium ion is held in an octahedral geometry; S430, S432 and D539 all make interactions through their side chains and V425, T428 and L589 interact with the potassium ion through backbone carbonyls. Residues suitable for site directed mutation were identified using PyMOL software, shown in Figure 6-4. Serine residues S430 and S432 were both mutated to alanine, as this will remove any polar interactions between the hydroxyl and the positively charged potassium ion. D539 makes an ionic interaction to the potassium ion, so D539A was chosen to remove this interaction, and D539N was chosen to preserve potential hydrogen bonding. Due to the close proximity of the potassium ion to the bound AICAR substrate, residue N431 was chosen as the residue sits between the S430 and S432 sites, and is oriented towards bound AICAR and potentially forms hydrogen bonds with the amino group of the imidazole ring and the carbonyl of the carboxamide group. N431A will disrupt any potential hydrogen bonds that could form through the side chain, and N431D will introduce a negative charge and eliminate the capability for the side chain to participate as a hydrogen bond donor. F590 was chosen as the phenylalanine ring has the correct orientation for a favourable T-shaped π-π stacking interaction with the imidazole ring of the AICAR substrate. F590A and F590I both remove the phenylalanine ring, and F590I was chosen to retain a similar steric bulk to the phenylalanine. These mutations will be analysed to investigate whether the potassium ion performs a structural role which supports the nearby AICAR binding site, either by stabilising the structure of the AICAR transformylase domain, or by stabilising the dimeric form of the enzyme, which is required for maximum catalytic activity.

The site-directed mutants S430A, N431A, N431D, S432A, D539A and D539N were kindly provided by Dr M. M. Spiering (Penn State University). These mutants were each cloned into a pET28a plasmid, designed to produce *N*-terminal $his_{(6)}$-tagged proteins overexpressed under the control of a T7 lac promoter. This same design approach was taken in creating mutants F590A and F590I.

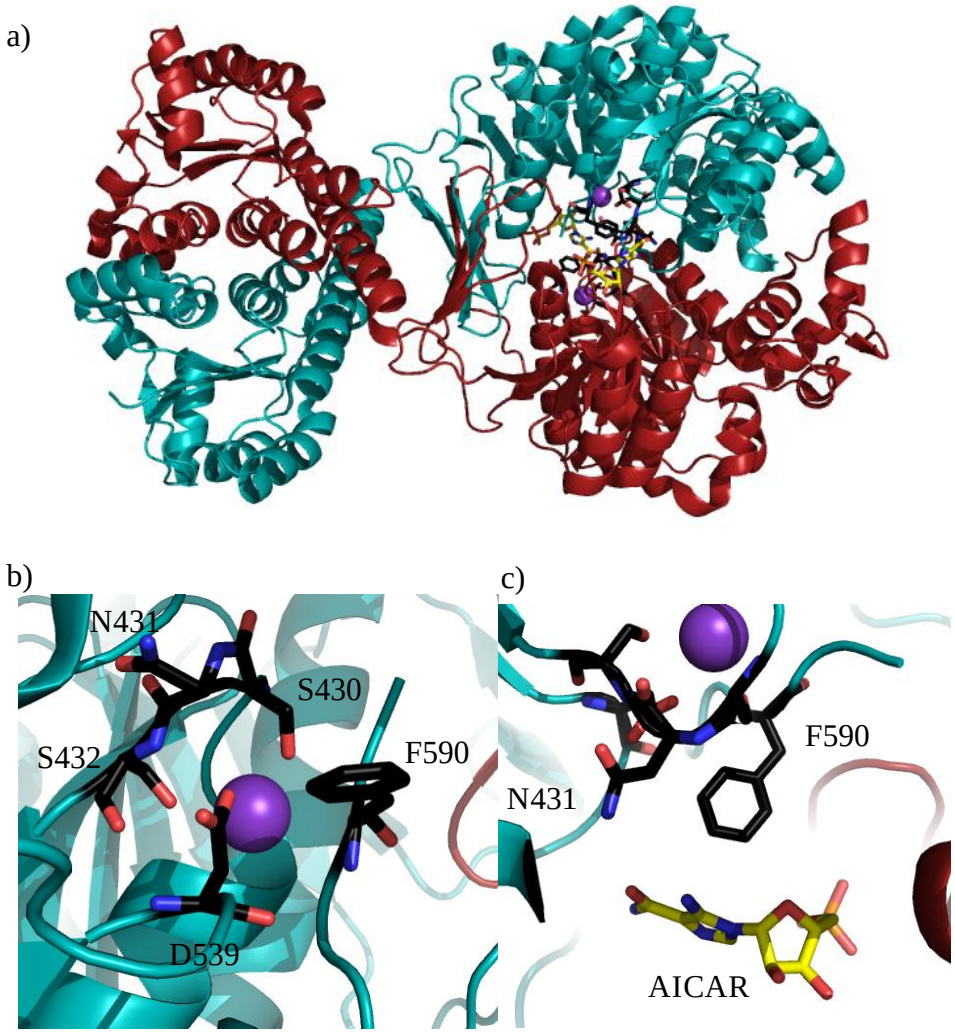

Figure 6-4: Schematic of the human ATIC, highlighting the residues surrounding the potassium binding site. a) Cartoon representation of the human ATIC crystal structure. Potassium is represented by purple spheres, AICAR is yellow and coloured by element, and residues selected for site directed mutation are black and coloured by element. b) Residues surrounding the potassium binding site. c) Residues directed towards the AICAR binding pocket.

6.2.1.1 Cloning of F590A and F590I

All cloning was performed using primers specified in the appendix, using the PCR programs stated in 2.7.1. The additional site-directed mutants of human ATIC were generated via the Quikchange site-directed mutagenesis protocol. Site-directed mutagenesis was performed on the pET28a plasmid containing the gene encoding for wild type human ATIC. Primers were designed to incorporate a single mutation at residue F590. Mutant F590A used the forward primer P01f and reverse primer P01r, mutant F590I used the forward primer P02f and used the reverse primer P02r with an annealing temperature of 55 °C. To digest the methylated template DNA the PCR product was digested using the restriction endonuclease Dpn1. The digested DNA was then transformed into XL10-Gold competent cells. Single colonies were selected and the plasmids containing the required mutations were extracted using a QIAprep Spin Miniprep (Qiagen). Conformation of the presence of the mutated ATIC gene was confirmed by agarose gel electrophoresis and sequencing (Appendix).

Proteins bearing *N*-terminal $his_{(6)}$-tags were expressed in *E. coli* BL21 (DE3), *E. coli* BL21* (DE3) and *E. coli* C41 (DE3) strains in auto-inducing media at 30 °C. After 24 h, the protein-containing cells were harvested by centrifugation and stored at -80 °C. The cells were lysed by sonication or cell disruption, and the lysates cleared by centrifugation before further purification. The $his_{(6)}$-tagged ATIC mutants were separated from other cellular proteins by Immobilized Metal ion Affinity Chromatography (IMAC). The crude cell lysates were applied to a Ni-NTA agarose resin under gravity flow. The column was washed step-wise with increasing concentrations of imidazole, to compete off weakly bound proteins. The ATIC mutant was eluted with a high concentration of imidazole (250 mM). Column fractions were analysed by a simple Bradford assay which detects the presence of proteins by a colour change from brown to blue, and by SDS-PAGE to assess the purity of the elution fractions obtained. An example SDS-polyacrylamide gel (Figure 6-5) shows some trace impurities that remained after the IMAC purification; these are likely to be *E. coli* proteins that contain a high number of sequential histidine amino acids that also have a high affinity for the Ni-NTA resin, or proteins that co-purified with human ATIC. The elution fractions containing the protein of interest were combined and concentrated (Amicon® Ultra-15 Centrifugal Filter, 10 kDa NMWL), before further purification on a Superdex 200 gel filtration column using the Pharmacia AKTÄPurifier FPLC system. The absorption of the eluent from the gel filtration column is monitored at 280 nm; an example trace is shown in Figure 6-5. The first peak, observed at approximately 8 ml volume is thought to be due to aggregated species caused by the concentration of the sample, prior to loading onto the gel filtration system. The peak obtained at 14 ml is the pure ATIC mutant of interest.

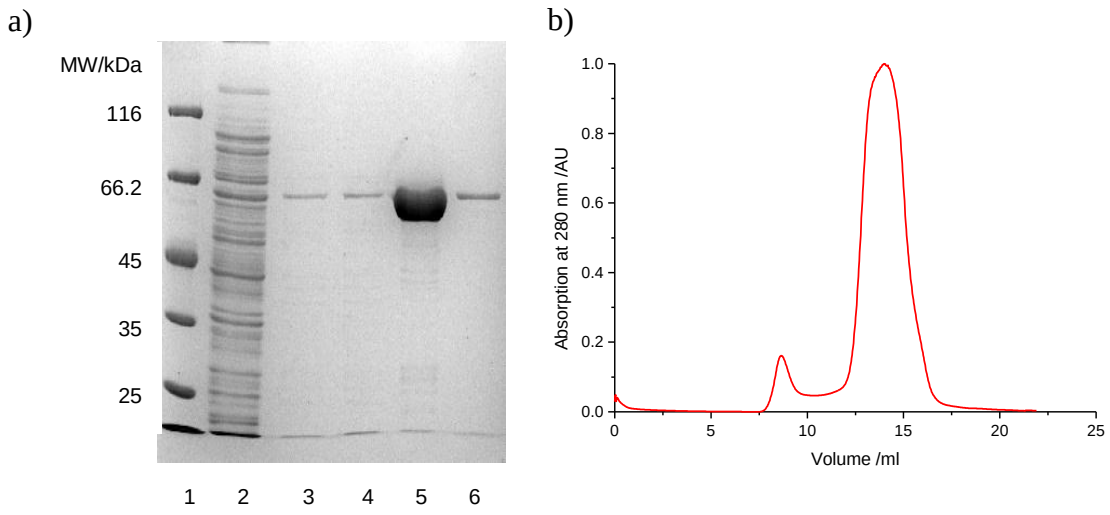

Figure 6-5: The purification of N431A site-directed mutant of human ATIC.

a) SDS-PAGE 10% of the purification of N431A ATIC from *E. coli* using a gravity flow column: lane 1: molecular weight marker, lane 2: flow through, lane 3: wash 1 (10 mM imidazole),, lane 4: wash 2 (150 mM imidazole),, lane 5: elution 1 (250mM imidazole), lane 6: elution 2.

b) Gel filtration using Superdex 200 10/300 column. Elution is monitored by absorption at 280 nm. Aggregates formed during concentration are eluted in the void volume of the column, 8 ml, with the pure N431A ATIC eluting at 14 ml.

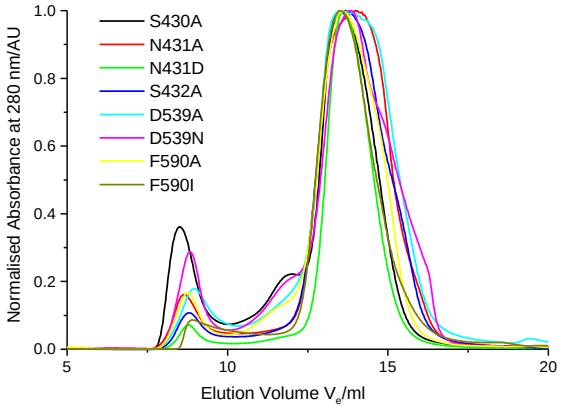

Figure 6-6: Normalised absorption traces at 280 nm for each of the potassium mutants. The first elution peak at approximately 8 ml is due to aggregates that form during the concentration process. The elution volume for each mutant is taken as the highest peak; this is then used to calculate the molecular mass using the equation $y = 13983e^{-4.59x}$ which was obtained from the calibration curve shown in Figure 2-2.

Table 6-1: Molecular mass for each mutant was determined by high resolution mass spectrometry and from the absorption traces obtained from size exclusion purification. The calculated mass was determined from the protein sequence.

Mutant	***Calculated mass /Da***	***Mass determined by mass spectrometry /Da***	***Calculated mass with the loss of methionine/ Da***	***Mass determined by gel filtration /kDa***
S430A	66763.2	66640.3	66631.0	129
N431A	66736.1	66608.0	66603.9	99
N431D	66780.1	nd	66647.9	120
S432A	66763.2	66646.1	66631.0	115
D539A	66735.1	66625.6	66632.9	132
D539N	66778.2	nd	66646.0	106
F590A	66703.1	66597.4	66570.9	122
F590I	66745.1	66643	66612.9	127

The calculated mass for each of the mutants was determined from the protein sequence. Under the denaturing conditions of SDS-PAGE analysis, all mutants displayed a band at approximately 66 kDa, which is comparable to the calculated masses. As the SDS-PAGE technique is also dependent on charge and size, the observed bands were deemed to be the species of interest. High resolution mass spectroscopy was used to confirm the mass of the mutants. These measured masses are presented in Table 6-1, and are consistent with the expected mass when the sample is considered to have lost the *N*-terminal methionine and gained a potassium ion.

Mass spectrometry confirmed the monomeric mass of all the mutants, except N431D and D539N which could not be observed by mass spectrometry. These two mutants were potentially unstable in the acetonitrile/formic acid solution used to prepare mass spectrometry samples. The apparent mass determined from the absorption traces at

280 nm, obtained from the size exclusion purification stage, suggests that all of the potassium mutants are present in their dimeric form under non-denaturing conditions, the same oligomeric form that is seen for wild-type human ATIC.

6.3 Characterisation of potassium binding site mutants

6.3.1.1 Thermal stability

The DSF studies performed on human and avian ATIC in Chapter 3, which studied the effects of various small molecules at different concentrations on protein stability, were repeated at a lower overall concentration of potassium, 5 mM in comparison with 25 mM, to investigate any effect potassium may have on the melting temperature of the proteins. The melting temperature of both proteins was also measured in the presence of 1 M KCl.

Interpretation of the DSF plots of ATIC show that the enzyme unfolds through two separate transitions (Chapter 3). For human ATIC, the largest of these transitions occurs at 46 °C, and a second transition characterised by a small broader peak at 57 °C. Avian ATIC has a large peak corresponding to a T_m of 43 °C and, similar to human ATIC, a small broad second hump at 51 °C.

The T_m is calculated from the peak of the curve, but the shape can also give information about the protein unfolding. When the potassium concentration is reduced to 5 mM, the larger unfolding peak is destabilised slightly, and a greater proportion of the area underneath the curves are occupying a lower temperature range, implying at the lower potassium concentration a greater proportion of the enzyme is unfolded below the T_m. The increase in T_m with increased K^+ ion concentration hints that the essential nature of potassium may have a structural role, as increasing the potassium concentration appears to increase the T_m of the first unfolding transition. Increasing the potassium does not eliminate the first transition and leave the second transition, as the intensity of the

fluorescence emission is comparable between the assays conducted at the different potassium concentrations, indicating a similar area of hydrophobicity has been exposed. As discussed in Chapter 3, the intense first peak is thought to be attributed to the dimer unfolding to the monomer. This process unveils an expansive hydrophobic region of approximately 5000 $Å^2$, which would account for the magnitude of the peak. Hence, this data suggests that the potassium ion, which is essential for maximal catalytic activity, could play a role in stabilising the dimeric form of the enzyme. The AICAR transformylase domain catalytic activity is dependent on dimerisation of the enzyme, so if potassium is required to stabilise the dimer, this would link to the essential nature of the potassium ion.

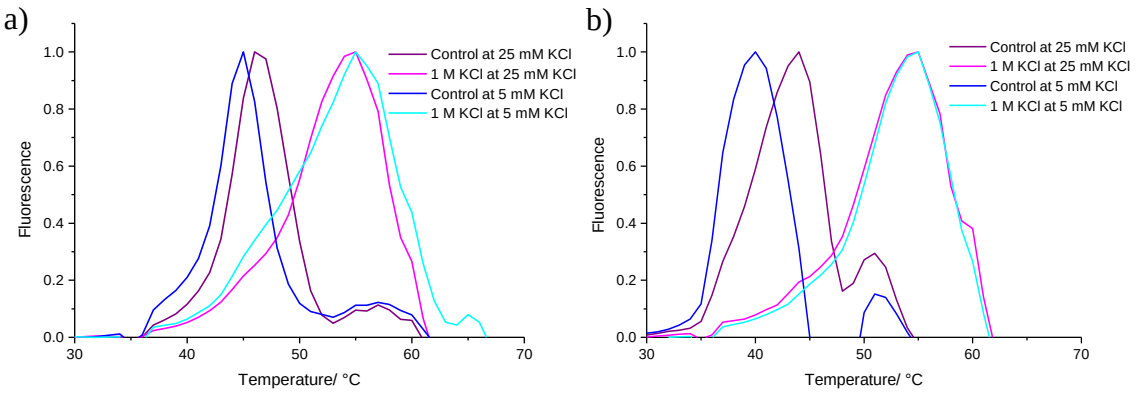

Figure 6-7: Summary of the fluorescence traces obtained by DSF for the experiments investigating the stabilising effects of potassium. a) human ATIC, b) avian ATIC.

Stabilisation is also seen with the addition of the various ligands and small molecules.For the human protein, there is a greater ΔT_m between the AICAR-containing experiments at the different potassium levels than seen with the apoprotein. At the higher concentration of potassium, AICAR has a greater stabilising effect than under low potassium conditions; the presence of more potassium allows the AICAR to impart more stability by holding the dimer together. This suggests that AICAR may play a part in maintaining the dimeric structure, or may bind more strongly to the dimeric form of

human ATIC. However, with 10-f-H_4F, there is no change in ΔT_m between low and high potassium, with the absolute T_m value between sets of experiments only varying by 1 °C which can be attributed to the stabilisation provided by the potassium, as shown by the control. This implies that the stabilisation added by 10-f-H_4F is not affected by potassium concentration, so the binding is either not dependent on having an effect on dimerisation, or the effects are too small to be measured by this technique. The greatest ΔT_m seen across the conditions examined was upon the addition of 1 M KCl to the apoprotein in 5 mM KCl, but the addition of 1 M KCl brings both high and low potassium experiments to the same T_m of 55 °C. 1 M KCl was chosen as this is an extremely high concentration, hence would represent the maximum stability that can be provided by potassium. It has been considered unlikely that this high concentration may be conferring stability simply through a crowding effect; performing DSF experiments solely examining the effects of increasing KCl concentration would investigate any crowding effects.

The ligands and other small molecules investigated have a greater stabilisation effect (ΔT_m) on avian ATIC than compared to the same conditions human ATIC. Larger stabilisation by AICAR and 10-f-H_4F is seen at the lower potassium concentration. The absolute values of the T_m are higher in the higher potassium containing buffer, as with human ATIC, but AICAR has a greater effect on stabilising the melting temperature in the lower potassium experiments. At low potassium, $PteGlu_4$ seems to show a concentration dependence, however, if the shape of the curves is taken into consideration, rather than just the maximum peak, the vast majority of the area below both curves overlap, suggesting a very similar unfolding profile, hence both concentrations of $PteGlu_4$ provide a very similar stabilisation. As with human ATIC, the addition of 1 M KCl brings the maximum stabilisation, corresponding to 55 °C.

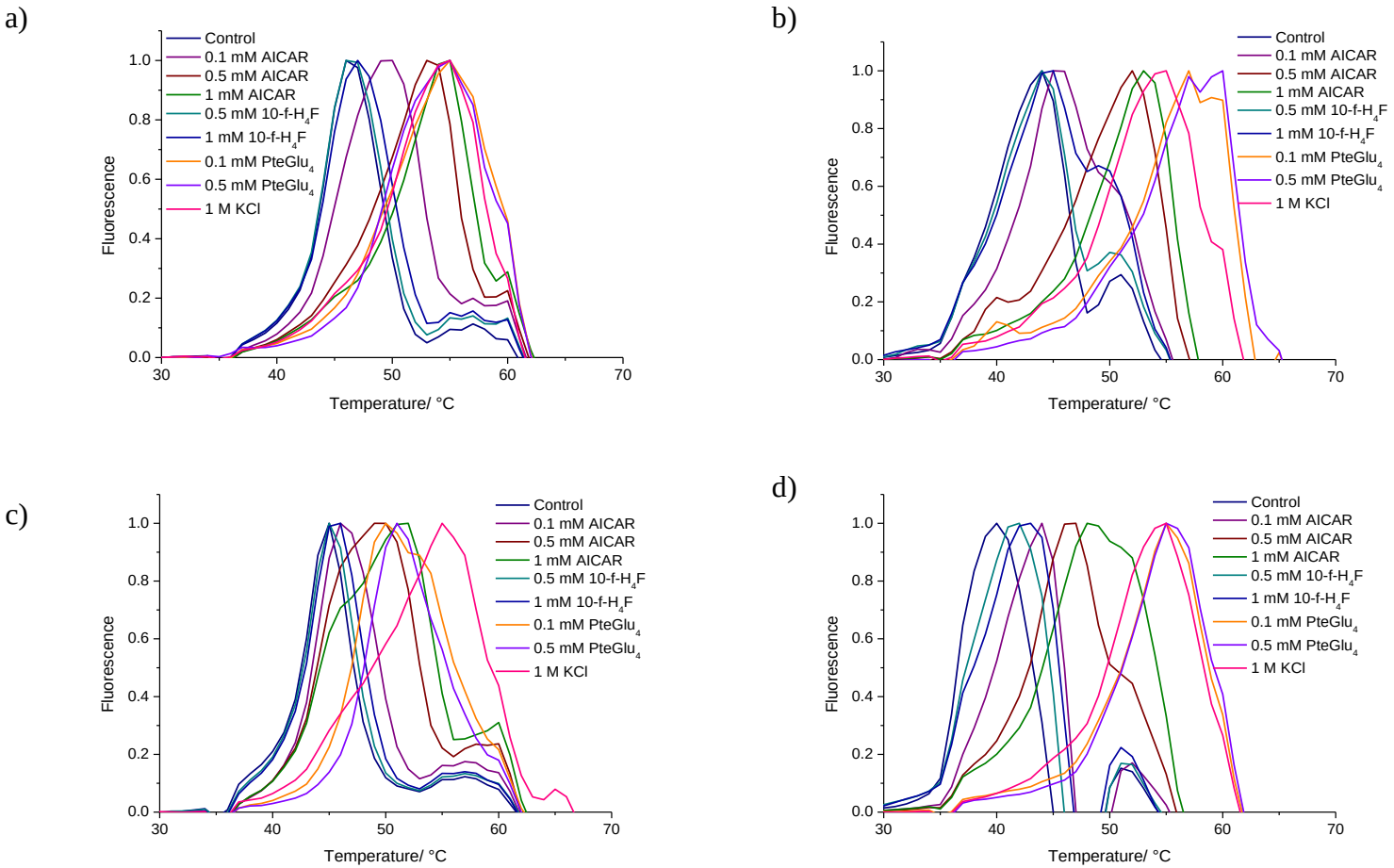

Figure 6-8:Normalised DSF traces for a) human ATIC in high potassium (25 mM) buffer, b) avian ATIC in high potassium buffer, c)human ATIC in low potassium (5 mM) buffer, d) avian ATIC in low potassium buffer, at certain concentrations of various small molecules

Table 6-2: T_m (°C) of human and avian ATIC, as apoproteins (control) and in the presence of various small molecules at specified concentrations, as measured by DSF. AICAR is the substrate for ATIC and 10-f-H_4F is representative of the cofactor used *in vivo*. $PteGlu_4$ was included in the experiment to monitor the effects of the polygluatmate tail of the *in vivo* cofactor on the thermal stability of the enzymes. The presence of potassium was also investigated, by addition of 1 M KCl and purification of each enzyme in both low potassium (5 mM KCl) and high potassium (25 mM) buffer to monitor any effects potassium may have on stability.

	Enzyme	***Control***	***0.1 mM AICAR***	***0.5 mM AICAR***	***1 mM AICAR***	***0.5 mM 10-f-H_4F***	***1 mM 10-f-H_4F***	***0.1 mM $PteGlu_4$***	***0.5 mM $PteGlu_4$***	***1 M K^+***
High K^+	Human	46	50	53	55	46	47	55	55	55
	Avian	44	45	52	53	44	45	57	60	55
Low K^+	Human	45	46	49	52	45	46	50	51	55
	Avian	40	44	47	48	42	43	55	55	55

Table 6-3:Changes in T_m (°C) on addition of various small molecules, as compared to apoenzyme (control).

	Enzyme	***Control***	***0.1 mM AICAR***	***0.5 mM AICAR***	***1 mM AICAR***	***0.5 mM 10-f-H_4F***	***1 mM 10-f-H_4F***	***0.1 mM $PteGlu_4$***	***0.5 mM $PteGlu_4$***	***1 M K^+***
High K^+	Human	0	4	7	9	0	1	9	9	9
	Avian	0	1	8	9	0	1	13	16	11
Low K^+	Human	0	1	4	7	0	1	5	6	10
	Avian	0	4	7	8	2	3	15	15	15

6.3.1.2 Summary

DSF was used to determine the melting temperature of each of the site directed mutants, under the same experimental conditions used for human ATIC at 25 mM KCl. The effects of the mutations on stability are show in Table 6-4. An example trace of the normalised DSF fluorescence output is shown in Figure 6-9 for mutant N431A.

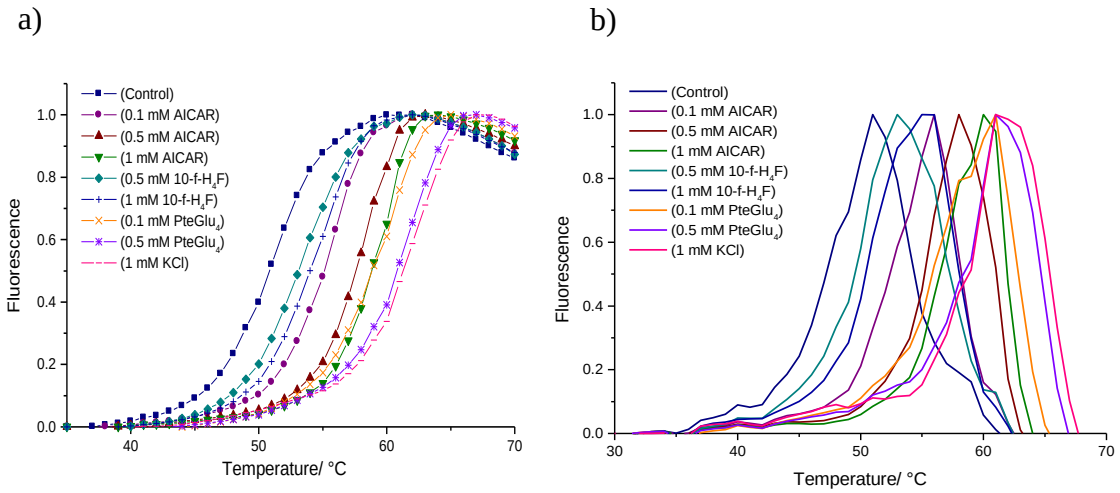

Figure 6-9: Normalised DSF data for N431A mutant. a) Normalised sigmoidal curves monitoring the change in fluorescence intensity with temperature with the incubation of various small molecules. b) Differential of the sigmoidal plot. The peak of each curve corresponds to the melting temperature of N431A; stabilisation in the presence of various small ligands can be seen by an increase in melting temperature.

Table 6-4: The change in melting temperature (ΔT/°C) caused by the single residue mutations in each of the potassium mutants. This was calculated as the difference between the T_m of human ATIC at 25 mM KCl (46 °C) and the T_m of each potassium mutant at 25 mM KCl, as determined by DSF (Table 6-5).

Enzyme	***S430A***	***N431A***	***N431D***	***S432A***	***D539A***	***D539N***	***F590A***	***F590I***
ΔT/°C to human ATIC	-1	+5	-1	0	-3	+4	-1	-2

Mutations S430A, N431D and S432A have no appreciable effect on the melting temperature of the apoprotein. Residue N431, which adopts a favourable position to hydrogen bond to the AICAR substrate in the human crystal structure, shows the largest stabilisation within this set of site-directed mutants when mutated to N431A, causing an increase in the melting temperature of 5 °C. This mutation will neutralise any potential H-bonding interactions between the side chain (aspargine to alanine) and AICAR. Neutralising these interactions has caused an appreciable increase in stability. This could be explained by the disruption of the hydrogen bonding to AICAR from the N431 side chain, which now allows for greater flexibility of the peptide chain which could position the backbone carbonyl of residue 431 to interact with the potassium ion more strongly. A more tightly held potassium ion would lead to a more stable dimeric structure and hence provide the increased T_m, as seen by DSF. Alternatively new Van der Waals interactions between the alanine side chain and surrounding amino acids could be providing a more favourable, more stable conformation. Mutating the aspargine residue to aspartate removes the ability of the side chain to function as a hydrogen bond donor. N431D shows a slight destabilisation of 1 °C when compared to the human apoprotein.

D539 interacts with the potassium ion through its negatively charged side chain. The D539A mutation neutralises the side chain, and as expected, a drop in stability (3 °C) is seen as the side chain can no longer hold the potassium ion in place. Unexpectedly, removing the negative charge by mutating to asparagine does not have the same destabilising effect. Mutating the side chain to incorporate both a hydrogen bond acceptor and hydrogen bond donor (D539N), results in an increase in the T_m. This is

most likely due to a rearrangement of the residues around the potassium binding site, potentially to rotate the D539N residue away from the potassium ion so that the backbone carbonyl interacts with the potassium ion, and/or so the aspargine side chain can form new favourable interactions with the surrounding residues. Whatever rearrangement occurs, the resulting structure is more stable than the wild-type human ATIC. Mutating F590 to remove the conjugated ring is expected to destroy the ability of ATIC to interact with the AICAR substrate through π-π stacking. Mutations F590A and F590I do not dramatically reduce the stability of the enzyme.

Table 6-5: T_m (°C) of site-directed mutants, apo (control) and in the presence of various ligands and cofactors at specified concentrations, as measured by DSF. All samples contained; 25 mM KCl and were heated from 25°C to 100°C at an increase of 1°C/s. T_m was calculated from the peak of the differential of fluorescence intensity.

Enzyme	***Control***	***0.1 mM AICAR***	***0.5 mM AICAR***	***1 mM AICAR***	***0.5 mM 10-f-H_4F***	***1 mM 10-f-H_4F***	***0.1 mM $PteGlu_4$***	***0.5 mM $PteGlu_4$***	***1 M K^+***
Human	46	50	53	55	46	47	55	55	55
S430A	45	45	45	46	45	45	48	48	56
N431A	51	56	58	60	53	55	61	61	61
N431D	45	45	45	45	45	46	56	56	51
S432A	46	47	47	51	47	47	51	53	51
D539A	43	44	45	46	44	45	51	53	48
D539N	50	50	50	51	51	51	53	53	56
F590A	45	45	45	44	45	45	48	50	50
F590I	44	45	45	45	45	45	51	56	48

Table 6-6: ΔT_m as compared to apoenzyme (control) calculated from Table 6-5.

Enzyme	***Control***	***0.1 mM AICAR***	***0.5 mM AICAR***	***1 mM AICAR***	***0.5 mM 10-f-H_4F***	***1 mM 10-f-H_4F***	***0.5 mM $PteGlu_4$***	***0.5 mM $PteGlu_4$***	***1 M K^+***
Human	0	4	7	9	0	1	9	9	9
S430A	0	0	0	1	0	0	3	3	11
N431A	0	5	7	9	2	4	10	10	10
N431D	0	0	0	0	0	1	11	11	6
S432A	0	1	1	5	1	1	5	7	5
D539A	0	1	2	3	1	2	8	10	5
D539N	0	0	0	1	1	1	3	3	6
F590A	0	0	0	-1	0	0	3	5	5
F590I	0	0	0	0	0	0	6	11	3

The site-directed mutants were also analysed by DSF under the same conditions as used for wild-type human ATIC, to assess what affect the mutations may have on the binding sites of AICAR, 10-f-H_4F, $PteGlu_4$ and K^+. The data obtained from DSF conducted on the site directed mutants is summarised in Tables 6-5, 6-6 and 6-7, and Figure 6-10. When comparing the DSF to that obtained for human ATIC, any mutation that causes a greater increase in ΔT_m than the ΔT_m seen for the wild-type can be considered to have caused an effect on the binding of the small molecule in question. The discussion below focuses on the broader changes seen within the melting temperatures of the mutants under the different experimental conditions, a change of 1 °C is not considered significant.

S430A and D539N show only a slight stabilisation resulting from AICAR addition. This behaviour differs dramatically to that seen in the wild-type protein, suggesting that these mutations have affected the AICAR active binding site. Compared to the wild-type protein, S432A and D539A show less overall stabilisation from AICAR, but they both still display some concentration dependence. No appreciable change in T_m is seen with 10-f-H_4F addition to S430A, S432A, D539A or D539N, suggesting that these mutations are not causing any changes to the residues surrounding the 10-f-H_4F binding site. A small increase in stability is seen with S430A and D539N upon the addition of $PteGlu_4$, but a greater increase is measured with S432A and D539A. S432A, D539 mutants all show a reasonable enhancement to the stability of around 5 °C in the presence of 1 M potassium, and S430A has a large ΔT_m of 11 °C. The stability gained from the potassium restores the melting temperature of S430A and D539N to that of the wild-type ATIC. This suggests that the destabilising effects of these mutations can be reversed by a high concentration of potassium.

Analysis of the N431 mutants shows the alanine mutation has a higher T_m compared to the aspartate mutation for all conditions tested. N431A shows an increase in stability with an increase in AICAR concentration, which is not mimicked with N431D. This suggests that whilst removing the hydrogen bonding capability of the N431 residue does not appear to affect AICAR binding, introducing a negative charge has abolished the stabilisation effects seen from the addition of AICAR. N431A has a greater increase in stability with 10-f-H_4F and displays a greater concentration dependence. This mutation has increased the effect 10-f-H_4F has on stability; potentially increasing the affinity of 10-f-H_4F for the ATIC protein. Both mutations of residue N431 have similar large increases in T_m with the addition of $PteGlu_{4,}$ larger than is seen for $PteGlu_4$ addition to the wild-type. N431A has a large ΔT_m of 10 °C upon addition of 1 M KCl which results in a T_m of 61 °C, which is the largest T_m observed for any of the proteins under any of the conditions assessed by DSF. Mutating N431 to alanine increases the stability of ATIC under all conditions investigated. This mutation causes a similar ΔT_m resulting from the addition of potassium as the wild-type ATIC, suggesting that removing the charge and reducing the steric bulk of residue 431 has not adversely affected the binding of the small molecules to the enzyme, but actually increases the apparent stability of the protein.

Site-directed mutants of F590 do not show any real increase in stabilisation in the presence of AICAR. This is as expected, given that the F590 phenyl ring is positioned to interact with AICAR through a favourable π-π stacking arrangement. At a concentration of 1 mM AICAR the F590I mutant is destabilised slightly by 1 °C, which could be due to the increased steric bulk of F590I side chain when compared to F590A, which does not show any destabilisation at this concentration. 10-f-H_4F has no effect on the melting temperature of either mutant, but with $PteGlu_4$ F590I is stabilised to a

greater extent than F590A, both mutants show an increase in T_m with increasing $PteGlu_4$ concentration. Increased potassium causes some stabilisation of the F590 mutants.

To summarise, S430A, N431D, D539N and both F590 mutants lose the ability for AICAR to increase the stability of the protein. S430A and D539N seem to have a knock-on effect, from their location at the potassium binding site, through to the AICAR binding pocket. The F590 mutants were hypothesised to reduce the protein's ability to bind AICAR as the mutations will disrupt the favourable quadrupole/quadrupole interactions from the T-shaped π-π stacking formation between the phenylalanine ring and the imidazole ring of the AICAR substrate. This hypothesis is supported by the lack of ΔT_m resulting from AICAR addition. S432A and D539A lead to a reduction in the degree of stabilisation provided by the addition of AICAR.

Table 6-7: Summary of the magnitude of effects different small molecule had on each enzyme, looking at the increase in stabilisation in the presence of the small molecule, not the final T_m. The results have been scaled compared to the responses of the other mutants. The +++ represents the highest stability increases from the ligand seen from the data set of all the mutants. ++ indicates a mid-range increase compared to the whole data set, + represents a small stabilisation, - signifies no increase in T_m across any of the concentration ranges used for the ligand.

Enzyme	*AICAR*	*10-f-H_4F*	*$PteGlu_4$*	*K^+*
Human	+++	+	+++	+++
S430A	+	-	+	+++
N431A	+++	+++	+++	+++
N431D	-	+	+++	++
S432A	++	+	++	++
D539A	++	++	+++	++
D539N	+	+	+	++
F590A	-	-	++	++
F590I	-	-	+++	+

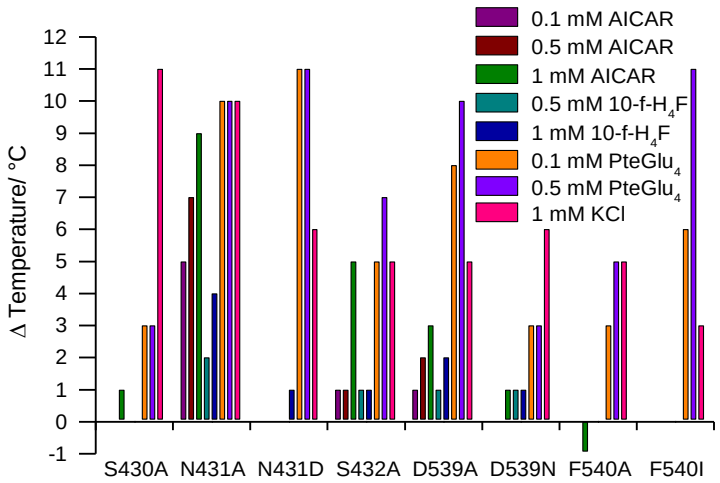

Figure 6-10: A graphical representation of the effects various small molecules had on the T_m of each of the potassium mutants of human ATIC, as measured by DSF.

6.3.1.3 Small molecule binding

Isothermal titration calorimetry was used to investigate the binding of AICAR and 10-f-H_4F to the site-directed mutants of human ATIC. These experiments were conducted to give an insight into if, and how, the mutations targeted at altering the potassium binding site (and potential interaction with AICAR) have affected the physical binding properties of the ligand and cofactor. The results of the binding of AICAR and 10-f-H_4F to human ATIC are analysed in Chapter 3, with an observed K_d for AICAR of 6.14 ± 1.37 μM and a K_d for 10-f-H_4F of 120 ± 11.48 μM The majority of the mutants show a reduced number of binding sites for AICAR, the results are shown in Table 6-8.

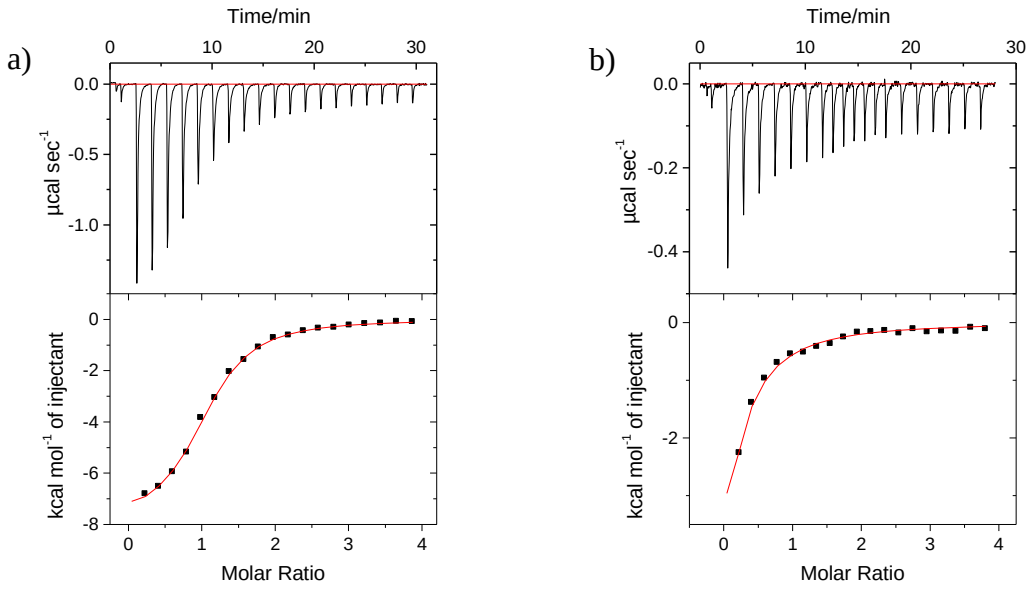

Figure 6-11: the final figure analysis of the ITC experiment titrating AICAR (1.1mM) into a) N431A (59μM) and b) S430A (60 μM) at 25 °C.

Table 6-8:Binding affinities of ligands and small molecules to site directed mutants of human ATIC determined by ITC. Measurements were taken using a MicroCal ITC_{200} at a constant temperature of 25 °C. Ligand:enzyme concentrations were adjusted as required to achieve saturation. Data were fitted using MicroCal Origin® software to calculate number of binding sites, dissociation constant and enthalpy of binding. [a]N431D was used at 41 μM and 63 μM for the AICAR and 10-f-H_4F experiments respectively.

Mutant	*Initial enzyme conc/ μM*	*AICAR*				*10-f-H_4F*			
		Ligand conc/ mM	*Number of sites*	*K_d/ μM*	*ΔH/ kcal mol^{-1}*	*Ligand conc/ mM*	*Number of sites*	*K_d/ μM*	*ΔH/ kcal mol^{-1}*
S430A	60	1.1	nd	37.71 ± 7.48	-52.10 ± 164.20	2	nd	nd	nd
N431A	59	1.1	1.04 ± 0.01	6.99 ± 0.45	-7.94 ± 0.12				
N431D	41/63[a]	0.5	0.20 ± 0.04	10.23 ± 1.51	-36.10 ± 7.64	2	1.35 ± 0.06	55.56 ± 4.27	-1.46 ± 0.08
S432A	47	0.75	0.26 ± 0.01	8.62 ± 0.46	-15.90 ± 0.84	2	nm	50.76 ± 6.05	-2.91 ± 0.14
D539A	37	0.75	0.69 ± 0.03	10.91 ± 1.04	-5.20 ± 0.87	2	0.71 ± 0.25	75.76 ± 9.79	-6.73 ± 2.53
D539N	45	1.0	0.11 ± 0.12	32.49 ± 5.69	-12.95 ± 14.62				
F590A	55	1.0	0.36 ± 0.11	47.24 ± 7.33	-8.25 ± 2.24				
F590I	52	1.0	0.29 ± 0.12	50.99 ± 5.75	-11.60 ± 5.34	2	0.74 ± 0.08	74.63 ± 4.39	-5.26 ± 0.61

The binding affinities for the ligand and cofactor to the S430A mutant are dramatically reduced compared to those measured for human ATIC. S430A binds AICAR very weakly with a K_d of 37.70 ± 7.48 μM and less than 5% of the binding sites occupied. The number of binding sites of AICAR to S430A is so small, and with such a comparably large error that no real binding is observed. No binding of 10-f-H_4F to S430A was detected suggesting the mutation has also removed the ability of the enzyme to bind the cofactor. N431A binds AICAR with the same affinity as human ATIC and a stoichiometry of 1, suggesting that AICAR binding to human ATIC has not been affected by the mutation. N431D has a slightly weaker binding constant for AICAR than human ATIC and the occupancy of the binding site is considerably reduced. However, due to the unusual enthalpy of binding measured, this data is considered unreliable. Unexpectedly, the N431D mutation has caused 10-f-H_4F to bind with a higher affinity than to human ATIC. As seen with the N431D mutant, S432A binds AICAR with a low number of binding sites and with a similar but slightly lower K_d when compared to human ATIC. S432A binds 10-f-H_4F with a K_d of 50.76 ± 6.05 μM, but the fit was such that the binding stoichiometry could not be determined. D539A binds AICAR with a K_d of 10.91 ± 1.04 μM, with 0.69 ± 0.03 binding sites, and binds 10-f-H_4F twice as strongly as human ATIC. D539N has a similar K_d as S430A which is 32.49 ± 5.69μM, and only has around 10% occupancy of the binding site. Both F590 mutants bind AICAR very weakly, with the lowest affinity measured of the site-directed mutants. AICAR binds to F590A and F590I with a K_d of 47.24 ± 7.33 μM and 50.99 ± 5.75 μM respectively. This is the weakest dissociation constant for AICAR seen amongst all of the site directed mutants. This would be as expected, if we are measuring AICAR binding to the AICAR transformylase site. Destroying the π-π

interaction between F590 and the substrate would significantly reduce the ability of the enzymes to bind AICAR.

6.4 AICAR KM of site-directed mutants

The apparent K_M for AICAR was determined for site directed mutants S430A, S432A, F590A and F590I (Table 6-9) at 25 °C and a fixed 10-f-H_4F concentration of 167 μM.

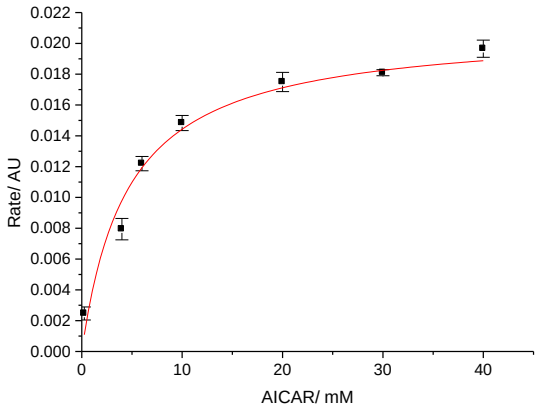

Figure 6-12: Effects of AICAR concentration of the activity of S430A. K_M was determined to be 4.58 ± 0.91 μM.

Table 6-9: AICAR K_M determined for selected site directed mutants.

Enzyme	***AICAR K_M/μM***
S430A	4.58 ± 0.91
S432A	3.81 ± 1.27
F590A	3.78 ± 2.30
F590I	60 ± 16

S430A, S432A and F590A all have a similar AICAR K_M to the human wild-type enzyme, but F590I has an increased K_M. The F590 residue is expected to help bind AICAR through π-π stacking. This suggests that the F590 residue is important for binding AICAR, but potentially in the F590A mutant something may bind in place of the missing phenylalanine, for example imidazole, to rescue activity. With the F590I

mutation, the steric bulk of the isoleucine side chain blocks the site, so the activity cannot be recovered by whatever rescues the F590A activity.

Mutants N431A, N431D and D539N all had a very low activity, which made kinetic analysis difficult. D539A displayed no AICAR transformylase activity. It should be noted that the site directed mutants lost activity upon storage (4 °C), so care was taken to conduct the kinetic analysis as soon as possible after the size exclusion purification of each of the mutants. Residues N431 and D539 are essential for ATIC activity and, due their orientations in the protein crystal structure, it seems possible that D539 is essential for potassium binding and N431 is essential for AICAR binding.

6.5 Discussion

Potassium is essential for maximal activity of human ATIC, with the K_a determined to be 796 ± 48 μM. This reliance on potassium cannot be reproduced with other monovalent metal cations, or even magnesium or calcium. Not even partial activity can be recovered by supplementing with other metal ions.

Potassium increases the thermal stability of ATIC. DSF studies have shown a large increase in the melting temperature in the presence of 1 M KCl. An increase in stability is also seen when conducting experiments at 25 mM KCl compared to 5 mM KCl. The stability observed is in the large unfolding peak, attributed to the unfolding of the dimer which would expose a huge hydrophobic surface. The addition of potassium appears to enhance the stability of the dimer.

Residues suitable for site directed mutations in the proximity of the potassium ion binding site were identified from the crystal structure of human ATIC. Mutants were created of the residues that have potential side chain interactions with the ion, generating S430A, S432A, D539A and D539N. N431A and N431D were chosen as residue 431 sits between the previously chosen serine residues, and has potential

hydrogen bonding interactions with the AICAR substrate. F590 also interacts with AICAR through a T-shaped π-π stacking arrangement between the phenylalanine ring of F590 and the imidazole ring of AICAR, hence, mutants F590A and F590I were analysed to investigate the effects of disrupting this interaction.

Each mutant was analysed in terms of thermal stability, evaluating the melting temperature by DSF under different conditions and concentrations of small molecules, and the physical binding properties, measured by ITC. Unfortunately, because of the confusion into the location of where the small molecules are binding, interpretation of the mutations in terms of alteration to AICAR binding and comparison to the parameters measured in Chapter 3 is difficult.

Both S430A and D539N show similar weak binding to AICAR with a very low number of binding sites observed, in fact, S430A has such low occupancy it essentially does not bind AICAR. This is consistent with the thermal stability data gained from DSF, as S430A and D539N show no significant increase in T_m in the presence of AICAR. Each of these mutations of the potassium binding site has decreased the enzymes' ability to bind AICAR.

The S432A and D539A mutations have slightly weaker binding constants for AICAR, as compared to human ATIC. The stability of these mutations is increased by the addition of AICAR, but the amount of stabilisation inferred is less than the stabilisation seen with human ATIC. S432A and D539A have slightly reduced the protein's affinity for AICAR. Mutations within the potassium binding site are having an effect on the proteins ability to bind substrate. This suggests the potassium ion may play a structural role, supporting the amino acid structure which is presented to the AICAR substrate, and possibly supporting the dimerisation of ATIC. A high concentration of KCl causes a huge increase in thermal stability in human ATIC, increasing the temperature at which the dimer appears to dissociate. This could be interpreted as the presence of potassium

stabilising the ATIC dimer. As AICAR binds through interactions formed from residues located on both monomer chains, the strongest binding must require dimerisation. If potassium plays a key role in the dimerisation of ATIC, this would explain the reduction in AICAR binding seen when the potassium binding site is altered.

ITC and DSF results for the pair of F590 mutants supports the proposal that F590 is important in the binding of AICAR through a T-shaped π-π interaction. Mutation to alanine and isoleucine significantly reduce AICAR binding, this pair of mutants have the weakest AICAR binding out of all the mutants investigated. AICAR also provides no increase to the thermal stability of the mutants; suggesting the dimeric structure is no longer stabilised by AICAR. The AICAR K_M for F590I is increased, whilst F590A has a similar K_M to human ATIC. It is thought that F590I cannot bind AICAR with the bulky isoleucine blocking the site, with the alanine mutation activity appears to be rescued, potentially due to imidazole remaining bound from the metal affinity purification, binding in place of the phenylalanine ring.

Unexpectedly, the N431A mutation actually produces a more stable protein, perhaps due to the reduction in side chain bulk, that allows the monomer chains to combine more tightly and effectively, increasing the T_m of the dimer. The binding parameters measured for AICAR to N431D were discounted due to the uncharacteristic enthalpy of binding. The increased stability of the N431A mutant could be exploited in crystallisation trials.

Excluding N431D, the trends and consistency seen between ITC and DSF results for the effects of the mutations on AICAR binding can be summarised as shown in Table 6-10. A K_d of greater than 30 μM corresponds to little, or no stabilisation to the melting temperature of the protein, as seen for S430A, D539N, F590A and F590I. For D539A, an AICAR K_d of 11 μM is accompanied by an increase in stability of 3 °C, and for

S432A a K_d of 8.5 μM corresponds to a ΔT_m of 5 °C. N431A and human ATIC have an AICAR K_d of 6-7 μM, and both show an increase in melting temperature of 9 °C. N431D is the only mutant investigated that is an exception, which following the trends seen with the other mutants, would be expected to have a ΔT_m of 3 °C measured by DSF to correspond to the K_d observed. As the strength of AICAR binding increases, so the amount of stability afforded to the enzyme by AICAR increases.

Table 6-10: Comparison of AICAR K_d determined by ITC and the corresponding ΔT_m obtained from DSF at 1 mM AICAR for human ATIC and the site directed mutants (excluding N431D). The greater the strength of binding for AICAR the greater the increase in the T_m, and hence stability provided by 1 mM AICAR.

K_d/ μM	ΔT_m/ °C
>30	≤1
~11	3
8.5	5
6-7	9

Kinetic studies suggest that N431 and D539 are essential for ATIC catalytic activity. However, N431A binds AICAR with a similar binding constant to the wild type protein. This suggests that AICAR may be binding to N431A in a different position, and has the same affinity as the wild type, but AICAR is now not correctly orientated for catalysis. It seems likely that D539 is essential in binding the potassium ion. This would suggest that potassium is important in maintaining the structure of the active site.

7 Summary and conclusions

7.1 Summary

ATIC is a dimeric bifunctional protein, with two distinct catalytic domains located on each monomer, which catalyses the penultimate and final steps of the *de novo* purine biosynthetic pathway. It has been extensively studied as a target for chemotherapeutics and anti-viral inhibitors, but the enzyme has not been fully characterised.

The AICAR transformylase domain catalyses the formyl group transfer from the 10-f-H_4F cofactor to the AICAR substrate to produce FAICAR and H_4F. The catalytic turnover can be measured by the rate of increasing absorption at 298 nm. A two dimensional, high-throughput assay was designed; this was used to measure the true substrate and cofactor K_M as 14.1 ± 4.5 μM and 41.6 ± 11.9 μM respectively. The data were fitted using an ordered binding model, assuming rapid equilibrium, which suggests that ATIC proceeds by an ordered binding mechanism, in which AICAR binds to the enzyme before the 10-f-H_4F cofactor can bind. This mechanism is supported by substrate and cofactor binding affinities, as measured by ITC.

$$E + AICAR \overset{K_1}{\leftrightarrow} [E - AICAR] + 10\text{fH}_4\text{F} \overset{K_2}{\leftrightarrow} [E - AICAR - 10\text{fH}_4\text{F}] \overset{k_{cat}}{\longrightarrow} P$$

The binding affinities of the substrate, cofactor and various small molecules have been investigated by ITC for human ATIC, avian ATIC, and the IMPCH domain. The IMPCH domain was isolated through the overexpression of a truncation mutant consisting of resides 1-200 of the full length human ATIC, to aid in identifying the binding location of the small molecules analysed.

$PteGlu_4$ was the tightest binding of the ligands analysed, and was significantly tighter than the *in vitro* cofactor, 10-f-H_4F. This suggests that the extra polyglutamated tail of the natural substrate is a major driving force in binding to ATIC. Due to the lack of

binding seen to the IMPCH truncation mutant, $PteGlu_4$ was confirmed to bind to the AICAR transformylase half of the protein, and provides evidence that it binds to the same site as 10-f- H_4F. XMP is observed to bind to both domains, with the tightest K_d of the substrate analogues investigated. This suggests that XMP may have been co-purified and be blocking binding to some of the sites; XMP may inhibit ATIC *in vivo* and provide a previously undiscovered regulation step. The binding parameters measured for AICAR titrated into IMPCH are consistent with those obtained for the full length human ATIC, suggesting the measured AICAR binding to human ATIC may have been caused by AICAR binding to the IMPCH domain, not to the AICAR transformylase domain as would be expected.

The thermal stability of ATIC was studied by DSC and DSF. The unfolding profile as measured by DSF shows a large hydrophobic unfolding transition, followed by a smaller unfolding at a slightly higher temperature. DSC measured an enthalpic unfolding event at a temperature that corresponds to the temperature of the smaller transition seen with DSF. The large unfolding peak was attributed to the entropically driven separation of the dimer, which would expose the large 5000 $Å^2$ hydrophobic interface. The lack of signal seen in the ITC dilution experiments supports the hypothesis that the dimerisation is an entropically-driven event. The second unfolding transition seen with DSF and DSC is thought to be due to the unfolding of the IMPCH domain, or the ATIC monomer. DSF was also used to show the stabilisation gained by human and avian ATIC in the presence of AICAR and $PteGlu_4$.

Size exclusion chromatography shows ATIC purifies as a dimer in solution, which was also confirmed by AUC. As the dimerisation constant could not be measured by ITC, due to the lack of an enthalpic signal as dimerisation is an entropic process, alternative fluorescence techniques were investigated. Human and avian ATIC were labelled with fluorescein- and rhodamine-containing peptides using a newly designed vector to enable

the *N*-terminal labelling of proteins through the reaction of the terminal glycine residue with depsipeptides catalysed by sortase. Unfortunately, neither FRET experiments nor fluorescence correlation spectroscopy could measure the monomer-dimer equilibrium of human or avian ATIC.

Potassium is essential for maximal ATIC activity. The metal dependence exhibited by human ATIC is unique for potassium; the presence of other monovalent cations does not rescue activity. The potassium dependence was defined as K_a = 796 ± 48μM. KCl was shown to increase the stability of human and avian ATIC when measured by DSF. Site directed mutants of residues in the proximity of the potassium ion binding site were characterised by DSF and ITC, and analysed for small molecule binding and increases to stability. Tighter binding corresponded to a greater increase in thermal stability in the presence of the small molecule.

Both S430A and D539N mutants both showed weak binding to AICAR with a very low number of binding sites observed. The S432A and D539A mutations have slightly weaker binding constants for AICAR, as compared to human ATIC. These results suggest potassium may play a key role in the stabilisation of AICAR, as mutations of the potassium binding site have impacted on AICAR binding. As AICAR binds through interactions formed from residues located on both monomer chains, the strongest binding must require dimerisation. If potassium stabilises the dimerisation of ATIC, this would explain the reduction in AICAR binding seen when the potassium binding site is altered.

ITC and DSF results for the pair of F590 mutants supports the proposal that F590 is important in the binding of AICAR through a T-shaped π-π interaction between the phenylalanine and imidazole of AICAR.

Unexpectedly, the N431A mutation produced a more a more stable protein as measured by DSF, perhaps due to the reduction in side chain bulk that allows the monomer chains to combine more tightly and effectively, increasing the T_m of the dimer.

However, as there is some uncertainty that the AICAR binding is measured in the AICAR transformylase site, the conclusions drawn from the small molecule experiments require conformation of the AICAR binding location, before there can be full confidence in the hypothesis for the effects of the site directed mutations.

Kinetic studies suggest that N431 and D539 are essential for ATIC catalytic activity. However, N431A binds AICAR with a similar binding constant to the wild type protein. This suggests that AICAR may be binding to N431A in a different position, and has the same affinity as the wild type, but AICAR is now not correctly orientated for catalysis. It seems likely that D539 is essential in binding the potassium ion. This would suggest that potassium is important in maintaining the structure of the active site.

7.2 Future work

It is not expected that the polyglutamate tail of the $PteGlu_4$ *in vivo* cofactor would interfere with AICAR binding. However, it would be interesting to repeat the two dimensional binding order assay with AICAR and $PteGlu_4$. This would measure the true cofactor K_M, and investigate if catalysis proceeds through the same binding model observed for AICAR and 10-f-H_4F.

The cloning of the AICAR tfase truncation mutant containing residues G360 to H592 should be completed. If overexpression of this construct is successful then AICAR tfase should be subjected to investigation by DSC, DSF and determination of small molecule binding constants by ITC. Characterisation of the two separate domains should give

more information with which to elucidate the trends seen in the full length human ATIC.

Endogenous small molecules of the *de novo* purine biosynthesis pathway could potentially be pulled through during ATIC purification. To analyse the likelihood and quantities of such molecules co-purifying, two experiments could be undertaken. A large concentration of *E. coli* containing overexpressed ATIC could be lysed, and then passed through a low molecular weight cut-off filter. The filtrate could then be analysed by HPLC against standards for AMP, XMP, IMP and AICAR. Subsequently, the same experiment could be repeated for *E. coli* cells which are an ATIC auxotroph.

To determine if the IMPCH truncation mutant dissociates from monomer to dimer with time, a sample of purified mutant should be subjected to size exclusion chromatography at regular time intervals (for example, every two hours). A change in oligomeric state would be indicated be a shift in the elution peak observed at 280 nm absorbance.

To fully evaluate the ITC data measured for small molecule binding to ATIC, the IMPCH knock-out mutations (Y104F/D125A and/or Y104W/D125A) need to be incorporated into full length ATIC. The (–)IMPCH full length ATIC will be analysed by DSF and ITC under the same conditions used for human ATIC, to unequivocally determine the binding affinities to the AICAR transformylase domain. The (–)IMPCH could be incorporated into the IMPCH truncation mutant to provide a negative control. The AICAR transformylase mutant (from Gly360 to His592) cloning will be completed. Hopefully, without the inclusion of the β-sheet, the transformylase domain will now overexpress in *E. coli* cells. If successful, the AICAR transformylase truncation will be analysed by ITC and DSF to complete the set of domain binding experiments.

It would be desirable to obtain crystal structures of the site-directed mutants to observe any structural rearrangements caused by the mutations. Double and/or triple mutations

of S430, S432 and D539 could be designed to completely remove the ability for ATIC to bind the potassium ion. These mutations could then be analysed by size exclusion and DSF to analyse if changes to the size and unfolding profile of the enzyme can be detected, determining whether potassium maintains the *C*-terminal structure.

Work conducted by J Murray (unpublished) has suggested the residue His592 is responsible for the lack of pH dependence displayed by ATIC, by acting as a buffer to the AICAR transformylase active site, as the H592F mutant displays a pH dependence. This residue is important for enzyme stability, mutant H592F must be stored in imidazole-containing buffers to maintain some catalytic activity. It is thought imidazole is able to bind in place of the histidine residue to stabilise the protein. Potassium could also be responsible for positioning this key H592 residue. This hypothesis can be investigated by studying the pH dependence of the potassium binding site directed mutants.

The site-directed mutant N431A had an increased thermal stability when compared to wild-type human ATIC. This increased stability could be exploited by using this mutant in further crystallography trials, potentially producing better quality crystals than were achieved for the wild-type ATIC.

The new vector construct developed to incorporate a TEV recognition site after an *N*-terminal his tag, could be applied to a wide range of systems. For example, homo- or heterodimeric proteins for which the dimerisation constant may be observed using the same techniques applied to ATIC (FRET and fluorescence correlation spectroscopy), monitoring protein cleavage reactions, or the visualisation of cell penetrating proteins.

7.3 Conclusions

The thesis has determined the ordered binding mechanism for AICAR transformylase using a new two-dimensional high-throughput assay. AICAR (K_M 14.1 ± 4.5 μM) binds the ATIC first, followed by 10-f-H_4F (41.6 ± 11.9 μM). The binding affinities for various ligands and small molecules have been determined by ITC, but further work is required to conclusively determine the location of the small molecule binding. Initial observations suggest XMP may act as an inhibitor of ATIC, potentially regulating the enzyme *in vivo*. Isolation and characterisation of the IMPCH domain was achieved to analyse binding to a single active site and deconvolute the binding parameters observed for both ATIC domains. Residue N431 is thought to be essential in orientating AICAR for AICAR transformylase catalysis.

The potassium dependence has been defined for the first time as K_a = 796 ± 48μM. The maximum catalytic activity achieved with potassium cannot be replicated with any other metal monocation. The presence of potassium enhances the thermal stability of ATIC. Residue D539 is thought to be essential in binding potassium, which may help structure the AICAR transformylase active site.

The unfolding profile of ATIC proceeds initially through the separation of the dimer, and then the IMPCH domain or monomer unfolds at a higher temperature.

The dimerisation of ATIC cannot be determined by ITC dilution experiments or fluorescent techniques. Evidence has been provided that shows the dimerisation of ATIC is an entropically driven process.

8 Bibliography

[1] J. L. Smith, *Current Opinion in Structural Biology* **1995**, *5*, 752-757.

[2] F. W. S. Barnes Jr., R., *Journal of Biological Chemistry* **1943**, *151*, 123.

[3] Y. Zhang, M. Morar, S. E. Ealick, *Cellular and Molecular Life Sciences* **2008**, *65*, 3699-3724.

[4] L. J. Messenger, H. Zalkin, *Journal of Biological Chemistry* **1979**, *254*, 3382-3392.

[5] P. B. Rowe, E. McCairns, D. Sauer, D. Fahey, *Advances in experimental medicine and biology* **1984**, *165 Pt A*, 421-426.

[6] J. M. H. Buchanan, S. C. , *Advances in Enzymology and Related Areas of Molecular Biology* **1959**, *21*.

[7] G. T. Shaw, S. E. , *Journal of Neurochemistry* **1976**, *27*.

[8] S. C. B. Hartman, J. M. 1959, 234, 1812., *The Journal of Biological Chemistry* **1959**, *234*, 1812.

[9] D. P. Nierlich, Magasani.B, *Biochimica Et Biophysica Acta* **1971**, *230*, 349-&.

[10] E. J. Mueller, E. Meyer, J. Rudolph, V. J. Davisson, J. Stubbe, *Biochemistry* **1994**, *33*, 2269-2278.

[11] J. G. L. Flaks, L. N. , *Methods in Enzymology* **1963**.

[12] aS. C. Daubner, J. L. Schrimsher, F. J. Schendel, M. Young, S. Henikoff, D. Patterson, J. Stubbe, S. J. Benkovic, *Biochemistry* **1985**, *24*, 7059-7062; bJ. L. Schrimsher, F. J. Schendel, J. Stubbe, *Biochemistry* **1986**, *25*, 4356-4365; cD. Schild, A. J. Brake, M. C. Kiefer, D. Young, P. J. Barr, *Proceedings of the National Academy of Sciences of the United States of America* **1990**, *87*, 2916-2920; dJ. Aimi, H. Qiu, J. Williams, H. Zalkin, J. E. Dixon, *Nucleic Acids Research* **1990**, *18*, 6665-6672.

[13] L. Y. Ni, K. L. Guan, H. Zalkin, J. E. Dixon, *Gene* **1991**, *106*, 197-205.

[14] J. Allsop, R. W. E. Watts, *Enzyme* **1983**, *30*, 172-180.

[15] P. G. Marko, E.; Zimmer, H. G.; Pechan, I.; Cremer, T. & Trendelenburg, C. , *Hoppe-Seyler's Zeitschrift für Physiologische Chemie* **1969**, *350*.

[16] S. Brosh, P. Boer, E. Zorefshani, O. Sperling, *Biochimica Et Biophysica Acta* **1982**, *714*, 181-183.

[17] E. McCairns, D. Fahey, D. Sauer, P. B. Rowe, *Journal of Biological Chemistry* **1983**, *258*, 1851-1856.

[18] R. Deacon, I. Chanarin, M. Lumb, J. Perry, *Journal of Clinical Pathology* **1985**, *38*, 1349-1352.

[19] J. Dominguez, L. A. Ordonez, *Journal of Neurochemistry* **1982**, *38*, 625-630.

[20] M. G. Gassmann, A. Stanzel, S. Werner, *Oncogene* **1999**, *18*, 6667-6676.

[21] K. Emmett, J. Patrick, B. Aronow, B. Ullman, *Journal of Cellular Physiology* **1985**, *125*, 277-287.

[22] A. M. D. Mackinnon, D. J. , *Biochimica et Biophysica Acta* **1973**, *319*.

[23] aC. A. Atkins, P. M. C. Smith, P. J. Storer, *Plant Physiology* **1997**, *113*, 127-135; bM. J. Boland, K. R. Schubert, *Archives of Biochemistry and Biophysics* **1983**, *220*, 179-187; cC. A. R. Atkins, A.; Rowe, P. B.; McCairns, E. & Sauer, D. , *Plant Physiology* **1982**, *70*; dK. A. Chapman, A. J. Delauney, J. H. Kim, D. P. S. Verma, *Plant Molecular Biology* **1994**, *24*, 389-395.

[24] A. M. Brown, S. L. Hoopes, R. H. White, C. A. Sarisky, *Biology Direct* **2011**, *6*.

[25] K. Ownby, H. M. Xu, R. H. White, *Journal of Biological Chemistry* **2005**, *280*, 10881-10887.

[26] M. Graupner, H. M. Xu, R. H. White, *Journal of Bacteriology* **2002**, *184*, 1471-1473.

[27] Y.-N. Kang, A. Tran, R. H. White, S. E. Ealick, *Biochemistry* **2007**, *46*, 5050-5062.

[28] M. H. el Kouni, *Pharmacology & Therapeutics* **2003**, *99*, 283-309.

[29] C. J. S. Walsh, I. W. 1968, 15, 763., *Journal of Protozoology* **1968**, *15*.

[30] J. K. Perrotto, D. B. & Gelderman, A. H., *Journal of Protozoology* **1971**, *18*.

[31] E. A. Rayl, B. A. Moroson, G. P. Beardsley, *Journal of Biological Chemistry* **1996**, *271*, 2225-2233.

[32] T. Sugita, H. Aya, M. Ueno, T. Ishizuka, K. Kawashima, *Journal of Biochemistry* **1997**, *122*, 309-313.

[33] J. M. Vergis, K. G. Bulock, K. G. Fleming, G. P. Beardsley, *Journal of Biological Chemistry* **2001**, *276*, 7727-7733.

[34] J. E. Baggott, C. L. Krumdieck, *Biochemistry* **1979**, *18*, 1036-1041.

[35] J. E. Baggott, T. Tamura, *Experimental Biology and Medicine* **2010**, *235*, 271-277.

[36] J. E. Baggott, G. L. Johanning, K. E. Branham, C. W. Prince, S. L. Morgan, I. Eto, W. H. Vaughn, *Biochemical Journal* **1995**, *308*, 1031-1036.

[37] J. E. Baggott, W. H. Vaughn, B. B. Hudson, *Biochemical Journal* **1986**, *236*, 193-200.

[38] aJ. E. Baggott, S. L. Morgan, W. M. Sams, J. Linden, *Archives of Dermatology* **1999**, *135*, 813-817; bJ. E. Baggott, T. Tamura, *Biomedicine & Pharmacotherapy* **2001**, *55*, 454-457.

[39] J. E. Baggott, C. B. Robinson, I. Eto, G. L. Johanning, P. E. Cornwell, *Journal of Inorganic Biochemistry* **1998**, *71*, 181-187.

[40] P. S. Brookes, J. E. Baggott, *Biochemistry* **2002**, *41*, 5633-5636.

[41] M. S. Warren, K. M. Mattia, A. E. Marolewski, S. J. Bankovic, *Pure and Applied Chemistry* **1996**, *68*, 2029-2036.

[42] J. E. Baggott, S. L. Morgan, *European Journal of Pharmaceutical Sciences* **2007**, *31*, 95-101.

[43] S. L. Black, M. J. Black, J. H. Mangum, *Analytical Biochemistry* **1978**, *90*, 397-401.

[44] E. Szabados, R. I. Christopherson, *Analytical Biochemistry* **1994**, *221*, 401-404.

[45] D. W. Wolan, C. G. Cheong, S. E. Greasley, I. A. Wilson, *Biochemistry* **2004**, *43*, 1171-1183.

[46] S. E. Greasley, P. Horton, J. Ramcharan, G. P. Beardsley, S. J. Benkovic, I. A. Wilson, *Nature Structural Biology* **2001**, *8*, 402-406.

[47] D. W. Wolan, S. E. Greasley, G. P. Beardsley, I. A. Wilson, *Biochemistry* **2002**, *41*, 15505-15513.

[48] D. W. Wolan, S. E. Greasley, M. J. Wall, S. J. Benkovic, I. A. Wilson, *Biochemistry* **2003**, *42*, 10904-10914.

[49] M. Wall, J. H. Shim, S. J. Benkovic, *Journal of Medicinal Chemistry* **1999**, *42*, 3421-3424.

[50] M. Wall, J. H. Shim, S. J. Benkovic, *Biochemistry* **2000**, *39*, 11303-11311.

[51] K. G. Bulock, G. P. Beardsley, K. S. Anderson, *Journal of Biological Chemistry* **2002**, *277*, 22168-22174.

[52] aE. Szabados, R. I. Christopherson, *International Journal of Biochemistry & Cell Biology* **1998**, *30*, 933-942; bE. Szabados, P. K. Wilson, R. I. Christopherson, in *Purine and Pyrimidine Metabolism in Man Ix, Vol. 431* (Ed.: A. C. P. M. M. M. Griesmacher), **1998**, pp. 241-244.

[53] J. H. Shim, M. Wall, S. J. Benkovic, N. Diaz, D. Suarez, K. M. Merz, *Journal of the American Chemical Society* **2001**, *123*, 4687-4696.

[54] L. Xu, Y. Chong, I. Hwang, A. D'Onofrio, K. Amore, G. P. Beardsley, C. Li, A. J. Olson, D. L. Boger, I. A. Wilson, *Journal of Biological Chemistry* **2007**, *282*, 13033-13046.

[55] J. M. Vergis, G. P. Beardsley, *Biochemistry* **2004**, *43*, 1184-1192.

[56] T. D. H. Bugg, *Introduction to Enzyme and Coenzyme Chemistry* **2004**, *2 ed*.

[57] J. G. E. Flaks, M. J. & Buchanan, J. M. , *Journal of Biological Chemistry* **1957**, *229*.

[58] R. F. Kinsinger, D. B. Kearns, M. Hale, R. Fall, *Journal of Bacteriology* **2005**, *187*, 8462-8469.

[59] C. D. Green, D. W. Martin, *Proceedings of the National Academy of Sciences of the United States of America* **1973**, *70*, 3698-3702.

[60] T. Iizasa, T. Miyamoto, *Biochemical Medicine and Metabolic Biology* **1987**, *38*, 292-299.

[61] T. Page, M. Coleman, *Biochimica Et Biophysica Acta-Molecular Basis of Disease* **2000**, *1500*, 291-296.

[62] D. V. B. Godin, M. A. & MacLeod, P. J. , *Research Communications in Chemical Pathology and Pharmacology* **1978**, *20*.

[63] aW. H. S. S. Thomson, I. , *Metabolism* **1978**, *27*; bF. Camina, M. I. NovoRodriguez, S. RodriguezSegade, M. CastroGago, *Clinica Chimica Acta* **1995**, *243*, 151-164.

[64] aS. Marie, B. Heron, P. Bitoun, T. Timmerman, G. Van den Berghe, M. F. Vincent, *American Journal of Human Genetics* **2004**, *74*, 1276-1281; bP. Hornik, P. Vyskocilova, D. Friedecky, T. Adam, *Journal of Chromatography B-Analytical Technologies in the Biomedical and Life Sciences* **2006**, *843*, 15-19.

[65] M. F. B. Vincent, F. & Van den Berghe, G., *Biochemical Journal* **1992**, *281*.

[66] N. V. Henin, M. F.; Gruber, H. E. & Van den Berghe, G. , *Faseb Journal* **1995**, *9*.

[67] B. F. K.-K. Holmes, E. J. & Winder, W. W. , *Journal of Applied Physiology* **1999**, *87*.

[68] aR. M. Pesi, V.; Jacomelli, G.; Peruzzi, L.; Camici, M.; Garcia-Gil, M.; Allegrini, S. & Tozzi, M. G. , *Neuroreport 11* **2000**; bM. P. Garcia-Gil, R.; Perna, S.; Allegrini, S.; Giannecchini, M.; Camici, M. & Tozzi, M. G. , *Neuroscience* **2003**, *117*.

[69] Y. Sidi, B. S. Mitchell, *Journal of Clinical Investigation* **1985**, *76*, 2416-2419.

[70] aD. S. Newcombe, *Pediatrics* **1970**, *46*; bL. N. Sweetman, W. L. , *Biochemical Medicine* **1970**, *4*; cJ. G. T. Puig, R. J.; Mateos, F. A.; Ramos, T. H.; Arcas, J. M.; Buno, A. S. & O'Neill, J. P. , *Medicine* **2001**, *80*.

[71] aA. C. Allison, R. W. E. Watts, T. Hovi, A. D. B. Webster, *Lancet* **1975**, *2*, 1179-1183; bA. C. Allison, T. Hovi, R. W. Watts, A. D. Webster, *Ciba Foundation symposium* **1977**, 207-224; cP. J. Benke, D. Dittmar, *Science* **1977**, *198*, 1171-1173.

[72] D. F. H. Wong, J. C.; Naidu, S.; Yokoi, F.; Marenco, S.; Dannals, R. F.; Ravert, H. T.; Yaster, M.; Evans, A.; Rousset, O.; Bryan, R. N.; Gjedde, A.; J., K. M. & Breese, G. R. , *Proceedings of the National Academy of Sciences of the United States of America* **1996**, *93*.

[73] G. W. B. Colleoni, J. A. Bridge, B. Garicochea, J. Liu, D. A. Filippa, M. Ladanyi, *American Journal of Pathology* **2000**, *156*, 781-789.

[74] F. E. Boccalatte, C. Voena, C. Riganti, A. Bosia, L. D'Amico, L. Riera, M. Cheng, B. Ruggeri, O. N. Jensen, V. L. Goss, K. Lee, J. Nardone, J. Rush, R. D. Polakiewicz, M. J. Comb, R. Chiarle, G. Inghirami, *Blood* **2009**, *113*, 2776-2790.

[75] C. Damm-Welk, W. Klapper, I. Oschlies, S. Gesk, S. Roettgers, J. Bradtke, R. Siebert, A. Reiter, W. Woessmann, *British Journal of Haematology* **2009**, *146*, 306-309.

[76] aG. W. B. Colleoni, B. Garicochea, M. Y. Lui, J. A. Bridge, D. A. Filippa, M. Ladanyi, *Laboratory Investigation* **2000**, *80*, 145A; bZ. G. Ma, J. Cools, P. Marynen, X. L. Cui, R. Siebert, S. Gesk, B. Schlegelberger, B. Peeters, C. De Wolf-Peeters, I. Wlodarska, S. W. Morris, *Blood* **2000**, *95*, 2144-2149; cW. Huang, X. Li, X. Yao, Y. Lu, B. Li, W. Sheng, H. Lu, A. Jin, X. Zhou, *Experimental and Molecular Pathology* **2009**, *86*, 121-126.

[77] B. P. Falini, S. & Zinzani, P. E. A., *Blood* **1999**, *93*.

[78] S. H. Fogarty, D. G. , *Biochimica Et Biophysica Acta* **2010**, *1804*.

[79] J. M. G. Corton, J. & Hawley, S. , *European Journal of Biochemistry* **1995**, *229*.

[80] J. T. Mankouri, P. R.; Gretto, S.; Hughes, M. E.; Griffin, S. D. C.; Dallas, M. L.; Green, K. A.; Hardie, D. G.; Peers, C. & Harris, M. , *PNAS* **2010**, *107*.

[81] aK. J. Capps, J. Humiston, R. Dominique, I. Hwang, D. L. Boger, *Bioorganic & Medicinal Chemistry Letters* **2005**, *15*, 2840-2844; bA. Tavassoli, S. J. Benkovic, *Angewandte Chemie-International Edition* **2005**, *44*, 2760-2763.

[82] G. P. Beardsley, B. A. Moroson, E. C. Taylor, R. G. Moran, *Journal of Biological Chemistry* **1989**, *264*, 328-333.

[83] T. H. Marsilje, M. A. Labroli, M. P. Hedrick, Q. Jin, J. Desharnais, S. J. Baker, L. T. Gooljarsingh, J. Ramcharan, A. Tavassoli, Y. Zhang, I. A. Wilson, G. P. Beardsley, S. J. Benkovic, D. L. Boger, *Bioorganic & Medicinal Chemistry* **2002**, *10*, 2739-2749.

[84] J. Desharnais, I. Hwang, Y. Zhang, A. Tavassoli, J. Baboval, S. J. Benkovic, I. A. Wilson, D. L. Boger, *Bioorganic & Medicinal Chemistry* **2003**, *11*, 4511-4521.

[85] C. G. Cheong, D. W. Wolan, S. E. Greasley, P. A. Horton, G. P. Beardsley, I. A. Wilson, *Journal of Biological Chemistry* **2004**, *279*, 18034-18045.

[86] D. L. Boger, N. E. Haynes, M. S. Warren, L. T. Gooljarsingh, J. Ramcharan, P. A. Kitos, S. J. Benkovic, *Bioorganic & Medicinal Chemistry* **1997**, *5*, 1831-1838.

[87] D. L. Boger, N. E. Haynes, M. S. Warren, J. Ramcharan, P. A. Kitos, S. J. Benkovic, *Bioorganic & Medicinal Chemistry* **1997**, *5*, 1853-1857.

[88] aD. L. Boger, N. E. Haynes, M. S. Warren, J. Ramcharan, A. E. Marolewski, P. A. Kitos, S. J. Benkovic, *Bioorganic & Medicinal Chemistry* **1997**, *5*, 1847-1852; bD. L. Boger, M. J. Kochanny, H. Cai, D. Wyatt, P. A. Kitos, M. S. Warren, J. Ramcharan, L. T. Gooljarsingh, S. J. Benkovic, *Bioorganic & Medicinal Chemistry* **1998**, *6*, 643-659.

[89] D. L. Boger, M. A. Labroli, T. H. Marsilje, Q. Jin, M. P. Hedrick, S. J. Baker, J. H. Shim, S. J. Benkovic, *Bioorganic & Medicinal Chemistry* **2000**, *8*, 1075-1086.

[90] D. Bissett, H. L. McLeod, B. Sheedy, M. Collier, Y. Pithavala, L. Paradiso, M. Pitsiladis, J. Cassidy, *British Journal of Cancer* **2001**, *84*, 308-312.

[91] O. Obajimi, J. C. Keen, P. W. Melera, *Prostate* **2009**, *69*, 1206-1221.

[92] J. K. DeMartino, I. Hwang, L. Xu, I. A. Wilson, D. L. Boger, *Journal of Medicinal Chemistry* **2006**, *49*, 2998-3002.

[93] C. J. Allegra, J. C. Drake, J. Jolivet, B. A. Chabner, *Proceedings of the National Academy of Sciences of the United States of America* **1985**, *82*, 4881-4885.

[94] T. Dervieux, T. L. Brenner, Y. Y. Hon, Y. M. Zhou, M. L. Hancock, J. T. Sandlund, G. K. Rivera, R. C. Ribeiro, J. M. Boyett, C. H. Pui, M. V. Relling, W. E. Evans, *Blood* **2002**, *100*, 1240-1247.

[95] aC. J. Allegra, R. L. Fine, J. C. Drake, B. A. Chabner, *Journal of Biological Chemistry* **1986**, *261*, 6478-6485; bC. J. Allegra, K. Hoang, G. C. Yeh, J. C. Drake, J. Baram, *Journal of Biological Chemistry* **1987**, *262*, 13520-13526.

[96] H. E. H. Gruber, M. E.; McAllister, D. R.; Laikind, P. K.; Lane, T. A.; Schmid-Scoenbein, G. W. & Engler, R. L. , *Circulation* **1989**, *80*.

[97] G. P. Budzik, L. M. Colletti, C. R. Faltynek, *Life Sciences* **2000**, *66*, 2297-2307.

[98] B. N. Cronstein, M. A. Eberle, H. E. Gruber, R. I. Levin, *Proceedings of the National Academy of Sciences of the United States of America* **1991**, *88*, 2441-2445.

[99] aJ. A. M. Wessels, S. M. van der Kooij, S. le Cessie, W. Kievit, P. Barerra, C. F. Allaart, T. W. J. Huizinga, H.-J. Guchelaar, R. Pharmacogenetics Collaborative, *Arthritis and Rheumatism* **2007**, *56*, 1765-1775; bA. Hinks, H. Moncrieffe, P. Martin, S. Ursu, S. Lal, L. Kassoumeri, T. Weiler, D. N. Glass, S. D. Thompson, L. R. Wedderburn, W. Thomson, *Annals of the Rheumatic Diseases* **2011**, *70*, 1395-1400.

[100] aT. Dervieux, N. Greenstein, J. Kremer, *Arthritis and Rheumatism* **2006**, *54*, 3095-3103; bT. Dervieux, D. Furst, D. O. Lein, R. Capps, K. Smith, M. Walsh, J. Kremer, *Arthritis and Rheumatism* **2004**, *50*, 2766-2774.

[101] E. Campalani, M. Arenas, A. M. Marinaki, C. M. Lewis, J. N. W. N. Barker, C. H. Smith, *Journal of Investigative Dermatology* **2007**, *127*, 1860-1867.

[102] P. W. Sholar, J. Baram, R. Seither, C. J. Allegra, *Biochemical Pharmacology* **1988**, *37*, 3531-3534.

[103] T. Yamaoka, M. Kondo, S. Honda, H. Iwahana, M. Moritani, S. Ii, K. Yoshimoto, M. Itakura, *Journal of Biological Chemistry* **1997**, *272*, 17719-17725.

[104] aP. Boer, B. Lipstein, A. Devries, O. Sperling, *Biochimica Et Biophysica Acta* **1976**, *432*, 10-17; bP. Bashkin, O. Sperling, *Biochimica Et Biophysica Acta* **1978**, *538*, 505-511; cE. Zorefshani, O. Sperling, *Biochimica Et Biophysica Acta* **1980**, *607*, 503-511.

[105] P. Boer, S. Giler, O. Sperling, *Life Sciences* **1998**, *62*, 2133-2139.

[106] aO. Sperling, P. Boer, B. Lipstein, B. Kupfer, S. Brosh, E. Zoref, P. Bashkin, A. de Vries, *Advances in experimental medicine and biology* **1977**, *76A*, 481-487; bM. M. Welch, F. B. Rudolph, *Journal of Biological Chemistry* **1982**, *257*, 3253-3256.

[107] aM. A. M. Becker, L. J.; Huisman, W. H.; Lazar, C. & Adams, W. B. , *Journal of Biological Chemistry* **1977**, *252*; bL. J. B. Meyer, M. A. , *Journal of Biological Chemistry* **1977**, *252*.

[108] aM. S. Hershfield, J. E. Seegmiller, *Journal of Biological Chemistry* **1976**, *251*, 7348-7354; bP. B. Rowe, E. McCairns, G. Madsen, D. Sauer, H. Elliott, *Journal of Biological Chemistry* **1978**, *253*, 7711-7721.

[109] E. W. W. Holmes, J. B. & Kelley, W. N. , *Journal of Biological Chemistry* **1973**, *248*.

[110] E. W. M. Holmes, J. A.; McCord, J. M.; Wyngaarden, J. B. & Kelley, W. N. , *Journal of Biological Chemistry* **1973**, *248*.

[111] C. A. Caperelli, P. A. Benkovic, G. Chettur, S. J. Benkovic, *Journal of Biological Chemistry* **1980**, *255*, 1885-1890.

[112] G. K. Smith, W. T. Mueller, G. F. Wasserman, W. D. Taylor, S. J. Benkovic, *Biochemistry* **1980**, *19*, 4313-4321.

[113] S. An, R. Kumar, E. D. Sheets, S. J. Benkovic, *Science* **2008**, *320*, 103-106.

[114] F. Verrier, S. An, A. M. Ferrie, H. Sun, M. Kyoung, H. Deng, Y. Fang, S. J. Benkovic, *Nature Chemical Biology* **2011**, *7*, 909-915.

[115] S. An, Y. Deng, J. W. Tomsho, M. Kyoung, S. J. Benkovic, *Proceedings of the National Academy of Sciences of the United States of America* **2010**, *107*, 12872-12876.

[116] Narayanaswamy, *et. al.*, *PNAS* **2009**, *106*.

[117] K. G. Rikova, A.; Zeng, Q.; Possemato, A.; Yu, J.; Haack, H.; Nardone, J.; Lee, K.; Reeves, C.; Li, Y.; Hu, Y.; Tan, Z.; Stokes, M.; Sullivan, L.; Mitchell, J.; Wetzel, R.; MacNeill, J.; Min Ren, J.; Yuan, J.; Bakalarski, C. E.; Villen, J.; Kornhauser, J. M.; Smith, B.; Li, D.; Zhou, X.; Gygi, S. P.; Gu, T.-L.; Polakiewicz, R. D.; Rush, J. & Comb M. , *J. Cell* **2007**, *131*.

[118] C. K. Choudhary, C.; Gnad, F.; Nielsen, M. L.; Rehman, M.; Walther, T. C.; Olsen, J. V. & Mann, M. , *Science* **2009**, *325*.

[119] B.-K. F. Cho, S. A.; Embree, M.; Park, Y.-S.; Kim, D. & Palsson, B. Ø. , *Nucleic Acids Research* **2011**, *39*.

[120] M. M. Arifuzzaman, M.; Itoh, A.; Nishikata, K.; Takita, C.; Saito, R.; Ara, T.; Nakahigashi, K.; Huang, H.-C.; Hirai, A.; Tsuzuki, K.; Nakamura, S.; Altaf-Ul-Amin, M.; Oshima, T.; Baba, T.; Yamamoto, N.; Kawamura, T.; Ioka-Nakamichi, T.; Kitagawa, M.; Tomita, M.; Kanaya, S.; Wada, C. & Mori, H. , *Genome Research* **2006**, *16*.

[121] J. D. H. Thompson, D. G. & Gibson, T. J. , *Nucleic Acids Research* **1994**, *22*, 4673.

[122] F. W. Studier, *Protein Expression and Purification* **2005**, *41*.

[123] E. Gasteiger, Hoogland, C., Gattiker, A., Duvand, S., Wilkins, M. R., Appel, R. D., & Bairoch, A. , *Protein Identification and Analysis Tools on the ExPASy Server* **2005**.

[124] T. W. Wiseman, S.; Brandts, J. F. & Lin, L. N. , *Analytical Biochemistry* **1989**, *179*.

[125] W. B. D. Turnbull, A. H. , *Journal of American Chemical Society* **2003**, *125*.

[126] B. H. Niesen F. H., Vedadi M., *Nature Protocols* **2007**, *2*.

[127] P. Schuck, *Biophysical. Journal* **2000**, *78*.

[128] W. C. Chan, White, P., *Fmoc Solid Phase Peptide Synthesis: A Practical Approach* **2000**.

[129] aL. D. O. Kay, M. J.; Hatefi, Y. & Huennekens, F. M. , *Journal of Biological Chemistry* **1960**, *235*; bD. B. R. Cosulich, B.; Smith Jr, J. M.; Hultquist, M. E. & Parker, R. P. , *Journal of American Chemical Society* **1952**, *74*; cD. R. Robinson, *Methods in Enzymology* **1963**, *6*.

[130] R. L. Blakely, Benkovic, S., J., *Folates and Pterins Vol.2 Chemsitry and Biochemsitry of Pterins* **1985**.

[131] S. J. Benkovic, L. Gooljarsingh, J. Ramcharan, J. H. Shim, M. Wall, *Biochemical Society Transactions* **2000**, *28*, A122.

[132] J. Kim, *J. Appl. Cryst.* **1991**, *24*.

[133] F. S. T. Liger, C. R. , *Optical Biosensors: Today and Tomorrow* **2011**.

[134] D. J. F. Williamson, M. A.; Webb, M. E. & Turnbull, B. E. , *Angewandte Chemie-International Edition* **2012**, *51*.

9 Appendix

9.1 ITC traces

9.1.1.1 Human ATIC

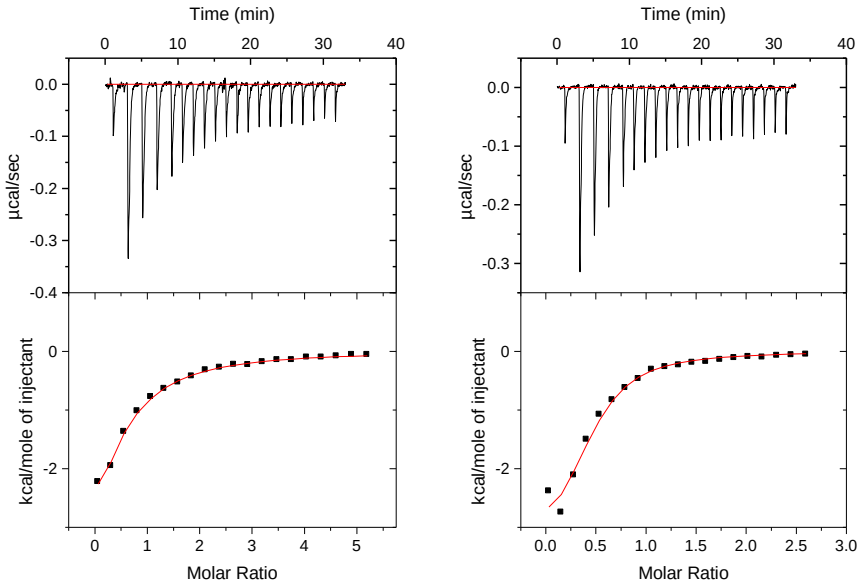

Figure 9-1: ITC of IMP binding (left) and AMP (right) to human ATIC measured at 25 °C.

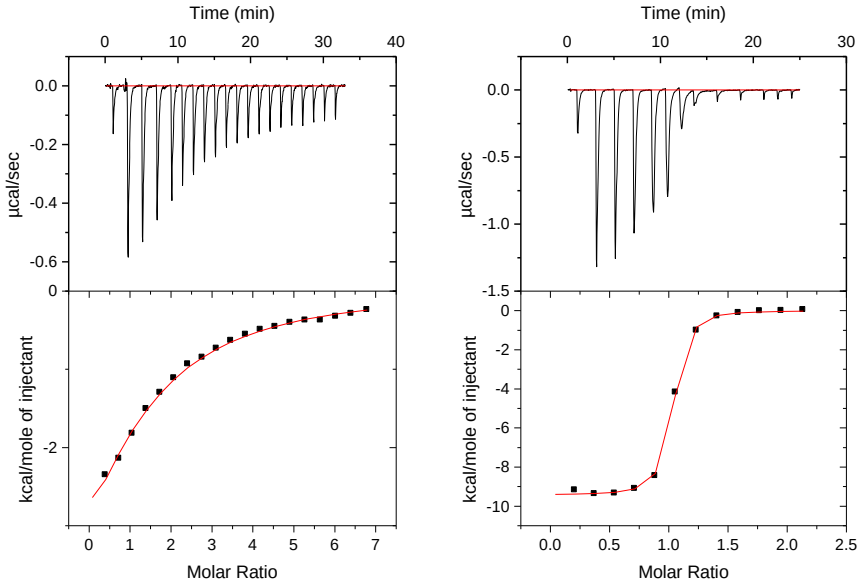

Figure 9-2: ITC of 10-f-H_4F binding (left) and $PteGlu_4$ (right) to human ATIC measured at 25 °C.

9.1.1.2 Avian ATIC

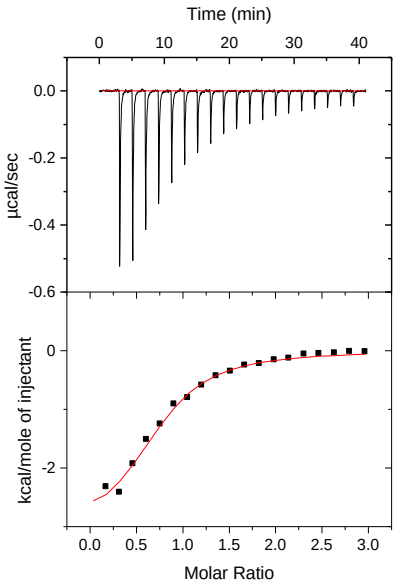

Figure 9-3: Figure 9-4: ITC of AMP binding to avian ATIC measured at 25 °C.

9.1.1.3 IMPCH truncation mutant

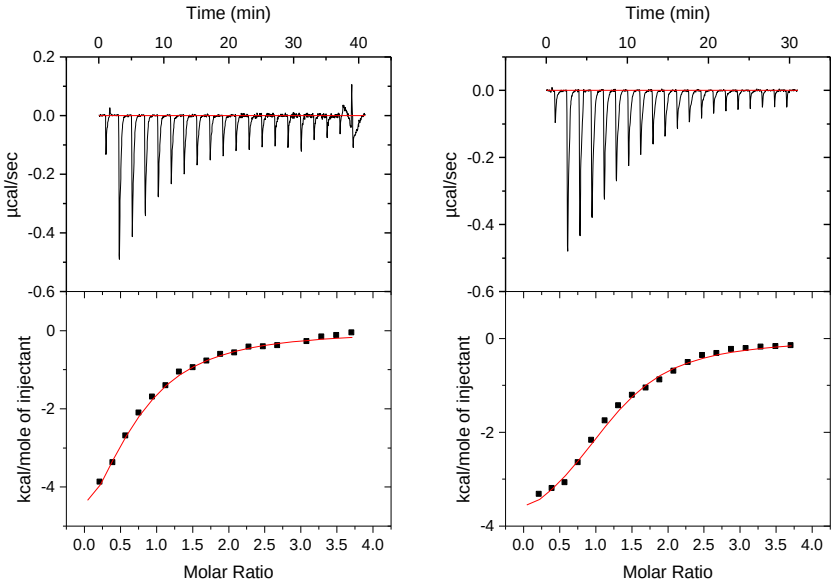

Figure 9-5: ITC of IMP binding (left) and XMP (right) to IMPCH truncation mutant measured at 25 °C.

9.1.1.4 Site directed mutants

9.1.1.5 AICAR binding

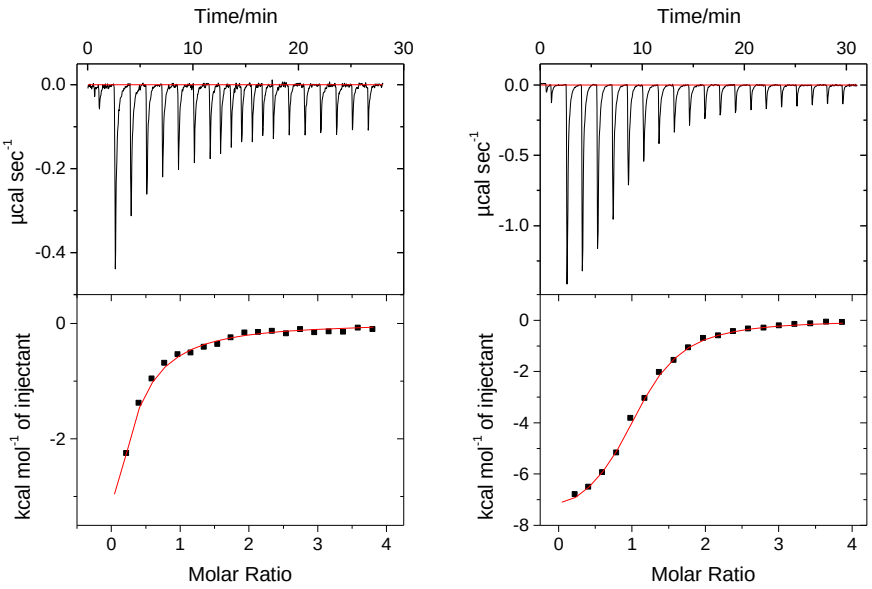

Figure 9-6: ITC of AICAR to S430A (left) and N431A (right) measured at 25 °C.

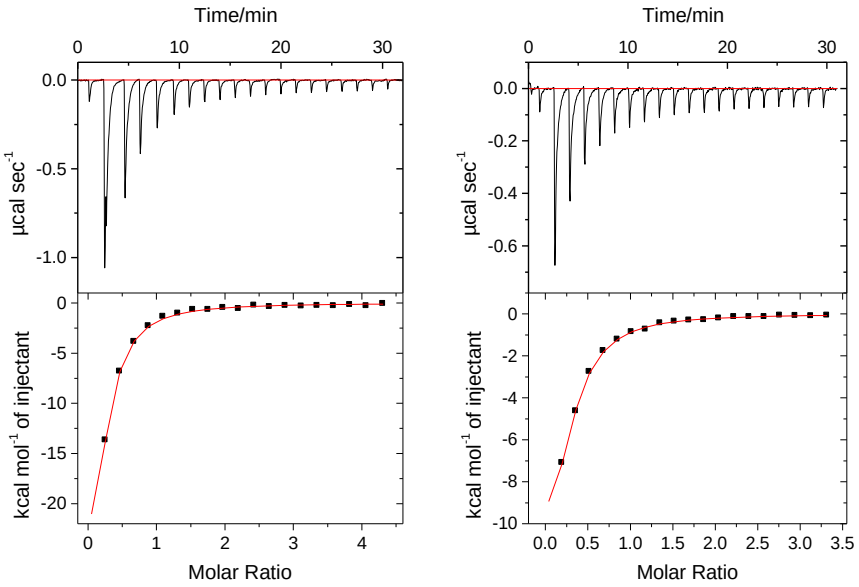

:

Figure 9-7: ITC of AICAR to S430A (left) and N431A (right) measured at 25 °C.

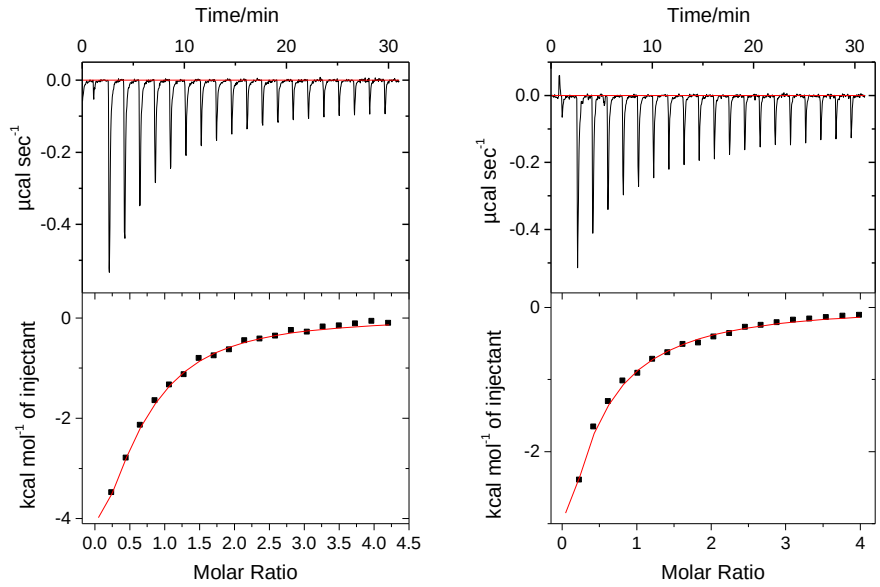

Figure 9-8: ITC of AICAR to D539A (left) and F590I (right) measured at 25 °C.

9.1.1.6 10-f-H4F binding

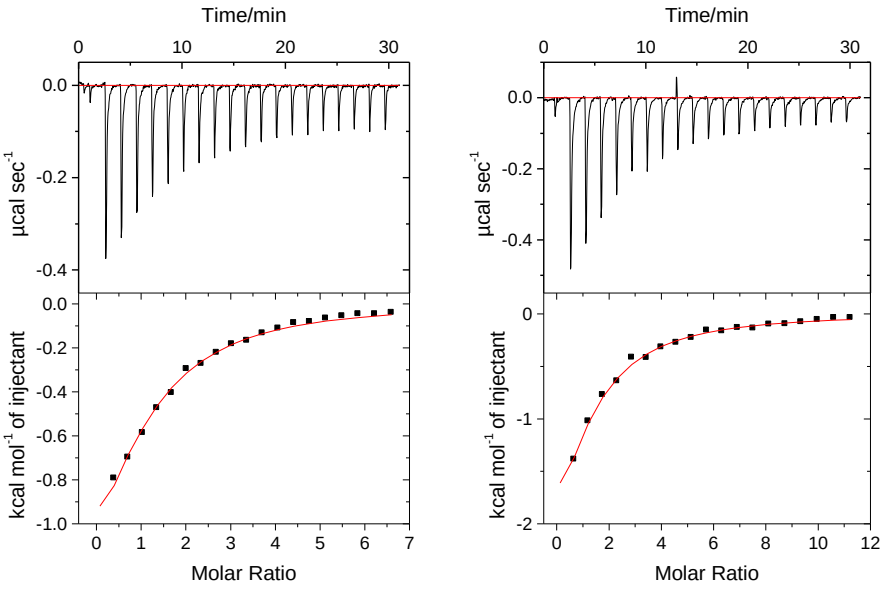

Figure 9-9: ITC of 10-f-H_4F into N431D (left) and D539A (right) measured at 25 °C.

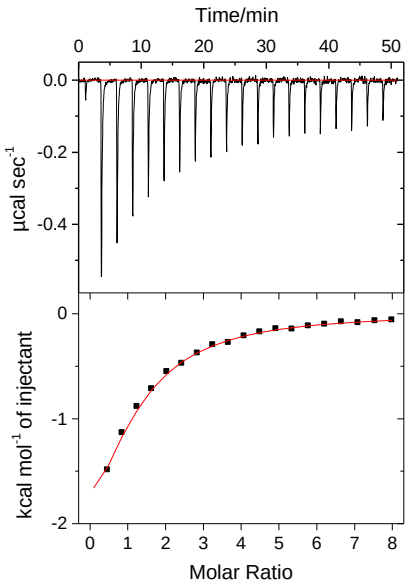

Figure 9-10: ITC of 10-f-H_4F into F590I measured at 25 °C.

9.2 Sequence Alignments

9.2.1.1 Site directed mutants

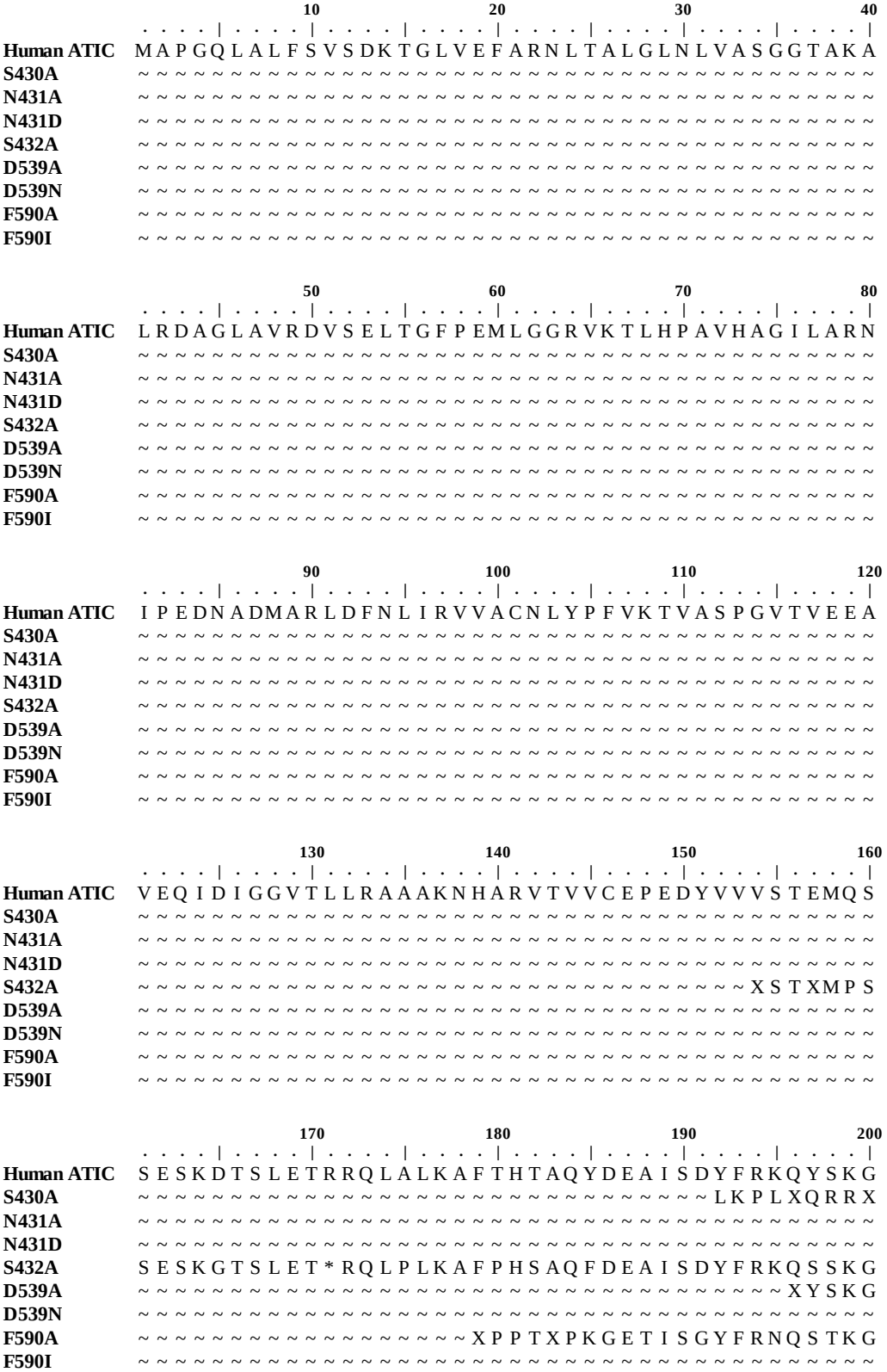

```
                          210                 220                 230                 240
                 . . . . | . . . . | . . . . | . . . . | . . . . | . . . . | . . . . | . . . . |
Human ATIC       V S Q M P L R Y G M N P H Q T P A Q L Y T L Q P K L P I T V L N G A P G F I N L
S430A            P D X X E X W X G I X ~ X Q T P A Q L Y P L Q P K L P I T V L N G A P G F I N L
N431A            ~ ~ ~ ~ X L R Y G M N P H Q T P A P A Y T L Q P K L P I P V L N G A P G F I N L
N431D            ~ ~ ~ ~ ~ ~ ~ ~ ~ ~ ~ ~ ~ ~ ~ ~ ~ ~ ~ ~ ~ ~ ~ ~ ~ ~ ~ ~ ~ ~ ~ ~ ~ ~ ~ ~ ~ ~ ~ ~ ~
S432A            G F Q M P L R Y G M N P H Q T P A Q L Y T X Q P K L P I T V L N G A P G F I N L
D539A            V F P I A * E I G * A P T Q T P A Q L Y T L Q P K L P I P V L N G A P G F I N L
D539N            ~ ~ ~ ~ ~ ~ ~ ~ ~ ~ ~ ~ ~ ~ ~ ~ ~ ~ ~ ~ ~ ~ ~ ~ ~ ~ ~ ~ ~ ~ ~ ~ ~ ~ ~ ~ ~ ~ ~ ~ ~
F590A            V F Q A P W X X W M N P L Q T L A Q L Y Q L Q P K L P I P V L N G A P G F I N L
F590I            ~ ~ ~ ~ ~ ~ ~ X E M N H N Q D P G K L Y X X Q X K X X I X S L N G A X E X I N X

                          250                 260                 270                 280
                 . . . . | . . . . | . . . . | . . . . | . . . . | . . . . | . . . . | . . . . |
Human ATIC       C D A L N A W Q L V K E L K E A L G I P A A A S F K H V S P A G A A V G I P L S
S430A            C D A L N A W Q L V K E L K E A L G I P A A A S F K H V S P A G A A V G I P L S
N431A            C D A L N A W Q L V K E L K E A L G I P A A A S F K H V S P A G A A V G I P L S
N431D            ~ ~ ~ ~ ~ ~ ~ ~ ~ ~ ~ ~ ~ ~ ~ ~ ~ ~ ~ ~ ~ ~ ~ ~ ~ ~ ~ ~ ~ ~ ~ ~ ~ ~ ~ ~ ~ ~ ~ ~ ~
S432A            C D A L N A W Q L V K E L K E A L G I P A A A S F K H V S P A G A A V G I P L S
D539A            C D A L N A W Q L V K E L K E A L G I P A A A S F K H V S P A G A A V G I P L S
D539N            ~ ~ ~ ~ ~ ~ ~ ~ ~ ~ ~ ~ ~ ~ ~ ~ ~ ~ ~ ~ ~ ~ ~ ~ ~ ~ ~ ~ ~ ~ ~ ~ ~ ~ ~ ~ ~ ~ ~ ~ ~
F590A            C D A L N A W Q L V K E F K E A L G I P A A A S F K H V S P A G A A V G I P L S
F590I            C D A X D A X Q A V X X L Q X A L X X P A A A X F K H V S X A X A A V X I P L S

                          290                 300                 310                 320
                 . . . . | . . . . | . . . . | . . . . | . . . . | . . . . | . . . . | . . . . |
Human ATIC       E D E A K V C M V Y D L Y K T L T P I S A A Y A R A R G A D R M S S F G D F V A
S430A            E D E A K V C M V Y D L Y K T L T P I S A A Y A R A R G A D R M S S F G D F V A
N431A            E D E A K V C M V Y D L Y K T L T P I S A A Y A R A R G A D R M S S F G D F V A
N431D            ~ ~ ~ ~ ~ ~ ~ ~ ~ ~ ~ ~ ~ ~ ~ ~ ~ ~ ~ ~ ~ ~ ~ ~ ~ ~ ~ ~ ~ ~ ~ ~ ~ ~ ~ G D L V A
S432A            E D E A K V C M V Y D L Y K T L T P I S A A Y A R A R G A D R M S S F G D F V A
D539A            E D E A K V C M V Y D L Y K T L T P I S A A Y A R A R G A D R M S S F G D F V A
D539N            ~ ~ ~ ~ ~ ~ ~ M V Y D L Y K T L T P I S A A Y A R A R G A D R M S S F G D F V A
F590A            E D E A K V C M V Y D L Y K T L T P I S A A Y A R A R G A D R M S S F G D F V A
F590I            E D E A K V C M V Y D L Y K T L T P I S A A Y A R A R G A D R M S S F G D F V A

                          330                 340                 350                 360
                 . . . . | . . . . | . . . . | . . . . | . . . . | . . . . | . . . . | . . . . |
Human ATIC       L S D V C D V P T A K I I S R E V S D G I I A P G Y E E E A L T I L S K K K N G
S430A            L S D V C D V P T A K I I S R E V S D G I I A P G Y E E E A L T I L S K K K N G
N431A            L S D V C D V P T A K I I S R E V S D G I I A P G Y E E E A L T I L S K K K N G
N431D            Y S D V W D V P T A N I F S R E V Y D G I I A P G Y E E E A L T I L S K K K N G
S432A            L S D V C D V P T A K I I S R E V S D G I I A P G Y E E E A L T I L S K K K N G
D539A            L S D V C D V P T A K I I S R E V S D G I I A P G Y E E E A L T I L S K K K N G
D539N            L S D V C D V P T A K I I S R E V S D G I I A P G Y E E E A L T I L S K K K N G
F590A            L S D V C D V P T A K I I S R E V S D G I I A P G Y E E E A L T I L S K K K N G
F590I            L S D V C D V P T A K I I S R E V S D G I I A P G Y E E E A L T I L S K K K N G

                          370                 380                 390                 400
                 . . . . | . . . . | . . . . | . . . . | . . . . | . . . . | . . . . | . . . . |
Human ATIC       N Y C V L Q M D Q S Y K P D E N E V R T L F G L H L S Q K R N N G V V D K S L F
S430A            N Y C V L Q M D Q S Y K P D E N E V R T L F G L H L S Q K R N N G V V D K S L F
N431A            N Y C V L Q M D Q S Y K P D E N E V R T L F G L H L S Q K R N N G V V D K S L F
N431D            N Y C V L Q M D Q S Y K P D E N E V R T L F G L H L S Q K R N N G V V D K S L F
S432A            N Y C V L Q M D Q S Y K P D E N E V R T L F G L H L S Q K R N N G V V D K S L F
D539A            N Y C V L Q M D Q S Y K P D E N E V R T L F G L H L S Q K R N N G V V D K S L F
D539N            N Y C V L Q M D Q S Y K P D E N E V R T L F G L H L S Q K R N N G V V D K S L F
F590A            N Y C V L Q M D Q S Y K P D E N E V R T L F G L H L S Q K R N N G V V D K S L F
```

```
F590I          N Y C V L Q M D Q S Y K P D E N E V R T L F G L H L S Q K R N N G V V D K S L F

                                410                 420                 430                 440
                    . . . . | . . . . | . . . . | . . . . | . . . . | . . . . | . . . . | . . . . |
Human ATIC     S N V V T K N K D L P E S A L R D L I V A T I A V K Y T Q S N S V C Y A K N G Q
S430A          S N V V T K N K D L P E S A L R D L I V A T I A V K Y T Q A N S V C Y A K N G Q
N431A          S N V V T K N K D L P E S A L R D L I V A T I A V K Y T Q S A S V C Y A K N G Q
N431D          S N V V T K N K D L P E S A L R D L I V A T I A V K Y T Q S D S V C Y A K N G Q
S432A          S N V V T K N K D L P E S A L R D L I V A T I A V K Y T Q S N A V C Y A K N G Q
D539A          S N V V T K N K D L P E S A L R D L I V A T I A V K Y T Q S N S V C Y A K N G Q
D539N          S N V V T K N K D L P E S A L R D L I V A T I A V K Y T Q S N S V C Y A K N G Q
F590A          S N V V T K N K D L P E S A L R D L I V A T I A V K Y T Q S N S V C Y A K N G Q
F590I          S N V V T K N K D L P E S A L R D L I V A T I A V K Y T Q S N S V C Y A K N G Q

                                450                 460                 470                 480
                    . . . . | . . . . | . . . . | . . . . | . . . . | . . . . | . . . . | . . . . |
Human ATIC     V I G I G A G Q Q S R I H C T R L A G D K A N Y W W L R H H P Q V L S M K F K T
S430A          V I G I G A G Q Q S R I H C T R L A G D K A N Y W W L R H H P Q V L S M K F K T
N431A          V I G I G A G Q Q S R I H C T R L A G D K A N Y W W L R H H P Q V L S M K F K T
N431D          V I G I G A G Q Q S R I H C T R L A G D K A N Y W W L R H H P Q V L S M K F K T
S432A          V I G I G A G Q Q S R I H C T R L A G D K A N Y W W L R H H P Q V L S M K F K T
D539A          V I G I G A G Q Q S R I H C T R L A G D K A N Y W W L R H H P Q V L S M K F K T
D539N          V I G I G A G Q Q S R I H C T R L A G D K A N Y W W L R H H P Q V L S M K F K T
F590A          V I G I G A G Q Q S R I H C T R L A G D K A N Y W W L R H H P Q V L S M K F K T
F590I          V I G I G A G Q Q S R I H C T R L A G D K A N Y W W L R H H P Q V L S M K F K T

                                490                 500                 510                 520
                    . . . . | . . . . | . . . . | . . . . | . . . . | . . . . | . . . . | . . . . |
Human ATIC     G V K R A E I S N A I D Q Y V T G T I G E D E D L I K W K A L F E E V P E L L T
S430A          G V K R A E I S N A I D Q Y V T G T I G E D E D L I K W K A L F E E V P E L L T
N431A          G V K R A E I S N A I D Q Y V T G T I G E D E D L I K W K A L F E E V P E L L T
N431D          G V K R A E I S N A I D Q Y V T G T I G E D E D L I K W K A L F E E V P E L L T
S432A          G V K R A E I S N A I D Q Y V T G T I G E D E D L I K W K A L F E E V P E L L T
D539A          G V K R A E I S N A I D Q Y V T G T I G E D E D L I K W K A L F E E V P E L L T
D539N          G V K R A E I S N A I D Q Y V T G T I G E D E D L I K W K A L F E E V P E L L T
F590A          G V K R A E I S N A I D Q Y V T G T I G E D E D L I K W K A L F E E V P E L L T
F590I          G V K R A E I S N A I D Q Y V T G T I G E D E D L I K W K A L F E E V P E L L T

                                530                 540                 550                 560
                    . . . . | . . . . | . . . . | . . . . | . . . . | . . . . | . . . . | . . . . |
Human ATIC     E A E K K E W V E K L T E V S I S S D A F F P F R D N V D R A K R S G V A Y I A
S430A          E A E K K E W V E K L T E V S I S S D A F F P F R D N V D R A K R S G V A Y I A
N431A          E A E K K E W V E K L T E V S I S S D A F F P F R D N V D R A K R S G V A Y I A
N431D          E A E K K E W V E K L T E V S I S S D A F F P F R D N V D R A K R S G V A Y I A
S432A          E A E K K E W V E K L T E V S I S S D A F F P F R D N V D R A K R S G V A Y I A
D539A          E A E K K E W V E K L T E V S I S S A A F F P F R D N V D R A K R S G V A Y I A
D539N          E A E K K E W V E K L T E V S I S S N A F F P F R D N V D R A K R S G V A Y I A
F590A          E A E K K E W V E K L T E V S I S S D A F F P F R D N V D R A K R S G V A Y I A
F590I          E A E K K E W V E K L T E V S I S S D A F F P F R D N V D R A K R S G V A Y I A

                                570                 580                 590                 600
                    . . . . | . . . . | . . . . | . . . . | . . . . | . . . . | . . . . | . . . . |
Human ATIC     A P S G S A A D K V V I E A C D E L G I I L A H T N L R L F H H * ~ ~ ~ ~ ~ ~ ~
S430A          A P S G S A A D K V V I E A C D E L G I I L A H T N L R L F H H * G S E F E L R
N431A          A P S G S A A D K V V I E A C D E L G I I L A H T N L R L F H H * G S E F E L R
N431D          A P S G S A A D K V V I E A C D E L G I I L A H T N L R L F H H * G S E F E L R
S432A          A P S G S A A D K V V I E A C D E L G I I L A H T N L R L F H H * G S E F E L R
D539A          A P S G S A A D K V V I E A C D E L G I I L A H T N L R L F H H * G S E F E L R
D539N          A P S G S A A D K V V I E A C D E L G I I L A H T N L R L F H H * G S E F E L R
```

Figure 9-11: Sequence alignment of the site directed mutants to human ATIC.

9.2.1.2 Human ATIC with TEV linker

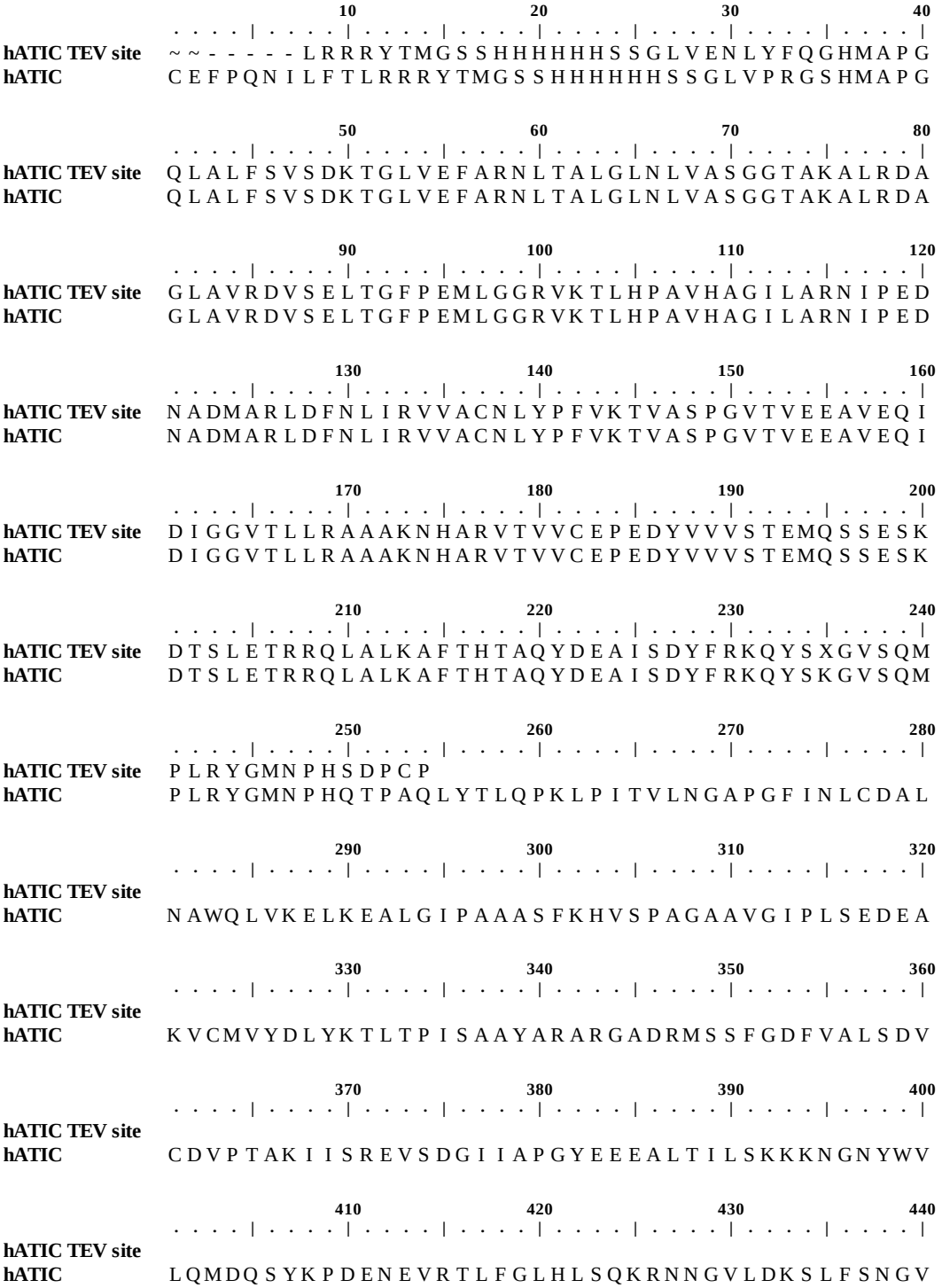

Figure 9-12: Sequence alignment of the human ATIC construct containing a TEV recognition site to human ATIC.

9.2.1.3 Avian ATIC with TEV linker

```
                          10                  20                  30                  40
                  . . . . | . . . . | . . . . | . . . . | . . . . | . . . . | . . . . | . . . . |
aATIC TEV site    R R R Y T M G S S H H H H H H S S G L V E N L Y F Q G H M A A R Q Q L A L L S V
aATIC             ~ ~ ~ ~ ~ ~ ~ ~ ~ ~ ~ ~ ~ ~ ~ ~ ~ ~ ~ ~ ~ ~ ~ ~ ~ ~ ~ ~ ~ ~ M A A R Q Q L A L L S V

                          50                  60                  70                  80
                  . . . . | . . . . | . . . . | . . . . | . . . . | . . . . | . . . . | . . . . |
aATIC TEV site    S E K A G L V E F A R S L N A L G L G L I A S G G T A T A L R D A G L P V R D V
aATIC             S E K A G L V E F A R S L N A L G L G L I A S G G T A T A L R D A G L P V R D V

                          90                  100                 110                 120
                  . . . . | . . . . | . . . . | . . . . | . . . . | . . . . | . . . . | . . . . |
aATIC TEV site    S D L T G F P E M L G G R V K T L H P A V H A G I L A R N I P E D N A D M N K Q
aATIC             S D L T G F P E M L G G R V K T L H P A V H A G I L A R N I P E D N A D M N K Q

                          130                 140                 150                 160
                  . . . . | . . . . | . . . . | . . . . | . . . . | . . . . | . . . . | . . . . |
aATIC TEV site    D F S L V R V V V C N L Y P F V K T V S S P G V T V P E A V E K I D I G G V A L
aATIC             D F S L V R V V V C N L Y P F V K T V S S P G V T V P E A V E K I D I G G V A L

                          170                 180                 190                 200
                  . . . . | . . . . | . . . . | . . . . | . . . . | . . . . | . . . . | . . . . |
aATIC TEV site    L R A A A K N H A R V T V V C D P A D Y S S V A K E M A A S K D K D T S V E T R
aATIC             L R A A A K N H A R V T V V C D P A D Y S S V A K E M A A S K D K D T S V E T R

                          210                 220                 230                 240
                  . . . . | . . . . | . . . . | . . . . | . . . . | . . . . | . . . . | . . . . |
aATIC TEV site    R H L A L K A F T H T A Q Y D A A I S D Y F R K E Y S K G V S Q L P L R Y G M N
aATIC             R H L A L K A F T H T A Q Y D A A I S D Y F R K E Y S K G V S Q L P L R Y G M N

                          250                 260                 270                 280
                  . . . . | . . . . | . . . . | . . . . | . . . . | . . . . | . . . . | . . . . |
aATIC TEV site    P H Q S P A Q L Y T T R P K L P L T V V N G S P G F I N L C D A L N A W Q L V K
aATIC             P H Q S P A Q L Y T T R P K L P L T V V N G S P G F I N L C D A L N A W Q L V K

                          290                 300                 310                 320
                  . . . . | . . . . | . . . . | . . . . | . . . . | . . . . | . . . . | . . . . |
aATIC TEV site    E L K Q A L G I P A A A S F K H V S P A G A A V G I P L S E E E A Q V C M V H D
aATIC             E L K Q A L G I P A A A S F K H V S P A G A A V G I P L S E E E A Q V C M V H D

                          330                 340                 350                 360
                  . . . . | . . . . | . . . . | . . . . | . . . . | . . . . | . . . . | . . . . |
aATIC TEV site    L H K T L T X L A S A Y A R S K
aATIC             L H K T L T P L A S A Y A R S R G A D R M S S F G D F I A L S D I C D V P T A K

                          370                 380                 390                 400
                  . . . . | . . . . | . . . . | . . . . | . . . . | . . . . | . . . . | . . . . |
aATIC TEV site
aATIC             I I S R E V S D G V V A P G Y E E E A L K I L S K K K N G G Y C V L Q M D P N Y

                          410                 420                 430                 440
                  . . . . | . . . . | . . . . | . . . . | . . . . | . . . . | . . . . | . . . . |
aATIC TEV site
aATIC             E P D D N E I R T L Y G L Q L M Q K R N N A V I D R S L F K N I V T K N K T L P

                          450                 460                 470                 480
                  . . . . | . . . . | . . . . | . . . . | . . . . | . . . . | . . . . | . . . . |
aATIC TEV site
aATIC             E S A V R D L I V A S I A V K Y T Q S N S V C Y A K D G Q V I G I G A G Q Q S R
```

Figure 9-13: Sequence alignment of the avian ATIC construct containing a TEV recognition site to avian ATIC.

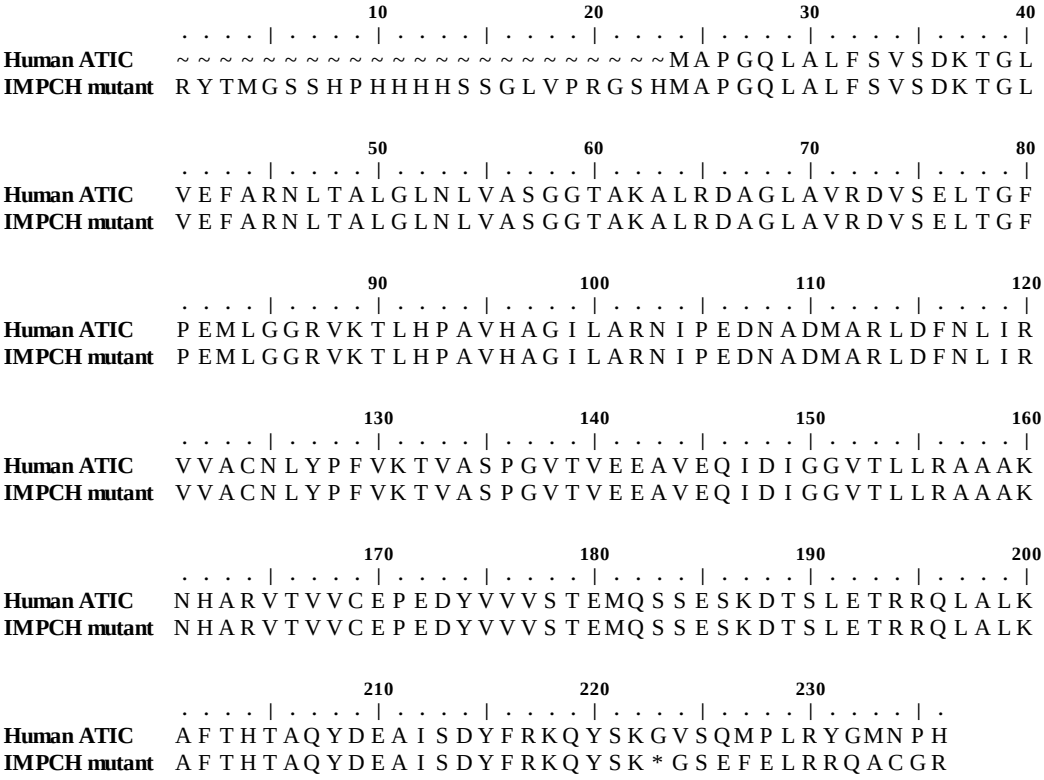

9.2.1.4 IMPCH truncation mutant

```
                                 10                  20                  30                  40
               . . . . | . . . . | . . . . | . . . . | . . . . | . . . . | . . . . | . . . . |
Human ATIC     ~ ~ ~ ~ ~ ~ ~ ~ ~ ~ ~ ~ ~ ~ ~ ~ ~ ~ ~ ~ ~ ~ ~ M A P G Q L A L F S V S D K T G L
IMPCH mutant   R Y T M G S S H P H H H H S S G L V P R G S H M A P G Q L A L F S V S D K T G L

                                 50                  60                  70                  80
               . . . . | . . . . | . . . . | . . . . | . . . . | . . . . | . . . . | . . . . |
Human ATIC     V E F A R N L T A L G L N L V A S G G T A K A L R D A G L A V R D V S E L T G F
IMPCH mutant   V E F A R N L T A L G L N L V A S G G T A K A L R D A G L A V R D V S E L T G F

                                 90                 100                 110                 120
               . . . . | . . . . | . . . . | . . . . | . . . . | . . . . | . . . . | . . . . |
Human ATIC     P E M L G G R V K T L H P A V H A G I L A R N I P E D N A D M A R L D F N L I R
IMPCH mutant   P E M L G G R V K T L H P A V H A G I L A R N I P E D N A D M A R L D F N L I R

                                130                 140                 150                 160
               . . . . | . . . . | . . . . | . . . . | . . . . | . . . . | . . . . | . . . . |
Human ATIC     V V A C N L Y P F V K T V A S P G V T V E E A V E Q I D I G G V T L L R A A A K
IMPCH mutant   V V A C N L Y P F V K T V A S P G V T V E E A V E Q I D I G G V T L L R A A A K

                                170                 180                 190                 200
               . . . . | . . . . | . . . . | . . . . | . . . . | . . . . | . . . . | . . . . |
Human ATIC     N H A R V T V V C E P E D Y V V V S T E M Q S S E S K D T S L E T R R Q L A L K
IMPCH mutant   N H A R V T V V C E P E D Y V V V S T E M Q S S E S K D T S L E T R R Q L A L K

                                210                 220                 230
               . . . . | . . . . | . . . . | . . . . | . . . . | . . . . | . . . . | .
Human ATIC     A F T H T A Q Y D E A I S D Y F R K Q Y S K G V S Q M P L R Y G M N P H
IMPCH mutant   A F T H T A Q Y D E A I S D Y F R K Q Y S K * G S E F E L R R Q A C G R
```

Figure 9-14: Sequence alignment of the IMPCH truncation mutant to human ATIC showing a stop codon at Gly200.